LASER POWDER BED FUSION OF TITANIUM MATRIX COMPOSITES

Laser Powder Bed Fusion of Titanium Matrix Composites

By

ESKANDAR FEREIDUNI, BSc., MSc.

A Thesis

Submitted to the School of Graduate Studies in Partial Fulfillment of the Requirements

for the Degree Doctor of Philosophy

McMaster University

DOCTOR OF PHILOSOPHY (2021) McMaster University

(Mechanical Engineering) Hamilton, Ontario

TITLE: Laser Powder Bed Fusion of Titanium Matrix Composites

AUTHOR: Eskandar Fereiduni

B.Sc. in Materials Science and Engineering (Yazd University, Yazd, Iran)

M.Sc. in Materials Science and Engineering (Sharif University of Technology, Tehran, Iran)

SUPERVISOR: Dr. M. A. Elbestawi

NUMBER OF PAGES: xxxii, 354

Preface

This Ph.D. thesis is an integrated article thesis, also known as sandwich thesis, which has been composed of seven main chapters all focusing on the laser powder bed fusion additive manufacturing of metal matrix composites, specifically titanium matrix composites. The chapters represent papers which are either published or under consideration for publication in authentic international journals.

Chapter 1 provides a comprehensive literature review on the process-structure-property relationships in additive manufacturing of metal matrix composites. This chapter is reprinted from the chapter published in the book entitled "*Additive Manufacturing of Emerging Materials*" as "Process-structure-property relationships in additively manufactured metal matrix composites" by Eskandar Fereiduni, and Mohamed Elbestawi. It is of note that a few revisions have been made to the published chapter mainly to update the acronyms of the additive manufacturing processes. These revisions have been added to Chapter 1 as footnotes where applicable.

Chapter 2 is focused on the preparation and characterization of composite powders meeting the requirements of the laser powder bed fusion process. The work presented in this chapter was previously published in the "*Materials*" journal as "Characterization of Composite Powder Feedstock from Powder Bed Fusion Additive Manufacturing Perspective" by Eskandar Fereiduni, Ali Ghasemi, and Mohamed Elbestawi.

Chapter 3 deals with a fundamental understanding of the laser/material interactions and the subsequent microstructural evolutions associated with the laser powder bed fusion processing of composite systems. The work presented in this chapter was previously published in the "*Materials and Design*" journal as "Selective laser melting of hybrid ex-

situ/in-situ reinforced titanium matrix composites: Laser/powder interaction, reinforcement formation mechanism, and non-equilibrium microstructural evolutions" by Eskandar Fereiduni, Ali Ghasemi, and Mohamed Elbestawi.

Chapter 4 is concerned with identifying the role that the location of the starting reinforcing agent plays in the laser powder bed fusion processing of ball milled composite powders. The work presented in this chapter was previously published in the "*Materials Letters*" journal as "Laser Powder Bed Fusion Processability of Ti-6Al-4V Powder Decorated by B_4C Particles" by Eskandar Fereiduni, Ali Ghasemi, Mohamed Elbestawi, Suraj Dinkar Jadhav, and Kim Vanmeensel.

Chapter 5 discusses the processability, microstructure evolution, and mechanical properties of the laser powder bed fusion fabricated titanium matrix composites and provides a detailed comparison between the composites and non-reinforced counterparts in the as-build condition. The work presented in this chapter is currently under consideration for publication in the *"Journal of Alloys and Compounds"* as "Microstructural characterization and mechanical properties of nano-scale/sub-micron TiB-reinforced titanium matrix composites fabricated by laser powder bed fusion" by Eskandar Fereiduni, Ali Ghasemi, and Mohamed Elbestawi.

Chapter 6 explores the influence of different heat treatment strategies on the microstructure and mechanical properties of the laser powder bed fusion fabricated titanium matrix composites and their non-reinforced counterparts. The work presented in this chapter is currently under consideration for publication in the *"Additive Manufacturing" journal* as "Unique opportunities for microstructure engineering via trace

B_4C addition to Ti-6Al-4V through laser powder bed fusion process: As-built and heat-treated scenarios" by Eskandar Fereiduni, Ali Ghasemi, and Mohamed Elbestawi.

Chapter 7 deals with evaluating the short-term creep performance of the laser powder bed fusion fabricated composite and non-reinforced parts in the as-built and heat-treated scenarios. The work presented in this chapter was previously published in the *"Journal of Manufacturing Processes"* as "TiB reinforced Ti-6Al-4V matrix composites with improved short-term creep performance fabricated by laser powder bed fusion" by Eskandar Fereiduni, Ali Ghasemi, and Mohamed Elbestawi.

Chapter 8 summarizes the main conclusions and contribution of the thesis, highlights the strength and limitations, and presents some suggestions for future work.

I declare that this thesis is an original report of my research, has been written by me and has not been submitted for any previous degree.

Eskandar Fereiduni

October 2021

Abstract

Laser powder bed fusion (L-PBF) is an additive manufacturing (AM) process in which an object is manufactured in a layer-by-layer manner from a batch of loose powder using a mobile laser beam as the heat source. Due to the layer-wise nature of the L-PBF process, it is capable of producing objects with complex shapes and unique geometries in bulk, porous, or cellular forms with potential applications in various industries, including aerospace, biomedical, and automotive, among others. The AM technology has recently attracted a great deal of attention in fabricating metal matrix composite (MMC) components with improved mechanical and functional properties than the non-reinforced metallic counterparts. However, full implementation of this promising technology in manufacturing high-quality MMCs is rather challenging in many aspects, such as preparing the starting material, obtaining defect-free parts, and finding suitable post-processing treatments.

This research deals with the fabrication of high-performance titanium matrix composites (TMCs) by L-PBF processing of the B_4C/Ti-6Al-4V(Ti64) composite powders. Results revealed that almost fully dense TMC samples could be achieved by optimizing the process variables. To tailor the mechanical properties of the fabricated TMCs, various heat treatment cycles were employed for both TMC and monolithic Ti64 parts. The microstructures of the as-built and heat-treated TMC and Ti64 samples were thoroughly examined and correlated to the microhardness, nanohardness, wear, scratch, compression, and short-term creep properties. In

addition, the strengthening mechanisms were investigated, and each mechanism's contribution to the compressive yield strengths was identified. Results revealed that the optimum heat treatment cycle for the fabricated TMC samples differs from that of the Ti64 alloy.

To my parents,

I owe you everything.

Acknowledgments

First and foremost, I would like to thank my supervisor, Professor Mohamed Elbestawi, who has been a tremendous mentor and teacher. Your insightful feedback pushed me to sharpen my thinking and brought my work to a higher level. I would like to thank you for your support and patience along the way in this four-year journey.

My sincere thanks must also go to the members of my supervisory committee, Dr. David Wilkinson and Dr. Eugene Ng, for their valuable and constructive feedback, interesting discussions, and insightful comments. There is no way to express how much it meant to me to have been a member of the AMG group at McMaster University. I want to thank my colleagues for the discussions, presentation rehearsals, and fruitful group meetings. I would particularly like to single out my closest friend, Ali Ghasemi, for his friendship, support, assistance, and taking the time to share his knowledge with me. I would like to thank Dr. J. E. Greedan and Evan Smith from the Department of Chemistry at McMaster University for providing us with the ball milling facility. I want to extend my thanks to the Center for Advanced Nuclear Systems (CANS) at McMaster University for providing us with the electron backscattered diffraction (EBSD) analysis facility. I am most grateful to our collaborators, Dr. Suraj Dinkar Jadhav, and Dr. Kim Vanmeensel at the Department of Materials Engineering, KU Leuven, Belgium, for lending me their expertise and intuition.

I deeply thank my parents for their unconditional trust, timely encouragement, and endless patience. I am forever indebted to my parents for giving me the opportunities and experiences to make me who I am. They selflessly encouraged me to explore new directions in life and seek my destiny. This journey would not have been possible if not for them, and I dedicate this milestone to them.

Contents

Page

Contents ..... **x**

List of Figures xviii

List of Tables xxxi

1 Chapter 1 Introduction and literature review **1**

1.1 Why AM instead of conventional manufacturing for MMC fabrication? **5**

1.2 Additively Manufactured MMCs (Challenges, Opportunities, and Existing Literature) **7**

1.2.1 Aluminum-Matrix Composites (AMCs) 7

1.2.2 Titanium-Matrix Composites (TMCs) 9

1.2.3 Nickel-based Matrix Composites 10

1.2.4 Copper-Matrix Composites 13

1.2.5 Iron-based Matrix Composites 14

1.3 Pre-Processing of Mixed Powder System **17**

1.4 Microstructural Evolution in Additively Manufactured MMCs **23**

1.5 Characteristics of Reinforcements Distributed in the Matrix **24**

1.5.1 Size and Morphology of Reinforcements 25

1.5.1.1 Ex-Situ Reinforced MMCs 25

1.5.1.2 In-Situ Reinforced MMCs 26

1.5.2 Distribution Pattern of Reinforcements 27

1.5.2.1 Effect of Scanning Speed 28

1.5.2.2 Effect of Energy Density 30

1.5.2.3 Effects of Size and Volume Fraction of Reinforcements 30

1.6 Reinforcement/Matrix Reactions 31

1.6.1 Reaction Mechanisms 31

1.6.2 Reinforcements/Matrix Interfacial Reaction 32

1.6.3 Formation of In-Situ Reaction Products 39

1.7 Microstructural Evolutions in the Matrix Induced by the Presence of Reinforcements 42

1.7.1 Microstructural Refinement of the Matrix 42

1.7.2 Texture of the Matrix 46

1.7.3 Microstructural Evolution and Phase Transformation 48

1.7.4 Formation of Supersaturated Matrix 52

1.7.5 Formation of Dislocations in the Matrix 53

1.8 Part Quality and Surface Integrity of AM Processed MMCs 55

1.8.1 Applied Energy Density 56

1.8.2 Characteristics of Mixed Powder System 59

1.9 Mechanical Properties of AM processed MMCs 62

1.9.1 Strengthening Mechanisms 63

1.9.1.1 Direct Strengthening 63

Reinforcement Volume Fraction 65

Reinforcement Type 66

Reinforcement Size 67

1.9.1.2 Indirect Strengthening 69

Grain Refinement of the Matrix 70

Increased Density of Dislocations in the Matrix 71

The Matrix Strengthening Caused by Microstructural Modifications 73

Solid Solution Strengthening of the Matrix 74

1.9.2 Weakening Mechanisms 75

1.9.2.1 Decreased Densification Level 76

1.9.2.2 Microstructure Coarsening 76

1.9.2.3 Microstructural Inhomogeneity 76

1.10 Wear Behavior 77

1.10.1 Effect of Size and Volume Fraction of Reinforcements 77

1.10.2 Effect of Applied Energy Density 80

1.11 References 81

2 Chapter 2 Characterization of Composite Powder Feedstock from Powder Bed Fusion Additive Manufacturing Perspective 97

2.1 Introduction 99

2.2 Materials and Methods 102

2.2.1 Powder Preparation 103

2.2.2 Powder Characterization 104

2.2.2.1 Microstructure and XRD Analysis 104

2.2.2.2 Particle Size, Size Distribution and Sphericity 104

2.2.2.3 Flow Characteristics 105

2.3 Results and Discussions 108

2.3.1 XRD Analysis: Plastic Deformation and Phase Formation 108

2.3.2 Microstructural Characterization 109

2.3.3 Particle Size, Size Distribution and Sphericity 114

2.3.4 Flow behavior and conditioned bulk density (CBD) 119

2.3.4.1 Flowability 119

2.3.4.2 Conditioned bulk density (CBD) 126

2.3.5 Material Loss 127

2.3.6 Selection of the best possible composite powder 128

2.4 Conclusions 129

2.5 References 132

3 Chapter 3 Selective laser melting of hybrid ex-situ/in-situ reinforced titanium matrix composites: Laser/powder interaction, reinforcement formation mechanism, and non-equilibrium microstructural evolutions 141

3.1 Introduction 143

3.2 Materials and Experimental Procedure 146

3.2.1 Powder Preparation 146

3.2.2 SLM processing and arc melting 148

3.2.3 Powder Characterization 149

3.2.4 Microstructural Characterization 150

3.2.5 Mechanical Properties 151

3.3 Results and Discussion 151

3.3.1 B_4C-decorated Ti64 composite powder feedstock 151

3.3.2 Laser/composite powder interaction 155

3.3.3 Guest B_4C particles: melting or dissolution? 159

3.3.4 Dissolution Mechanism of guest B_4C particles 162

3.3.5 Microstructural evolutions and solidification path of the 5wt.% B_4C/Ti64 composite system 166

3.3.6 Microhardness 174

3.4 Conclusions 176

3.5 References 178

4 Chapter 4 Laser Powder Bed Fusion Processability of Ti-6Al-4V Powder Decorated by B_4C Particles 184

4.1 Introduction 186

4.2 Materials and experimental procedure 187

4.3 Results and discussions 188

4.4 Conclusions 193

4.5 References 195

5 Chapter 5 Microstructural characterization and mechanical properties of nano-scale/sub-micron TiB-reinforced titanium matrix composites fabricated by laser powder bed fusion 197

5.1 Introduction 199

5.2 Materials and Experimental Procedure 202

5.2.1 Starting materials and preparation of the composite powder feedstock 202

5.2.2 Characterization of the powders 203

5.2.3 L-PBF processing 203

5.2.4 Microstructural observations and oxygen/nitrogen (O/N) analysis ... 205

5.2.5 Mechanical testing 206

5.3 Results 207

5.3.1 Composite powder feedstock 207

5.3.2 Densification level and processability 211

5.3.3 Microstructure evolution and phase analysis 215
5.3.4 Mechanical Properties 220
5.4 Discussions 225
5.4.1 Processability 225
5.4.2 Microstructure evolution 228
5.4.3 Mechanical Properties 235
5.5 Conclusions 241
5.6 References 243

6 Chapter 6 Unique opportunities for microstructure engineering via trace B_4C addition to Ti-6Al-4V through laser powder bed fusion process: As-built and heat-treated scenarios 251
6.1 Introduction 253
6.2 Materials and Experimental Procedure 255
6.2.1 Fabrication 255
6.2.2 Heat Treatment 256
6.2.3 Microstructural Characterization 257
6.2.4 Mechanical Properties Investigation 258
6.3 Results and Discussion 258
6.3.1 Heat treatment cycle selection 259
6.3.2 Microstructural Characterization 261
6.3.2.1 Grain structure and analysis of phases within the grains 261
6.3.2.1.1 As-built 262
6.3.2.1.2 Heat-treated 266

6.3.2.2 Size and volume fraction of micro-constituents- Ti64 vs. TMC 281
6.3.3 Mechanical Properties 286
6.3.3.1 Compression 286
6.3.3.2 Microhardness and scratch resistance 300
6.3.4 Selection of the optimum heat treatment cycle 302
6.4 Conclusions 303
6.5 References 304

7 Chapter 7 TiB reinforced Ti-6Al-4V matrix composites with improved short-term creep performance fabricated by laser powder bed fusion 312
7.1 Introduction 314
7.2 Materials and experimental procedure 317
7.3 Results 320
7.3.1 Creep properties 321
7.3.1.1 Creep strain-time curves 321
7.3.1.2 Post-creep microstructural characterization 322
7.3.1.3 Fractography of the creep samples 328
7.4 Discussion 330
7.5 Conclusions 336
7.6 References 339

8 Chapter 8 Summary, Strength, Limitations, and Future Work 346
8.1 Summary and conclusive remarks 347
8.2 Strength, limitations, and future work 351

List of Figures

Figure 1-1 Schematic of: (a) L-PBF and (b) DED processes [2]. 4

Figure 1-2 Schematic illustration of a DED system with simultaneous powder and wire feeding [3]. 5

Figure 1-3 Typical structure of a DED processed functionally graded composite material (FGCM) [4]. 5

Figure 1-4 Cross-sectional view of SLM processed Waspalloy showing the formation of cracks [72] 12

Figure 1-5 Scanning electron microscopy (SEM) images of (a) water atomized and (b) gas atomized high speed steel powder particles. (c) and (d) SEM micrographs of laser sintered powders shown in (a) and (b), respectively [128]. (Please see the footnote [129]) 18

Figure 1-6 SEM micrographs of: (a) CP-Ti and (b) TiB_2 powder particles [48]. 19

Figure 1-7 SEM images of CP-Ti and TiB_2 powders in Figure 1-6 mixed using ball milling for different times of: (a) 1 h, (b) 2 h, (c) 3h and (d) 4 h [48] 20

Figure 1-8 Schematic illustrations of laser beam interaction with two different categories of TiC/Ti mixed powder system [41] 22

Figure 1-9 SEM image of Ti6Al4V and BN powder particles premixed with diluting followed by drying [59]. 22

Figure 1-10 Microstructures of DLF processed TiC reinforced Ni matrix composites containing: (a) 20 and (b) 60 vol.% in-situ synthesized TiC [76] 27

Figure 1-11 The reinforcement/dendrite interactions in: (a) particle pushing and (b) particle engulfment mechanisms [100]. 29

Figure 1-12 SEM micrographs of SLM processed TiB_2 reinforced 316L stainless steel matrix composites containing: (a) 2.5 and (b) 15 vol.% reinforcement [121]. 31

Figure 1-13 SEM micrographs showing reaction layers between: (a) coarse TiN particle and the matrix in 10 wt.%+Ti6Al4V and (b) finer TiN particles and the matrix in 20 wt.%+Ti6Al4V TMCs fabricated by LENS process [58]. 34

Figure 1-14 (a) SEM micrograph showing an undissolved SiC particle in the matrix of LENS processed SiC/Ti system. (b) EDS line scan and (c) EDS elemental map analysis results from the reaction layer surrounding SiC particle in (a) [55]. 35

Figure 1-15 SEM micrographs showing the characteristics of reinforcement/matrix interfacial reaction layer formed in WC reinforced Inconel 718 matrix composites at linear laser energy densities of: (a), (b) 173 and (c), (d) 303 J/m [88]. 36

Figure 1-16 SEM images of LENS processed TiC reinforced Inconel 625 matrix composites having: (a) Ni-coated and (b) un-coated TiC as the starting reinforcing particle [85]. 37

Figure 1-17 (a-c) TEM images of the reinforcement/matrix interface in SLM fabricated BN reinforced Inconel 718 matrix composites and (d) line scan EDS analysis results showing the distribution of elements along the line in (a) [89]. 39

Figure 1-18 Microstructure of AMC fabricated by laser sintering of 20 wt.%SiC/$Al_7Si_{0.3}Mg$ powder mixture [21]. 40

Figure 1-19 Microstructures of LMD processed TiC reinforced Inconel 718 matrix composites processed with energy densities of: (a) 80, (b) 120 and (c) 160 kJ/m [80]. ... 41

Figure 1-20 TEM image indicating the growth of α phase from in-situ synthesized TiB precipitate in LENS processed TiB reinforced Ti6Al4V matrix composite [50]. 43

Figure 1-21 The microstructures of SLM processed: (a) non-reinforced 316L stainless steel, and TiB_2 reinforced 316L stainless steel matrix composites containing: (b) 2.5 and (c) 5 vol.% TiB_2 [121]. 45

Figure 1-22 Microstructures of SLM processed TiB_2 reinforced 316L stainless steel composites with starting: (a) directly mixed and (b) ball milled powder systems [122]. . 45

Figure 1-23 (a, c) Optical micrographs and (b, d) EBSD crystallographic orientation maps of SLM processed Inconel 738LC alloy. (a) and (b) are sections perpendicular to the building direction, while (c) and (d) are parallel to the building direction [148]. 47

Figure 1-24 SEM images (first row) and EBSD crystallographic orientation maps (second row) of SLM processed: (a, d) non-reinforced 316L stainless steel; and TiC reinforced

316L stainless steel matrix composites with: (b, e) micro-scale and (c, f) nano-scale TiC reinforcements [151]. 48

Figure 1-25 Optical micrographs of laser processed: (a) non-reinforced A356 Al alloy and (b) SiC reinforced A356 matrix composites [152]. 49

Figure 1-26 Microstructures of LENS processed TiC reinforced Inconel 690 matrix composites containing: (a) less than 15 and (b) 15-30 vol.% TiC as reinforcement [4]... 50

Figure 1-27 Microstructures of LENS processed: (a) non-reinforced Ti6Al4V alloy and (b) TiB reinforced Ti6Al4V composite [50]. 51

Figure 1-28 SEM micrographs of SLM fabricated: (a) non-reinforced pure iron and (b) SiC reinforced iron matrix composite [127]. 52

Figure 1-29 (a) SEM image of LENS processed TiC reinforced Ni matrix composite and (b) AES analysis map of C in the microstructure shown in (a). The thermal pseudocolor reveals the relative amount of C element [86]. 53

Figure 1-30 (a) HRTEM image of the TiC/Ni interface in LENS processed composites and (b) higher magnification image indicating a semi-coherent interface containing dislocations [86]. 54

Figure 1-31 TEM image showing high density of dislocations in the matrix of LENS processed TiC reinforced Inconel 625 matrix composites [85]. 55

Figure 1-32 SEM images of the surface morphology for SLM fabricated TiC reinforced TMCs processed with energy density of: (a) 360, (b) 180, (c) 120 and (d) 90 J/mm^3 [42]. 57

Figure 1-33 Cross-sectional optical micrograph of SLM processed SiC/AlSi10Mg mixed powder system showing the formation of inter-layer porosities [17]. 58

Figure 1-34 SEM micrographs showing: (a) microscopic shrinkage porosities at the Al_4SiC_4/matrix interface of SLM processed AMCs, and (b) interfacial micro-cracks at the Al_2O_3/Al interface of SLM fabricated AMCs [24]. 59

Figure 1-35 (a) Cross-sectional micrographs of additive layer manufactured Inconel 625 matrix composites with different types of reinforcements, and (b) SEM micrograph illustrating cracking in Al_2O_3 reinforced composites shown in (a) [75]. 60

Figure 1-36 SEM micrographs of SLM fabricated HA reinforced stainless steel matrix composites with HA content and scanning speed of: (a) $HA = 5$ vol. %, $\upsilon = 250\ mm/s$, (b) $HA = 15$ vol. %, $\upsilon = 250\ mm/s$ and (c) $HA = 5$ vol. %, $\upsilon = 400\ mm/s$ [117]. ... 61

Figure 1-37 SEM micrographs indicating TiB_2 reinforced 316L stainless steel matrix composites fabricated by SLM processing of (a) directly mixed and (b) ball-milled powder systems [122]. ... 62

Figure 1-38 Compressive stress-strain curves of SLM processed: (a) non-reinforced Al-12Si and Al-12Si-TNM composite; and (b) non-reinforced CP-Ti and TiB reinforced TMC [48]. ... 63

Figure 1-39 Variation of yield strength for LENS processed CP-Ti and TiB reinforced TMCs as a function of applied laser power [49]. ... 65

Figure 1-40 Schematic illustrations of failure modes in compression test for SLM fabricated CP-Ti and TiB reinforced TMCs. (Fig. 9 paper 39 Ti [49]) ... 69

Figure 1-41 Stress-strain curves of SLM produced Ti6Al4V and Ti6Al4V+10Mo parts [62]. ... 74

Figure 1-42 SEM micrographs of the worn surface for SLM processed TiC reinforced 316L stainless steel matrix nano-composites having: (a) 2.5 and (b) 15 vol.% TiC [119]. ... 79

Figure 2-1 Schematic illustration of: (a) ball milling and (b) regular mixing processes. 103

Figure 2-2 (a) XRD patterns of starting Ti-6Al-4V (Ti64) and B_4C powders as well as composite powder systems prepared by regular mixing and ball milling, and (b) The microstrain of Ti64 constituent in the developed composite powder systems derived from the XRD patterns. ... 109

Figure 2-3 SEM micrographs of starting: (a, b) Ti-6Al-4V (host) and (c) B_4C (guest) powder particles. (b) Higher magnification micrographs of the selected region in (a). The circles in (b) indicate the satellites. ... 110

Figure 2-4 SEM micrographs of 5wt.% B_4C/Ti-6Al-4V mixed powder systems subjected to regular mixing for: (a), (b) 1 h (R1); (c), (d) 3 h (R3); and (e), (f) 6 h (R6). The ellipses in (a), (c) and (e) indicate the free B_4C (guest) particles which are not attached to the Ti-6Al-4V (host) particles and are agglomerated. ... 111

Figure 2-5 SEM micrographs of 5wt.% B_4C/Ti-6Al-4V mixed powder systems subjected to ball milling for: (a), (b) 1 h (B1); (c), (d) 3 h (B3); and (e), (f) 6 h (B6). The ellipses in (a) show the free B_4C (guest) particles which are not attached to the Ti-6Al-4V (host) particles. 112

Figure 2-6 Cross-sectional SEM micrographs of: starting Ti-6Al-4V powder showing a martensitic microstructure after etching (a); 5wt.% B_4C/Ti-6Al-4V system subjected to ball milling for: (b), (c) 2 and (d)-(f) 6 h. (c) and (e) are higher magnification micrographs of the regions shown in (b) and (d), respectively. 114

Figure 2-7 The particle size distribution curves of: (a) starting Ti-6Al-4V (Ti64); (b) 2 h (R2) and (c) 6 h (R6) regularly mixed; (d) 2 h (B2) and (e) 6 h (B6) ball milled 5wt.% B_4C/Ti64 composite powder feedstocks. 116

Figure 2-8 The sphericity of the particles as a function of their size for: (a) regularly mixed, and (b) ball milled 5 wt.% B_4C/Ti64 composite powder feedstocks. In each case, the sphericity of the starting Ti-6Al-4V (Ti64) powder is provided as the reference..... 119

Figure 2-9 The flow behavior and conditioned bulk density results for 5wt.% B_4C/Ti-6Al-4V systems prepared by regular mixing and ball milling methods with different mixing times: (a) specific energy (SE), (b) basic flow energy (BFE), and (c) conditioned bulk density (CBD) of the composite powder systems compared to the reference powder (Ti64). 123

Figure 2-10 Schematic illustration presenting: (a) an overview of composite powder system with guest-decorated host particles; (b) and (c) close view of the selected regions showing “Mechanical Interlocking” and “Contact Surface Reduction” mechanisms, respectively; and (d) the contact area of two host powder particles when flowing relative to each other. 124

Figure 2-11 Schematic view presenting: (a) an overview of composite powder system with guest-embedded host particles; (b), (c) and (d) close view of the selected regions showing “Increased Surface Area”, “Host Particles Mechanical Interlocking” and “Surface Area Reduction” mechanisms, respectively. 125

Figure 2-12 Material loss as a function of the mixing time for the regularly mixed and ball milled 5wt.% B_4C/Ti-6Al-4V composite powders. The starting powder mixture was 100 gr, and the ball-to-powder ratio was 5:1. 128

Figure 3-1 SEM micrographs of the starting: (a) Ti-6Al-4V (Ti64) and (b) B4C powder particles. 146

Figure 3-2 Schematic view of the utilized stripe hatching scanning strategy which alternates 67^o between the subsequent layers. 149

Figure 3-3 SEM micrographs of the B_4C-decorated Ti-6Al-4V powder particles obtained by 90 min of ball milling. (b) Higher magnification micrograph of (a). (c) Enclosed view of the selected region in (b). 153

Figure 3-4 The particle size distribution curves of: (a) starting Ti-6Al-4V (Ti64) and (b) 5 wt. % B_4C/Ti64 TMC powder feedstock after 90 min of ball milling. 153

Figure 3-5 The sphericity of the particles as a function of their size for the starting Ti-6Al-4V (Ti64) as well as the 90 min ball-milled 5 wt.%B4C/Ti64 powder feedstock. 154

Figure 3-6 XRD patterns of the: (a) Ti-6Al-4V (Ti64), (b) B_4C, and (c) 5 wt.% B_4C/Ti64 systems. The rectangles indicate the diffraction peaks of the B_4C constituent in the TMC powder feedstock. 155

Figure 3-7 SEM micrographs of the SLMed: (a), (b) 5 wt.%B_4C/Ti64, and (c) Ti-6Al-4V (Ti64) systems processed with laser energy density of 50 J/mm^3 (P=200 W, V=1000 mm/s, h=100 μm and t=40 μm). The micrograph in (b) provides an enclosed view of a partially melted Ti64 (PM Ti64) particle surrounded by the partially dissolved B_4C guest particles. 159

Figure 3-8 Thermal diffusivity of bulk Ti-6Al-4V (Ti64) and B_4C as a function of the temperature [52, 53]. 159

Figure 3-9 (a) Schematic view of the thermal cycle during SLM processing of a single track. T_P, $(T_m)_{host}$ and λ are the maximum temperature of the melt pool, the melting point of the host powder, and the period in which the temperature is higher than the melting point of the host powder, respectively. (b) Schematic illustration of the thermal cycle during SLM of a single track for the 5wt.% B_4C/Ti64 composite system. The temperature in zones

(I) and (II) is higher and lower than $(T_m)_{host}$, respectively. The thermal cycles (1), (2), and (3) all lead to the hybrid ex-situ/in-situ reinforced TMCs. $(T_m)_{guest}$ corresponds to the melting point of the guest particles. 161

Figure 3-10 SEM micrographs of the 5wt.% B_4C/Ti64 composites SLMed with different laser powers of: (a) 200 W (E_V= 50 J/mm^3), (b) 250 W (E_V= 62.5 J/mm^3), and (c) 300 W (E_V= 75 J/mm^3). The scanning speed, hatch spacing, and layer thickness were 1000 mm/s, 100 µm, and 40 µm, respectively. The volume fraction of the residual B_4C particles (as represented by the dashed circles) decreased with increasing the laser power (volumetric energy density). 161

Figure 3-11 The schematic of the solid/liquid interaction between the B_4C particles and the liquid Ti64, representing the mechanism of guest particles dissolution in the molten Ti64 during SLM processing of 5wt.% B_4C/Ti64 powder system with direct melting of the host powder particles: (a) the solid B_4C and the liquid Ti64 phases at the beginning of the host particles melting, (b) interdiffusion between the solid and liquid phases to establish the equilibrium condition at the interface, (c) formation of solid and liquid layers with equilibrium C_S and C_L concentrations, respectively at the solid/liquid interface, (d) deviation from equilibrium conditions caused by the diffusion of B and C atoms from the equilibrium liquid layer surrounding the B_4C particles towards the bulk of the liquid, (e) re-establishment of the equilibrium conditions by further dissolution of the guest particles and enrichment of the adjacent liquid layer by B and C atoms, and (f) progression of the dissolution by deviation and re-establishment of equilibrium conditions at the interface until complete dissolution of guest particles. 164

Figure 3-12 The effect of B_4C particle size on its dissolution progression in the 5wt.% B_4C/Ti64 sample processed by the energy density of 62.5 J/mm^3 (P= 250 W, V= 1000 mm/s, h= 100 µm, t= 40 µm). The smaller the size of the guest B_4C particles, the higher the chance of complete dissolution. 166

Figure 3-13 (a) Overview of the 5wt.% B_4C/Ti64 composite microstructure, (b) EDS analysis of the Point A, and (c) EDS analysis of point B. The detected phases are believed to be TiC (point A) and TiB (point B) as the products of the in-situ reaction between the solid B_4C and the molten Ti64. Higher magnification micrographs showing the: (d) binary and (e) ternary eutectic reaction products and the martensitic matrix. 168

Figure 3-14 (a) Pseudo-binary phase diagram of Ti-B_4C system in the range of 0-10wt.% B_4C [59]; Schematic illustrations of: (b) equilibrium, and (c) non-equilibrium solidification path of the 5wt.% B_4C/Ti64 system. 171

Figure 3-15 The microstructure of the 5wt.% B_4C/Ti64 composite fabricated through conventional arc melting in: (a,b) graphite crucible, and (c,d) water-cooled copper crucible. (e) The microstructure of the matrix in the arc melted composites. 174

Figure 3-16 The variation of microhardness as a function of the volumetric laser energy density for the SLMed 5wt.% B_4C/Ti64 composite and Ti64 parts fabricated by the same process parameters. 176

Figure 4-1 SEM micrographs of: (a) Ti64, (b) B_4C, and (c) developed 3wt.%B_4C/Ti64 powders. (d) Optical absorption of powders vs. the wavelength. 188

Figure 4-2 SEM micrographs of the LPBF processed: (a-c) 3wt.%B_4C/Ti64 composite powder subjected to various e_V ; and (d) monolithic Ti64 system. “PD” in (a) refers to partially dissolved. 191

Figure 4-3. SEM micrographs of the LPBF-processed 3wt.%B_4C/Ti64 composite powder subjected to e_V of: (a) 33, (b) 71, and (c) 297 J/mm^3. Optical microscopy images showing cracks in the systems processed by e_V of: (d) 33, and (e) 297 J/mm^3. 193

Figure 5-1. Schematic view of the fabricated: (a) cubic samples, (b) wear test specimen, and (c) compression test specimen. As shown in (c), the printed cuboid specimens were subjected to wire electric discharge machining (EDM) to extract cylindrical compression test samples, as per ASTM-E9-09 standard. (Note: The provided dimensions are not proportional to the actual size). 205

Figure 5-2. SEM micrographs of: (a) 3wt.%B_4C/Ti64 [32], (b) monolithic Ti64 [32], and (c) 0.2wt.%B_4C/Ti64 powders. (d) Optical absorption versus the wavelength for the Ti64 [32] and B_4C [32] powders as well as the developed 0.2wt.%B_4C/Ti64 composite powder. The wavelength of 1070 nm represents the laser wavelength of the L-PBF machine used in this study to fabricate parts. 210

Figure 5-3. The variation of relative density versus the volumetric energy density (Ev) for Ti64 and TMC parts. The designated regions refer to the Ev range in which highly dense samples were achieved. 213

Figure 5-4. Non-etched OM images from the front view cross-sections of Ti64 parts fabricated by different sets of laser powders and scanning speeds. 214

Figure 5-5. Non-etched OM images from the front view cross-sections of TMC parts fabricated by different sets of laser powders and scanning speeds. 214

Figure 5-6. (a) OM 3D view of the microstructure of the L-PBF fabricated Ti64; (b), (c) higher magnification OM images of the selected areas of the front and top views shown in (a), respectively; (d) inverse pole figure (IPF-Z), and (e) band contrast EBSD maps of the front view of the Ti64 sample; (f) OM 3D view of the microstructure of the L-PBF fabricated TMC part; (g), (h) higher magnification OM images of the selected areas of the front and top views shown in (f), respectively; (i) inverse pole figure (IPF-Z), and (j) band contrast EBSD maps of the front view of the TMC sample. The employed laser powder, and scanning speed for both Ti64 and TMC samples were 250 W, and 1000 mm/s, respectively. 218

Figure 5-7. XRD patterns of the starting: (a) B_4C, and (b) Ti64 powders, as well as the L-PBF fabricated: (c) Ti64, and (d) TMC parts. Both Ti64 and TMC samples were manufactured using a laser power of 250 W and a scanning speed of 1000 mm/s. 219

Figure 5-8. Secondary electron (SE)-SEM images from the front view of the L-PBF fabricated TMC part. (a) General view in which the cross-section of a track has been highlighted. Higher magnification micrograph of the selected dashed square in (a) is shown in (b). The square regions marked as “A” and “B” in (b) are shown in a higher magnification in (c) and (d), respectively. 220

Figure 5-9. (a) The microhardness and nanohardness values, and (b) typical compressive engineering stress-strain curves of the L-PBF fabricated Ti64 and TMC parts. 221

Figure 5-10. (a), (b) the variation of COF versus sliding distance for Ti64 and TMC samples, respectively. Representative depth-width profile of the worn tracks for (c) Ti64, and (d) TMC samples obtained along the paths depicted in the 3D surface topography images in (e), and (f), respectively. 223

Figure 5-11. SEM images of the wear tracks after the sliding wear test for the L-PBF fabricated: (a), (b) Ti64; and (c), (d) TMC samples. Higher magnification micrographs of the selected regions in (a), and (c) and presented in (b), and (d), respectively. 225

Figure 5-12. (a) Equilibrium phase analysis diagram of the Ti64-B system with the B content in the range of 0-0.3 wt.%. The provided isopleth represents the investigated 0.2wt.%B_4C/Ti64 system which contains 0.156wt.%B. (b) Equilibrium phase analysis diagram of the Ti-6Al-XV, in which the isopleth of the Ti-6Al-4V (Ti64) alloy has been shown. Scheil-Gulliver solidifications models of the: (c) Ti64-0.2wt.%B_4C, and (d) Ti64 systems. The inset in (c) shows the variation of the TiB fraction within the specified temperature range (1530-1420 °C). (e)-(h) Schematic illustration of the solidification sequence of the 0.2wt.%B_4C/Ti64 system in the equilibrium condition. The liquid (L) becomes enriched from B and C as the solidification progresses. 231

Figure 5-13. (a), and (b) SEM micrographs of the last layer of the L-PBF fabricated TMC part. Higher magnification micrograph of the selected region in (a) is shown in (b). (c)-(g) Schematic illustration of the microstructure evolution of the last layer of the L-PBF fabricated TMC part during cooling. “M” in (g) refers to martensite. 234

Figure 5-14. The oxygen/nitrogen concentration in the L-PBF fabricated Ti64 and TMC samples..... 241

Figure 6-1. Schematic illustration of (a) cubic coupon, (b) compression test specimen, and (c) wear test specimen. “BD” in (a) refers to the building direction. 256

Figure 6-2. Differential scanning calorimetry (DSC) analysis results for the as-built Ti64 and TMC parts in heating (a, c) and cooling (b, d) stages. Higher magnification views of the selected regions in (a-d) are shown in (e-j) with the same background color. 260

Figure 6-3. Optical micrographs of the: (a) front and (b) top view sections of the as-built Ti64 sample. The band contrast, IPF-Z and reconstructed PBGs EBSD maps of the front and top views are shown in (c-e) and (f-h), respectively. The EBSD analysis was performed with a step size of 0.15 µm. 263

Figure 6-4. (a) Optical micrograph, (b) and (c) SEM micrographs, (d) band contrast EBSD map, (e) IPF-Z EBSD map, and (f) reconstructed PBGs of the front view of the as-built TMC sample. (g) Optical micrograph, (h) band contrast EBSD map, (i) the IPF-Z EBSD

map, (j) and reconstructed PBGs of the top view of the as-built TMC sample, respectively. The EBSD analysis was performed with a step size of 0.15 µm. 265

Figure 6-5. Optical micrographs of the: (a) front and (b) top views of the Ti64-850 sample. (c) and (d) SEM micrographs of the front view. (c) shows higher magnification view of the designated zone in (a), and (d) presents higher magnification of the selected region in (c). The band contrast, IPF-Z and phase EBSD maps of the front view are shown in (e-g), respectively. The EBSD analysis was performed with a step size of 0.05 µm. 268

Figure 6-6. (a) XRD patterns of the as-built and heat-treated Ti64 and TMC samples. Higher magnification view of the designated colored box in each pattern is shown in (b-e). 269

Figure 6-7. (a) Higher magnification IPF-Z EBSD map of the region designated in Figure 6-5(f). (b-g) PFs of a β grain and five different α grains adjacent to it, as marked in (a). 270

Figure 6-8. (a) Optical and (b) SEM micrographs of the front view of the Ti64-1050 sample. The band contrast, IPF-Z and phase EBSD maps of the front view are shown in (c-e), respectively. The EBSD analysis was performed with a step size of 0.1 µm. 272

Figure 6-9. (a) Higher magnification IPF-Z EBSD map of the region designated in Figure 6-8(d). (b-e) PFs of the α and β grains marked in (a). 273

Figure 6-10. Optical micrographs of the: (a) front and (b) top views of the TMC-850 sample. (c) and (d) SEM micrographs of the front view. (c) shows higher magnification view of the designated zone in (a), and (d) presents higher magnification view of the selected region in (c). The band contrast, IPF-Z, and phase EBSD maps of the front view are shown in (e-g), respectively. The EBSD analysis was performed with a step size of 0.05 µm. 275

Figure 6-11. (a) Higher magnification IPF-Z EBSD map of the region designated in Figure 6-10(f). (b-e) PFs of the α and β grains marked in (a). 276

Figure 6-12. (a) Optical and (b) SEM micrographs of the front view of the TMC-1050 sample. The band contrast, IPF-Z and phase EBSD maps of the front view are shown in (c, f), (d, g) and (e, h), respectively. The EBSD analysis was performed with a step size of: (c-e) 0.5 µm, and (f-h) 0.1 µm. 280

Figure 6-13. (a) Higher magnification IPF-Z EBSD map of the region designated in Figure 6-12(g). (b-g) PFs of the TiB needle, and α and β grains adjacent to it, as marked in (a). 281

Figure 6-14. (a) The α/α′ width of the Ti64 and TMC samples, and (b) the length, width, and aspect ratio of the TiB needles in the TMC samples in the as-built and heat-treated conditions. 283

Figure 6-15. The true stress-true strain curves of the: (a) Ti64 and (b) TMC samples in the as-built and heat-treated conditions. 291

Figure 6-16. Compressive (a) yield strength, (b) ultimate strength, and (c) elongation % at break of the Ti64 and TMC samples in the as-built and heat-treated conditions. The nanoindentation load-displacement curves of the as-built Ti64 sample are presented in (d). 292

Figure 6-17. (a) The contribution of each strengthening mechanism in the overall compressive yield strength of the Ti64 samples, and (b) the increment in the compressive yield strength of TMC samples over the non-reinforced counterparts caused by different strengthening mechanisms. 293

Figure 6-18. SEM micrographs from the cross-section of the: (a, b) Ti64-950, (c, d) TMC-950, (e, f) Ti64-1050, and (g, h) TMC-1050 samples after the compression test. The inset in each micrograph shows higher magnification view of the selected region in the same micrograph. “LD” refers to loading direction. 299

Figure 6-19. The microhardness of the Ti64 and TMC samples in the as-built and heat-treated conditions. 301

Figure 6-20. The penetration depth-scratch length profiles of the: (a) Ti64, and (b) TMC samples in the as-built and heat-treated conditions. 302

Figure 7-1. (a) General and (b) top views of the L-PBF fabricated creep test samples. The inset in (b) illustrates the locations where the post-creep microstructural characterization and fracture surface analysis were performed. 320

Figure 7-2. (a) Creep strain versus time curves for the as-built and heat-treated (HT) Ti64 and TMC samples, and (b) typical nanoindentation load-displacement curves of the as-built Ti64 and TMC samples. 322

Figure 7-3. Optical micrographs of the top view section of the as-built: (a), (c), (e) Ti64; and (b), (d), (f) TMC creep test samples after failure. (a), and (b) show the fracture sites, while (c), (d), (e), and (f) refer to locations further away from them. (e), and (f) present the microstructures of regions having a greater distance from the fracture site than (c) and (d), respectively. 324

Figure 7-4. (a) Optical micrograph, (b), and (c) SEM images of the top view section of the failed HT-Ti64 creep test sample adjacent to the fracture site. (e), and (f) are the EDS maps showing the elemental distribution of Al and V in the SEM image presented in (d). 326

Figure 7-5. (a) Optical micrograph, (b), and (c) SEM images of the top view section of the failed HT-TMC creep test sample adjacent to the fracture site. (e), (f), and (g) are the EDS maps showing the elemental distribution of Al, V, and B in the SEM image presented in (d). 327

Figure 7-6. SEM micrographs of the fracture surface of: (a) as-built Ti64, (b) as-built TMC, (c) HT-Ti64, and (d) HT-TMC creep test samples after failure. The inset in (a) shows a higher magnification image of the region selected by the dashed square. 329

Figure 7-7. The steady-state creep rate of the conventionally manufactured pure Ti, and Ti64 alloy, as well as the TiB/TiC/(TiB+TiC)-reinforced pure Ti, and Ti64 matrix composites compared with the as-built and heat treated Ti64 and TMC samples in this study fabricated by the L-PBF process. The temperature (T) and stress (σ) under which the creep test has been performed are listed. ([67] [68] [69] [70] [30] [71] [60] [66] [29]) . 336

List of Tables

Table 1-1 Mixed powder systems and AM techniques employed to fabricate various types of AMCs. 8

Table 1-2 Mixed powder systems and AM techniques employed to fabricate various types of TMCs. 10

Table 1-3 AM techniques employed to fabricate various types of nickel-based matrix composites. 12

Table 1-4 Mixed powder systems and AM techniques employed to fabricate various types of Cu-matrix composites. 14

Table 1-5 Mixed powder systems and AM techniques employed to fabricate various types of iron-based matrix composites. 16

Table 1-6 A comparison between the hardness of AM processed Ti6Al4V alloy in non-reinforced state and in MMCs containing different types of reinforcements. 70

Table 3-1 The processing parameters employed to fabricate 5wt.% B_4C/Ti64 and Ti64 parts. 149

Table 3-2 The particle size distribution results derived from the data in Figure 3-4, which present the cumulative distribution of D10, D50, and D90. 153

Table 4-1 Flowability and packing density of powders. 190

Table 5-1 The laser powders and scanning speeds employed to fabricate cubic parts. .. 204

Table 5-2. Flowability and packing density of powders obtained by the FT4 Freeman powder rheometer technique. 211

Table 5-3. Mechanical properties of the L-PBF fabricated Ti64 and TMC parts obtained by compression testing. 221

Table 5-4. The coefficient of friction (COF) and wear rate of L-PBF processed Ti64 and TMC samples. 223

Table 5-5. The properties and parameters used in obtaining the contribution of different strengthening mechanisms. 239

Table 5-6. The calculated values of strengthening mechanisms in the TMC part along with their contribution in the enhancement of the yield strength over the Ti64 counterpart. . 240

Table 6-1. The optimum set of process parameters used to print Ti64 and TMC parts. . 256

Table 6-2. The size and volume fraction of microstructural features of the as-built Ti64 and TMC samples. 282

Table 6-3. The size and volume fraction of microstructural features of the heat-treated Ti64 and TMC samples. 282

Table 6-4. The properties and parameters used in obtaining the contribution of different strengthening mechanisms. 290

Table 7-1. The creep parameters of the as-built and HT specimens tested at 600 °C under a stress of 200 MPa. 322

Chapter 1 Introduction and literature review

Complete Citation:

Fereiduni E, Elbestawi M. Process-structure-property relationships in additively manufactured metal matrix composites. In Additive Manufacturing of Emerging Materials 2019 (pp. 111-177). Springer, Cham.

During the past few decades, there has been a significant interest in developing and fabricating near-net-shape and complex parts made from novel materials such as bi-materials, composites, and complex materials. The parts produced from these materials could have outstanding combinations of properties, introducing them as potential candidates meeting the requirements of automotive, aerospace, rapid tooling, and biomedical industries.

Thanks to the significant advances in additive manufacturing (AM) of single materials and the optimized process parameters prescribed for fabrication of parts made of commercially available materials, near-net-shape components with high qualities could be fabricated from these materials using AM processes. However, the processing of composites and complex materials is rather challenging in some of the AM techniques. Moreover, AM processing of these materials is relatively new and needs extensive research to be fully explored.

Besides the flexibility in fabricating the components with complex geometries, recent advances in AM technology have paved the way for the design and manufacturing of parts with tailored properties, including composites, functionally graded materials (FGMs), and multifunctional materials. When combined with the basics of composite fabrication, AM technology can open new opportunities to develop composites with outstanding properties.

The ASTM-recognized AM methods involve materials extrusion, material jetting, sheet lamination, vat-photo-polymerization, binder jetting, directed energy deposition (DED), and powder bed fusion (PBF) [1]. Among various AM technologies available, only a few of them have shown their capability in composite fabrication. While major efforts have been made focusing on the fabrication of polymer matrix composites using AM

technology, limited research has been performed employing this technology to produce metal matrix composites (MMCs).

Although the electron beam has been used in a few works to fabricate MMCs, most AM processed coatings or three-dimensional (3D) MMC structures have been manufactured by employing laser beam as the heat source. The AM processes most widely used to fabricate MMCs are DED and PBF. Depending on whether the heat source in the PBF is a laser or an electron beam, the process is called laser powder bed fusion (L-PBF) or electron beam powder bed fusion (E-PBF), respectively. The L-PBF process is also called SLM[1] and DMLR[2]. It is worth noting that other terms may also be found in the literature for the DED process, including DMD[3], LENS[4], DLF[5], and DLD[6].

In the PBF processes, the powder is spread on a bed before the laser scanning process. However, in the DED processes with a powder-fed nature, the powder is coaxially blown with synchronous laser scanning. The schematic illustrations of the L-PBF and DED are provided in Figure 1-1, respectively.

[1] Selective laser melting
[2] Direct metal laser remelting
[3] Direct metal deposition
[4] Laser engineered net shaping
[5] Direct laser fabrication
[6] Direct laser deposition

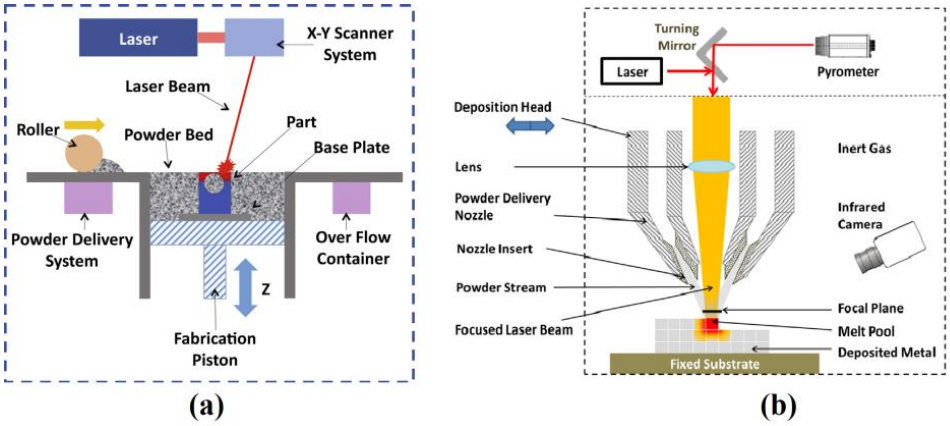

Figure 1-1 Schematic of: (a) L-PBF and (b) DED processes [2].

In the L-PBF process, a uniform layer of powder is first deposited on the base plate. Then, the predefined regions of this layer are melted by the laser beam, resulting in the formation of a single layer of the desired part. Next, the powder bed is lowered, and a new layer of deposited powder is subjected to the laser beam. These powder deposition and laser melting procedures are repeated, leading to the fabrication of parts layer-by-layer. Unlike the L-PBF, the DED process combines material delivery and laser systems to simultaneously deposit the material and fabricate the part in the same region.

When it comes to the fabrication of MMCs using AM processes, the desired powder blends are mixed using powder pre-processing techniques. While the pre-mixing of powder blends prior to the process is essential for fabricating MMCs using PBF-AM processes, quite different techniques may be employed in DED processes to manufacture such components. Because of benefitting from several nozzles (up to four or more), the existing DED systems facilitate the feeding of different powders to produce MMC structures. The DED systems could also be used to combine wire feeder and powder delivery nozzle to fabricate MMC structures (Figure 1-2). It is worth noting that the freedom in the feeding rate of powder and/or wire in DED processes provides the opportunity to fabricate functionally graded

composite materials (FGCMs) having varying contents of reinforcements and consequently mechanical properties along the building direction (Figure 1-3).

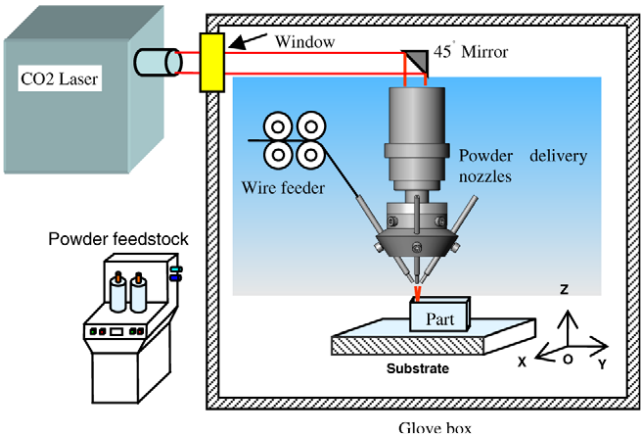

Figure 1-2 Schematic illustration of a DED system with simultaneous powder and wire feeding [3].

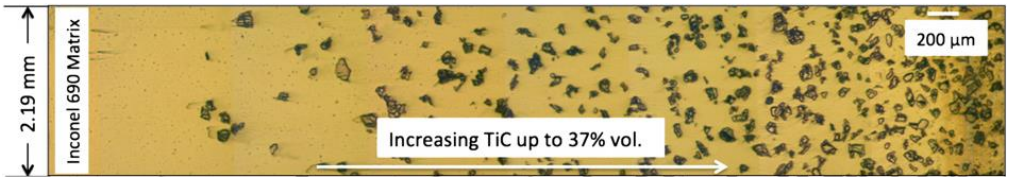

Figure 1-3 Typical structure of a DED processed functionally graded composite material (FGCM) [4].

1.1 Why AM instead of conventional manufacturing for MMC fabrication?

By integrating various fields, including engineering design, laser technology, materials science, and mechanical engineering, AM technology is regarded as a major revolution in manufacturing, introducing it as a "next-generation" technology. AM technology competes with conventional manufacturing processes in many aspects such as fabrication cost and time, design freedom, component accuracy, and part quality. The most significant

advantages of AM technology over conventional manufacturing techniques employed to fabricate MMCs components are as follows:

- Because of the need for expensive and dedicated tools such as molds and dies, most conventional manufacturing processes are not suitable candidates for small volume production and fabricating components with complex geometries. However, besides the capability for small volume production, the unique features associated with AM processes enable the technological opportunities to manufacture small quantities of near-net-shape custom-designed components rapidly and efficiently.
- The need for processing temperatures significantly higher than the melting point of the matrix combined with the relatively slow cooling rates involved in most conventional manufacturing processes may lead to noticeable grain growth and inversely affect the mechanical properties of fabricated MMCs. However, the extremely high cooling rates of AM processes result in substantially refined microstructures and improved mechanical properties compared with the conventionally processed counterparts. It is worth noting that the outstanding features of AM technology can also provide the fabrication of metal matrix nano-composites (MMnCs) with significantly improved mechanical properties.
- Fabrication of MMCs with conventional processing techniques has always been encountered with some major processing problems such as gas entrapment, reinforcement/matrix interfacial cracking, limited densification levels and non-uniform size distribution of reinforcements their segregation at the grain boundaries. Combinations of these phenomena result in premature failure, reduced strength, and decreased ductility of parts. The outstanding properties associated

with AM processes can significantly improve the performance of MMCs by reducing the porosity and developing larger numbers of fine precipitates with more homogenous distribution throughout the matrix.

- While some conventional manufacturing processes need additional steps to fabricate MMCs with in-situ synthesized reinforcements, AM technology facilitates the fabrication of these composites in a single step.

1.2 Additively Manufactured MMCs (Challenges, Opportunities, and Existing Literature)

1.2.1 Aluminum-Matrix Composites (AMCs)

The poor wear resistance and low hardness of aluminum (Al) is a serious impediment that limits its further development in industrial applications [5, 6]. Because of their outstanding combination of properties, including low density, low coefficient of thermal expansion (CTE), high hardness, improved wear resistance, and comprehensive mechanical properties, Al matrix composites (AMCs) reinforced with ceramic particles can meet most of the industrial requirements. Accordingly, these materials are considered promising candidates to be used widely in automotive, aerospace, microelectronics, and other related industries [7-9].

Manufacturing of Al alloy parts by AM processes is challenging due to three major reasons: (i) high laser reflectivity of the Al powder, (ii) high heat conductivity away from the melt pool through the already solidified material, and (iii) elevated affinity to oxygen, resulting in the formation of oxide layers on top of the melt pool [10, 11].

Among different Al alloys used as the matrix in AM processed AMCs, the most frequently investigated Al-Si alloys (especially Al-Si-Mg) because of their unique properties such as high fluidity and high weldability, low CTE, and good corrosion resistance. The binary Al-Si system is a eutectic system with eutectic composition at ~12 wt.% Si. By adding other alloying elements such as Mg (e.g., AlSi10Mg) and Cu, the Al-Si alloys can be strengthened either through heat treating or by employing rapid solidification techniques (e.g., melt spinning or AM), which leads to microstructural refinement. In the case of AlSi10Mg alloy, the formation of fine Mg_2Si precipitates can further improve the hardness and strength.

Among various AMCs systems (Table 1-1), those containing TiC and SiC as the starting ceramic reinforcing particle have attracted great attention in recent years. Table 1-1 summarizes the works performed to fabricate AMCs using AM processes.

Table 1-1 Mixed powder systems and AM techniques employed to fabricate various types of AMCs.

Ref.	Mixed Powder System	Matrix	Reinforcement	Process
[12]	TiC/AlSi10Mg	AlSi10Mg	TiC	SLM
[13]				
[14]				
[15]				
[16]				
[17]	SiC/AlSi10Mg	AlSi10Mg	Hybrid (Al_4SiC_4+SiC)	SLM
[18]			Al_4SiC_4	
[19]			Al_4C_4	DMLS
[20]	SiC/A356	A356	Al_4SiC_4	LS
[21]				
[22]	SiC/Al-4.5Cu-3Mg	Al-4.5Cu-3Mg	SiC	DMLS
[23]				
[24]	Al_2O_3/Al	Al	Al_2O_3	SLM
[25]	Al_2O_3/AlSi10Mg	AlSi10Mg	$Al_2Si_4O_{10}$	
[26]	AlN/AlSi10Mg	AlSi10Mg	AlN	
[27]	Al-20Si-5Fe-3Cu-1Mg	Al-20Si-5Fe-3Cu-1Mg	Al_4FeSi_2	

[28]	Al-12Si -TNM	$Al_{SS\text{-}Si\text{-}Ti}$ solid solution	Al_6MoTi
[29]	Al85Nd8Ni5Co2	Al	$AlNd_3$, Al_4CoNi, $AlNdNi_4$
[30]	Fe_2O_3/Al	Al	Al-Fe intermetallics, α-Al_2O_3
	Fe_2O_3/AlMg1SiCu	AlMg1SiCu	Al-Fe intermetallics, α-Al_2O_3
	Fe_2O_3/AlSi10Mg	AlSi10Mg	Al-Fe intermetallics, $Al_{0.5}Fe_3Si_{0.5}$

1.2.2 Titanium-Matrix Composites (TMCs)

Because of having high specific strength, sufficient stiffness, elevated high-temperature application, good fatigue and wear behavior, and outstanding corrosion resistance, titanium (Ti) and its alloys are widely used in various industrial sections such as chemical, aeronautical, and defense, among others [31, 32]. A major concern with Ti alloys is their limited wear performance, especially in applications demanding high resistance to abrasion and erosion. Accordingly, noticeable research has been performed in recent decades to incorporate ceramic reinforcing particles into the matrix for fabricating TMCs parts with improved mechanical properties and wear resistance [33-36]. These attempts include highly efficient surface modification techniques such as laser melt injection [34], laser cladding [37], and laser surface alloying [38], as well as manufacturing techniques like casting, powder metallurgy, and combustion synthesis [39] to fabricate bulk-form TMCs parts.

Due to their high modulus, high thermal stability, and having densities and thermal expansion coefficients close to those of Ti alloys, TiC and TiB are generally known as the most appropriate reinforcements for TMCs. TiC reinforced TMCs, and Ti matrix nano-composites (TMnCs) have been fabricated in recent years from different powder mixtures

such as TiC/Ti, SiC/Ti, and Ti/Al/graphite using various AM processes (Table 1-2). However, TiB reinforced ones have been manufactured mostly using LENS and SLM processes (Table 1-2). The TiB reinforcement is formed in these composites through the in-situ reaction between Ti and B elements in various mixed powder systems.

Table 1-2 Mixed powder systems and AM techniques employed to fabricate various types of TMCs.

Ref.	Mixed Powder System	Matrix	Reinforcement	Process
[40-43]	TiC/Ti	Ti	TiC	SLM
[44]				LPD
[45]	Ti, Al, Graphite elemental powder	Ti(Al) solid solution		SLM
[46]	SiC/Ti	Ti	TiB	SLM
[47]	TiB_2/Ti			SLM
[48]				
[49]	Elemental B/Ti			LENS
[50]	Elemental B/Ti6Al4V	Ti6Al4V		DLD
[51]				LENS
[36]	TiB_2/Ti6Al4V			DLF
[52]	TiB_2/TNZT(elemental Ti+Nb+Zr+Ta)	TNZT		LENS
[53]	B_4C/Ti	Ti	TiB+TiC	DLD
[54]	SiC/Ti		(unmelted SiC+TiC+$TiSi_2$+Ti_5Si_3)	LENS
[55]				
[56]	Si_3N_4/Ti		TiN	SLM
[57]	TiB_2/Ti		TiB	
[58]	TiN/Ti6Al4V	Ti6Al4V	TiN	LENS
[59]	BN/Ti6Al4V		(TiB+TiN)	
[60]				
[61]	Ta+Ti	Ti	Ta	SLM
[62]	Mo+Ti6Al4V	Ti6Al4V	Mo	

1.2.3 Nickel-based Matrix Composites

Because of having outstanding combinations of high-temperature workability and mechanical properties, high fatigue strength, and good oxidation and corrosion resistance, high-performance nickel-based superalloys are noticeably used in power generation,

aerospace, marine, chemical, and petrochemical industries [63-67]. Inconel series of Ni-based superalloys, both the precipitation and/or solution-hardened, are the most widely known ones with a fantastic combination of properties, introducing them as excellent choices for miscellaneous industrial applications. The high hardness, low thermal conductivity, and high work hardening rates associated with the nickel-based superalloys are the most important features introducing them as "difficult to machine" alloys [68]. Due to their tool-less nature, their ability to fabricate net or near-net-shape components, and their noticeably high freedom in geometry design, AM processes are considered fascinating processing routes for the fabrication of superalloys.

Most of the superalloys desired for high-temperature applications are in a precipitation hardened state in which the gamma prime (γ') phase consisting of Ni_3Al or Ni_3Ti precipitates is formed by Ti and/or Al in the alloy [69]. The increasing of Ti and Al concentration in the superalloy is one of the approaches for the enhanced content of γ' phase and consequently the improved high temperature properties of nickel-based superalloys. However, this technique is believed to be detrimental to the weldability/printability of the superalloy, since it increases the susceptibility to cracking [70], as shown in Figure 1-4. There exists a limit of weldability beyond which the superalloy is considered as "unweldable." The sum of Al, Ti, and Nb elements of this limit is ~4 at.%. The alloys exceeding this limit suffer from strain age cracking during the welding/AM process or when subjected to post-processing heat treatment cycles [71]. Accordingly, fabrication of high-quality parts from such alloy systems with AM processes would be challenging or impossible.

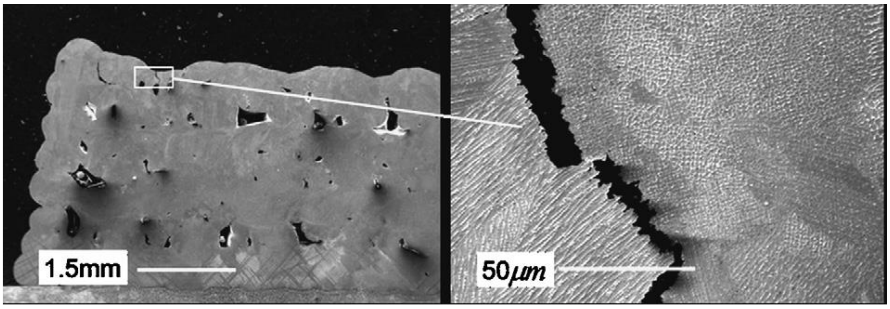

Figure 1-4 Cross-sectional view of SLM processed Waspalloy showing the formation of cracks [72].

To avoid cracking and further enhance the high-temperature performance of nickel-based superalloys, hard and temperature-resistant ceramic reinforcing particles can be incorporated into the nickel-based matrix to produce MMCs.

Because of having promising properties such as high hardness, outstanding thermal stability, and good wear and corrosion resistance [73, 74], TiC is the most frequently used ceramic reinforcing particle incorporated into the nickel-based superalloys to fabricate MMCs employing AM processes. Table 1-3 summarizes the works performed on AM processing of nickel-based superalloy matrix composites.

Table 1-3 AM techniques employed to fabricate various types of nickel-based matrix composites.

Ref.	Matrix	Reinforcement	Applied AM process
[75]	Inconel 625	Al_2O_3	LM
		SiC	
		TiC	
[4]	Inconel 690	TiC	DLD
[76]	Ni		DLF
[77]	Inconel 718		SLM
[78]			
[79, 80]			
[81]	Inconel 625		LMD
[82, 83]			
[84]			

[85]	Inconel 625		LENS
[86]	NiTi	TiC	
[87]	Ni	CNT	
[88]	Inconel 718	WC	SLM
[89]		BN	

1.2.4 Copper-Matrix Composites

Because of benefiting from outstanding combinations of high electrical and thermal conductivity and high resistance to fatigue and corrosion, copper (Cu) is extensively used in many applications, especially in electrical contacts [90, 91]. However, the limited wear resistance of pure Cu restricts its application in environments demanding high wear resistance [92, 93]. To overcome this imperfection, secondary hard reinforcing particles could be incorporated into the Cu matrix to develop Cu-matrix composites with significantly enhanced mechanical properties (e.g., improved wear resistance).

Cu-matrix composites have found their applications in many industrial parts such as high voltage electrical applications, arcing tips, current-carrying contacts, and electrodes of electric discharge machining (EDM) machines, among others [92, 94]. These components are conventionally fabricated by various processes, including powder metallurgy [91], squeeze casting [95], infiltration [92], and self-propagating high-temperature synthesis (SHS) [96].

Table 1-4 summarizes the works performed to fabricate Cu-matrix composites with various ceramic reinforcing particles using AM processes. Tungsten (W) is a refractory metal that has been widely incorporated into the Cu matrix to produce composites. However, the mutual insolubility of Cu and W and the poor wettability of W particles with the Cu melt are the major concerns with these MMCs, limiting their densification response [97].

Because of having a lower density, higher hardness, and higher stability than W, tungsten carbide (WC) could be considered as substituting reinforcement to W. To further improve the mechanical properties; i.e., hardness, strength, wear-resistance, and fracture toughness, the well-known WC-Co hard metal is also used as reinforcement to the Cu matrix in AM processed composite [98-103]. Rare earth (RE) elements have also been added in small amounts to AM processed Cu-matrix composites to improve processability, control the microstructural evolution, and enhance the mechanical properties of fabricated Cu matrix composites [103, 104].

Table 1-4 Mixed powder systems and AM techniques employed to fabricate various types of Cu-matrix composites.

Ref.	Mixed Powder System	Matrix	Reinforcement	Reinforcement Content	Process
[105]	Cu/Ti/C, Cu/Ni/Ti/C	Cu, CuNi	In-situ TiC	10 vol.%	SLM
[97, 106]	W/Cu	Cu	W	28, 40, 52 wt.%	DMLS
[104]	WC/Cu		WC	60 wt%	
[100, 102]	WC-Co/Cu		WC-Co	30 wt.%	
[101, 107]				20, 30, 40 wt.%	
[103]				50 wt.%	
[108]	CNT/Cu-10Sn	Cu-10Sn	CNT	0-20 vol.%	LENS

1.2.5 Iron-based Matrix Composites

As far as AM technology has come into existence, iron-based alloys have been among the most investigated materials due to their wide range of applications in various industries. For example, tool steels and stainless steels are two categories of iron-based alloys which have attracted great attention in the field of AM, especially when it comes to the fabrication of MMCs having these materials as the matrix.

H13 is a hot work tool steel with a medium carbon content that is extensively used to make tools for cutting, forming and shaping purposes because of outstanding properties such as high strength, high wear resistance, and sound stability at high temperatures [109]. However, when needing materials capable of withstanding harsh environments with extremely high loads and temperature gradients, they may not be the best candidates. Because of improved strength, wear resistance, reduced cost, and lower density, MMCs are believed to be the materials to serve in these environments [110].

Using AM processes, especially SLM, TiC, and TiB_2 have been used recently as reinforcing particles to fabricate H13 matrix nano-composites. Due to their high elastic modulus (EM), high thermal stability, low density, and high thermodynamic stability with the matrix, these reinforcing particles are among the best ceramic materials used as reinforcements to the steels matrices [111, 112]. While SiC has also been used as reinforcement to iron-based composites, its strong reactivity with the transition metals of the matrix may lead to the formation of detrimental phases at high temperatures and deteriorate the mechanical properties [113].

Stainless steels are also an important grade of iron-based alloys with many applications in many industrial fields, especially those needing materials with good mechanical properties and excellent corrosion resistivity. However, one of the major problems associated with stainless steel is its limited hardness and wear resistance.

Incorporating reinforcing particles into the stainless steel matrix to form MMCs has been considered an effective approach to produce parts with enhanced physical and mechanical properties that meet the requirements of high-tech industries (e.g., aerospace and biomedical) [114, 115]. Among various types of reinforcements (e.g., carbides, nitrides,

borides, and metal oxides) incorporated into steel by conventional processes, TiB_2, TiC, and hydroxyapatite (HA) are added to the stainless steel matrices using AM processes. The main purpose behind the addition of HA to stainless steel is to combine the relatively high strength of stainless steel with the outstanding biocompatibility of HA, leading to MMCs with excellent load-bearing and bioactive properties. These MMCs could be employed as internal, hip, and maxillofacial implants in the human body. Because finer HA particles have higher surface-to-volume ratios and are associated with higher bioactivity [117], attempts have also been made to replace the micro-sized HA particles with nanoparticles [116, 117]. Compared to the significantly sharp change in mechanical properties at the interface of coated implant parts, the uniform metallurgical bonding between the matrix and the reinforcements in MMCs can provide much more functional parts in biomedical applications. Table 1-5 presents the iron-based matrix composites made using AM technology.

Table 1-5 Mixed powder systems and AM techniques employed to fabricate various types of iron-based matrix composites.

Ref.	Mixed Powder System	Matrix	Reinforcement	Process
[118]	TiC/H13 steel MMnC	H13 steel	TiC	SLM
[119]	TiC/316L SS* MMnC	316L SS		
[120]				
[121]	TiB_2/316L SS MMnC	316L SS	TiB_2	
[122]				
[123]	TiB2/H13 steel MMnC	H13 steel		
[124]	TiC/Invar 36	Invar 36	TiC	DMLS
[125]	HA/316L SS MMC and MMnC	316L SS	Hydroxyapatite (HA)	SLM
[117]				
[126]	SiC/iron MMnC	Iron	SiC	
[127]	SiC/iron (with hybrid micro- and nano-size SiC)			

* SS refers to stainless steel

1.3 Pre-Processing of Mixed Powder System

Since the powder is used as the starting material to fabricate parts in most AM processes, its prerequisite conditions are crucial and significantly affect the quality of AM processed parts. The morphology of powder particles (e.g., size and shape) defines the extent of particle packing and consequently influences the thickness of deposited layers and the surface roughness. Due to the improved flowability and enhanced quality of parts fabricated by spherical powder particles, the gas atomized powders having such morphology are widely used in AM processes, especially the powder bed ones [128]. However, the limited flowability and mechanical interlocking and entangling of irregular-shaped powder particles limits the powder flow, makes the melt pool tracks non-homogeneous, and favors the formation of porosities in the solidified part. Figure 1-5 clearly compares the surface of selective laser sintered parts fabricated using irregular-shaped water atomized high-speed steel powders with spherical gas atomized powders.

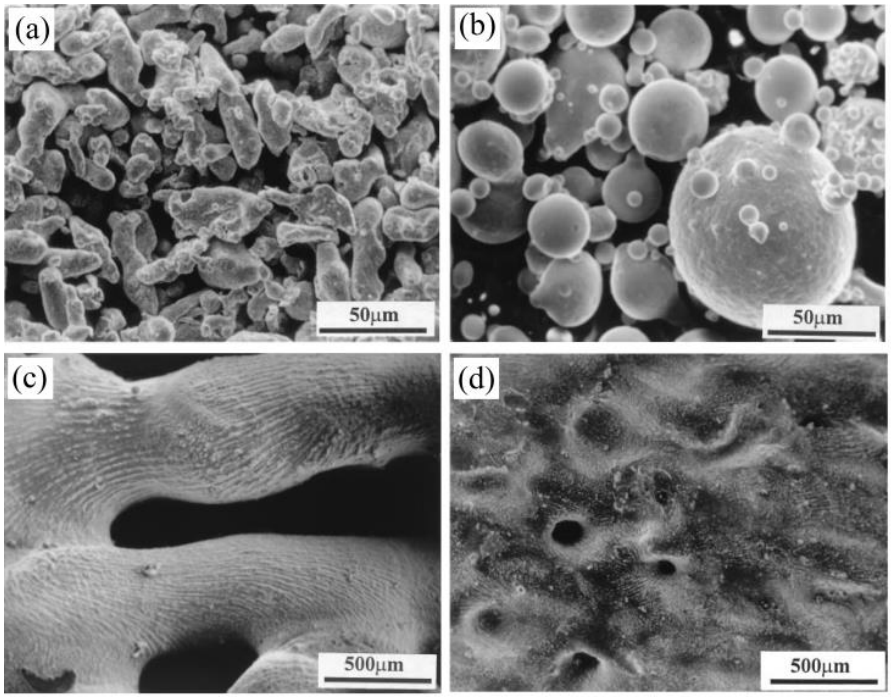

Figure 1-5 Scanning electron microscopy (SEM) images of (a) water atomized and (b) gas atomized high speed steel powder particles. (c) and (d) SEM micrographs of laser sintered powders shown in (a) and (b), respectively [128]. (Please see the footnote[7] [129])

Despite the noticeable technological advances in AM technology, there are still some limitations on the compositions of available powders. Accordingly, when MMCs are considered, desired powders should be blended, pre-processed, and then fed to fabricate parts.

Besides the direct mechanical mixing, ball milling has been regarded as one of the most applicable processes for mixing powders. During this process, the powder particles are imparted to tremendous energy induced by the balls, leading to fragmentation of brittle

[7] It is worth noting that not all powders produced by the water atomization (WA) process are irregular in shape. The powders fabricated by this method may also be quasi-spherical.

powder particles and induction of severe deformation or even fragmentation in the ductile ones [130].

The milling time significantly affects the morphology and distribution pattern of particles during the powder pre-processing stage. Figure 1-6 shows the spherical commercially pure (CP)-Ti and irregular-shaped TiB_2 starting powders used for fabricating TiB reinforced TMCs.

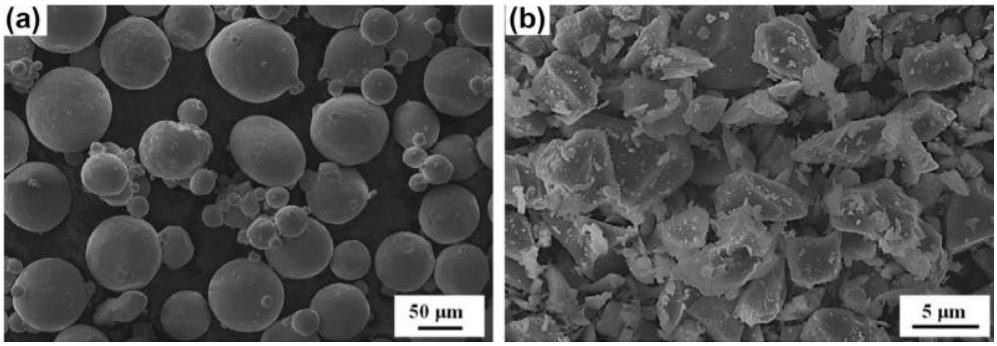

Figure 1-6 SEM micrographs of: (a) CP-Ti and (b) TiB_2 powder particles [48].

The morphology of these powder mixtures ball milled for 1-4 h are provided in Figure 1-7. As observed, relatively short milling time of 1 h led to the inhomogeneous distribution of TiB2 powder particles in the mixture with their limited connectivity to the Ti particles (Figure 1-7 (a)). Enhancement of milling time to 2 h provided the improved dispersion of TiB_2 ceramic particles around the Ti particles uniformly (Figure 1-7 (b)). Although the prolonged milling time could further improve the distribution of fragmented TiB_2 particles, it may transform the desired spherical shape of the mixed powder system to a flattened and irregular shape. This morphological change may not be of interest in the PBF-AM processes (Figure 1-7 (c) and (d)).

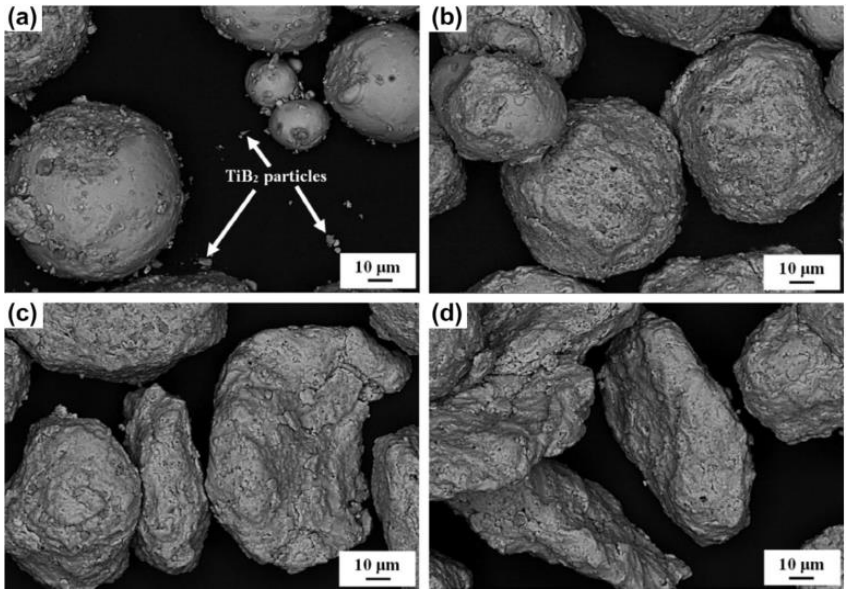

Figure 1-7 SEM images of CP-Ti and TiB_2 powders in Figure 1-6 mixed using ball milling for different times of: (a) 1 h, (b) 2 h, (c) 3h and (d) 4 h [48].

The applied milling time can also affect the chemical reactions activated in the powder system during mixing. Due to the short-term action of mechanical force and the resultant decreased energy subjected to the powder particles at relatively short milling times, the system may not undergo solid-state chemical reactions between the elements to form new phases. For instance, ball milling of the Ti and TiB_2 powder mixtures for as long as four hours does not activate the metallurgical bonding between the powders to form in-situ TiB phase from the reaction between Ti and B elements [48, 57]. However, the prolonged and continuous microscopic action of the mechanical force by ball-powder-ball collisions may favor such chemical reactions. For example, ball milling of Ti+SiC powder mixture for a relatively long milling time of 15 h favors the formation of TiC and Ti_5Si_3 phases [46].

In addition to the synthesis of new phases, the ball milling process may also provide some systems with solid solution formation. For example, mechanical alloying of Ti, Al, and graphite elemental powder mixtures before the SLM process reveals that while the TiC

phase forms in-situ within a short milling time due to its large negative enthalpy and Gibbs free formation energy, the Ti(Al) solid solution appears gradually with increased milling time [45].

The size of powder particles during ball milling is determined by the competition between two mechanisms of fracturing and cold-welding. While the fracturing mechanism tends to decrease the particle size, the cold-working mechanism favors the attachment of powder particles to form larger-sized particles. Therefore, the refining or coarsening of powder particles depends on whether the fracture mechanism or the cold-welding is predominant.

The category of mixed powder system is an important issue influencing the microstructural evolution and mechanical properties of fabricated MMCs parts. By changing the milling time from 4 to 10 h, Gu et al. [41] prepared two different TiC/Ti powder blends named directly mixed and ball milled, respectively. The mechanism of laser interaction with two different categories of powder blends is schematically presented in Figure 1-8. While the direct action of the laser beam on TiC particles for the directly mixed system results in simultaneous melting of TiC and Ti powder particles, the TiC particles in the ball-milled category are not directly exposed to the laser irradiation. Accordingly, TiC powder particles' dissolution occurs after the Ti's melting in the ball-milled system. These differences in the laser interaction affected the dissolution and re-precipitation of TiC particles and the microstructural evolution of laser processed MMCs.

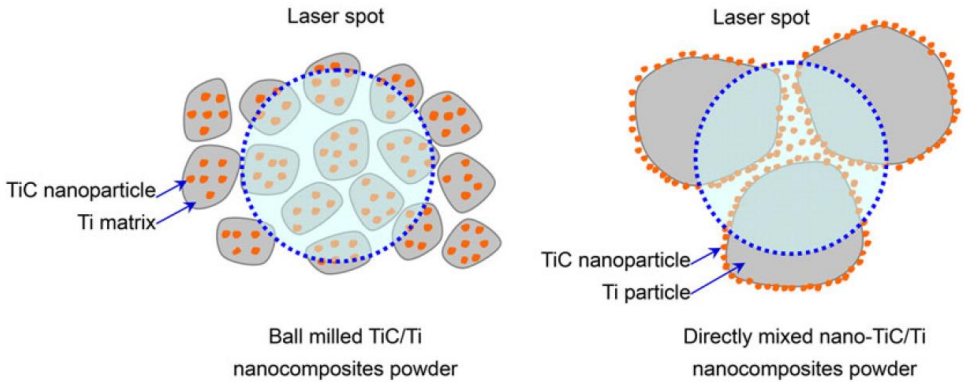

Figure 1-8 Schematic illustrations of laser beam interaction with two different categories of TiC/Ti mixed powder system [41].

In addition to the direct mechanical mixing and ball milling processes, blending of powders in some systems may be performed using dilute solutions followed by drying. To prepare suitable premixed composite powder, Das et al. [59] blended Ti6Al4V and BN powders with dilute polyvinyl alcohol solution in a tubular mixer for 24 h and then dried the mixed powders. The obtained mixture of powders in

Figure 1-9 reveals that the fine BN particles are uniformly coated on the surface of Ti6Al4V alloy powder particles. This type of rearrangement can facilitate the homogenous distribution of reaction products in the solidified microstructure.

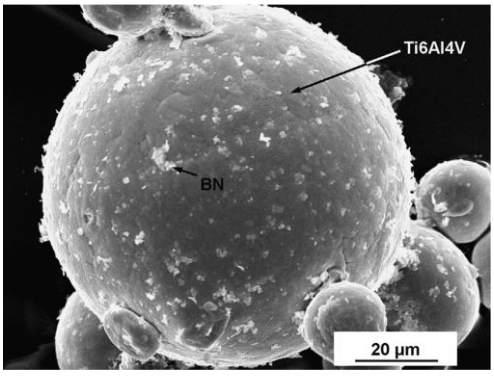

Figure 1-9 SEM image of Ti6Al4V and BN powder particles premixed with diluting followed by drying [59].

1.4 Microstructural Evolution in Additively Manufactured MMCs

As the laser beam interacts with a mixed powder system containing ceramic and metallic constituents, part of the mixed powder with a lower melting point melts first, while the part with noticeably higher melting point (usually ceramic reinforcing particles) may remain mostly unaffected and partially and/or completely melted. Therefore, the system may contain solid reinforcements distributed in a molten matrix.

Microstructural evolution in MMCs fabricated by AM processes is affected by several factors. Depending on the applied AM technique, selected process parameters (laser and scanning parameters), characteristics of mixed powder system, and the chemical affinity between the elements existing in the system, a part or all of the primarily added reinforcing particles may react with the surrounding liquid metal.

The laser and scanning parameters involve laser power, scanning speed, hatch spacing, layer thickness, and scanning strategy. To specify the amount of energy delivered to a unit volume of powder system during processing, the energy density has been defined by combining some important laser and scanning parameters as [131]:

$$E_\rho = \frac{P}{\pi r^2}\frac{2r}{\upsilon}\frac{2r}{h} \quad [1]$$

where P is the laser power (W), r represents the beam radius (mm), υ is the scanning speed, h signifies the hatch spacing, and E_ρ is the energy density (J/mm^2).

Referring to Eq. 1, the energy density has three terms. The first term is related to the laser intensity. The second term signifies the time a circle of radius r is exposed to the beam, while the third term indicates the number of laser exposures received by any point on the

surface [131]. The volumetric energy density is the most commonly used energy density in the literature, defined as the energy delivered to a unit volume [132]:

$$\eta = \frac{P}{vh\mathrm{t}} \quad [2]$$

where t is the layer thickness, and η signifies the energy density per volume (J/mm^3).

The characteristics of the mixed powder system include the features of powder particles before and after the pre-processing stage. When the mixed powder system contains ceramic reinforcing particles added to the metallic powder, the size and volume fraction of these ceramic particles have major effects on the laser absorptivity of the system and consequently the quality and mechanical properties of AM processed MMCs parts. The applied procedure employed to mix the powder particles may also influence the size, morphology, and distribution pattern of powder particles and consequently play a role in the properties of fabricated parts.

Generally, the microstructural features of AM processed MMCs can be categorized as:

(i) Characteristics of reinforcements distributed in the matrix,

(ii) Reinforcement/matrix reactions, and

(iii) Microstructural evolutions in the matrix induced by the presence of reinforcements.

These microstructural features have been discussed in the following for various AM processed MMCs systems.

1.5 Characteristics of Reinforcements Distributed in the Matrix

1.5.1 Size and Morphology of Reinforcements

The applied energy density and the characteristics of the mixed powder system are the two parameters playing the most important roles in the size and morphology reinforcements have in AM processed MMCs. Effects of these parameters on the features of reinforcements can be discussed in terms of the ex-situ or in-situ reinforced nature of MMCs.

1.5.1.1 Ex-Situ Reinforced MMCs

For the ex-situ reinforced MMCs where the primarily added reinforcing particles play the reinforcing role to the matrix in the solidified MMC structure, the elevated melt pool temperature and the reduced cooling rate associated with the enhanced energy density can lead to partial melting or dissolution of reinforcing particles and consequently decrease their size in the solidified MMC microstructure [18]. Moreover, the applied energy density may affect the shape of primarily added reinforcing particles in ex-situ reinforced MMCs. The research performed by Gu et al. [76] indicated that enhancement of energy density in LMD processed TiC reinforced Inconel 718 matrix composites changed the shape of TiC particles from primary irregular polyangular to near round shape with some degrees of smoothening and refinement. The improved wettability of reinforcing particles by the surrounding melt induced at elevated temperatures is believed to dissolve the edges of reinforcing particles and result in their smoothening [80]. It is worth noting that although the elevated energy density could make the ex-situ reinforcements smooth and homogenize their distribution in the microstructure [80, 81], the excessive energy density applied to the system may coarsen the microstructure of matrix [81].

1.5.1.2 In-Situ Reinforced MMCs

Based on the type of MMC system under investigation, the elements of reinforcing particles dissolved into the matrix may precipitate as a newly developed in-situ synthesized phase during solidification. When it comes to such systems, the used mixed powder system and the applied process parameters need to be thoroughly examined to control the characteristics of reinforcements (i.e., size and morphology).

By having the following consequences, the enhanced energy density may change the size and morphology of in-situ synthesized reinforcements:

(i) The elevated temperature and increased thermalization in the melt pool [40, 42, 82] which favours the coarsening of in-situ reaction products.

(ii) The intensified surface tension and resultant Marangoni flow in the melt pool.

(iii) The improved wettability of solid reinforcements by the surrounding melt [56].

(iv) The reduced cooling rate and prolonged lifetime of the liquid molten material, facilitating the growth of reinforcements.

The research performed by Li et al. [76] on DLF of Ni/Ti/C mixed powder system reveals a strong relationship between the size and volume fraction of in-situ synthesized TiC precipitates in the microstructure. As well-known, ceramic reinforcements usually have higher laser absorptivity than the metallic powder acting as the MMC matrix in MMCs. The enhanced volume fraction of in-situ synthesized TiC reinforcements is believed to increase the melt pool temperature, favoring the coarsening of in-situ synthesized reinforcements (Figure 1-10). Moreover, the increased content of solid reinforcements reduces the amount of molten material in the system and encourages the coalescence of reinforcements to form larger-sized precipitates.

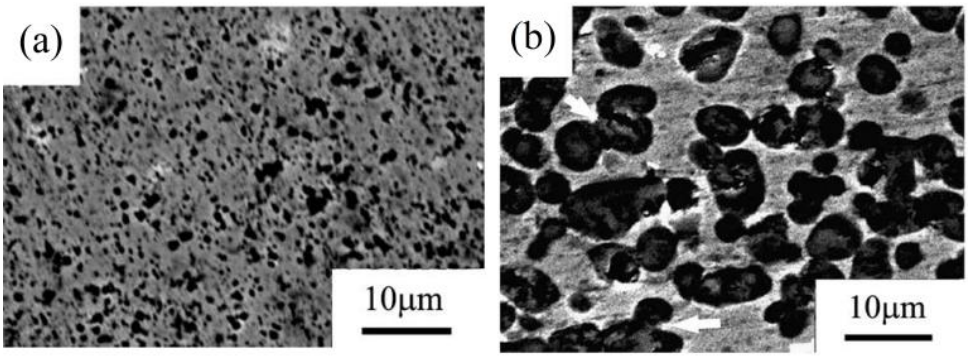

Figure 1-10 Microstructures of DLF processed TiC reinforced Ni matrix composites containing: (a) 20 and (b) 60 vol.% in-situ synthesized TiC [76].

Among various features of the mixed powder system, the size of starting powder particles is greatly important in the obtained MMCs structures. Because of benefiting from a higher surface-to-volume ratio, the finer primarily added reinforcing particles can enhance the laser absorptivity of the system and induce much more heat in the melt pool. This may affect the melting efficiency of starting reinforcing particles and the characteristics of subsequent in-situ synthesized precipitates.

1.5.2 Distribution Pattern of Reinforcements

The distribution pattern of reinforcements in AM processed MMCs is generally controlled by the mutual interaction between reinforcements and the solidification interface. Accordingly, the features of reinforcements and the properties of the solidification interface are the main factors affecting the distribution pattern of reinforcements. The solidification mode and growth velocity are two features of the interface having major effects on the distribution pattern of reinforcements in MMCs. The growth velocity (V_s) of the solidification interface is mainly determined by the applied scanning speed. However, the solidification mode is affected by several factors, including the processing parameters

and alloy type. Microstructural characterization of the AM processed MMCs reveals a non-planar solidification mode in most of these materials due to the following reasons:

(i) The solid reinforcements incorporated into the system may have different thermal conductivity and specific heat from the matrix. This may locally destabilize the planar solidification interface,

(ii) The laser-induced turbulence in the melt pool may demolish the planar solidification interface,

(iii) The dissolution of reinforcements into the surrounding melt may provide constitutional undercooling for the matrix. This can change the solidification mode of the matrix from planar to non-planar.

Therefore, the distribution pattern of reinforcements in the matrix of MMCs needs to be discussed in terms of the interaction between the reinforcements and the non-planar solidification interface (usually dendritic).

The following describes the most important factors affecting the distribution pattern of reinforcements in AM processed MMCs.

1.5.2.1 Effect of Scanning Speed

At relatively low solidification velocities (low scanning speeds), the reinforcements are pushed by the dendrite tips (solidification interface) into the adjacent melt, resulting in local pile-up of the majority of reinforcements and their aggregation along the boundaries of the solidified MMC structure (Figure 1-11 (a) and (b)) [100]. While most of the reinforcements may be located at the boundaries, a few may also be found within the grains [118, 122]. When the particle pushing mechanism is dominant, the reinforcements cannot restrict the crystal growth to a great extent [133].

In the case of particle engulfment mechanism where the solidification velocity (V_s) exceeds a critical velocity (V_{cr}), the solid reinforcements are kept stationary and are entrapped in the growing dendrites, bringing about a uniform distribution pattern of reinforcements in the matrix (Figure 1-11 (c) and (d)) [100]. V_{cr} is defined as [134]:

$$V_{cr} = \frac{\Delta\sigma_o d_0}{6(n-1)\eta r}\left(2 - \frac{k_p}{k_l}\right) \quad [3]$$

in which d_0 is the interatomic distance of the matrix alloy, n = 2 to 7, η is the melt viscosity, r is the radius of solid reinforcement which is assumed to be spherical, and k_p and k_l refer to thermal conductivities of reinforcement and liquid, respectively. $\Delta\sigma_o = \sigma_{ps} - (\sigma_{pl} + \sigma_{sl})$, in which σ_{ps}, σ_{pl} and σ_{sl} are reinforcement-interface, reinforcement-liquid and interface-liquid surface energies, respectively.

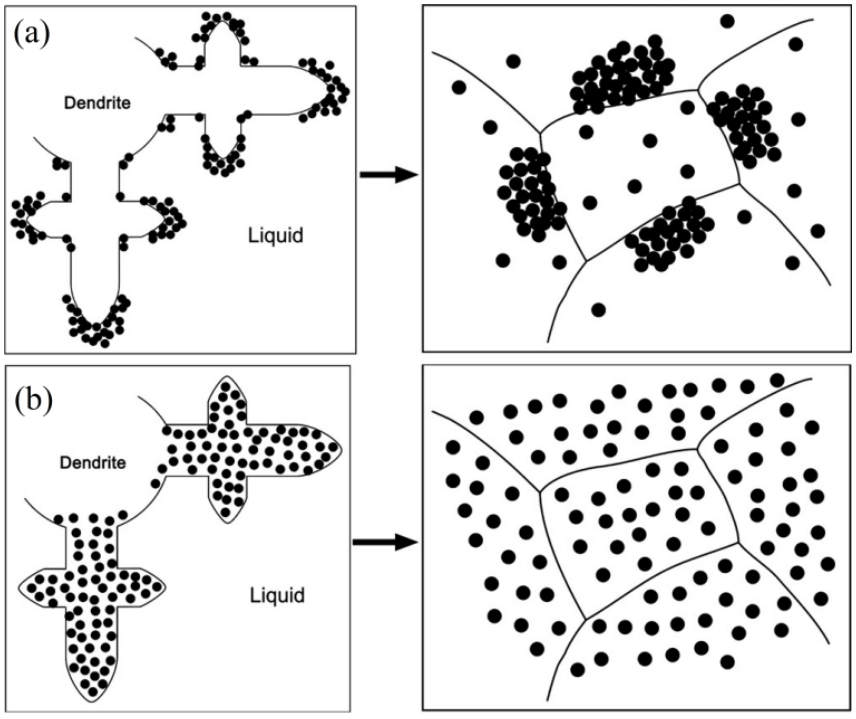

Figure 1-11 The reinforcement/dendrite interactions in: (a) particle pushing and (b) particle engulfment mechanisms [100].

1.5.2.2 Effect of Energy Density

The amount of energy density applied to the system is greatly important in determining the distribution pattern of reinforcements. Generally, relatively low energy densities are associated with the clustering of reinforcements and their inhomogeneous dispersion [79, 82]. However, the appropriate selection of energy density results in much more homogenous microstructures in terms of the distribution pattern of reinforcements due to: (i) decreased melt viscosity, (ii) improved wettability of reinforcements, and (iii) the intensified convective flow in the melt pool.

1.5.2.3 Effects of Size and Volume Fraction of Reinforcements

The size and volume fraction of reinforcements also play important roles in their distribution pattern and the crystal growth of the obtained microstructures. Using two different starting micro- and nano-sized TiC powder particles, AlMangour et al. [119] found the noticeable effect of reinforcement size on microstructural features of SLM processed TiC reinforced 316L stainless steel matrix composites. While the fabricated MMCs both showed cellular dendritic structures containing TiC reinforcements aggregated along the cell boundaries, those with nano-sized TiC particles had thinner walls of cellular structure.

In the case of MMCs with large-size reinforcements, the solidification interface may not push the particles, leading to their engulfment in dendrites or their entrapment into inter-dendritic regions. When the diameter of reinforcements is larger than a critical value (λ_{cr}), they are capable of avoiding crystal growth. The critical diameter of reinforcements is defined as [135]:

$$\lambda_{cr} = 2\lambda_1 R_d \quad [4]$$

where λ_1 refers to the primary dendrite arm spacing while R_d represents the radius of the dendrite tip.

Although high volume fractions of reinforcements enhance the chance for restriction of crystal growth and the subsequent grain refinement of the matrix, the particle pushing mechanism activated at low solidification velocities may promote the clustering of reinforcements to form agglomerates with larger effective sizes or greater effective thicknesses. For example, microstructural characterization of the SLM processed TiB_2 reinforced 316L stainless steel matrix nanocomposites presented in Figure 1-12 reveals that by the increased volume fraction of TiB_2 reinforcements from 2.5 to 15 vol.%, clustering of much more reinforcements along the cell boundaries leads to coarsening of walls of cellular structure [121].

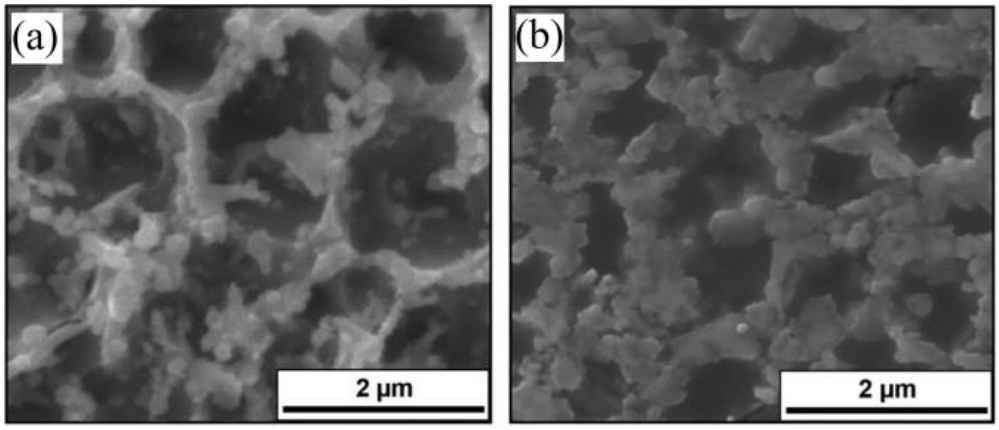

Figure 1-12 SEM micrographs of SLM processed TiB_2 reinforced 316L stainless steel matrix composites containing: (a) 2.5 and (b) 15 vol.% reinforcement [121].

1.6 Reinforcement/Matrix Reactions

1.6.1 Reaction Mechanisms

Generally, in-situ reaction products in MMCs are formed through five different mechanisms as the following:

(i) Solute precipitation: The in-situ formation of precipitates from the saturated solution through nucleation and the subsequent growth.

(ii) Solid-liquid interfacial reaction: The reaction between the melt and outer surface of solid particles dispersed in it. This mechanism results in the formation of a reaction layer around the solid particles. The reaction progress dictates the thickness of this reaction layer.

(iii) Combined solute precipitation and solid-liquid reaction: The existence of both solution precipitation and solid-liquid interfacial reaction for some systems.

(iv) Solid-solid interfacial reaction in the melt: The interfacial in-situ reaction between solid phases existing in a melt which leads to the formation of new phase.

(v) Solid diffusion reaction: The in-situ formation of new phase from the induced solid state diffusion reaction between solid particles.

Among different mechanisms discussed above, due to the presence of melt in the system, the in-situ reaction between the solid reinforcing particles and the molten material in AM processing mainly follows the first three mechanisms and is affected by the following factors:

(i) The amount and temperature of molten material formed during processing,

(ii) The solid solubility of particles in the melt,

(iii) Wettability of the particles with the molten material, and

(iv) Solid-phase diffusion in the melt.

1.6.2 Reinforcements/Matrix Interfacial Reaction

The physical and mechanical properties of the interface between the reinforcements and the matrix are the parameters playing significant roles in densification level and mechanical

properties of AM processed MMCs. Generally, the interfaces between the ceramic reinforcements and the metallic matrix in particulate reinforced MMCs are weak, introducing them as sensitive and potential locations for crack nucleation and propagation during sliding. However, the researches have recently shown the formation of good interfacial bondings between the reinforcements and the matrix in AM processed TiC reinforced Ni matrix [76], TiB_2 reinforced 316L stainless steel matrix [121], TiC reinforced Al matrix [27], and TiC reinforced titanium matrix [44] composites.

While the formation of interfacial reaction layers between reinforcements and matrix in some systems can modulate the difference between the deformation behaviors, improve the bonding coherence, and improve the mechanical properties of the fabricated MMCs, they may be detrimental to the mechanical properties in some other systems. Therefore, thorough efforts have been allocated in recent years for determining the characteristics of reinforcement/matrix interfaces in AM processed MMCs.

In addition to the powder particles considered to be melted and solidified as the metallic matrix, the high amount of energy associated with the AM processes can lead to the partial/complete melting and dissolution of the primarily added ceramic reinforcing particles with high melting points. The extent of these melting and dissolution is dictated by the energy density [136, 137]. In cases where a chemical potential exists for the reaction between the solid reinforcing particles and the molten matrix, reaction layers may be formed at the particle/matrix interfaces.

Depending on the elements existing in the mixed powder system, the in-situ reaction between elements may lead to a new or the same phase as the starting ceramic reinforcing particle. The in-situ reaction between the solid reinforcing particles and the melt for two

AM processed MMCs showing combined solution precipitation and solid-liquid reaction mechanisms are provided in Figure 1-13 and Figure 1-14. Figure 1-13 shows the microstructures for LENS processed TiN/Ti6Al4V mixed powder system with 10 and 20 wt.% TiN, respectively. Microstructural observations around a relatively large-sized SiC particle in LENS processed SiC/Ti powder mixture is also presented in Figure 1-14. The reaction layers around the TiN particles are believed to be TiN. However, that surrounding the SiC particles is detected as TiC, confirmed by energy-dispersive X-ray spectroscopy (EDS) line scan and compositional EDS map analysis results. The higher affinity of Ti to C compared with Si is the main driving force for the formation of TiC through SiC+Ti→TiC+Si exothermic reaction [138].

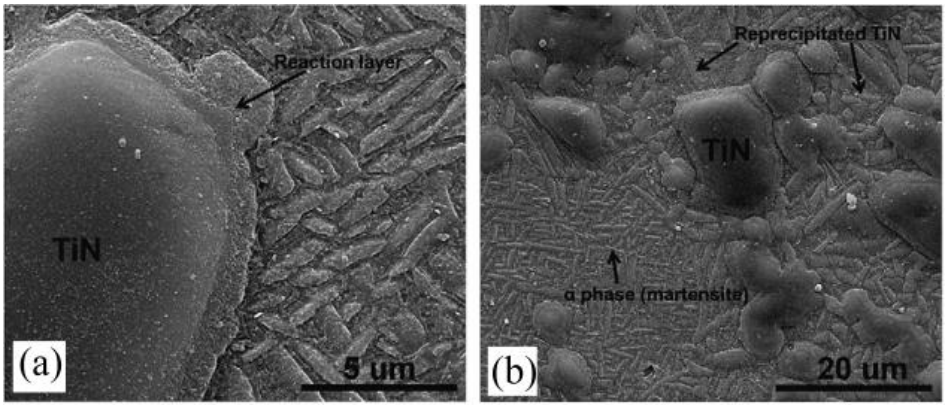

Figure 1-13 SEM micrographs showing reaction layers between: (a) coarse TiN particle and the matrix in 10 wt.%+Ti6Al4V and (b) finer TiN particles and the matrix in 20 wt.%+Ti6Al4V TMCs fabricated by LENS process [58].

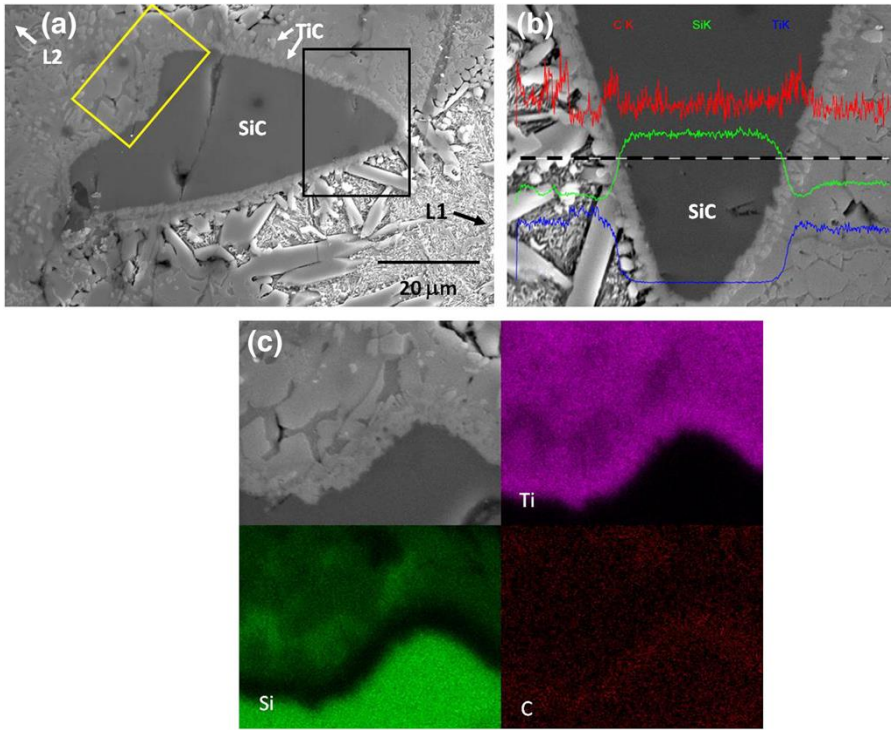

Figure 1-14 (a) SEM micrograph showing an undissolved SiC particle in the matrix of LENS processed SiC/Ti system. (b) EDS line scan and (c) EDS elemental map analysis results from the reaction layer surrounding SiC particle in (a) [55].

The features (e.g., thickness and chemical composition) of reaction layers around the reinforcing particles are affected by the applied processing parameters and the size of starting reinforcing particles. Referring to Figure 1-13, it can be found that reaction layers are thinner around the coarser TiN particles. The solubility of a solid particle in the surrounding liquid is negatively dependent on its size. Therefore, compared with the larger particles, the smaller ones have higher energy and solubility in the liquid. This size-dependency in solubility can generate a concentration gradient in the liquid during which the materials migrate from the small particles to the larger ones through diffusion in the liquid.

Figure 1-15 reveals the effect of laser energy density on the characteristics of the reaction layer formed at the interface of WC reinforcements and the Inconel 718 matrix. In this case, the strong carbide forming elements (e.g., Ni, Cr, Fe) existing in the molten matrix come into reaction with W and C elements on the surface of WC particles, leading to the formation of graded (W, M)C_x (M=Ni, Cr, Fe) interfacial layers. The melt pool's higher working temperature and the accelerated diffusivity of elements induced at higher energy densities are the main driving forces for the increase in the thickness of reaction layers [79, 80, 88].

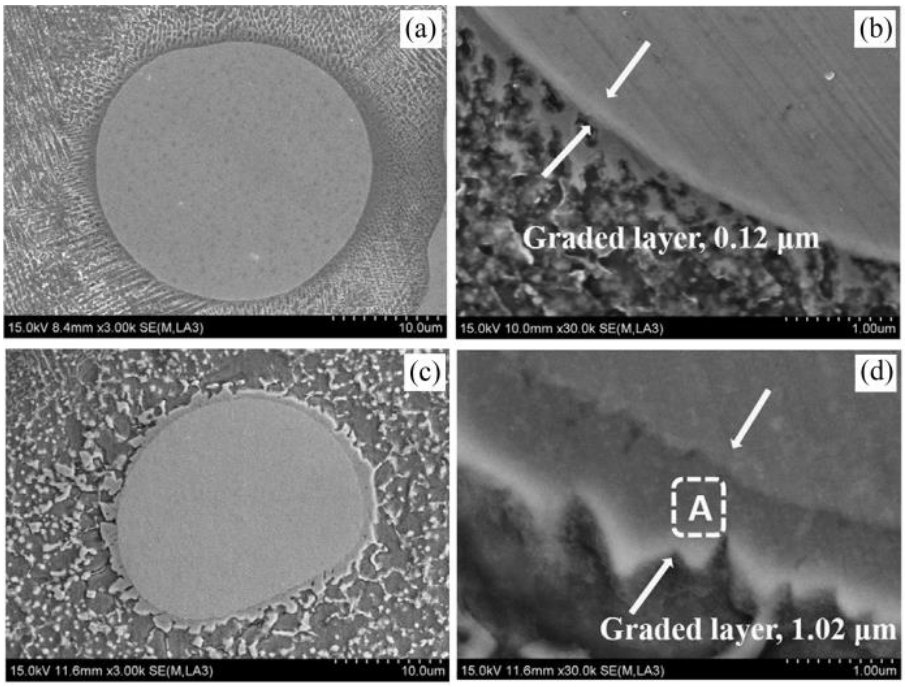

Figure 1-15 SEM micrographs showing the characteristics of reinforcement/matrix interfacial reaction layer formed in WC reinforced Inconel 718 matrix composites at linear laser energy densities of: (a), (b) 173 and (c), (d) 303 J/m [88].

Coating primarily added reinforcing particles could be considered one of the strategies to promote the wettability of reinforcing particles and simultaneously restrict, modify, or avoid unwanted interfacial reactions between the reinforcing particles and the matrix [85,

137, 139]. Using two different Ni-coated and uncoated TiC particles as starting reinforcing particles, Zheng et al. [86] employed the LENS process to fabricate TiC reinforced Inconel 625 matrix composites. Microstructural observations revealed that while a part of Ni coating on TiC particles melted and dissolved into the matrix due to the convective flow in the melt pool, TiC particles remained unaffected, with a thin layer of well-bonded Ni still remaining on their surface. On the other hand, uncoated TiC particles experienced partial melting when subjected to the same processing parameters (Figure 1-16).

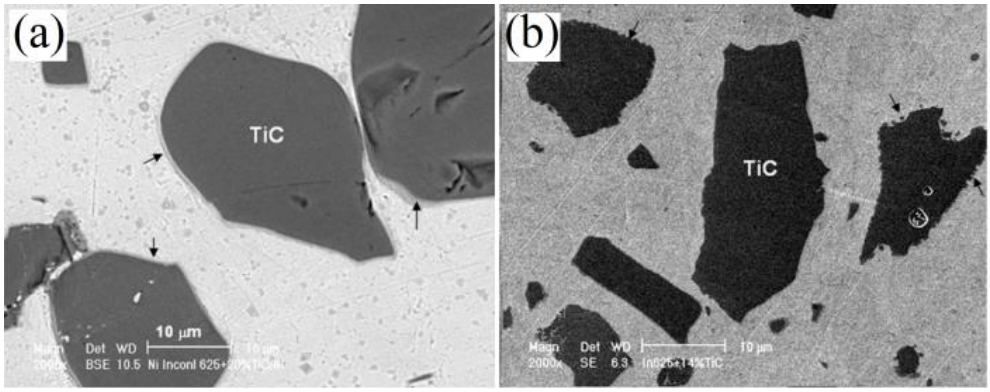

Figure 1-16 SEM images of LENS processed TiC reinforced Inconel 625 matrix composites having: (a) Ni-coated and (b) un-coated TiC as the starting reinforcing particle [85].

Despite the high energy delivered to the mixed powder system during AM processes, the starting reinforcements in some systems may experience partial melting or even remain as unmelted particles in the solidified microstructure. The interfacial region of reinforcements and the matrix in these kinds of MMCs may be almost free of reaction products. The transmission electron microscopy (TEM) characterization of the reinforcement/matrix interface in SLM processed ex-situ BN reinforced Inconel 718 matrix composites in Figure 1-17 indicated that while no reaction layers were formed at the interface, some small-sized particles of Inconel 718 matrix with spherical morphology existed at the interfacial regions.

The same kind of interface has also been observed in SLM processed TiC reinforced H13 matrix [118] and TiB_2 reinforced 316L stainless steel matrix nanocomposites [121].

The formation of reinforcement/matrix interface free of reaction layers may be ascribed to the following phenomena:

(i) The high activation energy barrier for breaking the bonds in the primarily added reinforcements [89, 140]

(ii) The combined effects of high diffusion and sudden cooling rates induced at the reinforcement/matrix interface of AM processed MMCs

(iii) The insufficient energy imparted to the powder system which may not be high enough for breaking the bonds in primarily added reinforcements

(iv) The limited solubility of reinforcements into the matrix [141]

(v) The minimized diffusion of matrix alloying elements into the solid reinforcements [89, 141].

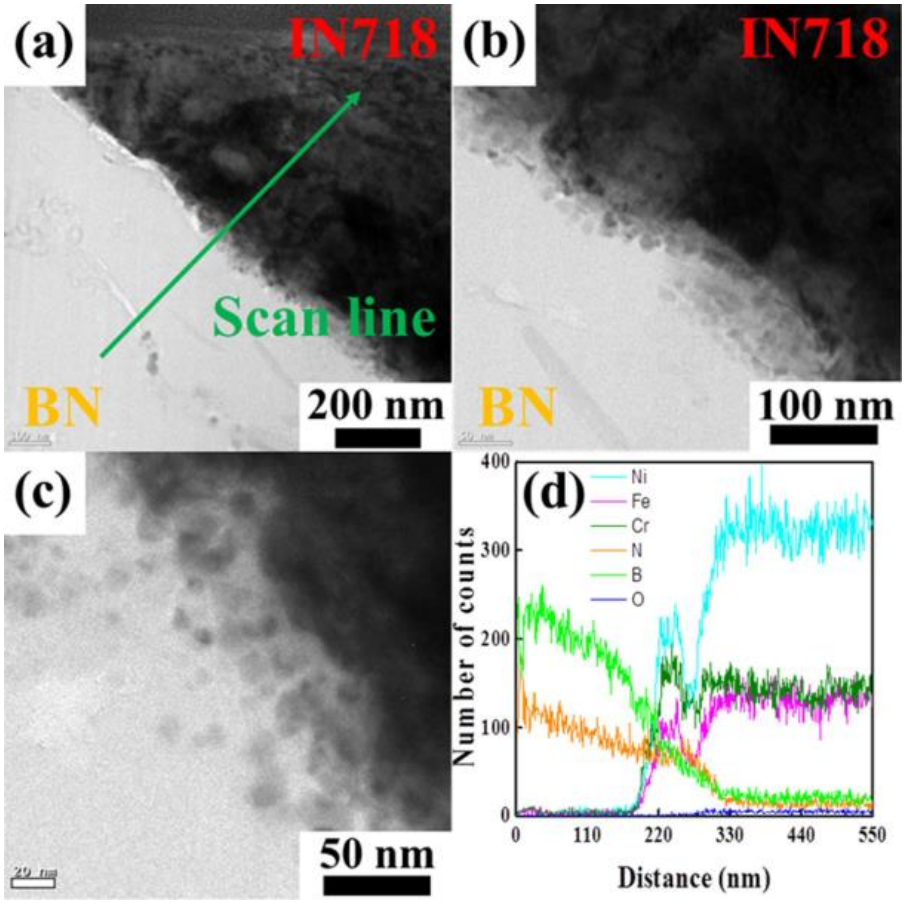

Figure 1-17 (a-c) TEM images of the reinforcement/matrix interface in SLM fabricated BN reinforced Inconel 718 matrix composites and (d) line scan EDS analysis results showing the distribution of elements along the line in (a) [89].

1.6.3 Formation of In-Situ Reaction Products

The part of primarily added powder particles melted and dissolved into the matrix can enrich and saturate the surrounding melt from the elements existing in the reinforcing particles. These elements may react with the elements existing in the molten matrix to form in-situ reaction products through the solution-precipitation mechanism. For instance, N atoms dissolved or diffused into the surrounding melt during laser processing of TiN/Ti system reprecipitated as in-situ TiN particles during solidification, especially in parts of the matrix where higher supersaturation of N was formed due to the closer spacing among

TiN particles (Figure 1-13). Another common mixed powder system showing solution precipitation mechanism is SiC/Al system. The in-situ reaction between the Al melt and SiC ceramic reinforcing particles ($4Al(l)+4SiC(s)\rightarrow Al_4SiC_4(s)+3Si$) results in the formation of plate-like Al_4SiC_4 phase adjacent to the SiC particles.

The Si released from this reaction combined with the Si came from the fully dissolved small-sized SiC particles and enhanced the Si content of the surrounding melt. If the Si content of the melt exceeds the equilibrium eutectic composition of Al-Si binary phase diagram, pro-eutectic silicon will be formed, followed by transformation of the remaining melt to Al+Si eutectic as the final solidification product [135]. The microstructure of laser-sintered 20 wt.%SiC/$Al_7Si_{0.3}Mg$ powder mixture in Figure 1-18 contains unmelted SiC particles as well as pro-eutectic Si and in-situ synthesized plate-like Al_4SiC_4 precipitates.

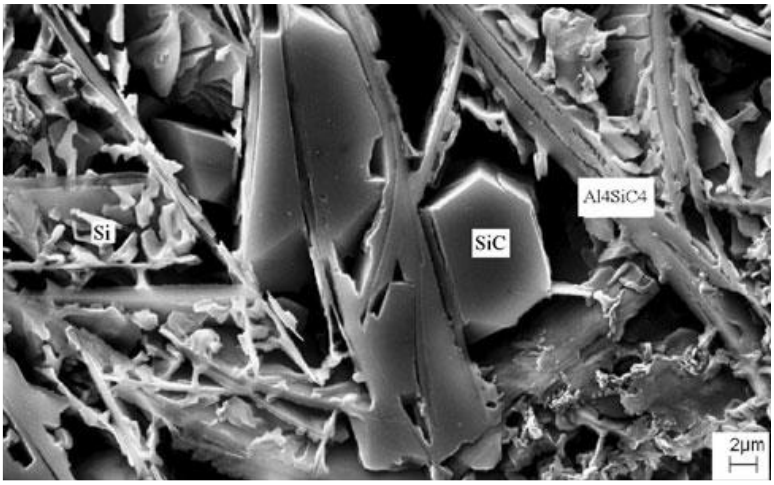

Figure 1-18 Microstructure of AMC fabricated by laser sintering of 20 wt.%SiC/$Al_7Si_{0.3}Mg$ powder mixture [21].

The amount of in-situ reactions in AM processes is controlled by the characteristics of the mixture powder system (e.g., size, shape, and volume fraction of the constituents), the employed AM technique, and the applied processing parameters.

Microstructures of TiC reinforced Inconel 718 matrix composites presented in Figure 1-19 clearly shows the effect of energy density on microstructural evolution of the reinforcements. At relatively low energy density, the primarily added TiC particles are remained unmelted, bringing about an ex-situ reinforced structure (Figure 1-19 (a)). Enhancement of the applied energy density forces the TiC particles to melt ad dissolve into the matrix. The Ti and C elements dissolved into the matrix reprecipitate again as in-situ synthesized TiC phase in the microstructure (Figure 1-19 (b)). At relatively high energy densities, full melting of primarily added TiC particles might lead to the formation of MMCs containing only in-situ synthesized TiC precipitates, which are noticeably finer than the ex-situ particles (Figure 1-19 (c)). Compared to the ex-situ added TiC particles, the superior interfacial bonding of in-situ ones with the matrix can contribute more to the strength of MMCs [58, 76].

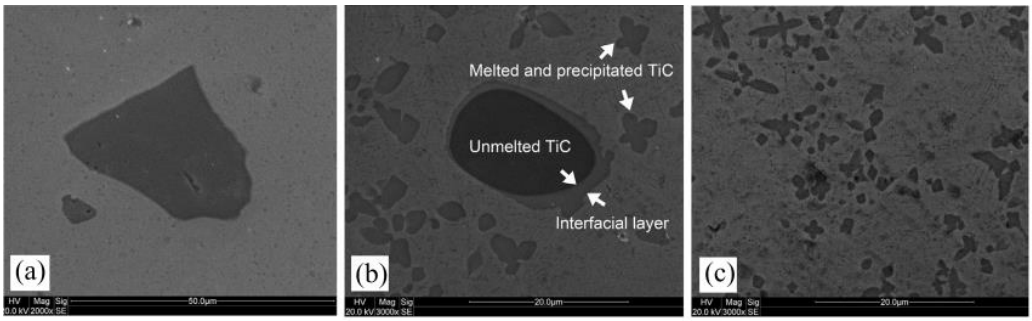

Figure 1-19 Microstructures of LMD processed TiC reinforced Inconel 718 matrix composites processed with energy densities of: (a) 80, (b) 120 and (c) 160 kJ/m [80].

When employing excessive energy densities, higher amounts and coarser reaction products may be formed in the MMCs. This could be attributed to the combinations of: (i) enhanced melting and dissolution of primarily added reinforcing particles, (ii) increased diffusion rate of alloying elements in the system, and (iii) elevated heat accumulation and significant internal energy around the in-situ synthesized precipitates.

1.7 Microstructural Evolutions in the Matrix Induced by the Presence of Reinforcements

1.7.1 Microstructural Refinement of the Matrix

Compared to the conventional manufacturing methods such as casting, the higher solidification and cooling rates associated with the AM processes lead to more significant microstructural refinement. The rapid solidification nature of AM processes is due to the very local heat input and noticeably small volumes of the molten material.

When using AM processes to fabricate MMCs, even finer microstructures can be achieved due to the presence of reinforcements in the system. Like other processing techniques such as casting and welding, solid reinforcing particles incorporated into the melt can promote heterogeneous nucleation during solidification and lead to grain refinement of the matrix. Therefore, the size, weight fraction, distribution pattern, and melting efficiency of these particles directly affect the solidification process and microstructural evolution of the matrix. For the ex-situ reinforced MMCs, the un-melted solid particles act as preferential sites for heterogeneous nucleation of grains. This is while for the in-situ ones, the newly developed precipitates formed at higher temperatures and distributed in the molten matrix play this role. The TEM image in Figure 1-20 shows an in-situ synthesized TiB precipitate acting as a nucleation site for the α phase in the Ti6Al4V matrix of LENS processed TiB reinforced TMC structure. Besides the role reinforcements play as nucleation sites, their grain growth-inhibiting effects caused by grain boundary pinning can also lead to matrix grain refinement.

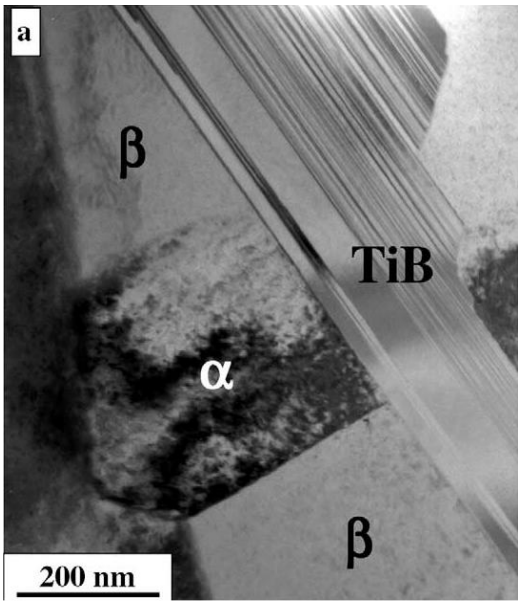

Figure 1-20 TEM image indicating the growth of α phase from in-situ synthesized TiB precipitate in LENS processed TiB reinforced Ti6Al4V matrix composite [50].

As an example of the matrix refinement, microstructural observations revealed that while the SLM processed CP-Ti had grains with average width and length of 2.1 and 15.3 μm, respectively, those for the matrix grains of TiB reinforced TMCs processed with the same parameters were noticeably decreased to 0.6 and 1.1 μm, respectively [49, 142]. In addition to the microstructural characterizations, the grain refinement of the matrix can also be identified by broadening, and decreased intensity of the matrix peaks in X-ray diffraction (XRD) patterns of the AM processed MMCs [80, 81, 119, 126].

The applied energy density is one of the major factors controlling the degree of microstructural refinement in AM processed MMCs. For example, while maintaining the columnar dendritic structure, enhancement of energy density from 30 to 100 kJ/m decreased the width of matrix dendrites from 3.8 to 1.3 μm in LMD processed TiC reinforced Inconel 625 matrix nano-composites. Such microstructural refinement was ascribed mainly to the increased dissolution of TiC particles and the subsequent larger

degrees of constitutional undercooling provided for the melt at elevated energy densities [82].

In cases where the dissolved elements have limited solubility in the matrix (e.g., B in Ti or Si in Al), the increased constitutional undercooling induced by partitioning of rejected solutes in front of the solid/liquid interface can make the solidification interface unstable and consequently give rise to the driving force for nucleation of much more grains at the solid/liquid interface. The rejected atoms segregated in front of the solidification interface can restrict the growth of nuclei and act as grain refiners as well [48]. In addition to the matrix grain refining, alloying elements existing in the system may also help refine in-situ synthesized precipitates. For instance, much finer Si precipitates have been achieved for SLM processed Al-20Si-5Fe-3Cu-1Mg alloy compared with Al-20Si [27, 143]. This has been attributed to the hindering effects of Fe, Cu and Mg alloying elements on growth of Si phase by two possible mechanisms: (i) a portion of Fe atoms are dissolved into Si precipitates, leading to the reduced activation of Si, and (ii) the Al_4FeSi_2 phase formed in the microstructure due to the presence of Fe retards the coarsening of Si precipitates by acting as barriers to the diffusion of Si atoms [27].

By increasing the number of nucleation sites for the matrix, higher amounts of reinforcements existing in the system can intensify the level of grain refinement experienced by the matrix [84, 121]. Figure 1-21 shows the microstructures for SLM processed pure 316L stainless steel and TiB_2 reinforced 316L stainless steel matrix composites containing 2.5 and 5 vol.% reinforcement, respectively. While the addition of 2.5 vol.% TiB_2 had a negligible effect on grain refinement of the matrix (Figure 1-21 (a)), a remarkable decrease in the grain size was observed for the MMCs containing a higher amount of TiB_2 (5 vol.%) (Figure 1-21 (c)).

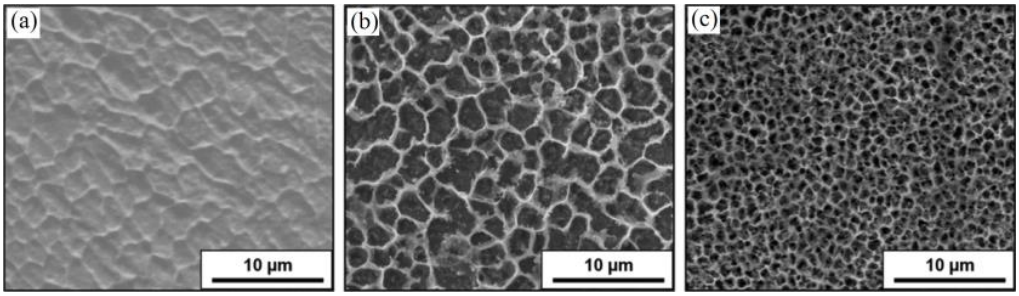

Figure 1-21 The microstructures of SLM processed: (a) non-reinforced 316L stainless steel, and TiB_2 reinforced 316L stainless steel matrix composites containing: (b) 2.5 and (c) 5 vol.% TiB_2 [121].

Since powder mixtures with a different arrangement of particles have quite different interactions with the laser/electron beam, the category of mixed powder system can significantly affect the microstructural characteristic of the matrix in AM processed composites. Figure 1-22 (a) and (b) show the microstructures for the SLM processed 15 vol.% TiB_2/316L stainless steel mixed powder systems prepared by direct mixing and ball milling, respectively. As being observed, the ball-milled powder category shows relatively finer cells of cellular structure.

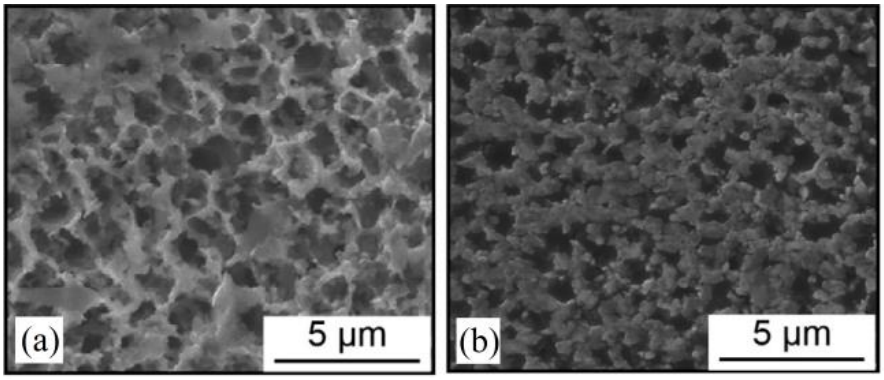

Figure 1-22 Microstructures of SLM processed TiB_2 reinforced 316L stainless steel composites with starting: (a) directly mixed and (b) ball milled powder systems [122].

1.7.2 Texture of the Matrix

One of the most notable features of AM processed parts is the anisotropy of the microstructure. This phenomenon is due to the large directional thermal gradients or high values of thermal gradient (G) to solidification rate (R) ratio (G/R) generated by the characteristic layer-by-layer nature of AM processes. Since the heat conduction in the building direction is typically higher than in other directions, the crystals grow preferentially along this direction. The anisotropy in microstructure can be associated with the anisotropy in mechanical properties [144-146]. The anisotropy in microstructure has been reported in the literature for many materials fabricated by AM processes [144, 146-148]. Figure 1-23 shows the optical micrographs, and electron backscattered diffraction (EBSD) orientation maps of SLM processed Inconel 738LC alloy obtained from sections perpendicular and parallel to the building direction. The grain shape anisotropy is obvious in the micrographs, with the long axis of grains oriented along the building direction.

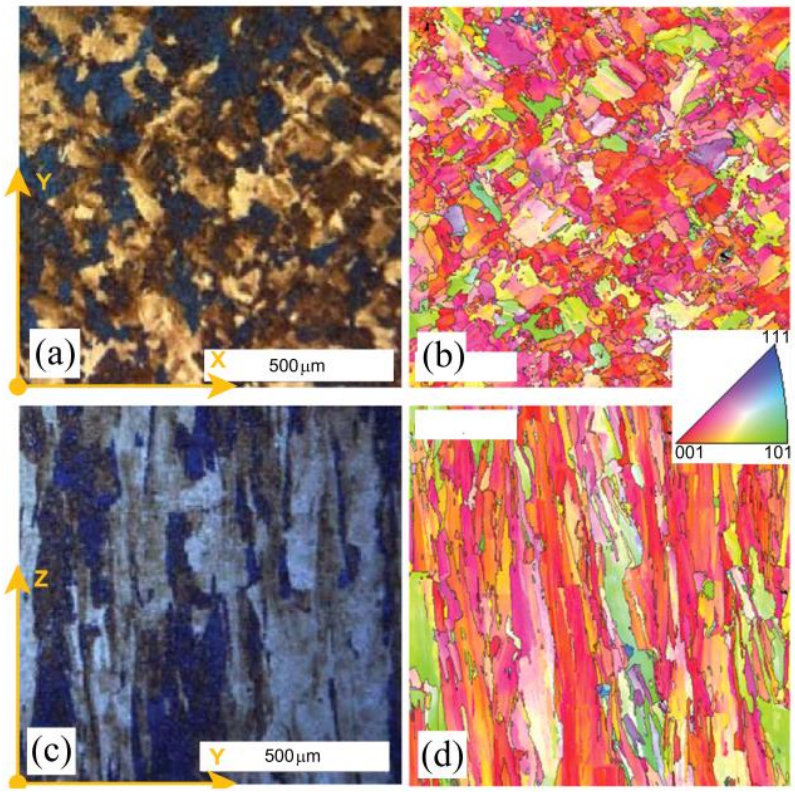

Figure 1-23 (a, c) Optical micrographs and (b, d) EBSD crystallographic orientation maps of SLM processed Inconel 738LC alloy. (a) and (b) are sections perpendicular to the building direction, while (c) and (d) are parallel to the building direction [148].

Application of scan strategies with rotating scan directions is an applicable technique employed to break up such anisotropic microstructures in AM processed parts. While the rapid solidifications rates associated with the AM processes enhance R, the basic concept behind most of these scan strategies is shortening of scan tracks to decrease the thermal gradient (G) and consequently decline the G/R ratio [149]. Incorporation of reinforcements into the melt pool may also affect the texture of the matrix in AM processed MMCs parts. Besides acting as preferential sites for the nucleation of grains, these reinforcements can retard the directional growth of grains during the solidification process [81, 127, 146, 150, 151]. As shown in SEM and EBSD micrographs in Figure 1-24, the TiC reinforcements

refined the microstructure and ceased the directional growth of the matrix, and led to much more isotropic structures. Thus, both the grain refining and directionality prohibiting were much pronounced for the MMCs containing nano-scale reinforcements.

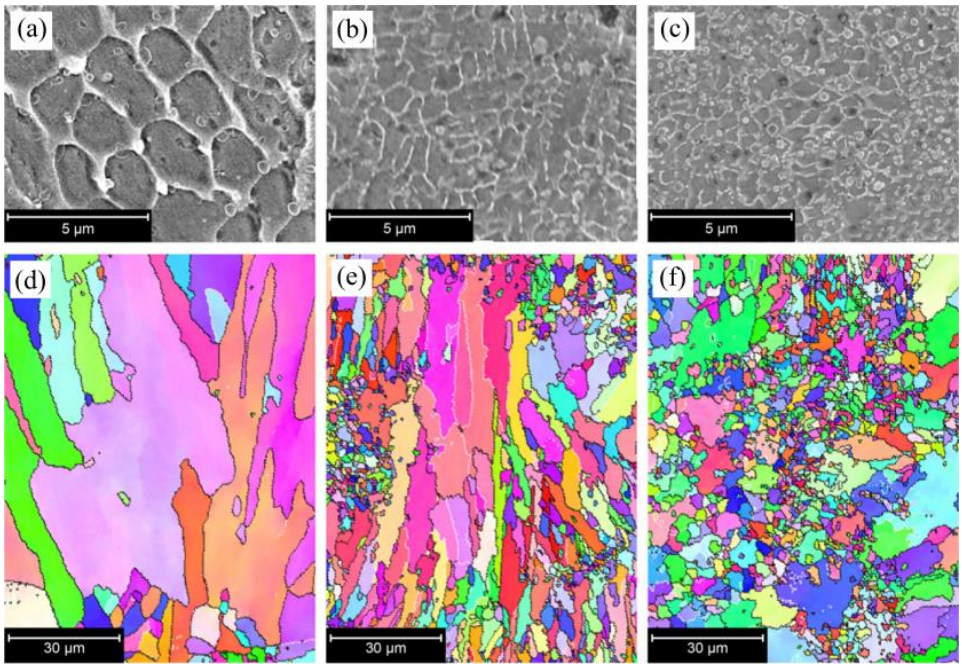

Figure 1-24 SEM images (first row) and EBSD crystallographic orientation maps (second row) of SLM processed: (a, d) non-reinforced 316L stainless steel; and TiC reinforced 316L stainless steel matrix composites with: (b, e) micro-scale and (c, f) nano-scale TiC reinforcements [151].

1.7.3 Microstructural Evolution and Phase Transformation

Due to the variations in multiple modes of heat, mass, and momentum transfer and the probable chemical reactions, the addition of reinforcements to the system may activate different consolidation mechanisms and microstructural evolutions in the matrix of AM processed MMCs [121]. The microstructures obtained from laser remelting of pure A356 powder and A356/SiC powder mixture in Figure 1-25 reveal the major roles reinforcements play in the matrix structure. While the laser-sintered pure A356 part shows a directional

solidification of columnar grains, incorporation of SiC reinforcements into the system leads to an equiaxed grain structure.

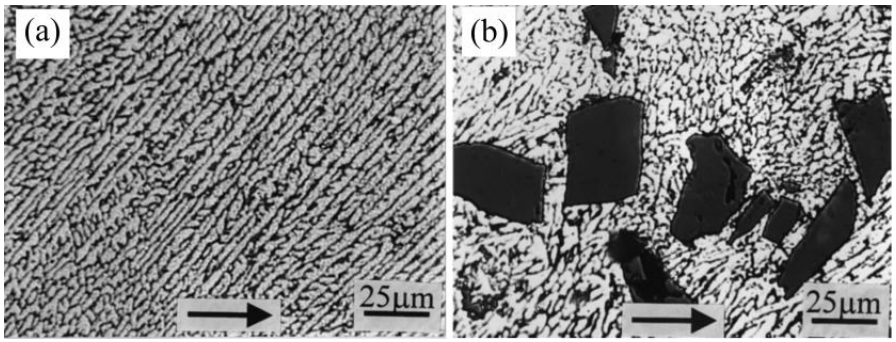

Figure 1-25 Optical micrographs of laser processed: (a) non-reinforced A356 Al alloy and (b) SiC reinforced A356 matrix composites [152].

The transition in grain growth mode by adding reinforcements has been reported in the literature for various systems. Even if the volume fraction of reinforcements is not as high enough to completely transit the solidification mode, such transition can be induced at least in reinforcement-containing regions [153]. Using the LENS process to fabricate functionally graded metal matrix composites (FGMMCs), Wilson and Shin [4] studied the effect of TiC content on the microstructural evolution of the Inconel 690 matrix. When the TiC content was less than 15 vol.%, the matrix was mainly composed of a columnar dendritic structure. However, a transition from columnar dendritic structure to finer elongated grains occurred for the MMCs with 15-30 vol.% TiC, leading to the microstructure having groups of elongated grains as its major fraction (Figure 1-26).

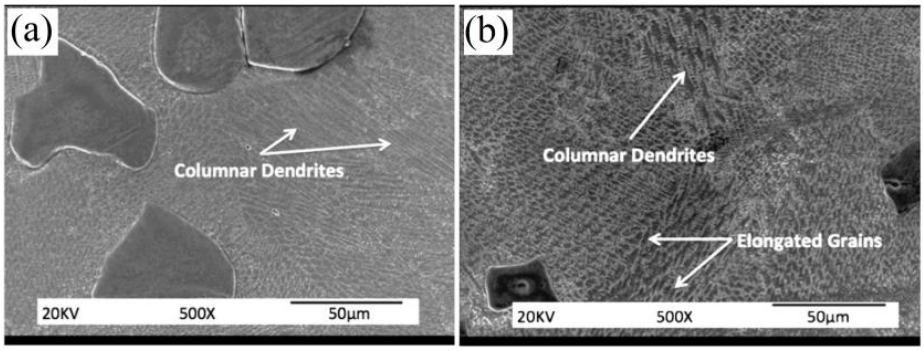

Figure 1-26 Microstructures of LENS processed TiC reinforced Inconel 690 matrix composites containing: (a) less than 15 and (b) 15-30 vol.% TiC as reinforcement [4].

For the composite systems in which the reinforcements do not act as heterogeneous nucleation sites for the matrix, the grain boundary pinning and grain growth restriction caused by reinforcements may create sufficient undercooling and provide enough time for new grains to develop. Besides grain refinement, this mechanism also contributes to structural transition [154]. By acting as barriers to solute diffusion and heat transfer, the solid reinforcements can cause disturbance in the solute field and temperature field in the solidification front [155]. As a consequence, irregular growth modes may be activated for the matrix of MMCs during solidification.

The reinforcements can also influence the phase transformation in the matrix of AM processed MMCs. Microstructural characterizations of the non-reinforced Ti6Al4V alloy fabricated by AM processes indicates that the fast cooling rates associated with these processes favor the transformation of β phase to α' martensite, leading to microstructures containing Widmanstatten laths of martensitic α' phase in a β phase matrix [50, 62]. When considering TMCs having Ti6Al4V alloy as the matrix, microstructural features of the matrix may differ from the non-reinforced Ti6Al4V fabricated with the same process and similar processing parameters. For instance, as shown in Figure 1-27, the formation of primary TiB precipitates in TiB reinforced Ti6Al4V matrix composites refines the α/β

microstructure of the matrix and changes the morphology of α precipitates to an equiaxed or globular type [36, 50]. This could be due to the roles TiB precipitates play as additional heterogeneous nucleation sites for the α phase in the β matrix. In addition to the changes in morphology, the volume fraction of phases formed in the matrix can be affected by the reinforcements. As reported by Balla et al. [58], although having the same acicular morphology, the matrix of TiN reinforced Ti6Al4V matrix composites contained larger amounts of α phase than the non-reinforced LENS processed Ti6Al4V alloy.

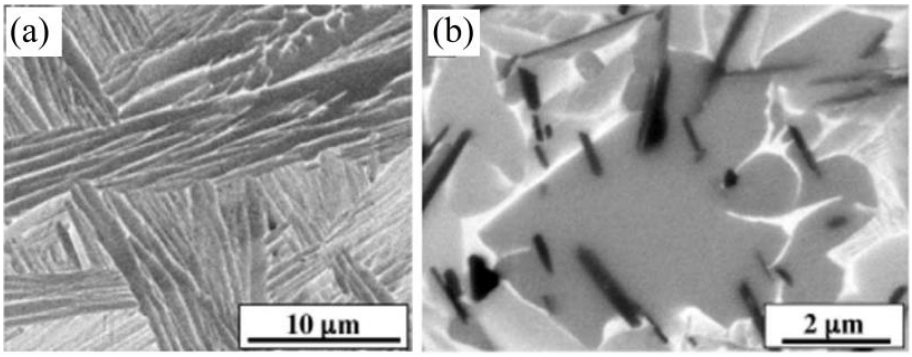

Figure 1-27 Microstructures of LENS processed: (a) non-reinforced Ti6Al4V alloy and (b) TiB reinforced Ti6Al4V composite [50].

The elements dissolved into the matrix in AM processed MMCs can change the microstructural evolution and phase transformation of the matrix. For instance, the stabilizing effect of dissolved N atoms in the matrix and the rapid cooling rates associated with the AM processes are the main reasons responsible for the formation of needle-like martensitic α phase in TiN reinforced Ti6Al4V matrix composites [58, 156]. The dissolution of SiC reinforcements into the surrounding melt during SLM processing of SiC/iron mixed powder system also resulted in a major microstructural transition in the matrix [126, 127]. Due to the extremely low content of carbon in the iron powder (~0.03 %), a ferritic (α-Fe) microstructure was obtained for the non-reinforced parts even at

extremely high cooling rates of the SLM process (Figure 1-28 (a)). However, the partial melting and dissolution of SiC particles to C and Si in the SiC reinforced iron-based MMCs led to the increased carbon content of the melt and paved the way for the formation of pearlite and martensite constituents in the matrix (Figure 1-28 (b)).

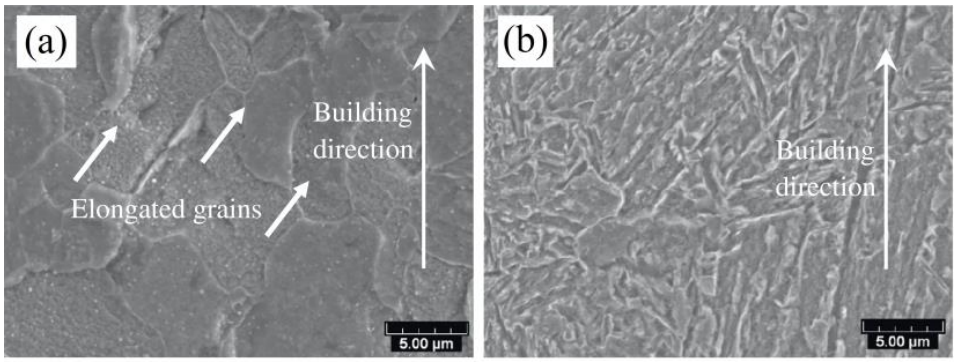

Figure 1-28 SEM micrographs of SLM fabricated: (a) non-reinforced pure iron and (b) SiC reinforced iron matrix composite [127].

1.7.4 Formation of Supersaturated Matrix

The rapid solidification rates of the AM processes can extend the solid solubility limit of alloying elements in the matrix and cause some distortions in its lattice structure. These distortions can be identified by the shift that occurred in the position of XRD peaks corresponding to the matrix phases [80, 81]. The supersaturation of matrix from alloying elements may contribute to enhancing mechanical properties through the solid solution strengthening mechanism [47, 157-160]. As reported by Prashanth et al. [28], in addition to the in-situ synthesized high strength Al6MoTi reinforcement phase formed in an Al12Si-TNM system, the development of an Al matrix supersaturated with both Ti and Si elements was responsible for further improvement in the hardness of SLM fabricated composites. The same phenomenon has been observed by Gopagoni et al. [86] when using the LENS process to fabricate in-situ synthesized TiC reinforced Ni matrix composites from a mixed

elemental powder system of Ni-10Ti-10C. Despite the negligible solid solubility of C in Ni, the rapid solidification rates led to diffusion-limited trapping of C in Ni to form a saturated solid solution matrix, as confirmed by high-resolution Auger electron spectroscopy (AES) analysis of the fabricated MMCs (Figure 1-29).

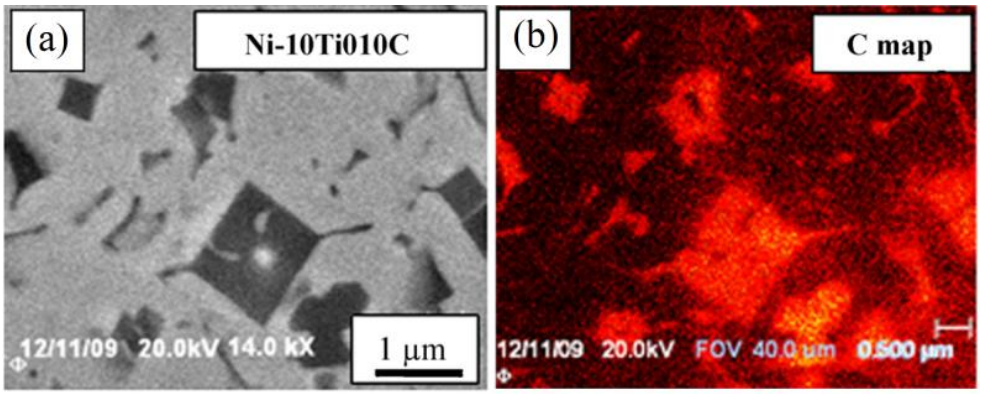

Figure 1-29 (a) SEM image of LENS processed TiC reinforced Ni matrix composite and (b) AES analysis map of C in the microstructure shown in (a). The thermal pseudocolor reveals the relative amount of C element [86].

1.7.5 Formation of Dislocations in the Matrix

To accommodate the misfit in CTE and EM induced between the reinforcements and the matrix during rapid melting and cooling, a large amount of thermal stresses are formed in the matrix of AM processed MMCs. These stresses may be high enough to cause plastic deformation, which is inclined to be portioned more toward the substantially softer phase (the metallic side of the interface), especially adjacent to the reinforcements/matrix interface. For instance, when cooled down from laser processing to room temperature, the difference between average CTEs of TiC reinforcement and Inconel 625 matrix can generate thermal stress over 500 MPa, which is beyond the yield strength of Inconel 625 in the annealed form [85]. The strains induced by these stresses are partially relieved by the formation of misfit dislocation network substructures at the interface known as

geometrically necessary dislocations (GNDs). High-resolution TEM (HRTEM) observation of the TiC/Ni interface in AM processed TiC reinforced Ni matrix composites provided in Figure 1-30 indicates the formation of dislocations that separate coherent regions of perfect lattice matching at the TiC/Ni interface. The intensity of the thermal stress and consequently the density of GNDs are reduced by moving away from the reinforcement/matrix interface.

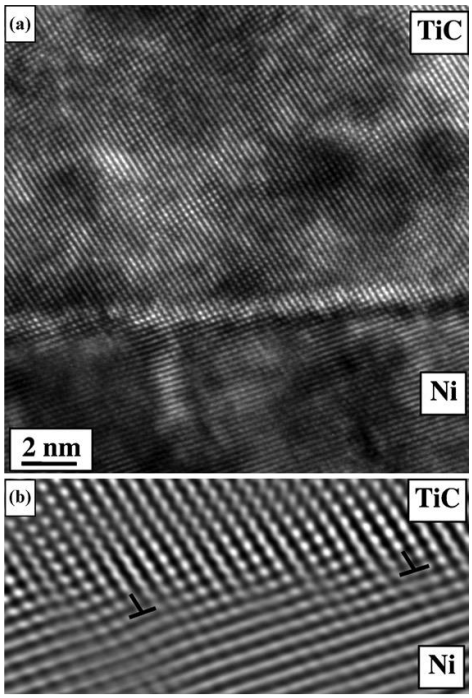

Figure 1-30 (a) HRTEM image of the TiC/Ni interface in LENS processed composites and (b) higher magnification image indicating a semi-coherent interface containing dislocations [86].

In addition to the reinforcement/matrix interfacial regions, misfit dislocation substructures can also be generated at the interface of different phases existing in the matrix. For instance, as revealed by TEM analysis, both the β/TiB and α/β interfaces in AM processed TiB reinforced Ti6Al4V matrix composites contain misfit dislocation substructures [50]. These

dislocations could be beneficial to the enhancement of strength based on the dislocation strengthening mechanism discussed.

It is worth noting that the fast cooling rates (in the order of ~10^6-10^8 K/s), as well as the multiple reheating cycles associated with the AM processes, can also lead to the generation of dislocations in the matrix of MMCs, as shown in Figure 1-31.

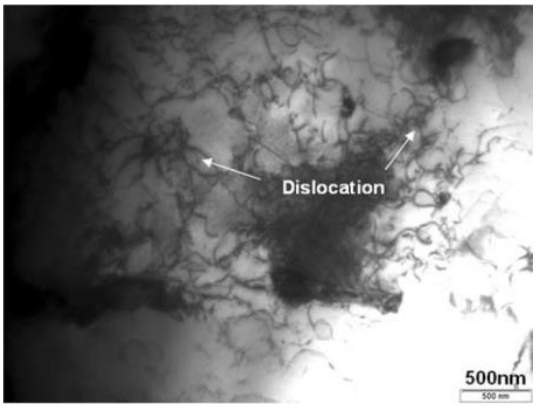

Figure 1-31 TEM image showing high density of dislocations in the matrix of LENS processed TiC reinforced Inconel 625 matrix composites [85].

1.8 Part Quality and Surface Integrity of AM Processed MMCs

Generally, the most important defects in AM processed parts limiting the densification level are porosities and cracks. The porosity in AM processed parts is originated mainly from the melt pool behavior and the quality of the starting powder particles. Several resources are responsible for forming porosities in AM processed parts, including gas voids, solidification shrinkage, lack of melting, and local evaporation of some elements when subjected to temperatures exceeding their boiling point [123, 125].

The bonding performance between the adjacent tracks and subsequent layers plays a significant role in the densification level of parts [81]. A good bonding between the tracks and layers can guarantee the fabrication of parts with sound densification levels. This can

be achieved by good wetting and effective contribution of previously solidified materials in the freshly deposited molten material. Moreover, the wetting behavior of solid reinforcements with the surrounding molten material affects the porosity level in AM processing of MMCs.

If the process parameters are not correctly chosen, the instability of the laser track can generate high surface roughness or even cause balling effect. In addition, the incorrect overlapping of adjacent tracks and/or layers caused by inappropriate selection of hatch spacing and/or layer thickness may also leave the inter-track and/or inter-layer regions unmelted, leading to the formation of porosities. The following describes the effects of applied energy density and the characteristics of mixed powder systems as two major factors influencing the part quality and surface integrity of AM processed MMCs.

1.8.1 Applied Energy Density

The applied processing parameters (energy density) play significant roles in the part quality and surface integrity of AM processed parts. Figure 1-32 presents the surface morphology for SLM fabricated TiC reinforced TMCs processed with varying energy densities by changing the scanning speeds. The fabricated part showed a dense surface with no pores and spherical balls at relatively high energy density. However, the decrease in the applied energy density (increasing the scan speed) enhanced the surface roughness by the formation of larger balls as well as porosities among neighbor balls or adjacent tracks. The formation of balls on the surface is due to the occurrence of balling effect, where the fresh molten material cannot wet the underlying substrate. Under this condition, the continuous melt track transforms to several spherical-shaped agglomerates to obtain the equilibrium state.

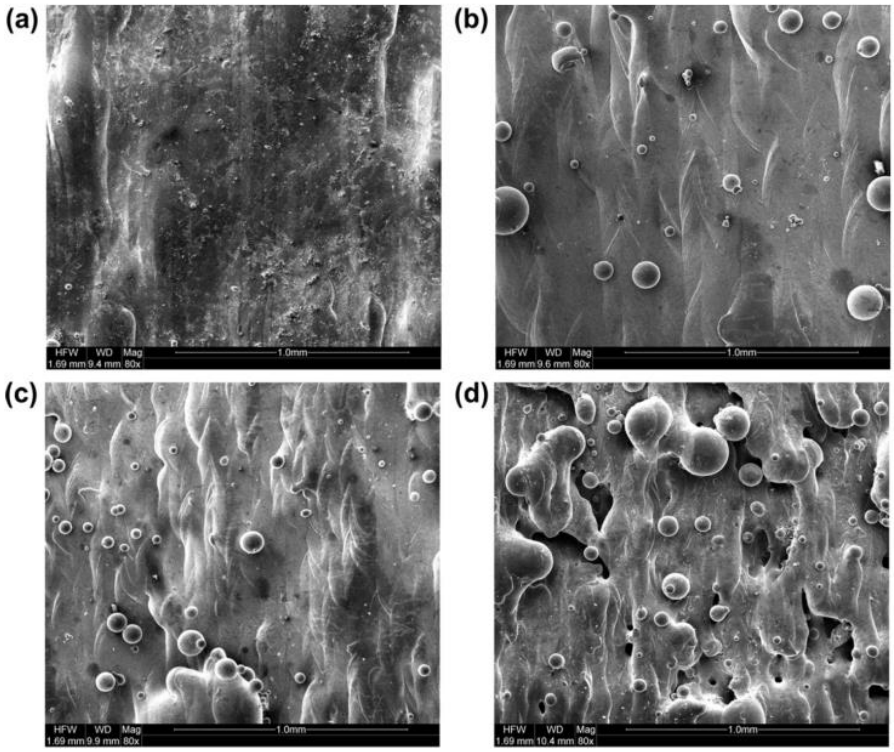

Figure 1-32 SEM images of the surface morphology for SLM fabricated TiC reinforced TMCs processed with energy density of: (a) 360, (b) 180, (c) 120 and (d) 90 J/mm^3 [42].

The poor surface integrity and quality of AM processed MMCs parts obtained at relatively low energy densities could be discussed in terms of the melt pool features under this condition which favor the formation of less dense parts. These features involve:

(i) The low working temperatures, decreased volume of melt pool and limited amount of molten material [78, 125]

(ii) The shortened lifetime of the molten material induced by higher solidification rates [78, 88]

(iii) The enhanced viscosity, limited convective flow and reduced liquid-solid rheological performance in the melt pool [118, 123]

(iv) The decreased wettability of solid reinforcements with the surrounding melt [77, 82, 123]

The reduced wettability and limited spreading of molten material to the outward combined with the poor dilution between the fresh depositing track and the previously deposited track/layer leads to a weak interfacial bonding and consequently results in the formation of porosities in inter-layer/inter-track locations [77, 81, 82, 88], as shown in Figure 1-33. However, the increased volume of melt and the decreased melt viscosity obtained at sufficient energy densities can enhance the wettability and improve the bonding between the tracks and/or layers. In addition, the high stirring in the melt pool caused by intensified Marangoni flow could also assist the melt with better wetting of previously solidified layers and/or tracks. Accordingly, MMCs with better surface integrities and higher densification levels could be achieved.

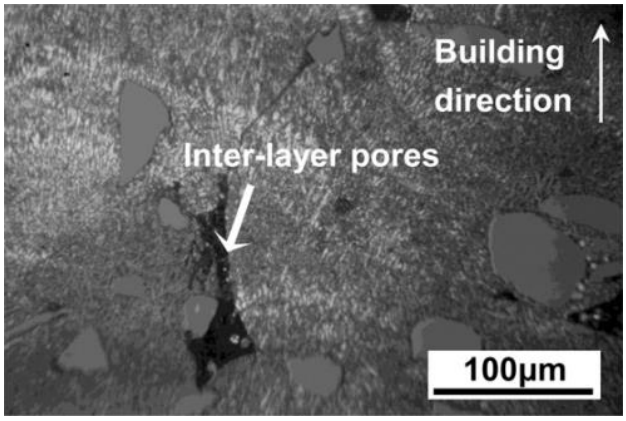

Figure 1-33 Cross-sectional optical micrograph of SLM processed SiC/AlSi10Mg mixed powder system showing the formation of inter-layer porosities [17].

The high-temperature gradients induced at excessive energy densities may enhance the risk of balling and lead to the accumulation of stress in parts of the previously deposited material experiencing remelting. These stresses may be responsible for the delamination of layers, distortion of parts, or even the appearance of cracks [78]. Moreover, excessive energy density may result in interfacial microscopic shrinkage porosities, and thermal micro-cracks at the reinforcement/matrix interface in AM processed MMCs [18, 24].

Figure 1-34 (a) shows such porosities at the reinforcement/matrix interfaces in SLM processed SiC/AlSi10Mg powder mixture, while Figure 1-34 (b) indicates thermally induced interfacial micro-cracks formed in AM processed Al_2O_3 reinforced AMCs.

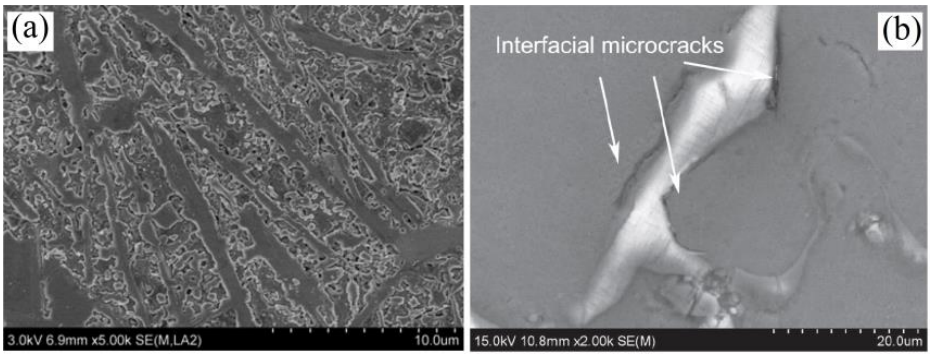

Figure 1-34 SEM micrographs showing: (a) microscopic shrinkage porosities at the Al_4SiC_4/matrix interface of SLM processed AMCs, and (b) interfacial micro-cracks at the Al_2O_3/Al interface of SLM fabricated AMCs [24].

1.8.2 Characteristics of Mixed Powder System

The characteristics of mixed powder systems affecting the densification level of AM processed MMCs include the type, size, and volume fraction of reinforcements and the category of the mixed powder system.

For a given volume fraction of reinforcements, the limited wettability of larger reinforcing particles leads to higher amounts of larger-sized porosities in the solidified MMCs parts.

Cross-sectional optical micrographs of AM processed Inconel 625 matrix composites in Figure 1-35 (a) reveal the significant influence of reinforcement type on the defects. As observed, the SiC reinforced MMCs contain a large volume of porosities and interconnected macro-cracks propagated both vertically and horizontally. Compared with the SiC reinforced MMCs, the Al_2O_3 reinforced ones had much lower porosities and fewer cracks. The formation of porosities in this type of MMCs was attributed to the thermal

destruction of Al_2O_3 during the process, leading to the release of oxygen and their subsequent capturing to form bubbles. This is while the enrichment of edges of cracks from Nb and Mo elements gave evidence of liquation cracking (Figure 1-35 (b)). Despite the SiC and Al_2O_3 reinforced MMCs, those reinforced with TiC were almost free of defects.

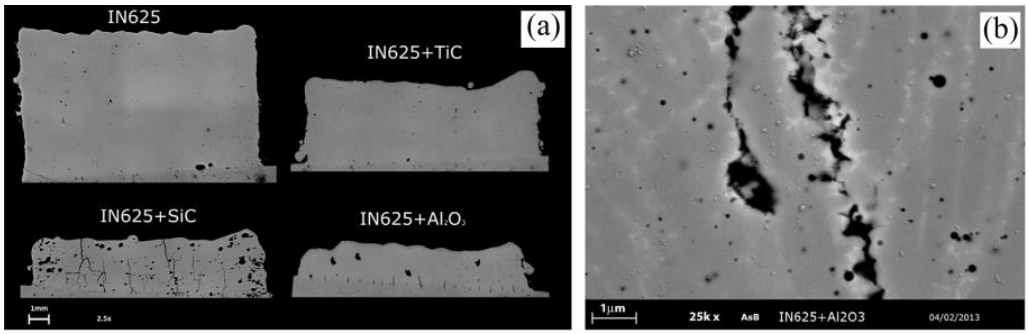

Figure 1-35 (a) Cross-sectional micrographs of additive layer manufactured Inconel 625 matrix composites with different types of reinforcements, and (b) SEM micrograph illustrating cracking in Al_2O_3 reinforced composites shown in (a) [75].

The enhanced volume fraction of reinforcements is generally associated with worsening of the densification level mainly due to: (i) the increased melt pool viscosity, which results in decreased wettability and favored spheroidization of melt pool, (ii) the elevated melt pool instability, and (iii) the occurrence of balling effect [119, 121].

Due to the higher brittleness of ceramic reinforcements compared to the metallic matrix, the enhanced volume fraction of reinforcements and their probable agglomeration may favor the formation of cracks in the AM processed MMCs. For example, aggregation of Ca and P elements (formed by dissolution of HA) along the boundaries of laser tracks in SLM processed HA reinforced stainless steel matrix composites introduced the boundaries as potential locations for crack nucleation and propagation when subjected to the residual stresses of the process. While the enhanced volume fraction of HA promoted this mechanism and led to the formation of larger and higher amounts of cracks, the elevated

scanning speeds declined the amount of aggregation and reduced the risk of cracking (Figure 1-36). The decrease in the melt pool size caused by the elevated scanning speeds may also lead to insufficient overlapping of tracks and consequently increase the porosity level (Figure 1-36) [117]. However, it should be noted that the local accumulation of residual stress caused by the application of relatively high scan speeds (high cooling rates) can enhance the crack formation susceptibility in some systems [78, 161].

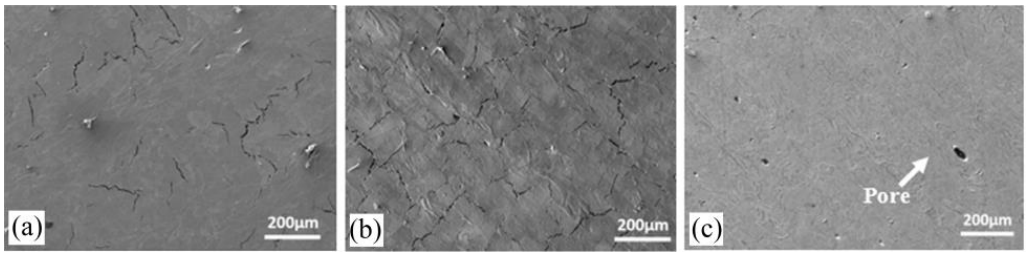

Figure 1-36 SEM micrographs of SLM fabricated HA reinforced stainless steel matrix composites with HA content and scanning speed of: (a) $HA = 5$ vol. %, $\upsilon = 250\ mm/s$, (b) $HA = 15$ vol. %, $\upsilon = 250\ mm/s$ and (c) $HA = 5$ vol. %, $\upsilon = 400\ mm/s$ [117].

The category of mixed powder systems can also affect both the type and amount of defects. For example, using two different powder categories; i.e., directly mixed and ball milled TiB_2/316L stainless steel mixed powder systems, AlMangour et al. [122] indicated that while the porosities were more evident in the directly mixed powder system, larger and more severe cracks were characterized for the ball-milled powder category (Figure 1-37). The formation of cracks was related to the liquation cracking at the boundaries, solidification shrinkage, and the limited wettability caused by the application of inappropriate processing parameters.

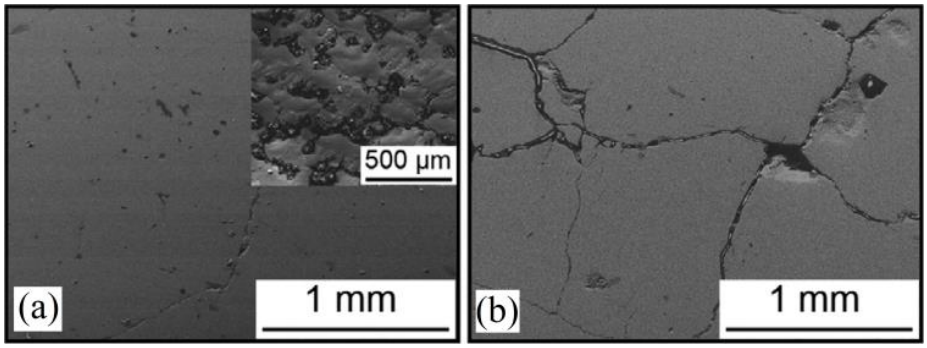

Figure 1-37 SEM micrographs indicating TiB_2 reinforced 316L stainless steel matrix composites fabricated by SLM processing of (a) directly mixed and (b) ball-milled powder systems [122].

1.9 Mechanical Properties of AM processed MMCs

As far as the AM technology has been considered, it has been revealed that it provides the fabrication of parts with superior mechanical properties, including higher hardness, improved strength, and comparable ductility than those manufactured by conventional processing techniques. While the addition of reinforcements to the matrix to form MMCs structures helps to enhance the hardness, strength, and work hardening compared to the non-reinforced parts, they may render the fabricated MMCs parts extremely brittle (Figure 1-38) [28, 48, 49]. As shown in compressive stress-strain curves in Figure 1-38 (a), Al-12Si-TNM AMCs fabricated by SLM showed yield and ultimate strengths of ~420 and ~636 MPa, respectively, which were higher than those for the non-reinforced Al-12Si samples having yield and ultimate strengths of ~283 and ~475 MP, respectively. However, the AMCs broke at ~6% total strain while the non-reinforced parts did not experience fracture until 60% of deformation. Toughness measurements of the CP-Ti and TiB reinforced TMCs fabricated with the same SLM processing parameters also show a ~50% decrease for the composites than the non-reinforced part [49]. The decreased ductility and toughness of MMCs compared to the non-reinforced structures can be ascribed to the insufficient ductility, the high brittleness, and limited ability of the hard and brittle

reinforcements to accommodate the plastic deformation [47, 49]. The increase in the content of these reinforcements can make the fabricated MMCs less ductile [44].

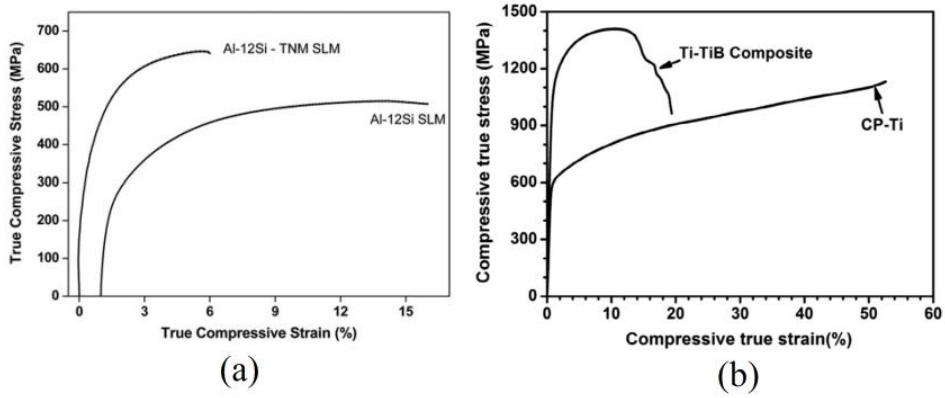

Figure 1-38 Compressive stress-strain curves of SLM processed: (a) non-reinforced Al-12Si and Al-12Si-TNM composite; and (b) non-reinforced CP-Ti and TiB reinforced TMC [48].

1.9.1 Strengthening Mechanisms

Generally, the strengthening of MMCs is determined by the contribution of direct and indirect strengthening mechanisms. Direct strengthening is also known as "classical" strengthening and is concerned with the load transfer from the softer matrix to the harder reinforcements. However, the indirect strengthening is based on the matrix strengthening induced by the presence of reinforcements.

1.9.1.1 Direct Strengthening

Based on the simple rule of mixture, incorporation of reinforcements into the matrix to form MMC structures is almost associated with the improved hardness and strength since a fraction of the matrix is substituted by harder phase(s) [4, 47, 85, 121, 160, 162, 163]. The rapid solidification rates associated with the AM processes result in inherently strong bonding coherence between the reinforcements and the matrix. Based on the interfacial strengthening mechanism, such kind of interface aids to the effective load transfer from the

matrix to the reinforcement and consequently improves the flow stress and strength of AM processed MMCs [29, 44, 47, 126, 127]. The formation of graded interfacial layers at the interface of ceramic reinforcements and the metallic matrix in some systems can also enhance the interfacial bonding strength and increase mechanical properties [88]. By hindering the movement of dislocations, the reinforcements distributed in the matrix can restrain its local micro-deformation and improve the strength [81, 126, 127, 164].

The amount of increment in the strength of discontinuously reinforced MMCs is affected by some variables, including the type, size, shape, distribution state, and volume fraction of reinforcements and their orientation with the applied loading direction. For example, for MMCs containing short whisker-shaped reinforcements aligned in the tensile loading direction, the shear-lag model developed by Nardone and Prewo predicts the increase in yield strength as [165, 166]:

$$\Delta\sigma = \sigma_{ym} V_r \left[\frac{(l+t)A}{4l}\right] \quad [5]$$

where σ_{ym} is the yield strength of the matrix, V_r represents the volume fraction of reinforcements, l is the size of reinforcement parallel to the loading direction, t is the thickness of reinforcement, and $A = {}^{l}/_{t}$ signifies the aspect ratio of reinforcements. Based on Eq. 5, those MMCs containing reinforcements with larger aspect ratios are associated with higher strengths for a given volume fraction of reinforcements. This reveals the importance of reinforcement shape and morphology on the strength of MMCs. Figure 1-39 shows the variation in yield strength of LENS processed CP-Ti and TiB reinforced TMCs as a function of the applied laser power. As being observed, the obtained MMCs had higher strengths than the non-reinforced parts. The main reason for the improvement in the strength of MMCs was the increase in the aspect ratio of TiB precipitates caused by the

elevated laser power (e.g., change in aspect ratio from 8.35 to 13.32 for laser powers of 125 to 200 W, respectively).

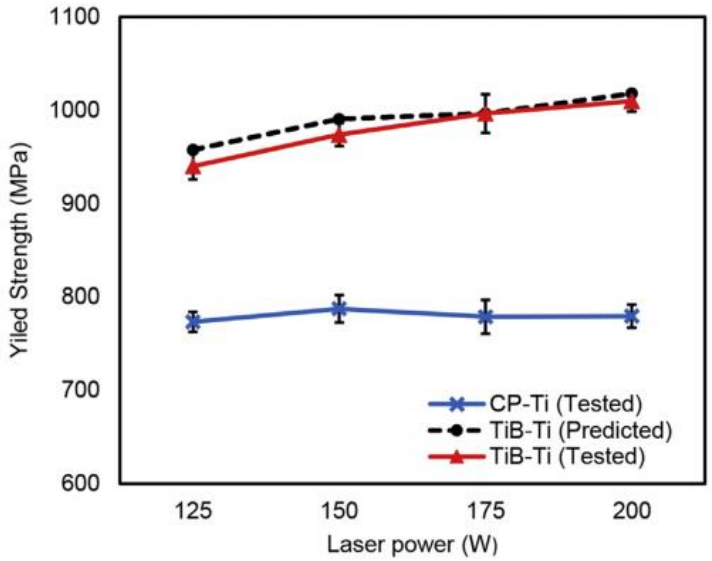

Figure 1-39 Variation of yield strength for LENS processed CP-Ti and TiB reinforced TMCs as a function of applied laser power [49].

The following describes the effects some other reinforcement features have on the mechanical properties of AM processed MMCs.

Reinforcement Volume Fraction

When the MMCs contain equiaxed particulate shaped reinforcements with an aspect ratio of 1, Eq. 5 is simplified as:

$$\Delta\sigma = \frac{1}{2}\sigma_{ym}V_r \qquad [6]$$

Accordingly, the increase in yield strength of MMCs could be linearly correlated with the volume fraction of reinforcements distributed in the matrix. The significant improvement in mechanical properties of AM processed MMCs with the enhancement of reinforcement volume fraction has been reported in several research studies [30, 44, 55, 58, 76, 119, 167].

For instance, the increase in volume fraction of in-situ synthesized TiC reinforcements from 20 to 60 vol.% led to the significant enhancement of hardness from 365 to 1898 HV in TiC reinforced Ni matrix composites [76]. In another research, the increase in TiB_2 content from 5 to 10 wt.% resulted in noticeably high hardnesses of 560 and 750 HV, respectively, for the obtained in-situ TiB reinforced Ti6Al4V matrix composites. The non-reinforced Ti6Al4V parts processed with the same parameters had a hardness of 340 HV [36]. The research performed by Balla et al. [58] to fabricate TiN reinforced Ti6Al4V composite coatings using the LENS process revealed an increasing trend in hardness from 527 to 1138 HV with the enhancement of TiN content from 10 to 40 wt.%. However, the LENS processed pure Ti6Al4V in their research had a hardness of 394 HV.

Recently, the concept of improvement in mechanical properties due to the enhancement of reinforcement volume fraction has been applied to develop AM processed FGCMs. These materials benefit from varying content of reinforcements and consequently gradient mechanical properties along the building direction [4, 44, 168, 169].

Reinforcement Type

Due to the differences in characteristics of reinforcements (melting point, hardness, EM, CTE, etc.), the mechanical properties of AM processed MMCs are strongly dependent on the type of reinforcement. Using three different ceramic particles of Al_2O_3, SiC, and TiC as reinforcement to Inconel 625 matrix, Cooper et al. [75] indicated that while the addition of Al_2O_3 did not have a notable influence on hardness, major ~130% and 32% improvements in the mean hardness were obtained for the SiC and TiC reinforced MMCs, respectively, compared to the non-reinforced part. In another research, Oh and Lee [170] found that while the Ti6Al4V substrate had a hardness of 320 HV in their study, different levels of hardening (520, 715, and 728 HV for TiC, SiC, and hybrid SiC+TiC reinforced

MMCs, respectively) were achieved for the deposited coatings containing different reinforcements.

When it comes to high-temperature applications, the reinforcement type plays a crucial role in MMC structure. Using various ceramic reinforcements (TiC, TiN, and TiC+TiN) added to the Ti6Al6V matrix, Yun et al. [160] found the highest hardness of 937 HV for TiN reinforced composite, and the lowest hardness for the TiC reinforced one (554 HV). The hardness of the hybrid reinforced composite was 726 HV, located between those having either TiC or TiN as reinforcement. The high-temperature hardness measurements of the fabricated MMCs revealed a gradual decrease from room temperature to 450 °C, followed by a rather rapid decline to 900 °C. To the same feature as the room temperature hardness, the TiN and TiC reinforced MMCs had the highest and lowest hardness values, respectively. Even at a temperature as high as 450 °C, the TiN reinforced specimen showed a hardness 3.5 times greater than that of the substrate, introducing TiN as an appropriate reinforcement for Ti matrix at high-temperature applications. In cases where there exists no intermediate phase between the reinforcement and the matrix (e.g., TiB and Ti), the reinforcements are stable and in equilibrium with the matrix, leading to the extended high-temperature application of the MMC structure.

Reinforcement Size

As well-known, one of the major concerns with conventionally processed particle reinforced MMCs is the limited interfacial wetting and bonding coherence between the reinforcements and the matrix, making the large-sized ceramic reinforcements prone to cracking when subjected to external loading. This consequently results in poor ductility as well as premature failure of MMCs parts [171]. Both the strength and ductility of MMCs are noticeably influenced by the size of reinforcements [172]. Generally, the MMCs

containing finer reinforcements are associated with higher hardness and strength and improved ductility. The improvement in strength due to the reinforcement refinement can be described based on the Orowan mechanism. This mechanism accounts for the interaction of dislocations with reinforcements and is active when the non-shearable reinforcements act as pinning points for dislocations. It should be noted that this mechanism is effective when the size of reinforcements is smaller than 1 μm [173]. The Orowan-Ashby equation defines the Orowan stress as [174]:

$$\Delta\sigma_{or} = \frac{0.13Gb}{\lambda} \ln\frac{d}{2b} \quad [7]$$

in which b and G are the Burger's vector and shear modulus of the matrix, respectively. d represents the equivalent diameter of reinforcement, and λ is the inter-particle spacing.

For a given volume fraction of reinforcements, the decrease in the size of reinforcements (d) is associated with the declined inter-particle spacing (λ). Accordingly, the pinning effect of particles for mobile dislocations becomes more pronounced, leading to higher Orowan stresses required for further deformation and enhanced strength. It is worth noting that the unpinning of dislocations caused by bowing leads to dislocation loops around the reinforcements. This also decreases the effective inter-particle spacing and elevates the required bypassing stress for the next dislocations encountering the reinforcements, leading to higher work hardening rates and strengthening the MMCs structure [175, 176].

In addition to the enhanced hardness, strength, and even ductility, the refining of reinforcements can significantly affect the toughness of MMCs. For example, the decreased size of TiB precipitates combined with their improved distribution pattern along the grain boundaries of the Ti matrix (3D quasi-continuous network microstructure (3DCQN)) led to the significant increase in toughness of TMCs from 201 to 320 J/mm^3 for

parts processed with laser powers of 125 and 200 W, respectively [49]. As schematically illustrated in Figure 1-40, this finding was ascribed to: (i) the refinement of TiB precipitates, (ii) crack propagation along both the TiB-rich regions (grain boundaries) and TiB-lean areas (within grains) of the 3DQCN structure, and (iii) the crack tip blunting and deflection by the ductile matrix of the 3DQCN structure.

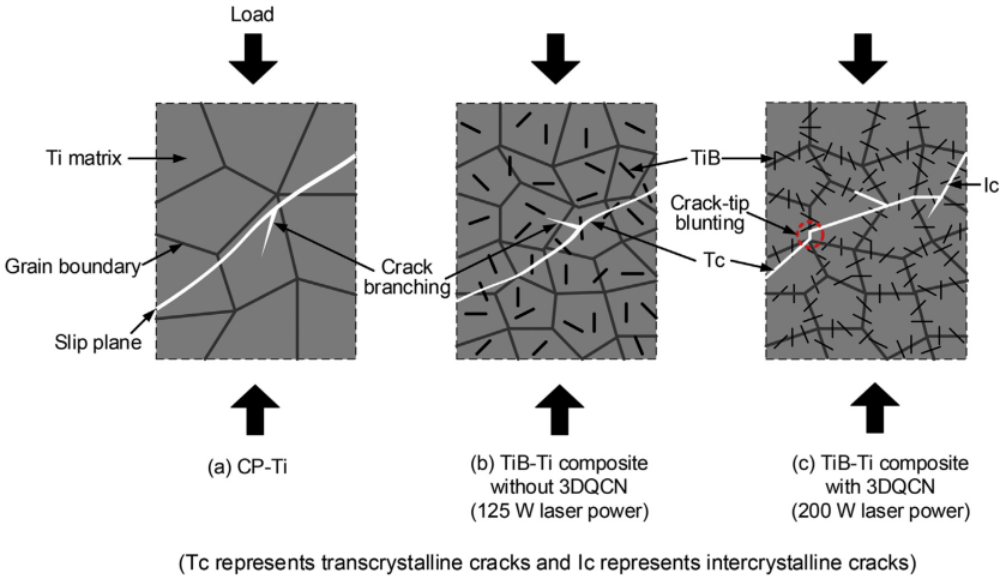

Figure 1-40 Schematic illustrations of failure modes in compression test for SLM fabricated CP-Ti and TiB reinforced TMCs. (Fig. 9 paper 39 Ti [49])

The effect of reinforcement refining on the improvement of mechanical properties could be even more effective when the size of reinforcements is further reduced from micrometer to nanometer scale. This can further intensify the interaction of dislocations with the reinforcements and result in more remarkable improvements in mechanical properties [177, 178].

1.9.1.2 Indirect Strengthening

As thoroughly described in Section 1.7.3, the incorporation of reinforcement into the system to fabricate MMCs structures is associated with some microstructural changes in

the matrix. These changes can affect the mechanical properties of the matrix and consequently the MMCs parts. To gain a better insight into the effect of reinforcements on matrix strengthening, Table 1-6 provides some comparisons between the hardness of Ti6Al4V alloy in a non-reinforced state and the Ti6Al4V matrix of AM processed TMCs reinforced with various types of reinforcements. As being observed, the Ti6Al4V matrix in TMCs shows considerably higher hardness values than that of the non-reinforced Ti6Al4V alloy. However, the amount of improvement in hardness varies depending on the employed reinforcement.

Table 1-6 A comparison between the hardness of AM processed Ti6Al4V alloy in non-reinforced state and in MMCs containing different types of reinforcements.

Mixed Powder System	**Matrix Hardness in MMC**	**Hardness of Non-reinforced Ti6Al4V**	**Ref.**
TiC/Ti6Al4V	340	320	[170] [160]
SiC/ Ti6Al4V	415		[170]
(TiC+SiC)/Ti6Al4V	460		[170]
TiN/Ti6Al4V	412		[160]
(TiC+TiN)/Ti6Al4V	434		[160]

The mechanisms involved in matrix hardening of AM fabricated MMCs are known as indirect strengthening mechanisms and include:

Grain Refinement of the Matrix

As discussed in Section 1.7.1, the reinforcements incorporated into the matrix of AM processed MMCs refine the microstructure by acting as preferential grain nucleation sites and grain growth inhibitors. Because of the significant role grain boundaries play in hindering the movement of dislocations, the increased volume of grain boundaries caused by grain refinement enhances the microstructure resistance to plastic deformation during

loading and consequently improves the strength of the material. Hall-Petch effect is a well-known strengthening mechanism that considers the effect of grain size on material strength. Based on this mechanism, the effect of reinforcement-induced grain refinement on the enhancement of strength can be expressed as [179]:

$$\Delta\sigma_{HP} = k_{HP}\left(\frac{1}{\sqrt{d_2}} - \frac{1}{\sqrt{d_1}}\right) \quad [8]$$

in which k_{HP} is the Hall-Petch constant for the matrix while d_2 and d_1 represent the average grain sizes of the matrix in MMC structure and non-reinforced specimen, respectively. As discussed previously, the incorporation of reinforcements into the system led to the microstructural refinement of the matrix than that of the non-reinforced state. This refining was more severe for MMCs containing higher volume fractions and/or finer reinforcements. The relationship among matrix grain size, reinforcement size and reinforcement content has been demonstrated by the Zener equation as [180]:

$$d_m = \frac{4\alpha d_p}{3v_p} \quad [9]$$

where d_m represents the matrix grain size, α is a proportionality constant, d_p signifies the reinforcement size and v_p is the reinforcement volume fraction.

Increased Density of Dislocations in the Matrix

Based on discussions in Section 1.7.5, a noticeable density of dislocations can be generated in the matrix of AM processed MMCs. These dislocations are believed to have various resources, including multiple reheating cycles induced in parts due to the nature of AM process and the difference between the CTE and EM of reinforcements and the matrix. While the generation of dislocation by repeated reheating cycle is common in all AM processes, those induced by CTE and EM differences are limited to the composite

structures. GNDs are formed adjacent to the reinforcement/matrix interface (in the matrix) to accommodate these mismatches. This phenomenon increases the work hardening rate and strengthens the MMCs. The increase in the yield strength of MMCs caused by both the CTE and EM mismatches can be expressed as [181]:

$$\Delta\sigma_{dis} = \sqrt{(\Delta\sigma_{CTE})^2 + (\Delta\sigma_{EM})^2} \quad [10]$$

where $\Delta\sigma_{CTE}$ and $\Delta\sigma_{geo}$ represent the stress increment caused by CTE and EM mismatch between the reinforcement and the matrix, respectively. The effects of CTE and EM mismatches on the strength of MMCs can be expressed by the Taylor relationship as Eqs. 11 and 12, respectively [166, 182]:

$$\sigma_{CTE} = M\beta Gb\sqrt{\rho_{CTE}} \quad [11]$$

$$\sigma_{EM} = \sqrt{3}\alpha Gb\sqrt{\rho_{EM}} \quad [12]$$

in which M is the Taylor factor, β and α are constants in the order of 1.25 and 0.5, respectively. ρ_{CTE} and ρ_{EM} represent the density of dislocations induced by CTE and EM mismatches, respectively, and are defined as [177, 183]:

$$\rho_{CTE} = \frac{A\Delta\alpha\Delta T V_r}{bd_p(1-V_r)} \quad [13]$$

$$\rho_{EM} = \frac{6V_r}{\pi d^3}\varepsilon \quad [14]$$

where A is a geometric constant varying between 10-12 based on the geometry of reinforcement, $\Delta\alpha$ represents the difference in CTE, ΔT is the temperature change from the processing to testing temperature, and ε signifies the plastic strain of the matrix.

As the deformation proceeds, the increase in dislocation density results in the reduced space between them, which elevates the load required for further deformation.

The Matrix Strengthening Caused by Microstructural Modifications

As previously discussed, microstructural modifications of the matrix induced by the presence of reinforcements include:

(i) The transition in the solidification mode

(ii) The change in the morphology of phases(s)

(iii) The change in the volume fraction of phase(s)

(iv) The phase transformation

Each of these microstructural modifications can lead to the improvement in the mechanical properties of fabricated MMCs. For instance, while the additively manufactured pure iron yields a ferritic matrix, the SiC/pure iron composite system shows a pearlitic and/or martensite matrix. The change in the microstructure of the matrix caused by the addition of SiC leads to the enhanced strength of SiC-reinforced iron matrix MMCs compared to the non-reinforced parts [126, 127]. Moreover, the formation of the martensitic α' phase in TMCs caused by the dissolution of reinforcements in the matrix well assists the improved mechanical properties of AM processed parts [160, 170]. While the general concept behind the fabrication of most MMCs is the improvement in hardness and strength, the outstanding properties of AM technology combined with the microstructural engineering of the matrix have recently led to the development of MMCs with excellent ductility [61, 62].

Figure 1-41 illustrates the stress-strain curves of SLM processed non-reinforced Ti6Al4V alloy and 10 wt.% Mo/Ti6Al4V powder mixture. In case of MMC containing Mo as metallic reinforcement, the partial dissolution of Mo particles into the matrix changed the fully α' martensitic microstructure of the matrix to a β phase one. Because of the lower

strength and higher ductility of β phase compared to α', fabricated composites showed lower Young's modulus, lower yield, and ultimate tensile strengths, and noticeably higher elongation than the non-reinforced Ti6Al4V parts made by the same processing parameters.

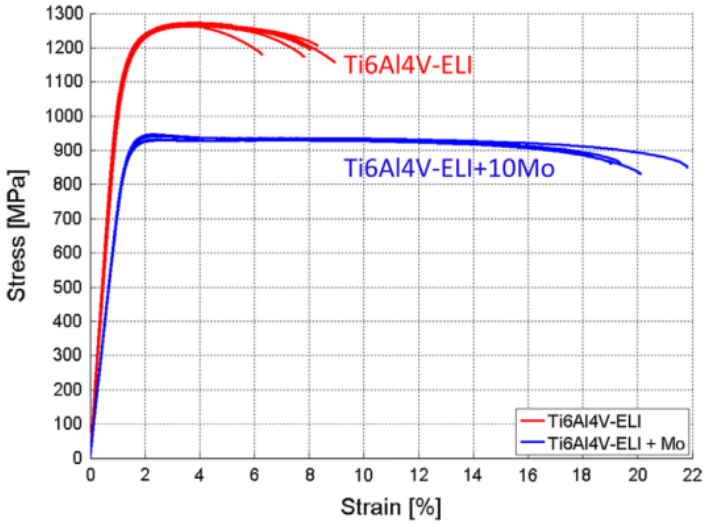

Figure 1-41 Stress-strain curves of SLM produced Ti6Al4V and Ti6Al4V+10Mo parts [62].

Solid Solution Strengthening of the Matrix

Solid solutions can be formed in both equilibrium and non-equilibrium states. For any rational concentration of solutes, the spacing between the solute atoms will be noticeably less than even the grain sizes in nanoscale. The non-equilibrium alloys fabricated by non-equilibrium processing routes can contain solid solutions with much larger size misfit than the equilibrium alloys. AM processing techniques, due to their extremely rapid cooling rates and non-equilibrium nature, can significantly extend the solution limit of alloying elements into the matrix and consequently favor the solid solution strengthening mechanism. It is worth mentioning that the ball milling process used as a promising technique to mix the powders before the AM processing of MMCs can also extend the equilibrium solid solubility limit of solute elements into the matrix [130]. The mechanical

alloying provides the synthesis of metastable (non-equilibrium) supersaturated solid solutions from blended elemental powders in binary or higher-order systems and ceramic-metallic powder mixtures.

The contribution of solid solution strengthening mechanism to the strength can be expressed as [174]:

$$\Delta\sigma_{ss} = \beta G \delta^{p} c^{q} \quad [15]$$

where β is a constant, $\delta = |(r_{matrix} - r_{solute})/r_{matrix}|$ is the misfit strain, and c represents the atomic fraction of the solute. p and q values are dependent on solute spacing and the dislocation-solute interactions [184]. The solute atoms entrapped in the lattice sites of the matrix make some distortions to the lattice structure. Accordingly, higher amounts of stress will be required for the movement of dislocations in the distorted structure, leading to enhanced strength. The larger the misfit strain, the higher the supersaturated solid solution strengthening.

1.9.2 Weakening Mechanisms

While several strengthening mechanisms can enhance mechanical properties in AM processed MMCs, there are some other factors inversely affecting these properties. The weakening mechanisms can lead to the fabrication of MMCs having even inferior mechanical properties than the non-reinforced state [19, 89]. Moreover, these mechanisms may intensify the degrees of fluctuations in the mechanical properties of fabricated MMCs [121]. The most important weakening mechanisms which may be active in AM processed MMCs include:

1.9.2.1 Decreased Densification Level

As discussed in Section 1.8, the decreased densification level in AM processed MMCs mostly involves the formation of porosities and micro-cracks. When existing in the structure, these defects may act as stress concentrating regions, favoring the initiation and propagation of cracks during loading. Moreover, their growth or coalescence by mechanical or thermal stresses may result in catastrophic failure of engineering MMCs components [185].

1.9.2.2 Microstructure Coarsening

The microstructural coarsening in the AM processed MMCs may include the coarsening of matrix structure and/or the reinforcements. The major reason for such a phenomenon is the excessive energy density applied to the system during processing [18, 24, 125]. The coarsening of reinforcements may also lead to the microstructural inhomogeneity in MMCs and deteriorate the mechanical properties [28].

1.9.2.3 Microstructural Inhomogeneity

The inhomogeneity in the distribution state of reinforcements in AM processed MMCs is due to the application of inappropriate processing parameters. Compared with the MMCs possessing a homogeneous distribution pattern of reinforcements, those containing non-homogeneous distribution states are generally associated with decreased strength and ductility. When having a non-homogenous distribution of reinforcements, some regions of the matrix are left non-reinforced, making them weaker than the reinforced areas. Moreover, if the MMC microstructures with inhomogeneous distribution pattern of reinforcements contain clusters or agglomerates of hard and brittle reinforcements, the parts may be much more prone to cracking when subjected to external loading.

1.10 Wear Behavior

Wear is defined as the progressive material loss caused by the relative motion of contacting substance and the surface [77]. Wear is regarded as a complex phenomenon during which the real contact area between contacting surfaces is consistently smaller than the apparent contact area, leading to relatively high localized load transfer through the contact points. Abrasive, erosive, adhesive, surface fatigue, cavitation, and tribo-chemical are the classifications presented for wear. Pin-on-Disc is one of the most common tests used for measuring the sliding friction and wear characteristics of materials. The coefficient of friction (COF) and wear rate obtained from the wear test are employed to study the wear behavior of materials. The lower the COF and wear rate, the higher the wear resistance of the material. Microstructural observation of the wear surface is a helpful tool for characterizing the wear properties.

Besides the extrinsic factors (e.g., applied load, sliding velocity and distance, surface finish, environment, and temperature), the intrinsic properties of MMCs (e.g., characteristics of reinforcements and the matrix as well as the reinforcement/matrix interface) play significant roles in wear performance of MMCs. The effects of reinforcement feature and applied energy density on the wear behavior of AM processed MMCs have been discussed in the following.

1.10.1 Effect of Size and Volume Fraction of Reinforcements

For a given MMC system, the volume fraction of reinforcements is known as the parameter playing the most important role in wear resistance [186, 187]. However, when investigating the change in wear resistance as a function of reinforcement volume fraction, the size and morphology of reinforcements need to be considered. The effect of size and volume

fraction of reinforcements on wear resistance of MMCs could be discussed in terms of inter-particle spacing (λ), which is defined as [111]:

$$\lambda \propto \frac{d}{\sqrt{f}} \quad [16]$$

where d represents the size, and f signifies the volume fraction of reinforcements. The decrease in size and increase in volume fraction of reinforcements is believed to improve the wear resistance of composites. The enhanced content of reinforcements in MMCs provides the matrix with higher amounts of reinforcements protecting the plastic flow of the ductile matrix. This enhances the hardness and strength of the composite. In addition, it may lead to the formation of larger areas of stain-hardened tribo-layer on the wear surface during sliding [121]. Moreover, in some cases where the reinforcements have lubricating behavior (e.g., BN ceramic reinforcements in Inconel 718 matrix composites [89]), MMCs containing higher amounts of them may show improved wear behavior. It should be noted that the improving trend in wear resistance achieved with the increased content of reinforcements is valid as long as the spalling of reinforcements is avoided, and they are remained in the matrix during wear sliding [111]. This reveals the supporting ability of the matrix to the reinforcements as an important point in the wear resistance of MMCs.

In addition to the improvement in wear resistance, the increase in reinforcement volume fraction may change the wear mechanism. For instance, as shown in Figure 43, the increase in TiC content from 2.5 to 15 vol.% in SLM processed TiC reinforced 316L stainless steel matrix nanocomposites changed the wear mechanism from abrasive to adhesive [119]. In another study on DLF processing of TiC reinforced Ni matrix composites, the increase in volume fraction of in-situ synthesized TiC precipitates from 20 to 60 vol.% changed the morphology of worn surfaces from gross grooves to fine scratches [76].

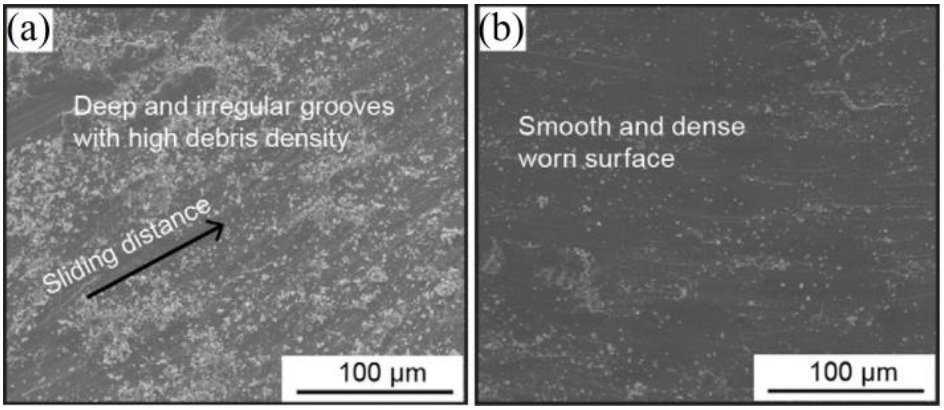

Figure 1-42 SEM micrographs of the worn surface for SLM processed TiC reinforced 316L stainless steel matrix nano-composites having: (a) 2.5 and (b) 15 vol.% TiC [119].

The improved wear resistance of AM processed MMCs obtained by the decrease in size of reinforcements could be attributed to the following reasons:

(i) The increased densification level and improved microstructural homogeneity which both decrease the preferential locations for crack nucleation [17]

(ii) Compared with the coarser reinforcements, the stronger interfacial bonding of finer ones with the matrix lowers their protrusion and separation when subjected to the shear stress during sliding

(iii) The enhanced hardness and strength of MMCs

(iv) The restricting actions that fine reinforcements play in plastic deformation and flow of surface material during sliding. Compared with the rough surface containing deep and irregular grooves showing severe surface plowing during sliding for MMCs with relatively coarse reinforcements, those with finer ones may lead to narrower and shallower grooves

(v) The elevated grain refinement of the matrix which leads to much more severe plastic deformation of the wear surface and paves the way for the formation of strain-hardened tribo-layer [17].

1.10.2 Effect of Applied Energy Density

The amount of energy density subjected to the system during AM processing significantly influences the wear resistance of fabricated MMCs parts. Several parameters have been reported in the literature for the weak wear resistance of AM processed MMCs fabricated by relatively low energy densities. The appropriate selection of process parameters can provide the powder system with sufficient energy density. This consequently results in the production of MMCs with sound wear resistance due to the following phenomena:

(i) The improvement in densification level [24, 79, 82]

(ii) The formation of microstructures with much uniform and homogenous distribution pattern of reinforcements [14, 24, 79, 82]

(iii) The enhanced microhardness [24, 77, 82]

(iv) The improvement of reinforcement/matrix interfacial bonding or the formation of a more effective graded interfacial reaction layer between the reinforcements and the matrix in some systems. These layers can effectively transfer the load from the softer matrix to the harder reinforcements and provide the MMCs parts with less wear.

When employing excessive energy density, the coarsening of microstructure (both the reinforcement ad the matrix) and the microscopic shrinkage porosities and micro-cracks formed, especially at the reinforcement/matrix interface, may weaken the wear performance of MMCs [13, 24, 81].

1.11 References

[1] A.C.F.o.A.M. Technologies, A.C.F.o.A.M.T.S.F.o. Terminology, Standard Terminology for Additive Manufacturing Technologies, ASTM International2012.

[2] S.M. Thompson, L. Bian, N. Shamsaei, A. Yadollahi, An overview of Direct Laser Deposition for additive manufacturing; Part I: Transport phenomena, modeling and diagnostics, Additive Manufacturing 8 (2015) 36-62.

[3] F. Wang, J. Mei, X. Wu, Compositionally graded Ti6Al4V+ TiC made by direct laser fabrication using powder and wire, Materials & design 28(7) (2007) 2040-2046.

[4] J.M. Wilson, Y.C. Shin, Microstructure and wear properties of laser-deposited functionally graded Inconel 690 reinforced with TiC, Surface and Coatings Technology 207 (2012) 517-522.

[5] S.-w. Lim, T. Imai, Y. Nishida, T. Choh, High strain rate superplasticity of TiC particulate reinforced magnesium alloy composite by vortex method, Scripta metallurgica et materialia 32(11) (1995) 1713-1717.

[6] M.O. Shabani, A. Mazahery, Computational modeling of cast aluminum 2024 alloy matrix composites: Adapting the classical algorithms for optimal results in finding multiple optima, Powder technology 249 (2013) 77-81.

[7] T. Rajmohan, K. Palanikumar, S. Arumugam, Synthesis and characterization of sintered hybrid aluminium matrix composites reinforced with nanocopper oxide particles and microsilicon carbide particles, Composites Part B: Engineering 59 (2014) 43-49.

[8] V. Umasankar, M.A. Xavior, S. Karthikeyan, Experimental evaluation of the influence of processing parameters on the mechanical properties of SiC particle reinforced AA6061 aluminium alloy matrix composite by powder processing, Journal of Alloys and Compounds 582 (2014) 380-386.

[9] S. Ozden, R. Ekici, F. Nair, Investigation of impact behaviour of aluminium based SiC particle reinforced metal–matrix composites, Composites Part A: Applied Science and Manufacturing 38(2) (2007) 484-494.

[10] D. Buchbinder, H. Schleifenbaum, S. Heidrich, W. Meiners, J. Bültmann, High power selective laser melting (HP SLM) of aluminum parts, Physics Procedia 12 (2011) 271-278.

[11] E. Louvis, P. Fox, C.J. Sutcliffe, Selective laser melting of aluminium components, Journal of Materials Processing Technology 211(2) (2011) 275-284.

[12] D. Gu, H. Wang, D. Dai, P. Yuan, W. Meiners, R. Poprawe, Rapid fabrication of Al-based bulk-form nanocomposites with novel reinforcement and enhanced performance by selective laser melting, Scripta Materialia 96 (2015) 25-28.

[13] D. Gu, H. Wang, D. Dai, Laser additive manufacturing of novel aluminum based nanocomposite parts: tailored forming of multiple materials, Journal of Manufacturing Science and Engineering 138(2) (2016) 021004.

[14] D. Gu, H. Wang, D. Dai, F. Chang, W. Meiners, Y.-C. Hagedorn, K. Wissenbach, I. Kelbassa, R. Poprawe, Densification behavior, microstructure evolution, and wear property of TiC nanoparticle reinforced AlSi10Mg bulk-form nanocomposites prepared by selective laser melting, Journal of Laser Applications 27(S1) (2015) S17003.

[15] P. Yuan, D. Gu, D. Dai, Particulate migration behavior and its mechanism during selective laser melting of TiC reinforced Al matrix nanocomposites, Materials & Design 82 (2015) 46-55.

[16] D. Gu, P. Yuan, Thermal evolution behavior and fluid dynamics during laser additive manufacturing of Al-based nanocomposites: Underlying role of reinforcement weight fraction, Journal of Applied Physics 118(23) (2015) 233109.

[17] F. Chang, D. Gu, D. Dai, P. Yuan, Selective laser melting of in-situ Al4SiC4+ SiC hybrid reinforced Al matrix composites: Influence of starting SiC particle size, Surface and Coatings Technology 272 (2015) 15-24.

[18] D. Gu, F. Chang, D. Dai, Selective laser melting additive manufacturing of novel aluminum based composites with multiple reinforcing phases, Journal of Manufacturing Science and Engineering 137(2) (2015) 021010.

[19] D. Manfredi, F. Calignano, M. Krishnan, R. Canali, E.P. Ambrosio, S. Biamino, D. Ugues, M. Pavese, P. Fino, Additive manufacturing of Al alloys and aluminium matrix composites (AMCs), Light metal alloys applications, InTech2014.

[20] A. Simchi, D. Godlinski, Effect of SiC particles on the laser sintering of Al–7Si–0.3 Mg alloy, Scripta Materialia 59(2) (2008) 199-202.

[21] A. Simchi, D. Godlinski, Densification and microstructural evolution during laser sintering of A356/SiC composite powders, Journal of materials science 46(5) (2011) 1446-1454.

[22] S.K. Ghosh, P. Saha, Crack and wear behavior of SiC particulate reinforced aluminium based metal matrix composite fabricated by direct metal laser sintering process, Materials & Design 32(1) (2011) 139-145.

[23] S.K. Ghosh, P. Saha, S. Kishore, Influence of size and volume fraction of SiC particulates on properties of ex situ reinforced Al–4.5 Cu–3Mg metal matrix composite prepared by direct metal laser sintering process, Materials Science and Engineering: A 527(18) (2010) 4694-4701.

[24] J. Jue, D. Gu, K. Chang, D. Dai, Microstructure evolution and mechanical properties of Al-Al 2 O 3 composites fabricated by selective laser melting, Powder Technology 310 (2017) 80-91.

[25] L. Wang, J. Jue, M. Xia, L. Guo, B. Yan, D. Gu, Effect of the Thermodynamic Behavior of Selective Laser Melting on the Formation of In situ Oxide Dispersion-Strengthened Aluminum-Based Composites, Metals 6(11) (2016) 286.

[26] D. Dai, D. Gu, Influence of thermodynamics within molten pool on migration and distribution state of reinforcement during selective laser melting of AlN/AlSi10Mg composites, International Journal of Machine Tools and Manufacture 100 (2016) 14-24.

[27] P. Ma, Y. Jia, K.G. Prashanth, S. Scudino, Z. Yu, J. Eckert, Microstructure and phase formation in Al–20Si–5Fe–3Cu–1Mg synthesized by selective laser melting, Journal of Alloys and Compounds 657 (2016) 430-435.

[28] K.G. Prashanth, S. Scudino, A.K. Chaubey, L. Löber, P. Wang, H. Attar, F.P. Schimansky, F. Pyczak, J. Eckert, Processing of Al–12Si–TNM composites by selective laser melting and evaluation of compressive and wear properties, Journal of Materials Research 31(1) (2016) 55-65.

[29] K. Prashanth, H.S. Shahabi, H. Attar, V. Srivastava, N. Ellendt, V. Uhlenwinkel, J. Eckert, S. Scudino, Production of high strength Al85Nd8Ni5Co2 alloy by selective laser melting, Additive Manufacturing 6 (2015) 1-5.

[30] S. Dadbakhsh, L. Hao, Effect of Al alloys on selective laser melting behaviour and microstructure of in situ formed particle reinforced composites, Journal of alloys and compounds 541 (2012) 328-334.

[31] L. Xiao, W. Lu, J. Qin, Y. Chen, D. Zhang, M. Wang, F. Zhu, B. Ji, Creep behaviors and stress regions of hybrid reinforced high temperature titanium matrix composite, Composites Science and Technology 69(11) (2009) 1925-1931.

[32] A.A. da Silva, J.F. dos Santos, T.R. Strohaecker, An investigation of the fracture behaviour of diffusion-bonded Ti6Al4V/TiC/10p, Composites science and technology 66(13) (2006) 2063-2068.

[33] J. Vreeling, V. Ocelik, J.T.M. De Hosson, Ti–6Al–4V strengthened by laser melt injection of WC p particles, Acta Materialia 50(19) (2002) 4913-4924.

[34] Y. Pei, V. Ocelik, J.T.M. De Hosson, SiC p/Ti6Al4V functionally graded materials produced by laser melt injection, Acta Materialia 50(8) (2002) 2035-2051.

[35] J. Candel, V. Amigó, J. Ramos, D. Busquets, Sliding wear resistance of TiC p reinforced titanium composite coating produced by laser cladding, Surface and Coatings Technology 204(20) (2010) 3161-3166.

[36] F. Wang, J. Mei, X. Wu, Direct laser fabrication of Ti6Al4V/TiB, Journal of materials processing technology 195(1) (2008) 321-326.

[37] J. DuttaMajumdar, L. Li, Development of titanium boride (TiB) dispersed titanium (Ti) matrix composite by direct laser cladding, Materials Letters 64(9) (2010) 1010-1012.

[38] W. Pang, H. Man, T. Yue, Laser surface coating of Mo–WC metal matrix composite on Ti6Al4V alloy, Materials Science and Engineering: A 390(1) (2005) 144-153.

[39] T. Yamamoto, A. Otsuki, K. Ishihara, P. Shingu, Synthesis of near net shape high density TiB/Ti composite, Materials Science and Engineering: A 239 (1997) 647-651.

[40] D. Gu, W. Meiners, Y.-C. Hagedorn, K. Wissenbach, R. Poprawe, Bulk-form TiCx/Ti nanocomposites with controlled nanostructure prepared by a new method: selective laser melting, Journal of Physics D: Applied Physics 43(29) (2010) 295402.

[41] D. Gu, H. Wang, G. Zhang, Selective laser melting additive manufacturing of Ti-based nanocomposites: the role of nanopowder, Metallurgical and Materials Transactions A 45(1) (2014) 464-476.

[42] D. Gu, Y.-C. Hagedorn, W. Meiners, K. Wissenbach, R. Poprawe, Nanocrystalline TiC reinforced Ti matrix bulk-form nanocomposites by Selective Laser Melting (SLM): Densification, growth mechanism and wear behavior, Composites Science and Technology 71(13) (2011) 1612-1620.

[43] D. Gu, G. Meng, C. Li, W. Meiners, R. Poprawe, Selective laser melting of TiC/Ti bulk nanocomposites: Influence of nanoscale reinforcement, Scripta Materialia 67(2) (2012) 185-188.

[44] Y. Zhang, Z. Wei, L. Shi, M. Xi, Characterization of laser powder deposited Ti–TiC composites and functional gradient materials, journal of materials processing technology 206(1) (2008) 438-444.

[45] D. Gu, Z. Wang, Y. Shen, Q. Li, Y. Li, In-situ TiC particle reinforced Ti–Al matrix composites: powder preparation by mechanical alloying and selective laser melting behavior, Applied Surface Science 255(22) (2009) 9230-9240.

[46] D. Gu, D. Dai, G. Zhang, H. Wang, Growth mechanisms of in situ TiC in laser melted Ti–Si–C ternary system, Applied Physics Letters 101(17) (2012) 171603.

[47] H. Attar, L. Löber, A. Funk, M. Calin, L. Zhang, K. Prashanth, S. Scudino, Y. Zhang, J. Eckert, Mechanical behavior of porous commercially pure Ti and Ti–TiB composite materials manufactured by selective laser melting, Materials Science and Engineering: A 625 (2015) 350-356.

[48] H. Attar, M. Bönisch, M. Calin, L.-C. Zhang, S. Scudino, J. Eckert, Selective laser melting of in situ titanium–titanium boride composites: processing, microstructure and mechanical properties, Acta Materialia 76 (2014) 13-22.

[49] Y. Hu, W. Cong, X. Wang, Y. Li, F. Ning, H. Wang, Laser deposition-additive manufacturing of TiB-Ti composites with novel three-dimensional quasi-continuous network microstructure: effects on strengthening and toughening, Composites Part B: Engineering 133 (2018) 91-100.

[50] R. Banerjee, P. Collins, A. Genc, H. Fraser, Direct laser deposition of in situ Ti–6Al–4V–TiB composites, Materials Science and Engineering: A 358(1) (2003) 343-349.

[51] A. Genç, R. Banerjee, D. Hill, H. Fraser, Structure of TiB precipitates in laser deposited in situ, Ti-6Al-4V–TiB composites, Materials Letters 60(7) (2006) 859-863.

[52] S. Nag, S. Samuel, A. Puthucode, R. Banerjee, Characterization of novel borides in Ti–Nb–Zr–Ta+ 2B metal-matrix composites, Materials characterization 60(2) (2009) 106-113.

[53] Y. Zhang, J. Sun, R. Vilar, Characterization of (TiB+ TiC)/TC4 in situ titanium matrix composites prepared by laser direct deposition, Journal of Materials Processing Technology 211(4) (2011) 597-601.

[54] M. Das, V.K. Balla, D. Basu, S. Bose, A. Bandyopadhyay, Laser processing of SiC-particle-reinforced coating on titanium, Scripta Materialia 63(4) (2010) 438-441.

[55] M. Das, S. Bysakh, D. Basu, T.S. Kumar, V.K. Balla, S. Bose, A. Bandyopadhyay, Microstructure, mechanical and wear properties of laser processed SiC particle reinforced coatings on titanium, Surface and Coatings Technology 205(19) (2011) 4366-4373.

[56] D. Gu, C. Hong, G. Meng, Densification, microstructure, and wear property of in situ titanium nitride-reinforced titanium silicide matrix composites prepared by a novel selective laser melting process, Metallurgical and Materials Transactions A 43(2) (2012) 697-708.

[57] H. Attar, K.G. Prashanth, L.-C. Zhang, M. Calin, I.V. Okulov, S. Scudino, C. Yang, J. Eckert, Effect of powder particle shape on the properties of in situ Ti–TiB composite materials produced by selective laser melting, Journal of Materials Science & Technology 31(10) (2015) 1001-1005.

[58] V.K. Balla, A. Bhat, S. Bose, A. Bandyopadhyay, Laser processed TiN reinforced Ti6Al4V composite coatings, Journal of the mechanical behavior of biomedical materials 6 (2012) 9-20.

[59] M. Das, K. Bhattacharya, S.A. Dittrick, C. Mandal, V.K. Balla, T.S. Kumar, A. Bandyopadhyay, I. Manna, In situ synthesized TiB–TiN reinforced Ti6Al4V alloy composite coatings: microstructure, tribological and in-vitro biocompatibility, Journal of the mechanical behavior of biomedical materials 29 (2014) 259-271.

[60] M. Das, V.K. Balla, D. Basu, I. Manna, T.S. Kumar, A. Bandyopadhyay, Laser processing of in situ synthesized TiB–TiN-reinforced Ti6Al4V alloy coatings, Scripta Materialia 66(8) (2012) 578-581.

[61] S.L. Sing, W.Y. Yeong, F.E. Wiria, Selective laser melting of titanium alloy with 50 wt% tantalum: Microstructure and mechanical properties, Journal of Alloys and Compounds 660 (2016) 461-470.

[62] B. Vrancken, L. Thijs, J.-P. Kruth, J. Van Humbeeck, Microstructure and mechanical properties of a novel β titanium metallic composite by selective laser melting, Acta Materialia 68 (2014) 150-158.

[63] H.N. Moosavy, M.-R. Aboutalebi, S.H. Seyedein, M. Goodarzi, M. Khodabakhshi, C. Mapelli, S. Barella, Modern fiber laser beam welding of the newly-designed precipitation-strengthened nickel-base superalloys, Optics & Laser Technology 57 (2014) 12-20.

[64] T.-Y. Kuo, Effects of pulsed and continuous Nd–YAG laser beam waves on welding of Inconel alloy, Science and Technology of Welding and Joining 10(5) (2005) 557-565.

[65] X. Xing, X. Di, B. Wang, The effect of post-weld heat treatment temperature on the microstructure of Inconel 625 deposited metal, Journal of Alloys and Compounds 593 (2014) 110-116.

[66] Y. Chen, K. Zhang, J. Huang, S.R.E. Hosseini, Z. Li, Characterization of heat affected zone liquation cracking in laser additive manufacturing of Inconel 718, Materials & Design 90 (2016) 586-594.

[67] C.-M. Kuo, Y.-T. Yang, H.-Y. Bor, C.-N. Wei, C.-C. Tai, Aging effects on the microstructure and creep behavior of Inconel 718 superalloy, Materials Science and Engineering: A 510 (2009) 289-294.

[68] D. Thakur, B. Ramamoorthy, L. Vijayaraghavan, Study on the machinability characteristics of superalloy Inconel 718 during high speed turning, Materials & Design 30(5) (2009) 1718-1725.

[69] R.C. Reed, The superalloys: fundamentals and applications, Cambridge university press2008.

[70] M. Henderson, D. Arrell, R. Larsson, M. Heobel, G. Marchant, Nickel based superalloy welding practices for industrial gas turbine applications, Science and Technology of Welding and Joining 9(1) (2004) 13-21.

[71] J.C. Lippold, S.D. Kiser, J.N. DuPont, Welding metallurgy and weldability of nickel-base alloys, John Wiley & Sons2011.

[72] K.A. Mumtaz, P. Erasenthiran, N. Hopkinson, High density selective laser melting of Waspaloy®, Journal of materials processing technology 195(1) (2008) 77-87.

[73] T. Lei, J. Ouyang, Y. Pei, Y. Zhou, Microstructure and wear resistance of laser clad TiC particle reinforced coating, Materials science and technology 11(5) (1995) 520-525.

[74] B. Mei, R. Yuan, X. Duan, Investigation of Ni 3 Al-matrix composites strengthened by TiC, Journal of materials research 8(11) (1993) 2830-2834.

[75] D.E. Cooper, N. Blundell, S. Maggs, G.J. Gibbons, Additive layer manufacture of Inconel 625 metal matrix composites, reinforcement material evaluation, Journal of Materials Processing Technology 213(12) (2013) 2191-2200.

[76] Y. Li, P. Bai, Y. Wang, J. Hu, Z. Guo, Effect of TiC content on Ni/TiC composites by direct laser fabrication, Materials & Design 30(4) (2009) 1409-1412.

[77] Q. Jia, D. Gu, Selective laser melting additive manufacturing of TiC/Inconel 718 bulk-form nanocomposites: Densification, microstructure, and performance, Journal of Materials Research 29(17) (2014) 1960-1969.

[78] Q. Shi, D. Gu, M. Xia, S. Cao, T. Rong, Effects of laser processing parameters on thermal behavior and melting/solidification mechanism during selective laser melting of TiC/Inconel 718 composites, Optics & Laser Technology 84 (2016) 9-22.

[79] D. Gu, C. Hong, Q. Jia, D. Dai, A. Gasser, A. Weisheit, I. Kelbassa, M. Zhong, R. Poprawe, Combined strengthening of multi-phase and graded interface in laser additive manufactured TiC/Inconel 718 composites, Journal of Physics D: Applied Physics 47(4) (2013) 045309.

[80] C. Hong, D. Gu, D. Dai, A. Gasser, A. Weisheit, I. Kelbassa, M. Zhong, R. Poprawe, Laser metal deposition of TiC/Inconel 718 composites with tailored interfacial microstructures, Optics & Laser Technology 54 (2013) 98-109.

[81] C. Hong, D. Gu, D. Dai, M. Alkhayat, W. Urban, P. Yuan, S. Cao, A. Gasser, A. Weisheit, I. Kelbassa, Laser additive manufacturing of ultrafine TiC particle reinforced Inconel 625 based composite parts: tailored microstructures and enhanced performance, Materials Science and Engineering: A 635 (2015) 118-128.

[82] S. Cao, D. Gu, Laser metal deposition additive manufacturing of TiC/Inconel 625 nanocomposites: Relation of densification, microstructures and performance, Journal of Materials Research 30(23) (2015) 3616-3628.

[83] S. Cao, D. Gu, Q. Shi, Relation of microstructure, microhardness and underlying thermodynamics in molten pools of laser melting deposition processed TiC/Inconel 625 composites, Journal of Alloys and Compounds 692 (2017) 758-769.

[84] C. Hong, D. Gu, D. Dai, S. Cao, M. Alkhayat, Q. Jia, A. Gasser, A. Weisheit, I. Kelbassa, M. Zhong, High-temperature oxidation performance and its mechanism of TiC/Inconel 625 composites prepared by laser metal deposition additive manufacturing, Journal of Laser Applications 27(S1) (2015) S17005.

[85] B. Zheng, T. Topping, J.E. Smugeresky, Y. Zhou, A. Biswas, D. Baker, E.J. Lavernia, The influence of Ni-coated TiC on laser-deposited IN625 metal matrix composites, Metallurgical and Materials Transactions A 41(3) (2010) 568-573.

[86] S. Gopagoni, J. Hwang, A. Singh, B. Mensah, N. Bunce, J. Tiley, T. Scharf, R. Banerjee, Microstructural evolution in laser deposited nickel–titanium–carbon in situ metal matrix composites, Journal of Alloys and Compounds 509(4) (2011) 1255-1260.

[87] J. Hwang, A. Neira, T. Scharf, J. Tiley, R. Banerjee, Laser-deposited carbon nanotube reinforced nickel matrix composites, Scripta Materialia 59(5) (2008) 487-490.

[88] T. Rong, D. Gu, Formation of novel graded interface and its function on mechanical properties of WC 1− x reinforced Inconel 718 composites processed by selective laser melting, Journal of Alloys and Compounds 680 (2016) 333-342.

[89] S.H. Kim, G.-H. Shin, B.-K. Kim, K.T. Kim, D.-Y. Yang, C. Aranas, J.-P. Choi, J.-H. Yu, Thermo-mechanical improvement of Inconel 718 using ex situ boron nitride-reinforced composites processed by laser powder bed fusion, Scientific reports 7(1) (2017) 14359.

[90] D. Gu, Y. Shen, Influence of phosphorus element on direct laser sintering of multicomponent Cu-based metal powder, Metallurgical and Materials Transactions B 37(6) (2006) 967-977.

[91] J. Zhang, Y. Zhou, Microstructure, mechanical, and electrical properties of Cu–Ti 3 AlC 2 and in situ Cu–TiC x composites, Journal of Materials Research 23(4) (2008) 924-932.

[92] P. Deshpande, J. Li, R. Lin, Infrared processed Cu composites reinforced with WC particles, Materials Science and Engineering: A 429(1) (2006) 58-65.

[93] P. Deshpande, R. Lin, Wear resistance of WC particle reinforced copper matrix composites and the effect of porosity, Materials Science and Engineering: A 418(1) (2006) 137-145.

[94] G. Gusmano, A. Bianco, R. Polini, P. Magistris, G. Marcheselli, Chemical synthesis and sintering behaviour of highly dispersed W/Cu composite powders, Journal of materials science 36(4) (2001) 901-907.

[95] H. Xing, X. Cao, W. Hu, L. Zhao, J. Zhang, Interfacial reactions in 3D-SiC network reinforced Cu-matrix composites prepared by squeeze casting, Materials Letters 59(12) (2005) 1563-1566.

[96] S. Rathod, O. Modi, B. Prasad, A. Chrysanthou, D. Vallauri, V. Deshmukh, A. Shah, Cast in situ Cu–TiC composites: synthesis by SHS route and characterization, Materials Science and Engineering: A 502(1) (2009) 91-98.

[97] D. Gu, Y. Shen, Influence of Cu-liquid content on densification and microstructure of direct laser sintered submicron W–Cu/micron Cu powder mixture, Materials Science and Engineering: A 489(1) (2008) 169-177.

[98] E. Breval, J. Cheng, D. Agrawal, P. Gigl, M. Dennis, R. Roy, A. Papworth, Comparison between microwave and conventional sintering of WC/Co composites, Materials Science and Engineering: A 391(1) (2005) 285-295.

[99] D. Gu, Y. Shen, L. Zhao, J. Xiao, P. Wu, Y. Zhu, Effect of rare earth oxide addition on microstructures of ultra-fine WC–Co particulate reinforced Cu matrix composites prepared by direct laser sintering, Materials Science and Engineering: A 445 (2007) 316-322.

[100] D. Gu, Y. Shen, J. Xiao, Influence of processing parameters on particulate dispersion in direct laser sintered WC–Co p/Cu MMCs, International Journal of Refractory Metals and Hard Materials 26(5) (2008) 411-422.

[101] D. Gu, Y. Shen, Influence of reinforcement weight fraction on microstructure and properties of submicron WC–Co p/Cu bulk MMCs prepared by direct laser sintering, Journal of alloys and compounds 431(1) (2007) 112-120.

[102] D. Gu, Y. Shen, Processing and microstructure of submicron WC–Co particulate reinforced Cu matrix composites prepared by direct laser sintering, Materials Science and Engineering: A 435 (2006) 54-61.

[103] D. Gu, Y. Shen, The role of La2O3 in direct laser sintering of submicrometre WC–Cop/Cu MMCs, Journal of Physics D: Applied Physics 41(9) (2008) 095308.

[104] D. Gu, Y. Shen, Microstructures and properties of direct laser sintered tungsten carbide (WC) particle reinforced Cu matrix composites with RE–Si–Fe addition: A comparative study, Journal of Materials Research 24(11) (2009) 3397-3406.

[105] L. Lu, J. Fuh, Z. Chen, C. Leong, Y. Wong, In situ formation of TiC composite using selective laser melting, Materials Research Bulletin 35(9) (2000) 1555-1561.

[106] D. Gu, Y. Shen, Effects of processing parameters on consolidation and microstructure of W–Cu components by DMLS, Journal of Alloys and Compounds 473(1) (2009) 107-115.

[107] D. Gu, Y. Shen, WC–Co particulate reinforcing Cu matrix composites produced by direct laser sintering, Materials Letters 60(29) (2006) 3664-3668.

[108] A. Bhat, V.K. Balla, S. Bysakh, D. Basu, S. Bose, A. Bandyopadhyay, Carbon nanotube reinforced Cu–10Sn alloy composites: Mechanical and thermal properties, Materials Science and Engineering: A 528(22) (2011) 6727-6732.

[109] J.F. Shackelford, Y.-H. Han, S. Kim, S.-H. Kwon, CRC materials science and engineering handbook, CRC press2016.

[110] I. Ibrahim, F. Mohamed, E. Lavernia, Particulate reinforced metal matrix composites—a review, Journal of materials science 26(5) (1991) 1137-1156.

[111] E. Pagounis, V. Lindroos, M. Talvitie, Influence of reinforcement volume fraction and size on the microstructure and abrasion wear resistance of hot isostatic pressed white iron matrix composites, Metallurgical and Materials Transactions A 27(12) (1996) 4171-4181.

[112] F. Akhtar, Microstructure evolution and wear properties of in situ synthesized TiB 2 and TiC reinforced steel matrix composites, Journal of Alloys and Compounds 459(1) (2008) 491-497.

[113] T. Shen, C. Koch, K. Wang, M. Quan, J. Wang, Solid-state reaction in nanocrystalline Fe/SiC composites prepared by mechanical alloying, Journal of materials science 32(14) (1997) 3835-3839.

[114] J. Abenojar, F. Velasco, J. Torralba, J. Bas, J. Calero, R. Marce, Reinforcing 316L stainless steel with intermetallic and carbide particles, Materials Science and Engineering: A 335(1) (2002) 1-5.

[115] K.K. Chawla, Metal matrix composites, Wiley Online Library2006.

[116] M. Fathi, A. Hanifi, V. Mortazavi, Preparation and bioactivity evaluation of bone-like hydroxyapatite nanopowder, Journal of materials processing technology 202(1) (2008) 536-542.

[117] Q. Wei, S. Li, C. Han, W. Li, L. Cheng, L. Hao, Y. Shi, Selective laser melting of stainless-steel/nano-hydroxyapatite composites for medical applications: Microstructure, element distribution, crack and mechanical properties, Journal of Materials Processing Technology 222 (2015) 444-453.

[118] B. AlMangour, D. Grzesiak, J.-M. Yang, Nanocrystalline TiC-reinforced H13 steel matrix nanocomposites fabricated by selective laser melting, Materials & Design 96 (2016) 150-161.

[119] B. AlMangour, D. Grzesiak, Selective laser melting of TiC reinforced 316L stainless steel matrix nanocomposites: Influence of starting TiC particle size and volume content, Materials & Design 104 (2016) 141-151.

[120] B. AlMangour, D. Grzesiak, J.-M. Yang, Scanning strategies for texture and anisotropy tailoring during selective laser melting of TiC/316L stainless steel nanocomposites, Journal of Alloys and Compounds 728 (2017) 424-435.

[121] B. AlMangour, D. Grzesiak, J.-M. Yang, Rapid fabrication of bulk-form TiB 2/316L stainless steel nanocomposites with novel reinforcement architecture and improved performance by selective laser melting, Journal of Alloys and Compounds 680 (2016) 480-493.

[122] B. AlMangour, D. Grzesiak, J.-M. Yang, Selective laser melting of TiB 2/316L stainless steel composites: The roles of powder preparation and hot isostatic pressing post-treatment, Powder Technology 309 (2017) 37-48.

[123] B. AlMangour, D. Grzesiak, J.-M. Yang, Selective laser melting of TiB 2/H13 steel nanocomposites: Influence of hot isostatic pressing post-treatment, Journal of Materials Processing Technology 244 (2017) 344-353.

[124] A. Gåård, P. Krakhmalev, J. Bergström, Microstructural characterization and wear behavior of (Fe, Ni)–TiC MMC prepared by DMLS, Journal of Alloys and Compounds 421(1) (2006) 166-171.

[125] L. Hao, S. Dadbakhsh, O. Seaman, M. Felstead, Selective laser melting of a stainless steel and hydroxyapatite composite for load-bearing implant development, Journal of Materials Processing Technology 209(17) (2009) 5793-5801.

[126] B. Song, S. Dong, C. Coddet, Rapid in situ fabrication of Fe/SiC bulk nanocomposites by selective laser melting directly from a mixed powder of microsized Fe and SiC, Scripta Materialia 75 (2014) 90-93.

[127] B. Song, S. Dong, P. Coddet, G. Zhou, S. Ouyang, H. Liao, C. Coddet, Microstructure and tensile behavior of hybrid nano-micro SiC reinforced iron matrix composites produced by selective laser melting, Journal of Alloys and Compounds 579 (2013) 415-421.

[128] H. Niu, I. Chang, Selective laser sintering of gas and water atomized high speed steel powders, Scripta Materialia 41(1) (1999) 25-30.

[129] T. Fedina, J. Sundqvist, J. Powell, A.F.H. Kaplan, A comparative study of water and gas atomized low alloy steel powders for additive manufacturing, Additive Manufacturing 36 (2020) 101675.

[130] C. Suryanarayana, Mechanical alloying and milling, Progress in materials science 46(1) (2001) 1-184.

[131] J. Xie, P. Fox, W. O'Neill, C. Sutcliffe, Effect of direct laser re-melting processing parameters and scanning strategies on the densification of tool steels, Journal of materials processing technology 170(3) (2005) 516-523.

[132] L. Thijs, F. Verhaeghe, T. Craeghs, J. Van Humbeeck, J.-P. Kruth, A study of the microstructural evolution during selective laser melting of Ti–6Al–4V, Acta Materialia 58(9) (2010) 3303-3312.

[133] H. De Vries, G. Den Ouden, Influence of welding on structure of Al–Mg–Si matrix composites, Materials science and technology 15(2) (1999) 202-206.

[134] D. Stefanescu, B. Dhindaw, S. Kacar, A. Moitra, Behavior of ceramic particles at the solid-liquid metal interface in metal matrix composites, Metallurgical Transactions A 19(11) (1988) 2847-2855.

[135] B. Dutta, M. Surappa, Directional dendritic solidification of a composite slurry: Part II. Particle distribution, Metallurgical and Materials Transactions A 29(4) (1998) 1329-1339.

[136] B. Zheng, Y. Zhou, J. Smugeresky, J. Schoenung, E. Lavernia, Thermal behavior and microstructure evolution during laser deposition with laser-engineered net shaping: part II. Experimental investigation and discussion, Metallurgical and Materials Transactions A 39(9) (2008) 2237-2245.

[137] B. Zheng, J. Smugeresky, Y. Zhou, D. Baker, E. Lavernia, Microstructure and properties of laser-deposited Ti6Al4V metal matrix composites using Ni-coated powder, Metallurgical and Materials Transactions A 39(5) (2008) 1196-1205.

[138] I. Gotman, E. Gutmanas, P. Mogilevsky, Interaction between SiC and Ti powder, Journal of materials research 8(10) (1993) 2725-2733.

[139] J.E. Smugeresky, B. Zheng, Y. Zhou, D. Baker, A. Biswas, E.J. Lavernia, SYNTHESIS AND CHARACTERIZATION OF HYBRID AL/AL3NI FOAM MATERIALS VIA LENS (R) DEPOSITION OF NI-COATED AL POWDER, Sandia National Laboratories (SNL-CA), Livermore, CA (United States), 2008.

[140] Z. Liu, Y. Gong, W. Zhou, L. Ma, J. Yu, J.C. Idrobo, J. Jung, A.H. MacDonald, R. Vajtai, J. Lou, Ultrathin high-temperature oxidation-resistant coatings of hexagonal boron nitride, Nature communications 4 (2013) 2541.

[141] J. Bolton, M. Youseffi, Fracture toughness of sintered metal matrix composites based upon high speed steels enriched with hard ceramic carbides, Powder metallurgy 36(2) (1993) 142-152.

[142] H. Attar, M. Calin, L. Zhang, S. Scudino, J. Eckert, Manufacture by selective laser melting and mechanical behavior of commercially pure titanium, Materials Science and Engineering: A 593 (2014) 170-177.

[143] P. Ma, K.G. Prashanth, S. Scudino, Y. Jia, H. Wang, C. Zou, Z. Wei, J. Eckert, Influence of annealing on mechanical properties of Al-20Si processed by selective laser melting, Metals 4(1) (2014) 28-36.

[144] B.E. Carroll, T.A. Palmer, A.M. Beese, Anisotropic tensile behavior of Ti–6Al–4V components fabricated with directed energy deposition additive manufacturing, Acta Materialia 87 (2015) 309-320.

[145] X. Tan, Y. Kok, Y.J. Tan, M. Descoins, D. Mangelinck, S.B. Tor, K.F. Leong, C.K. Chua, Graded microstructure and mechanical properties of additive manufactured Ti–6Al–4V via electron beam melting, Acta Materialia 97 (2015) 1-16.

[146] L. Thijs, M.L.M. Sistiaga, R. Wauthle, Q. Xie, J.-P. Kruth, J. Van Humbeeck, Strong morphological and crystallographic texture and resulting yield strength anisotropy in selective laser melted tantalum, Acta Materialia 61(12) (2013) 4657-4668.

[147] Z. Wang, T.A. Palmer, A.M. Beese, Effect of processing parameters on microstructure and tensile properties of austenitic stainless steel 304L made by directed energy deposition additive manufacturing, Acta Materialia 110 (2016) 226-235.

[148] K. Kunze, T. Etter, J. Grässlin, V. Shklover, Texture, anisotropy in microstructure and mechanical properties of IN738LC alloy processed by selective laser melting (SLM), Materials Science and Engineering: A 620 (2015) 213-222.

[149] A. Hussein, L. Hao, C. Yan, R. Everson, Finite element simulation of the temperature and stress fields in single layers built without-support in selective laser melting, Materials & Design 52 (2013) 638-647.

[150] I. Sulima, P. Klimczyk, P. Malczewski, Effect of TiB2 particles on the tribological properties of stainless steel matrix composites, Acta Metallurgica Sinica (English Letters) 27(1) (2014) 12-18.

[151] B. AlMangour, M.-S. Baek, D. Grzesiak, K.-A. Lee, Strengthening of stainless steel by titanium carbide addition and grain refinement during selective laser melting, Materials Science and Engineering: A 712 (2018) 812-818.

[152] K. Zhang, G. Chen, Effect of SiC particles on crystal growth of Al–Si alloy during laser rapid solidification, Materials Science and Engineering: A 292(2) (2000) 229-231.

[153] B. Dutta, M. Surappa, Microstructure evolution during multidirectional solidification of Al-Cu-SiC composites, Composites Part A: Applied Science and Manufacturing 29(5-6) (1998) 565-573.

[154] J. Sekhar, R. Trivedi, Solidification microstructure evolution in the presence of inert particles, Materials Science and Engineering: A 147(1) (1991) 9-21.

[155] P. Rohatgi, K. Pasciak, C. Narendranath, S. Ray, A. Sachdev, Evolution of microstructure and local thermal conditions during directional solidification of A356-SiC particle composites, Journal of materials science 29(20) (1994) 5357-5366.

[156] S. Sathish, M. Geetha, N. Pandey, C. Richard, R. Asokamani, Studies on the corrosion and wear behavior of the laser nitrided biomedical titanium and its alloys, Materials Science and Engineering: C 30(3) (2010) 376-382.

[157] E.J. Lavernia, T.S. Srivatsan, The rapid solidification processing of materials: science, principles, technology, advances, and applications, Journal of Materials Science 45(2) (2010) 287.

[158] M. Salehi, K. Dehghani, Structure and properties of nanostructured aluminum A413. 1 produced by melt spinning compared with ingot microstructure, Journal of Alloys and Compounds 457(1) (2008) 357-361.

[159] E. Huskins, B. Cao, K. Ramesh, Strengthening mechanisms in an Al–Mg alloy, Materials Science and Engineering: A 527(6) (2010) 1292-1298.

[160] E. Yun, K. Lee, S. Lee, Correlation of microstructure with high-temperature hardness of (TiC, TiN)/Ti–6Al–4V surface composites fabricated by high-energy electron-beam irradiation, Surface and Coatings Technology 191(1) (2005) 83-89.

[161] C. Ma, D. Gu, D. Dai, G. Yu, M. Xia, H. Chen, Thermodynamic behaviour and formation mechanism of novel titanium carbide dendritic crystals within a molten pool of selective laser melting TiC/Ti–Ni composites, CrystEngComm 19(7) (2017) 1089-1099.

[162] E. Fereiduni, S.G. Banadkouki, Reliability/unreliability of mixture rule in a low alloy ferrite–martensite dual phase steel, Journal of alloys and compounds 577 (2013) 351-359.

[163] E. Fereiduni, S.G. Banadkouki, Improvement of mechanical properties in a dual-phase ferrite–martensite AISI4140 steel under tough-strong ferrite formation, Materials & Design 56 (2014) 232-240.

[164] C. Ma, D. Gu, D. Dai, W. Chen, F. Chang, P. Yuan, Y. Shen, Aluminum-based nanocomposites with hybrid reinforcements prepared by mechanical alloying and selective laser melting consolidation, Journal of Materials Research 30(18) (2015) 2816-2828.

[165] R. Aikin, L. Christodoulou, The role of equiaxed particles on the yield stress of composites, Scripta metallurgica et materialia 25(1) (1991) 9-14.

[166] Q.B. Nguyen, M. Gupta, Enhancing compressive response of AZ31B using nano-Al 2 O 3 and copper additions, Journal of Alloys and Compounds 490(1) (2010) 382-387.

[167] S. Dadbakhsh, L. Hao, P. Jerrard, D. Zhang, Experimental investigation on selective laser melting behaviour and processing windows of in situ reacted Al/Fe 2 O 3 powder mixture, Powder technology 231 (2012) 112-121.

[168] W. Liu, J. DuPont, Fabrication of functionally graded TiC/Ti composites by laser engineered net shaping, Scripta Materialia 48(9) (2003) 1337-1342.

[169] R. Mahamood, E.T. Akinlabi, Laser metal deposition of functionally graded Ti6Al4V/TiC, Materials & Design 84 (2015) 402-410.

[170] J.C. Oh, S. Lee, Correlation of microstructure with hardness and fracture properties of (TiC, SiC)/Ti–6Al–4V surface composites fabricated by high-energy electron-beam irradiation, Surface and Coatings Technology 179(2) (2004) 340-348.

[171] J.S. Moya, S. Lopez-Esteban, C. Pecharroman, The challenge of ceramic/metal microcomposites and nanocomposites, Progress in materials science 52(7) (2007) 1017-1090.

[172] S.C. Tjong, Novel nanoparticle-reinforced metal matrix composites with enhanced mechanical properties, Advanced engineering materials 9(8) (2007) 639-652.

[173] W. Miller, F. Humphreys, Strengthening mechanisms in particulate metal matrix composites, Scripta metallurgica et materialia 25(1) (1991) 33-38.

[174] D. Hull, D.J. Bacon, Introduction to dislocations, Butterworth-Heinemann2001.

[175] W. Wong, M. Gupta, Development of Mg/Cu nanocomposites using microwave assisted rapid sintering, Composites Science and Technology 67(7) (2007) 1541-1552.

[176] Z. Szaraz, Z. Trojanova, M. Cabbibo, E. Evangelista, Strengthening in a WE54 magnesium alloy containing SiC particles, Materials Science and Engineering: A 462(1) (2007) 225-229.

[177] A. Sanaty-Zadeh, Comparison between current models for the strength of particulate-reinforced metal matrix nanocomposites with emphasis on consideration of Hall–Petch effect, Materials Science and Engineering: A 531 (2012) 112-118.

[178] Z. Zhang, D. Chen, Contribution of Orowan strengthening effect in particulate-reinforced metal matrix nanocomposites, Materials Science and Engineering: A 483 (2008) 148-152.

[179] E. Hall, The deformation and ageing of mild steel: III discussion of results, Proceedings of the Physical Society. Section B 64(9) (1951) 747.

[180] C. Goh, J. Wei, L. Lee, M. Gupta, Properties and deformation behaviour of Mg–Y 2 O 3 nanocomposites, Acta Materialia 55(15) (2007) 5115-5121.

[181] T. Clyne, P. Withers, An introduction to metal matrix composites, Cambridge University Press1995.

[182] R.E. Smallman, A. Ngan, Physical metallurgy and advanced materials, Butterworth-Heinemann2011.

[183] Q. Nguyen, M. Gupta, Enhancing compressive response of AZ31B magnesium alloy using alumina nanoparticulates, Composites Science and Technology 68(10) (2008) 2185-2192.

[184] R. Labusch, A statistical theory of solid solution hardening, physica status solidi (b) 41(2) (1970) 659-669.

[185] W. Soboyejo, Mechanical properties of engineered materials, CRC press2002.

[186] P. Bindumadhavan, H.K. Wah, O. Prabhakar, Dual particle size (DPS) composites: effect on wear and mechanical properties of particulate metal matrix composites, Wear 248(1) (2001) 112-120.

[187] G.V. Kumar, C. Rao, N. Selvaraj, Mechanical and tribological behavior of particulate reinforced aluminum metal matrix composites–a review, Journal of minerals and materials characterization and engineering 10(01) (2011) 59.

Chapter 2 Characterization of Composite Powder Feedstock from Powder Bed Fusion Additive Manufacturing Perspective

Complete Citation:

Fereiduni E, Ghasemi A, Elbestawi M. Characterization of composite powder feedstock from powder bed fusion additive manufacturing perspective. Materials. 2019 Jan;12(22):3673.

Abstract

This research aims at evaluating the characteristics of the 5 wt.% B_4C/Ti-6Al-4V composite powder feedstock prepared by two different categories of mechanical mixing for powder bed fusion (PBF) additive manufacturing (AM) of metal matrix composites (MMCs). Microstructural features, particle size, size distribution, sphericity, conditioned bulk density and flow behavior of the developed powders were examined. The flowability of the regularly mixed powders was significantly lower than that of the Ti-6Al-4V powder. However, the flowability of the ball milled systems was a significant function of the milling time. The decrease in the flowability of the 2 h ball milled powder compared to the Ti-6Al-4V powder was attributed to the mechanical interlocking and the entangling caused by the B_4C particles fully decorating the Ti-6Al-4V particles. Although the flattened/irregular shape of powder particles in the 6 h milled system acted to reduce the flowability, the overall surface area reduction led to higher flowability than that for the 2 h milling case. Regardless of the mixing method, incorporation of B_4C particles to the system decreased the apparent density of Ti-6Al-4V powder. The composite powder obtained by 2 h of ball milling was suggested as the best possible condition meeting the requirements of PBF-AM processes.

Keywords: Additive manufacturing; Powder bed fusion; Selective laser melting; Regular mixing; Ball milling; Flowability; Ti-6Al-4V

2.1 Introduction

Metal matrix composites (MMCs) are outstanding materials bilaterally benefitting from the properties of at least two constituents: the metal matrix (usually an alloy), and the reinforcement (in general, an oxide, an intermetallic compound, a carbide or a nitride) [1-3]. Incorporation of reinforcements into the metallic matrix is generally associated with the improvement in hardness, specific strength, wear resistance, fracture toughness, and stiffness compared to the monolithic counterparts [4-7]. Owing to their desired structural and functional properties, MMCs have found their application in numerous technological fields including automotive, aerospace and biomedical industries [8, 9].

Several conventional manufacturing processes already exist for incorporating reinforcements into the metallic matrices to produce a wide variety of MMCs [10-14]. However, it is rather challenging to fabricate geometrically complex parts using these processes. Additive manufacturing (AM) is regarded as a major revolution in the manufacturing technology which competes with conventional manufacturing processes in many aspects including but not limited to the design freedom, fabrication cost and time, accuracy and the part quality [15, 16].

Powder bed fusion (PBF) refers to the AM processes in which an object is manufactured layer-by-layer from a batch of loose powder using a mobile heat source. During this process, a thin layer of powder is deposited on the building platform by the recoater. The powder flow behavior during the recoating process plays a critical role on the uniformity, surface roughness and the thickness of the deposited powder layer and consequently the dimensional accuracy of the final part [17, 18]. On the other hand, the powder bed packing density directly affects the density and mechanical properties of the additively

manufactured components [19, 20]. Therefore, the flowability and the packing density of the powders need to be investigated prior to the AM process to ensure the soundness of the final parts [21-24].

The desired properties of MMCs are achieved when the reinforcements are homogeneously distributed throughout the matrix with a strong reinforcement/matrix interfacial bonding [25, 26]. Conventional MMC fabrication methods generally yield inhomogeneous microstructures, making it rather difficult to fully exploit the strengthening potentials of reinforcements. Therefore, it is of crucial importance to develop new fabrication routes providing more homogenous distribution of reinforcements within the matrix [16]. The noticeably localized melt pool and the extremely high solidification rates associated with the PBF-AM technology can lead to MMC structures which are much more homogenous than the conventionally processed parts [27]. However, there are still some challenges with the PBF-AM processing of MMCs for achieving highly uniform microstructures due to the following reasons [3, 28]:

i. In nano-composites, reinforcing particles tend to agglomerate and form coarsened clusters in the matrix due to the presence of van der Waals attraction forces among them.

ii. A large difference between the densities of the reinforcing particles and the liquid matrix encourages the non-uniform distribution of reinforcements in the microstructure.

iii. The convection flows (i.e., Marangoni effect) induced in the melt pool may not be sufficient to disperse the reinforcing particles throughout the system.

Therefore, when it comes to the PBF-AM of MMCs, particular emphasis should be placed on pre-processing of the composite powder feedstock in order to achieve parts with homogenous microstructures and consequently uniform mechanical properties. Development of a suitable composite powder feedstock with uniform distribution of reinforcing particles is the first step to mitigate the mentioned challenges.

Since the feedstock of MMCs is not commercially available for the AM processing [29], several techniques have been employed in recent years to prepare these powders. The mechanical routes such as regular mixing [30-32] and ball milling [33-39], and non-mechanical methods including gas atomization of a pre-alloyed system [40, 41], agent-assisted deposition [42, 43] and electrodeposition [44, 45] are among these methods. Compared to the mechanical mixing routes which have attracted a great deal of attention in recent years, the non-mechanical methods have been rarely adopted to prepare composite powder feedstocks for AM purposes. Although the non-mechanical methods can probably produce composite powder systems with a better flowability and a more uniform distribution state of powder constituents compare to the mechanical routes, they are much more complex and expensive. Due to their low cost as well as their applicability to many powder systems, the mechanical routes are the most frequently used methods in powder feedstock preparation for the PBF-AM of MMCs [29, 46].

Incorporation of the guest powder particles (e.g., ceramic particles) in the host powder particles (usually metallic particles) leads to the production of composite powder feedstocks with different characteristics from the individual constituents. The particle size, particle size distribution, and distribution state of the guest powder particles are among these features which dictate the apparent density, flowability, and laser absorptivity of the composite powder [15, 16]. The laser absorptivity influences the heat absorption, and the

melt pool size [44, 47, 48] while, the flowability and the apparent packing density of the powder play crucial roles in layer thickness (dimensional accuracy) and density of the final part [17, 49-52]. A literature review of the AM processing of MMCs reveals that the mixing of powders in most cases has been performed to achieve a distribution of free (non-attached) guest particles throughout the mixed powder system [30-39, 53-55]. On the other hand, preserving the spherical shape of metallic powder particles has been considered in some of these studies [36, 53, 55, 56]. However, the effect of powder preparation routes and process variables on the composite powder features affecting the quality of AM processed parts is still unclear and needs in-depth analysis and characterization from the AM perspective to obtain high-quality MMCs.

The present research aims to study the characteristics of the mechanically mixed 5 wt.% B_4C/Ti-6Al-4V (Ti64) composite powder feedstock from the PBF-AM viewpoint. For this purpose, the regular mixing and the ball milling methods were employed with different mixing times to prepare a wide variety of mixed powder systems. The effects of the mixing method and the mixing time on size, size distribution, sphericity, shape, distribution state of guest particles, phase formation, plastic deformation, apparent density, and flow behavior of the prepared composite powder systems were studied. Moreover, the mechanisms involved in the flow behavior of the developed feedstocks were identified, and the best possible powder feedstock meeting the requirements of PBF-AM processing of MMCs was proposed.

2.2 Materials and Methods

2.2.1 Powder Preparation

The powders used in this research were Ti64 (15-45 μm) and B_4C (1-3 μm) named as "host" and "guest" powders, respectively. The nominal chemical composition of these powders is provided in Table 1. For preparing the composite powder feedstock, the regular mixing and the ball milling processes were employed, which are schematically shown in Figure 2-1. In both cases, the mixed powder systems contained 5 wt.% B_4C (guest), and the powders were mixed under a protective argon gas atmosphere to avoid oxidation. The mixing process was performed using a high-performance planetary Pulverisette 6 machine at a fixed rotational speed of 200 rpm and mixing times in the range of 1-6 h. The regularly mixed and the ball milled samples have been marked as R(1-6) and B(1-6), respectively, depending on their mixing time. In the regular mixing, the powders were mixed without balls. However, stainless steel balls with a diameter of 10 mm were added to the system in the ball milling process. The ball-to-powder ratio was selected to be 5:1, and every 30 min. of the milling was followed by a 15 min. pause in order to avoid the temperature rise during the process [57]. For each composite powder system, the mass was measured after the mixing to find the material loss.

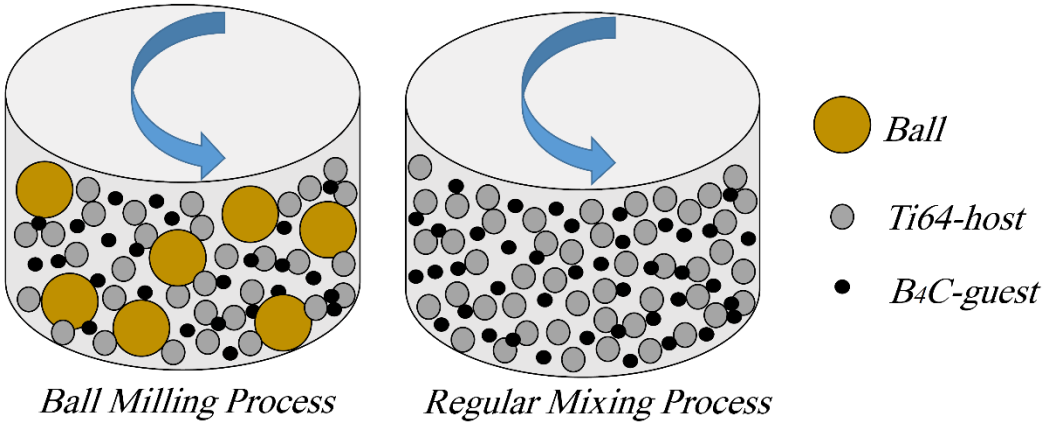

Figure 2-1 Schematic illustration of: (a) ball milling and (b) regular mixing processes.

Table 1. Nominal chemical composition of the starting Ti-6Al-4V and B_4C powders.

Powder	**Elements (wt.%)**								
Ti-6Al-4V (host)	Ti	Al	V	Fe	O	N	C	H	B
	Bal.	6.3	4.0	0.03	0.1	0.01	0.01	<0.1	-
B_4C (guest)	B_4C	Al	V	Fe	O	N	Free C	H	Free B
	Bal.	<0.001	-	<0.001	<0.04	<0.001	3	-	4

2.2.2 Powder Characterization

2.2.2.1 Microstructure and XRD Analysis

The morphology of the starting Ti64 (host) and B_4C (guest) powders, as well as the composite powder systems, were studied using Vega Tescan scanning electron microscopy (SEM) operating at an accelerating voltage of 20 kV. The X-ray diffraction (XRD) analysis was employed to study the effect of the mixing method and the mixing time on the phase formation and the plastic deformation of the developed composite powder feedstocks. This analysis was performed at ambient temperature over a wide range of $2\theta = 20\text{-}80°$ using a PANalytical X'Pert powder X-ray diffractometer (Cu Kα target, operating at the voltage and the current of 45 kV and 35 mA, respectively, with a step size of 0.0167°) equipped with X-ray monochromator. In order to have a better understanding of the microstructural features, the starting Ti64 and composite powders were also sectioned and characterized using SEM.

2.2.2.2 Particle Size, Size Distribution and Sphericity

A Retsch Camsizer X2 machine was used to measure the particle size, size distribution and sphericity of the Ti64 and the developed 5wt.% B_4C/Ti64 composite powder systems

fabricated through the regular mixing and ball milling methods. This equipment utilizes a high-resolution dual-camera system to characterize fine and agglomerating powders ranging from 800 nm to 8 mm in diameter [58]. The reported results are the average of three measurements. The sphericity of the powder particles was calculated based on the equation suggested by ISO 9276-6 standard [59]:

$$Sphericity = \frac{4\pi A}{P^2} \quad [1]$$

where P and A are the measured circumference and area covered by a particle projection, respectively. Given the fact that the sphericity of an ideal sphere is unity, deviation from the ideal spherical shape results in lower sphericities.

2.2.2.3 Flow Characteristics

The flow behavior of powder particles could be characterized using different techniques such as ring shear cell tester, Hausner ratio (HR), angle of repose (AOR)/Hall flowmeter, avalanche angle and Freeman Technology 4 (FT4) powder rheometer [60-62]. When deciding to choose one of these techniques, characteristics of both the technique and the process need to be considered since the selected flowability measurement technique should be as close to the employed process as possible. In recent years, the FT4 Powder Rheometer has emerged as a unique technology to measure the flow behavior of the powder, whilst the powder is in motion. In this device, a precision 'blade' is rotated and moved downwards through the powder bed through a fixed mass of powder to establish a flow pattern. The work required to drive the rotating impeller a certain distance into the powder bed yields the flow energy. Due to its dynamic nature, this technique is capable of differentiating the flowability of powders that exhibit similar behavior under other flow measurement techniques [63]. The FT4 powder rheometer technique provides measurement of several parameters related to the process performance of powders. The interaction of the precision

blade with the powder in this technique resembles that of recoater/powder in PBF-AM process. It is worth noting that the control over the speed of the blade provided by this technique enables the characterization of powder sensitivity to the changes in flow rate. This unique feature also facilitates analysis of the powder flowability for different PBF-AM machines having different recoater speeds.

The flow characteristics of the host powder as well as the developed composite powder feedstocks in the present study were measured using a FT4 powder rheometer. In order to study the powder rheological properties using this technique, the standard "Stability and Variable Flow Rate (SVFR)" method was employed, which consists of a stable tip speed zone with seven test cycles followed by a variable tip speed zone having four test cycles. During each test cycle, the precision blade rotated downwards and upwards through the fixed mass of powder to establish a flow pattern, where the powder resistance to the blade yielded the flow properties. During the stability part, the blade operated with a tip speed of -100 mm/s (anti-clockwise) and a helix angle of 5^{o}. For the variable flow rate zone, the tip speed varied as -100, -70, -40 and -10 mm/s for the test cycles eight, nine, ten and eleven, respectively, with the same helix angle of 5^{o}. The upward speed remained constant at 40 mm/s, and the helix angle was -5^{o} upwards throughout the experiment. It is noteworthy that before all tests, a conditioning cycle was performed which involves the downward and then upward movement of the blade into the powder bed to gently slice the powder and provide a reproducible, uniform and low stress packing state, allowing an objective comparison of samples. For each sample in this study, three tests were run to ensure consistency of the results. The flow characteristics of the samples were studied by analyzing the variation in the flow energy as well as by measuring the basic flowability and specific energy (SE).

Besides, the conditioned bulk density (CBD) of the samples was examined to study the powder bed density.

The basic flowability, defined as the ability of the powder to flow when forced, is qualitatively measured as the basic flow energy (BFE). The BFE represents the energy required for the rotation of the blade for the seventh test cycle ($BFE = E_{test\ 7,down}$) of the stable tip speed part.

The SE shows the energy required to establish a particular flow pattern in a precise volume of conditioned powder and is defined as the average energy of the upward blade rotation for the 7th and 8th test cycles divided by the mass of the remaining powder in the vessel (Eq. 2). By gently lifting the powder, the upward motion of blade generates a low stress and unconfined flow mode in the powder.

$$SE = \frac{\frac{E_{test\ 7,up} + E_{test\ 8,up}}{2}}{m_{split}} \quad [2]$$

where m_{split} is the mass of the powder after the excess powder is removed.

The CBD describes the packing state or the density of the powder in its reference state. In order to measure the CBD, each powder system was gently filled in a 25 ml volume splitting cylindrical vessel having a diameter of 25 mm. The conditioning process was performed with a conditioning blade, which slices the powder bed to remove the excess air and create a uniform powder bed having a low stress packing state. After conditioning, the vessel was split in order to remove the excess mass of powder, so that the remaining powder has a volume of 25 ml. For each sample, three measurements were performed, and the average value was reported as the CBD, based on Eq. 3:

$$CBD = {}^{m_{split}}/_{v_{split}} \quad [3]$$

in which v_{split} signifies the volume of the powder (the vessel volume), after the excess powder is removed.

2.3 Results and Discussions

2.3.1 XRD Analysis: Plastic Deformation and Phase Formation

Figure 2-2(a) presents the XRD patterns of the starting host and guest powders as well as the developed composite powder systems subjected to the regular mixing and the ball milling for different mixing times. The diffraction peaks of Ti64 in the R6 system had almost the same position and intensity as that of the starting Ti64. However, those for the B2 and the B6 systems exhibited the Ti64 diffraction peaks with the decreased intensity and increased width. The observed phenomenon was more pronounced for the B6 sample than for the B2 system. Moreover, a close examination of the Ti64 peaks in the ball milled systems revealed that the severe plastic deformation induced in the ball milling process led to the shift in the peaks position due to the structural changes such as the crystallite refinement and the accumulation of micro-strain [64, 65]. The lattice micro-strain of the Ti64 constituent in the composite powder systems were determined using the standard Williamson-Hall analysis as follows [66]:

$$\beta\cos\theta = \left[\frac{k\lambda}{t}\right] + 4\varepsilon\sin\theta \quad [4]$$

where k is the shape factor (0.9), λ represents the wavelength of the X-ray (1.5406), θ signifies the diffraction angle, t is the effective crystallite size, β is the full width at the half maximum of the XRD peak, and ε is the micro-strain. By constructing a linear plot of ($\beta\cos\theta$) against ($4\sin\theta$), the slope gives the strain ($\boldsymbol{\varepsilon}$). According to the micro-strain results provided in Figure 2-2 (b), the B2 and B6 systems showed increased lattice strain

compared to the regularly mixed feedstocks. Also, longer milling times led to higher lattice strain (B6 compared to B2) due to the higher levels of plastic deformation imparted to the powder particles.

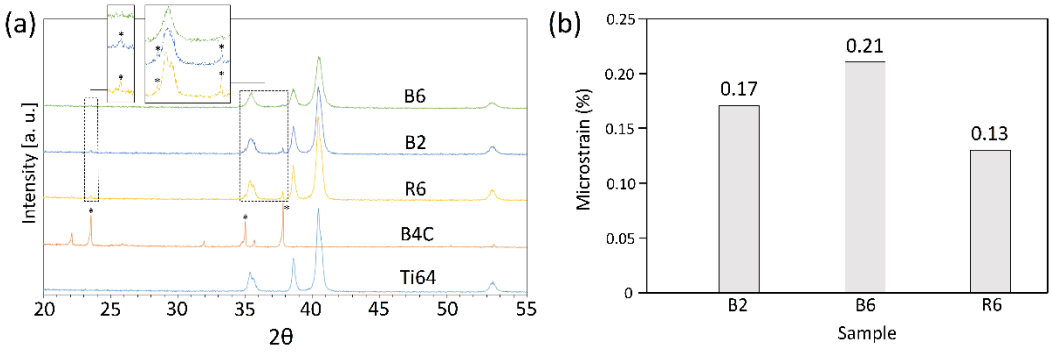

Figure 2-2 (a) XRD patterns of starting Ti-6Al-4V (Ti64) and B_4C powders as well as composite powder systems prepared by regular mixing and ball milling, and (b) The microstrain of Ti64 constituent in the developed composite powder systems derived from the XRD patterns.

Referring to Figure 2-2(a), all the peaks obtained for the composite powder feedstocks corresponded to those for the Ti64 and B_4C powders due to two probable scenarios: (i) no *in-situ* reaction has been activated in the system during the applied range of mixing times, or (ii) if formed, the amount of *in-situ* synthesized phases is below the detection limit of the XRD analysis. As indicated in Figure 2-2(a), the intensity of the B_4C peaks in the R6 composite powder system decreased compared to those for the starting B_4C powder. When employing the ball milling method, the intensity of these weak peaks further decreased for the B2 sample and finally disappeared in the B6 system.

2.3.2 Microstructural Characterization

Figure 2-3 presents SEM micrographs of the starting host Ti64 and the guest B_4C powders used in this research. As observed in Figure 2-3(a), (b), the starting host powder particles had an almost spherical morphology and a very smooth surface, which are both

characteristics of the gas atomized Ti64 powders [17]. However, B_4C particles exhibited an irregular morphology (Figure 2-3(c)). Despite their smooth surface, some of the Ti64 particles have satellites. These satellites are formed when the finer solidified particles stick to the molten or semi-molten surface of the coarser ones as a result of the in-flight collisions before the solidification of the coarser molten droplets [67].

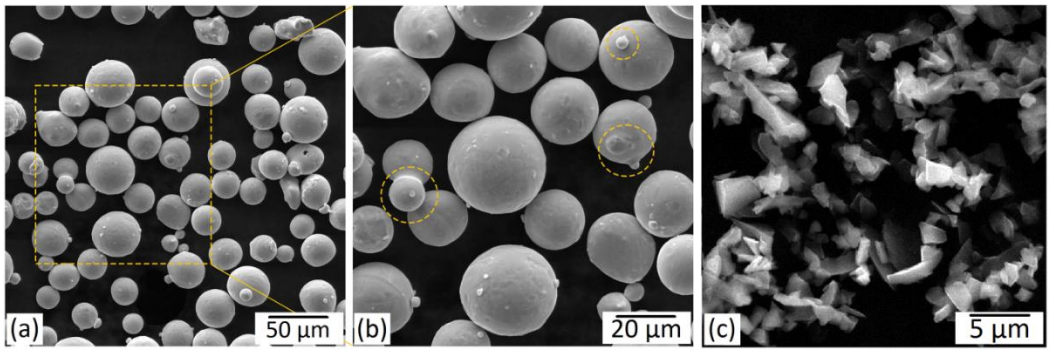

Figure 2-3 SEM micrographs of starting: (a, b) Ti-6Al-4V (host) and (c) B_4C (guest) powder particles. (b) Higher magnification micrographs of the selected region in (a). The circles in (b) indicate the satellites.

The micrographs of the regularly mixed and the ball milled composite powders subjected to various mixing times are provided in Figure 2-4 and Figure 2-5, respectively.

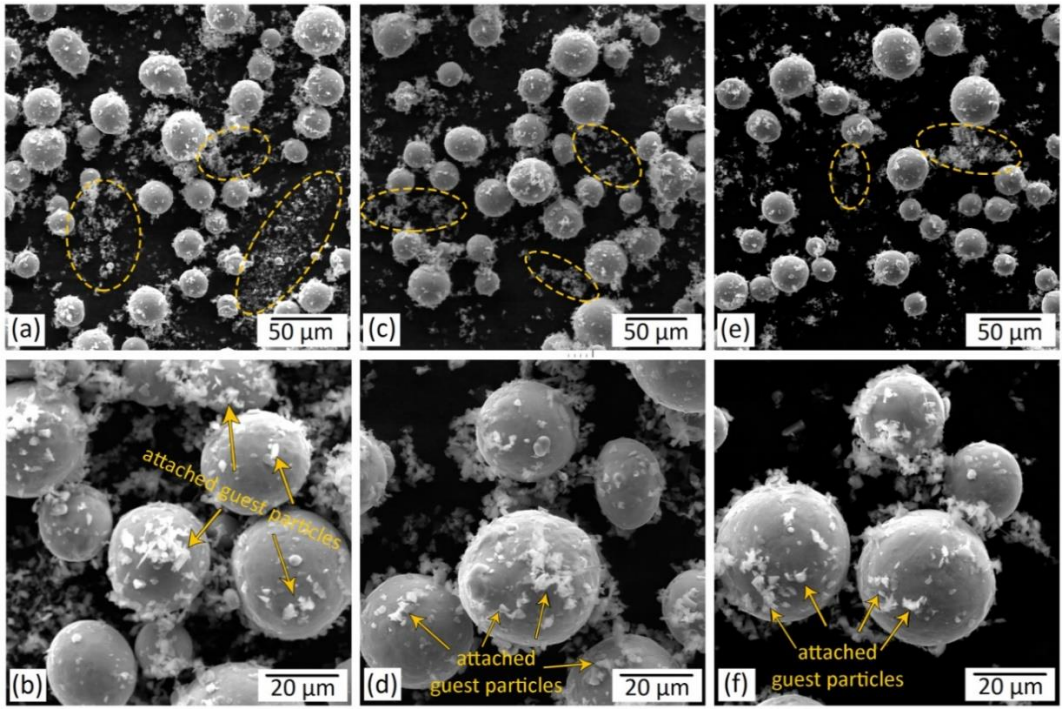

Figure 2-4 SEM micrographs of 5wt.% B_4C/Ti-6Al-4V mixed powder systems subjected to regular mixing for: (a), (b) 1 h (R1); (c), (d) 3 h (R3); and (e), (f) 6 h (R6). The ellipses in (a), (c) and (e) indicate the free B_4C (guest) particles which are not attached to the Ti-6Al-4V (host) particles and are agglomerated.

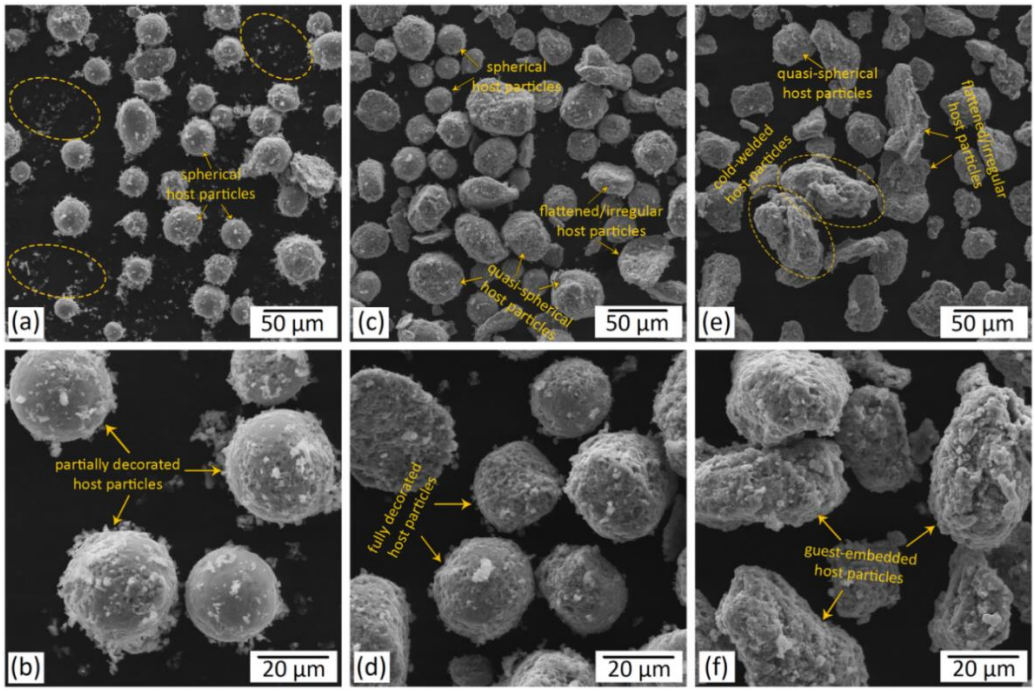

Figure 2-5 SEM micrographs of 5wt.% B_4C/Ti-6Al-4V mixed powder systems subjected to ball milling for: (a), (b) 1 h (B1); (c), (d) 3 h (B3); and (e), (f) 6 h (B6). The ellipses in (a) show the free B_4C (guest) particles which are not attached to the Ti-6Al-4V (host) particles.

The cross-sectional SEM micrographs of the starting Ti64 powder as well as the B2 and the B6 powder systems are presented in Figure 2-6.

As can be observed in Figure 2-4, the Ti64 host particles maintained their spherical morphology when employing the regular mixing method even with mixing times as long as 6 h (R6). However, even after a long mixing time of 6 h (R6), many of the guest particles were not attached to the host powder particles (Figure 2-4(e)), meaning that noticeably longer mixing times may be still required to provide more guest-to-host attachment. The guest particles which are not attached to the host powder particles tend to form agglomerates (as depicted in Figure 2-4(a), (c) and (e)). Despite this fact, the regular mixing

method has been adopted in numerous studies to produce composite powders due to its relative simplicity [30-32, 68, 69].

Depending on the employed mixing time, the host powder particles experienced different levels of plastic deformation during the ball milling process (Figure 2-5 and Figure 2-6). At relatively short milling time of 1-2 h, the host power particles preserved their spherical shape (Figure 2-5 (a) and Figure 2-6 (b), (c)). Higher amounts of plastic deformation imparted to the system by longer milling time of 3 h (B3) resulted in some spherical to quasi-spherical/irregular shape change (Figure 2-5(c)). Also, due to the extended time that the hard guest particles were hitting their surface, the enhanced milling time increased the surface roughness of the host powder particles. In the prolonged milling time of 6 h (B6), the desired spherical shape of the host particles altered to a flattened/irregular shape (Figure 2-5(e), (f) and Figure 2-6(d)-(f)). Microstructural observations also revealed the cold-welding of the ductile host powder particles during the ball milling process. Longer mixing times were found to cause intensified cold-welding in the applied range of ball milling time (Figure 2-5 and Figure 2-6). Even at relatively short mixing time of 1 h, a significant guest-to-host attachment was obtained in the ball milling process, while still a few free B_4C particles could be observed in the composite powder (Figure 2-5(a), (b)). Increasing the mixing time to 3 h eliminated the non-attached B_4C particles and led to the host particles fully decorated by the guest ones (Figure 2-5(c), (d)). Further enhancement of the mixing time to 6 h caused the embedment of the guest particles into the host powder particles (Figure 2-5(e), (f) and Figure 2-6(d)-(f)).

The observed shape change and the agglomeration of the particles both observed at relatively long milling times are known as the main issues limiting the application of such composite powder systems in PBF-AM processes [29, 36]. Sieving has been suggested as

one of the strategies that could be employed to tailor the particle size in the powder systems subjected to the extended milling times [70]. While being successful with particle size, this technique does not control the particle shape. Therefore, depending on the ductility of the host powder particles, appropriate milling times need to be found for each system to control the final shape of the particles.

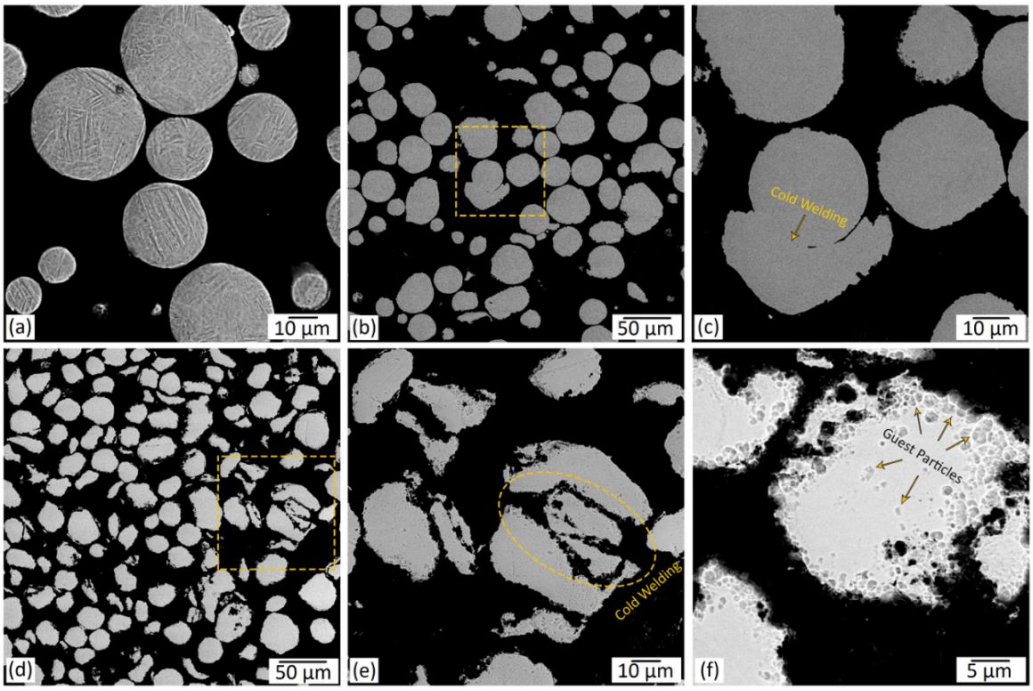

Figure 2-6 Cross-sectional SEM micrographs of: starting Ti-6Al-4V powder showing a martensitic microstructure after etching (a); 5wt.% B_4C/Ti-6Al-4V system subjected to ball milling for: (b), (c) 2 and (d)-(f) 6 h. (c) and (e) are higher magnification micrographs of the regions shown in (b) and (d), respectively.

2.3.3 Particle Size, Size Distribution and Sphericity

Figure 2-7 presents the results of particle size distribution for the starting Ti64 powder as well as the developed 5wt.% B_4C/Ti64 powder feedstocks prepared by the regular mixing and ball milling methods for 2 and 6 h of mixing. As being observed in Figure 2-7(b), (c), the regularly mixed powder systems have a bimodal size distribution, while the ball milled

composite powders show a mono-modal size distribution (Figure 2-7(d), (e)). This can be attributed to the non-attached B_4C particles in the regularly mixed cased as opposed to the full attachment of the guest particles to the host powder particles in the ball milled powder systems. It is worth noting that even a relatively long mixing time of 6 h in the regular mixing method was not successful in full guest-to-host attachment (Figure 2-4(e), (f)). However, relatively short mixing time of 1 h in the ball milling method led to the B_4C particles well-attached to the host powder particles (Figure 2-5(a), (b)). The enhanced milling time provided attachment of more guest particles to the surface of the host particles, eliminating the free guest particles in the composite powder (Figure 2-5(c), (d)). Application of longer milling times (B6) resulted in the embedment of B_4C particles into the host powder particles (Figure 2-5(e), (f) and Figure 5(f)). The severe weakening (or even disappearance) of the B_4C diffraction peaks in this system (B6 powder in Figure 2-2(a)) may be attributed to their embedment into the ductile host powder particles.

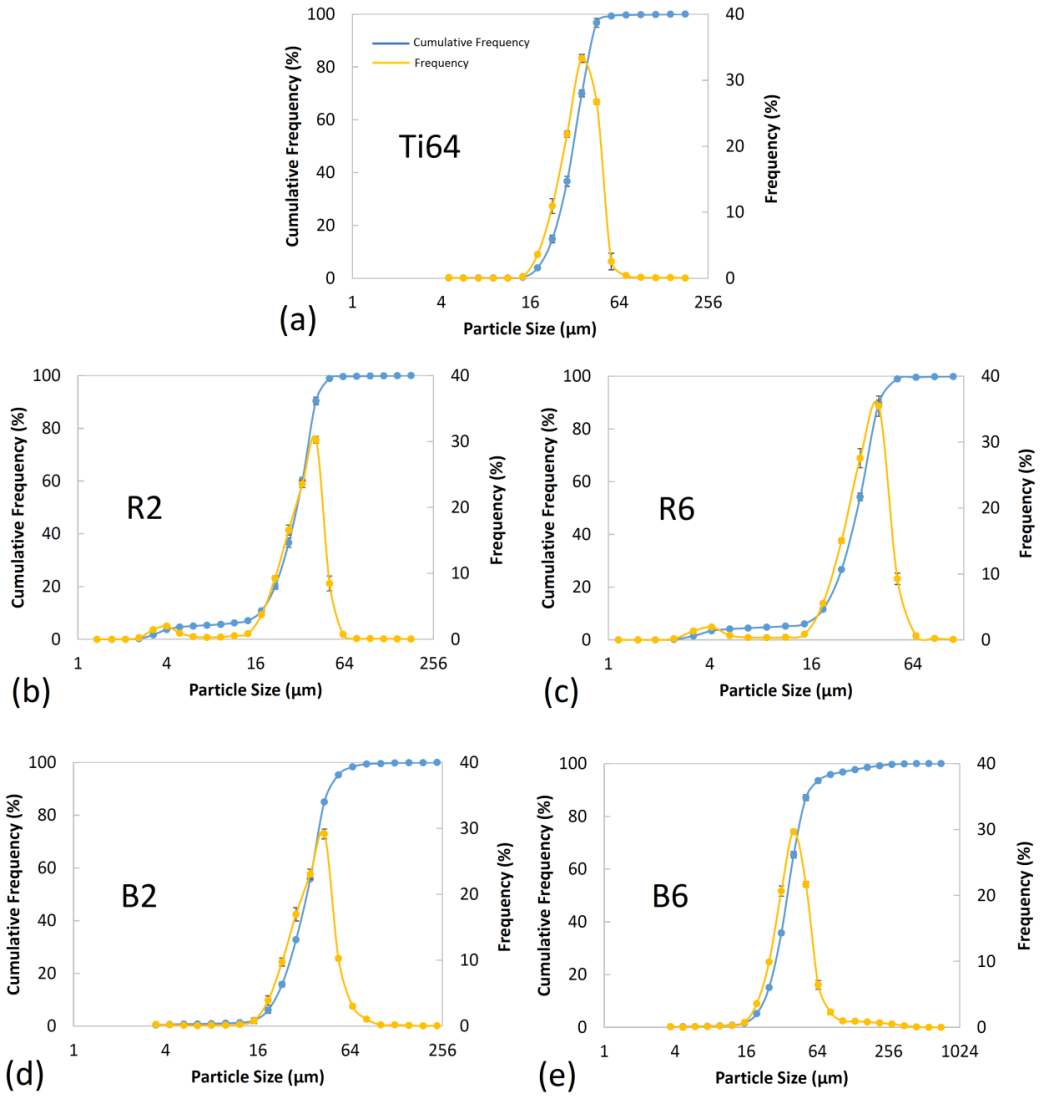

Figure 2-7 The particle size distribution curves of: (a) starting Ti-6Al-4V (Ti64); (b) 2 h (R2) and (c) 6 h (R6) regularly mixed; (d) 2 h (B2) and (e) 6 h (B6) ball milled 5wt.% B_4C/Ti64 composite powder feedstocks.

The D10, D50, and D90 of the powder systems derived from the cumulative frequency shown in Figure 6 are provided in Table 2. Referring to Figure 2-7 and Table 2, the regularly mixed composite powders showed almost the same particle size and particle size distribution as that of the starting Ti64 powder. The slight deviation in D10 and D50 of R2 and R6 systems from those for Ti64 is caused by the presence of free guest B_4C particles

with a significantly smaller particle size compared to the host Ti64 particles (Figure 2-4). Due to its non-equilibrium nature, the ball milling process involves persistent deformation, cold-welding, and fracture of powder particles [71, 72]. The size of the powder particles subjected to the ball milling process is determined by the competition between two major mechanisms, namely, cold-welding and fracture [71]. While the cold-welding mechanism facilitates the formation of larger-sized particles by attachment of the host powder particles, the fracture mechanism favors the decrease in particle size. Hence, the refining or coarsening of powder particles during the ball milling process depends on whether the cold-welding or the fracture mechanism is dominant [73]. For the applied range of milling times, the particle size showed an ascending trend with enhancing the mixing time as a result of the cold-welding mechanism being dominant (Figure 2-5(e) and Figure 2-6(b), (c), (e)). For instance, D90 for the B2 and B6 samples is 12 and 35% higher than that of Ti64 powder, respectively. The particle coarsening in the ball milled composite samples is caused by the guest-to-host attachment as well as the cold-welding of host particles. The decoration of host particles is the dominant factor in increasing the particle size in the B2 sample due to the limited cold-welding caused by the relatively short mixing time (Figure 2-5 and Figure 2-6). However, the significant cold-welding induced by the prolonged mixing time in the B6 sample is the main factor governing the particle coarsening, since the guest particles are embedded into the host Ti64 powder (not decorating the host particles). Based on the D90 of the B6 sample (Table 2) and Figure 2-7, 10% of particles have sizes in the range of 62-275 μm. These particle sizes are noticeably larger than the starting Ti64 powder particles having 0.3% of particles exceeding 62 μm in size.

Table 2. The particle size distribution results presenting the cumulative distribution of D10, D50, and D90 for the Ti-6Al-4V (Ti64) and the developed composite powders.

Sample	D10 (μm)	D50 (μm)	D90 (μm)
Ti64	23.39±0.515	35.04±0.360	45.71±0.878
R2	18.81±0.564	33.91±0.420	45.24±0.497
R6	20.12±0.070	33.92±0.310	45.49±0.570
B2	22.89±0.061	37.01±0.362	51.28±0.210
B6	25.20±0.207	40.30±0.221	61.94±1.437

Figure 2-8 shows the sphericity of the powder particles with respect to their size for the starting Ti64 powder as well as the developed composite powders. In the regular mixing case shown in Figure 2-8 (a), the sphericity of the host powder particles is the same as the starting Ti64 particles (18-50 μm). This can be ascribed to the absence of plastic deformation in the regular mixing method as well as the limited attachment of the guest B_4C particles to the host ones (Figure 2-4). The non-attached B_4C particles existing in the R2 and R6 samples showed particle sizes in the range of 3-18 μm, representing the formation of agglomerated guest particles (Figure 2-4). The relatively low sphericity of these agglomerates originates from their irregular shape (Figure 2-3(c)). According to Figure 2-8(b), three different zones can be defined in the sphericity-particle size curves for the B2 and B6 samples. Zones (I), (II) and (III) refer to the particle sizes in the range of (5-18), (18-65) and (>65) μm for B2, and (10-25), (25-80) and (>80) μm for B6, respectively. Since the B2 and B6 samples are free from non-attached B_4C particles, Zone (I) signifies the fractured host powder particles showing lower sphericity than the starting Ti64 particles. In zone (II), the deformation and cold-welding as well as the decoration of the host particles by the guest ones lead to the decreased sphericity compared to the Ti64 powder. Since the short milling time of 2 h resulted in the limited cold-welding, the host

particles decoration and deformation are believed to be the dominant factors slightly decreasing the sphericity of the B2 sample. According to Figure 2-5(a), (b) and Figure 2-6(b), (c), most of the host powder particles preserved their spherical shape at short milling times. However, due to the embedment of the guest particles into the host ones in the B6 sample (absence of decoration), deformation and cold-welding of the host particles are responsible for the sphericities lower than the B2 sample. Zone (III) which is mostly visible in the B6 sample represents the cold-welded quasi-spherical/irregular shape powder particles (agglomerates) with sizes much larger than the starting Ti64 particles (Figure 2-5(e), (f) and Figure 2-6(d)-(f)). The sphericity of these agglomerates follows a decreasing trend by increasing their size.

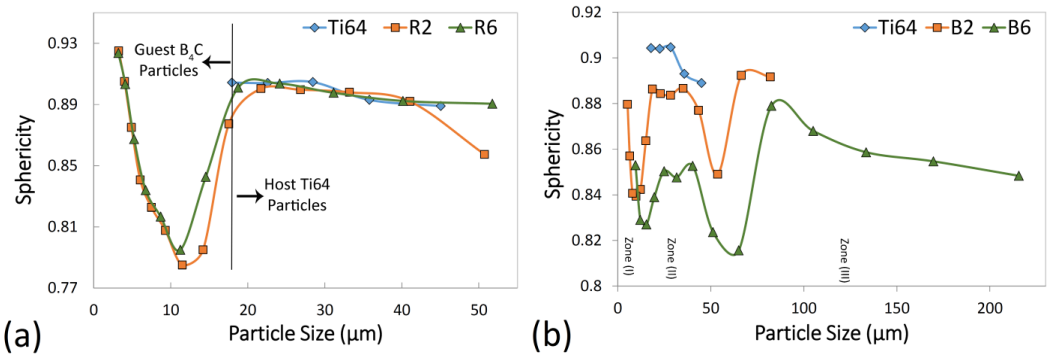

Figure 2-8 The sphericity of the particles as a function of their size for: (a) regularly mixed, and (b) ball milled 5 wt.% B_4C/Ti64 composite powder feedstocks. In each case, the sphericity of the starting Ti-6Al-4V (Ti64) powder is provided as the reference.

2.3.4 Flow behavior and conditioned bulk density (CBD)

2.3.4.1 Flowability

As can be observed in Figure 2-9(a) and (b), all of the developed composite powder systems showed lower flowability (higher BFE and SE) as compared to the host powder (Ti64). The flow response of the composite powders was found to be dependent on the blade

movement direction. In downward movement (BFE), the ball milled composite powders exhibited higher flow energy (lower flowability) compared to the regularly mixed composite systems (Figure 2-9(b)). However, considering the upward movement of the blade (SE), the ball milled powders showed better flowability (Figure 2-9(a)). The major difference between the BFE and SE is the confined flow of the powder in the former case due to the effect of the bottom of the vessel. Since the recoater interacts with powder in an unconfined state during the powder layer deposition process, the SE is a better representative of the powder flow in PBF-AM processes.

As the microstructural and sphericity characterizations revealed in Figure 2-5, Figure 2-6, and Figure 2-8, the plastic deformation induced with longer milling times led to some degrees of shape change for the host powder particles from spherical to quasi-spherical/moderately flattened. Besides, the surface roughness of the host particles increased. The surface roughening (not the shape change) of Ti64 particles in the ball milled composite powders subjected to relatively short mixing times (1-3 h) can be attributed mainly to the guest B_4C particles hitting their surface due to two reasons:

i. The guest B_4C powder particles are noticeably harder than the host Ti64 powder particles [22, 74-76]. Accordingly, the noticeably harder B_4C particles have a great potential to scratch, punch and roughen the surface of softer Ti64 particles. Since having the same hardness, the host-host inter-particle collisions might not affect the surface roughness of the host particles.

ii. As the microstructural observations of the starting powders revealed (Fig. 3), the guest B_4C particles have an irregular shape as opposed to the spherical shape of the host Ti64 particles. The collision of irregular-shaped B_4C particles with the

spherical-shape Ti64 particles has a higher chance to make the surface of Ti64 particles rough compared to the host-host collisions.

It is worth noting that the guest B_4C particles affect the surface roughness of the host Ti64 particles only if the extreme guest-host collisions are provided by the metallic balls (ball milling). As the microstructural characterizations revealed, the regular mixing did not affect the surface roughness of Ti64 particles even at relatively long mixing times such as 6 h (Fig. 4).

The increase in the SE (decreased flowability) in the B2 feedstock compared to the Ti64 reference sample may be attributed to the contribution of two different factors: (i) the change in the particle morphology [77], and (ii) the decoration of the host particles by the guest particles. The slight spherical to quasi-spherical shape change and the surface roughening of the host particles seem not to play major roles on the reduction of powder flowability of B2 sample. Therefore, the considerable increase in the SE for this system could be related to the presence of the decorating guest powder particles. Corresponding suggested mechanism is schematically illustrated in Figure 2-10. The guest-decorated host powder particles may experience two different interactions during their flow. While the "mechanical interlocking" mechanism decreases the flowability by resisting the free flow of the powder particles relative to each other (Figure 2-10(b)), the "contact surface reduction" mechanism may improve the flowability of the system [78] (Figure 2-10(c)). Compared to the non-decorated host powder system, the inter-particle tangling caused by the decorating guest particles leads to the enhanced flow resistivity. On the other hand, if not forming tangles, presence of the decorating guest particles lowers the contact surface area required for the movement of a guest-decorated host particle (particle 1) from position (I) to position (II) relative to another particle assumed to be fixed (particle 2) (as shown in

Figure 2-10(d)). By reducing the inter-particle friction and adhesion force, this mechanism can improve the flowability [78-80]. As mentioned earlier, although the slight change in the morphology of the host powder particles in the B2 case could have adverse effects on the flowability, these factors seem not to be predominant in the flowability reduction due to their negligible deviation from the starting host powder particles. Accordingly, the significant decrease in the flowability of the B2 powder system could be due to the dominance of the “mechanical interlocking” mechanism over the “contact surface reduction” mechanism. The contribution of the “mechanical interlocking” and the “contact surface reduction” mechanisms in the overall powder flowability is a major function of the guest particle size. When having nano-scale guest powder particles deposited on the surface of the primarily cohesive host powder particles, the artificially generated nano-scale roughness has been reported to enhance the flowability [79, 81-83]. Based on the mechanism provided in Figure 2-10, this could be attributed to the “contact surface reduction” combined with the lack of active "mechanical interlocking" sites in such composite powder systems, reducing the chance of particle entangling.

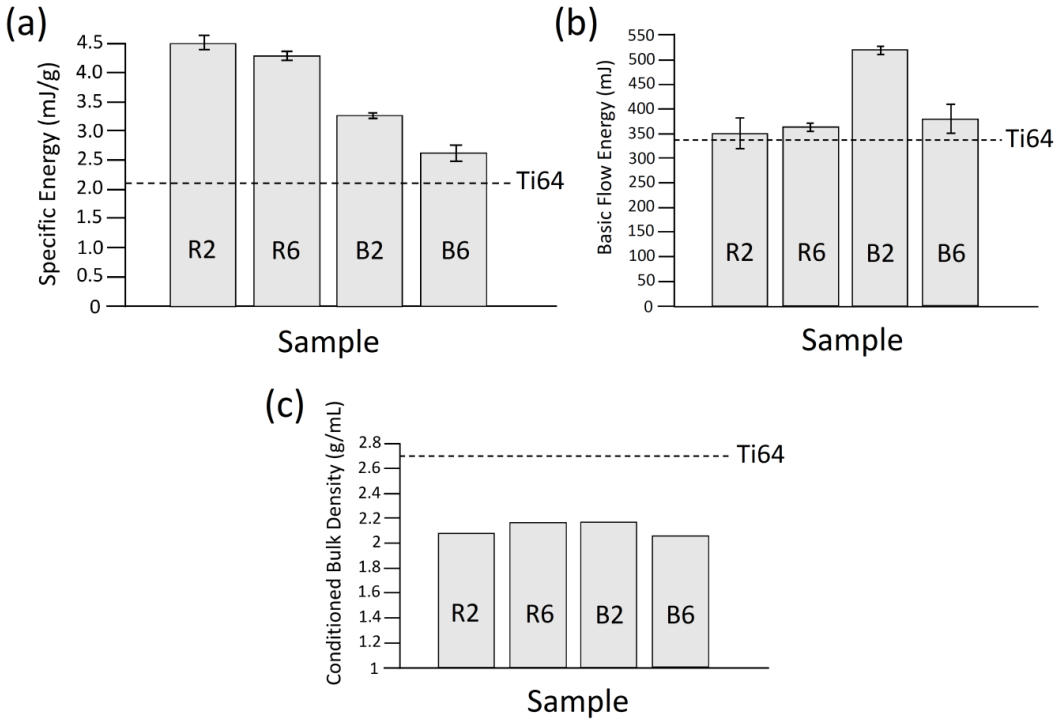

Figure 2-9 The flow behavior and conditioned bulk density results for 5wt.% B_4C/Ti-6Al-4V systems prepared by regular mixing and ball milling methods with different mixing times: (a) specific energy (SE), (b) basic flow energy (BFE), and (c) conditioned bulk density (CBD) of the composite powder systems compared to the reference powder (Ti64).

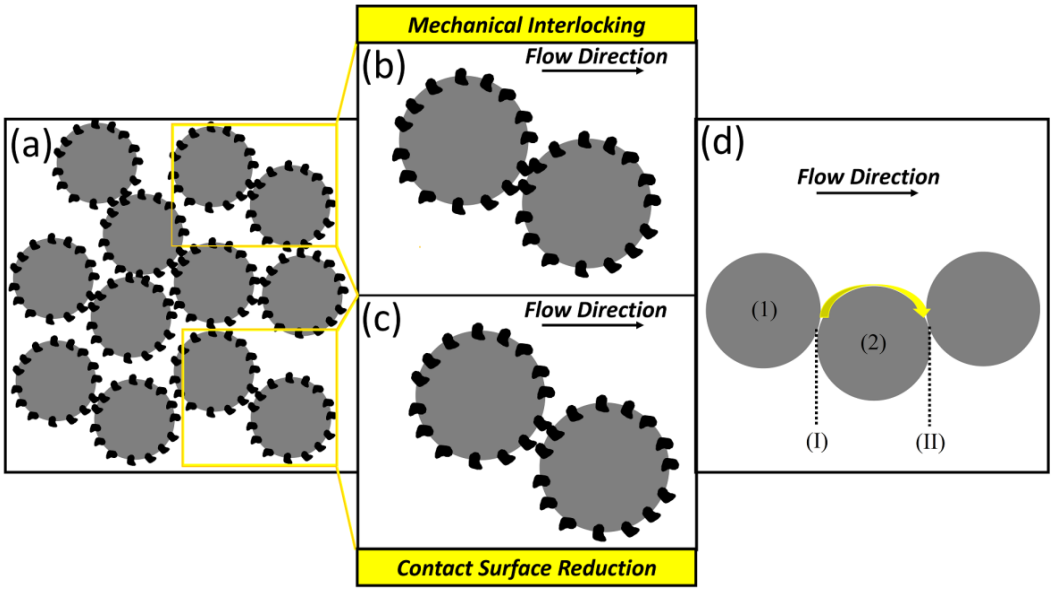

Figure 2-10 Schematic illustration presenting: (a) an overview of composite powder system with guest-decorated host particles; (b) and (c) close view of the selected regions showing "Mechanical Interlocking" and "Contact Surface Reduction" mechanisms, respectively; and (d) the contact area of two host powder particles when flowing relative to each other.

As indicated in Figure 2-9(a), the B6 sample showed lower SE (better flowability) than the B2 one. In order to describe this finding, the mechanisms influencing the flowability of B6 sample need to be explored. Referring to Figure 2-11, the flowability of the B6 powder feedstock is determined by the contribution of three mechanisms. Although the significant spherical to flattened/irregular shape change as well as the inter-locking of the guest-embedded host particles in such system act to decrease the flowability [84-86], the increased particle size caused by the dominancy of the cold-welding over the fracture mechanism may reduce the effective surface area of the powder particles and consequently favor higher flowability [86] (Figure 2-7(e) and Table 2). Therefore, the overall flow behavior of such composite powder system is governed by the competition among these mechanisms. The slight dominance of the inter-locking and shape change mechanisms over

the surface area reduction in the B6 system is believed to be the reason for the small increment in its SE compared to the Ti64 case (Figure 2-11).

Referring to Figure 2-9(a), the regularly mixed powder systems depicted SEs about twice that of the host particles. The observed phenomenon can be discussed based on the microstructural characterization of the powder systems. As shown in Figure 2-4 and Figure 2-8, the regularly mixed powder feedstocks had the guest particles almost non-attached to the completely spherical (non-deformed) host particles. Accordingly, neither the host particle shape change nor the decoration-induced tangling can be the reason behind the lower flowability of regularly mixed powders. However, the enhanced inter-particle friction caused by the presence of fine non-attached guest powder particles with extremely high surface-to-volume ratio can explain the drastic increase in the SE of these samples.

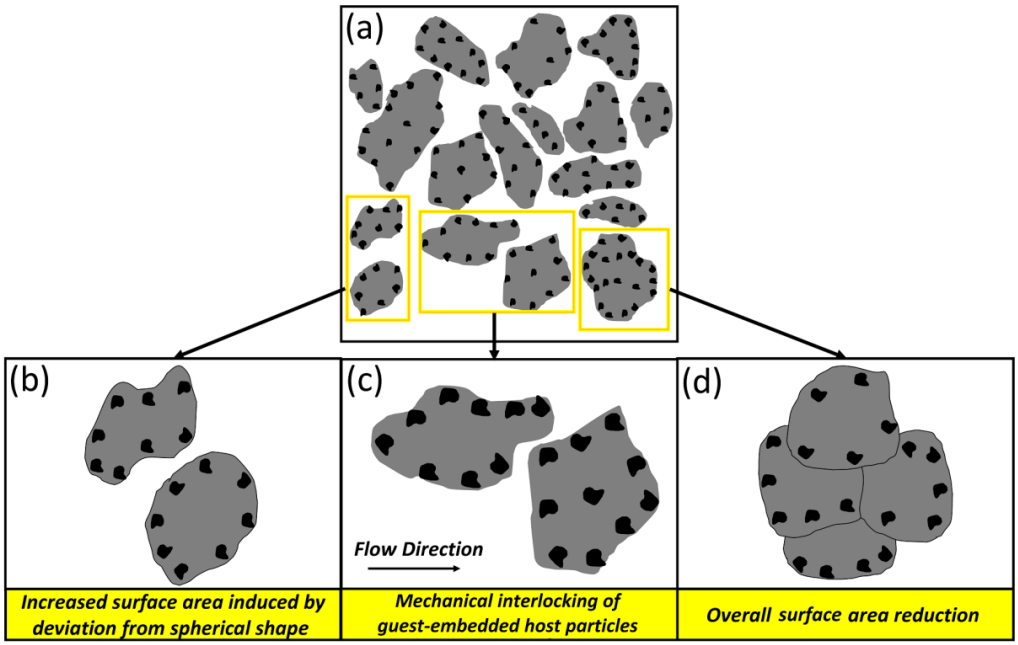

Figure 2-11 Schematic view presenting: (a) an overview of composite powder system with guest-embedded host particles; (b), (c) and (d) close view of the selected regions showing “Increased

Surface Area", "Host Particles Mechanical Interlocking" and "Surface Area Reduction" mechanisms, respectively.

2.3.4.2 Conditioned bulk density (CBD)

The packing density of the powder as the starting material in the PBF-AM processes has a significant influence on the quality of the parts produced. The density of the powders in this study was analyzed by their conditioned bulk density (CBD). Referring to Figure 2-9(c), regardless of the mixing method and time, incorporation of the guest powder particles to form composite powder feedstocks decreased the CBD compared to the starting host powder (Ti64). A portion of this decrease is due to the addition of less dense material (B_4C) to the Ti64 powder. Moreover, the increased inter-particle friction arising from the irregular shape of the B_4C particles combined with the large particle size distributions acts to reduce the packing density of the composite powder feedstocks compared to Ti64 powder [83, 87, 88]. In general, the higher random loose packing provided by the lower friction among the powder particles results in higher CBD. In the case of starting host powder particles, there is only the host/host inter-particle friction which determines the powder density. However, the introduction of the guest particles into the host powder leads to the emergence of new friction sources, namely, host/guest, and guest/guest inter-particle frictions which could be responsible for the lower CBD of the composite powders as compared to the Ti64 host powder.

Presence of free (non-attached) guest particles in the composite powder leads to the guest/host and guest/guest inter-particle frictions in addition to the host/host ones. According to Figure 2-9(c), the higher CBD of the R6 sample compared to the R2 one is due to the lower amounts of free B_4C particles existing in the system (Figure 2-4). Attachment of the guest to the host powder particles eliminates the host/guest inter-particle

friction which leads to the decrease in the host/host inter-particle friction by reducing their contact surface area. The morphology of powder particles has also a significant impact on the packing density of the powder bed and consequently the density of the final component [89, 90]. While the full decoration of the host particles by the guest particles in the B2 system promotes achieving higher CBD, the slight deviation of the host particles from spherical shape adversely influences the density (Figure 2-6(b), (c) and Figure 2-8(b)). Therefore, the same CBD as that of the R6 system was obtained for the B2 case. The significant morphological change of the host particles in the B6 sample could be the main reason behind its low CBD. The flattened/irregular shape of the powder particles in the B6 system renders a poor packing due to the elevated inter-particle friction [87]. It is also worth noting that the formation of agglomerated guest particles in the regularly mixed composite systems adversely affects their potential in occupying the host particles interstices.

2.3.5 Material Loss

The mechanical mixing processes involve some material loss due to the cold-welding of the powder particles to the balls and/or jar. Therefore, the amount of the starting and final powder needs to be quantified. Figure 2-12 presents the variation in the powder mass for both the regularly mixed and ball milled composite powders as a function of the mixing time. The material loss for both the regularly mixed and ball milled cases is negligible (<1%). However, the regular mixing resulted in lower material loss than the ball milling method due to the absence of balls.

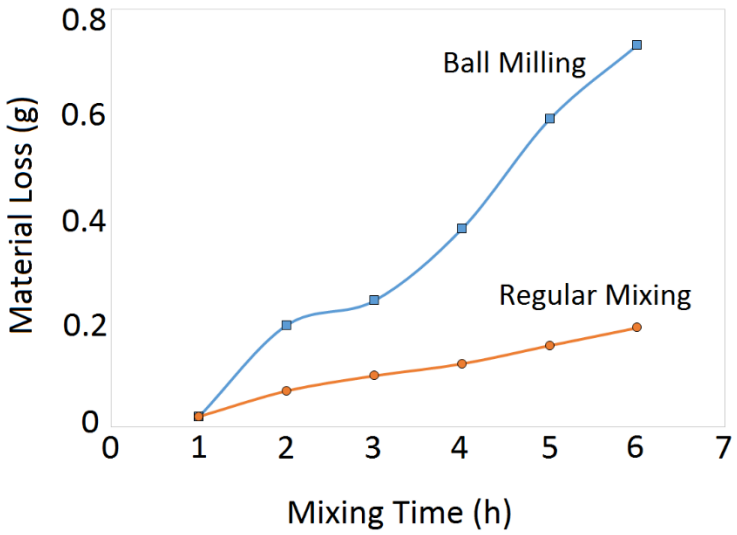

Figure 2-12 Material loss as a function of the mixing time for the regularly mixed and ball milled 5wt.% B_4C/Ti-6Al-4V composite powders. The starting powder mixture was 100 gr, and the ball-to-powder ratio was 5:1.

2.3.6 Selection of the best possible composite powder

The ideal mixed powder system for the PBF-AM processing of MMCs needs to have: (i) non-free guest powder particles which are uniformly and homogeneously distributed throughout the system, (ii) host powder particles preserving their desired spherical shape, and (iii) the same flow behavior and apparent packing density as the starting host powder constituent. Although preserving the spherical shape of the host particles, the inadequate guest-host attachment associated with the regular mixing results in heterogeneous final MMC parts with improper distribution of the guest particles (or in-situ formed phases) or even their agglomeration. In addition, the regularly mixed composite powders showed noticeably lower flowability compared to the ball milled composite systems. These issues restrict the implementation of the regularly mixed (R2 and R6) powder feedstocks in the PBF-AM of MMCs. Ball milling of the powders for relatively long milling times (B6) significantly improves the distribution state of the guest particles throughout the system by

their embedment into the host powder particles. However, the significant spherical to flattened/irregular shape change and the particle coarsening are the main drawbacks of such powder feedstocks (Figure 2-7, Figure 2-8, and Table 2). While the particle coarsening issue can be solved by sieving, this strategy may not be cost-and-time effective, especially for high-priced materials. When employing shorter milling times (2 h), the composite powder system showed almost spherical host particles fully decorated by the guest powder particles, meeting some of the requirements mentioned for the ideal composite powder feedstock (best possible case). Although such a powder ensures achieving homogenous MMC parts due to the proper host/guest attachment and the lack of non-attached (free) agglomerated guest particles, the decorating guest particles act as obstacles to the free flow of host particles and consequently sacrifice the flowability. Proper selection of the recoater speed in PBF-AM processes could be a strategy to solve this issue when using such composite powder feedstocks [91]. Based on the above discussions, the composite powder system prepared by relatively short milling time of 2 h (B2) is suggested as the best possible case for PBF-AM processes.

2.4 Conclusions

The characteristics of the 5 wt.% B_4C(guest)/Ti-6Al-4V(host) mixed powder systems were studied from powder bed fusion (PBF)- additive manufacturing (AM) perspective. For this purpose, the regular mixing and the ball milling methods were employed with a wide range of milling times (1-6 h) to produce composite powder feedstocks. The developed powders were examined using microstructural characterization, phase formation, particle size, size distribution, sphericity, apparent density, and flow behavior analyses. Moreover, the mechanisms playing role in the flowability of the mixed powder systems were analyzed

based on the microstructural observations and the flow measurement results. The main outcomes can be outlined as follows:

1. With the regular mixing, the shape of the host powder particles remained unchanged until 6 h of mixing. The ball milling method led to the change in the shape of host powder particles from spherical to quasi-spherical and then to flattened/irregular shape by increasing the milling time, resulting in the decreased particle sphericity compared to the starting host particles.

2. The regular mixing method did not provide acceptable attachment of the guest B_4C particles to the host particles. However, milling times as short as 2 h in the ball milling case provided the host particles with a full decoration by the guest particles. Longer milling time (6 h) led to the guest particles embedded in the severely deformed host particles.

3. Although the basic flow energy (BFE) results are in contradiction with specific energy (SE) measurements, the SE is believed to be a better representative of the powder layer deposition during PBF-AM process due to the unconfined and low-stress state of the powder.

4. Although being highly dependent on the mixing process variables, the flowability of the developed composite powders was lower than that of the reference Ti-6Al-4V powder. The regularly mixed and ball-milled composite powders exhibited ~110%, and 24–57% increase in SE compared to the Ti-6Al-4V powder, respectively.

5. The ball milled feedstocks showed lower SE (better flowability) than the regularly mixed powders. The flow behavior of developed composite feedstocks was discussed based on the underlying mechanisms.

6. The produced composite powder systems showed 18-24% decrease in density compared to the reference Ti-6Al-4V powder.

7. The composite powder benefitting from fully-decorated spherical-shape host particles is suggested as the best possible mechanically processed feedstock for PBF-AM processes. The relatively low flowability of this powder system should be considered when defining the recoater speed in PBF-AM processes.

Acknowledgements: The authors would like to thank Henry Ma and Allan Rogalsky from the MSAM (Multi-scale Additive Manufacturing) Laboratory at the University of Waterloo for the flowability and particle size measurement tests.

2.5 References

[1] M. Dadkhah, A. Saboori, P. Fino, An Overview of the Recent Developments in Metal Matrix Nanocomposites Reinforced by Graphene, Materials 12(17) (2019) 2823.

[2] S.Q. Wu, H.Z. Wang, S.C. Tjong, Mechanical and wear behavior of an Al/Si alloy metal-matrix composite reinforced with aluminosilicate fiber, Composites Science and Technology 56(11) (1996) 1261-1270.

[3] S.C. Tjong, Recent progress in the development and properties of novel metal matrix nanocomposites reinforced with carbon nanotubes and graphene nanosheets, Materials Science and Engineering: R: Reports 74(10) (2013) 281-350.

[4] J. Zhang, R.J. Perez, C.R. Wong, E.J. Lavernia, Effects of secondary phases on the damping behaviour of metals, alloys and metal matrix composites, Materials Science and Engineering: R: Reports 13(8) (1994) 325-389.

[5] L. Liu, W. Li, Y. Tang, B. Shen, W. Hu, Friction and wear properties of short carbon fiber reinforced aluminum matrix composites, Wear 266(7) (2009) 733-738.

[6] H. Dieringa, Properties of magnesium alloys reinforced with nanoparticles and carbon nanotubes: a review, Journal of Materials Science 46(2) (2011) 289-306.

[7] Y. Liu, J. Ding, W. Qu, Y. Su, Z. Yu, Microstructure evolution of TiC particles In situ, synthesized by laser cladding, Materials 10(3) (2017) 281.

[8] D. Miracle, Metal matrix composites–from science to technological significance, Composites science and technology 65(15-16) (2005) 2526-2540.

[9] G. Geandier, L. Vautrot, B. Denand, S. Denis, In Situ Stress Tensor Determination during Phase Transformation of a Metal Matrix Composite by High-Energy X-ray Diffraction, Materials 11(8) (2018) 1415.

[10] A.I. Mertens, J. Lecomte-Beckers, On the Role of Interfacial Reactions, Dissolution and Secondary Precipitation During the Laser Additive Manufacturing of Metal Matrix Composites: A Review, in: I.V. Shishkovsky (Ed.), New Trends in 3D Printing, InTech, Rijeka, 2016, p. Ch. 09.

[11] K.U. Kainer, Basics of Metal Matrix Composites, Metal Matrix Composites, Wiley-VCH Verlag GmbH & Co. KGaA2006, pp. 1-54.

[12] S. Suresh, Fundamentals of metal-matrix composites, Elsevier2013.

[13] M. Rosso, Ceramic and metal matrix composites: Routes and properties, Journal of Materials Processing Technology 175(1-3) (2006) 364-375.

[14] J. Wang, X. Guo, J. Qin, D. Zhang, W. Lu, Microstructure and mechanical properties of investment casted titanium matrix composites with B4C additions, Materials Science and Engineering: A 628 (2015) 366-373.

[15] E. Fereiduni, M. Elbestawi, Process-structure-property relationships in additively manufactured metal matrix composites, Additive Manufacturing of Emerging Materials, Springer2019, pp. 111-177.

[16] E. Fereiduni, M. Yakout, M. Elbestawi, Laser-based additive manufacturing of lightweight metal matrix composites, Additive Manufacturing of Emerging Materials, Springer2019, pp. 55-109.

[17] A.T. Sutton, C.S. Kriewall, M.C. Leu, J.W. Newkirk, Powder characterisation techniques and effects of powder characteristics on part properties in powder-bed fusion processes, Virtual and Physical Prototyping 12(1) (2017) 3-29.

[18] U. Ali, Y. Mahmoodkhani, S.I. Shahabad, R. Esmaeilizadeh, F. Liravi, E. Sheydaeian, K.Y. Huang, E. Marzbanrad, M. Vlasea, E. Toyserkani, On the measurement of relative powder-bed compaction density in powder-bed additive manufacturing processes, Materials & Design 155 (2018) 495-501.

[19] A. Rausch, V. Küng, C. Pobel, M. Markl, C. Körner, Predictive simulation of process windows for powder bed fusion additive manufacturing: influence of the powder bulk density, Materials 10(10) (2017) 1117.

[20] G. Jacob, A. Donmez, J. Slotwinski, S. Moylan, Measurement of powder bed density in powder bed fusion additive manufacturing processes, Measurement Science and Technology 27(11) (2016) 115601.

[21] M. Narvan, K.S. Al-Rubaie, M. Elbestawi, Process-structure-property relationships of AISI H13 tool steel processed with selective laser melting, Materials 12(14) (2019) 2284.

[22] E. Fereiduni, A. Ghasemi, M. Elbestawi, Selective laser melting of hybrid ex-situ/in-situ reinforced titanium matrix composites: Laser/powder interaction, reinforcement formation mechanism, and non-equilibrium microstructural evolutions, Materials & Design 184 (2019) 108185.

[23] F. Calignano, P. Minetola, Influence of Process Parameters on the Porosity, Accuracy, Roughness, and Support Structures of Hastelloy X Produced by Laser Powder Bed Fusion, Materials 12(19) (2019) 3178.

[24] E. Mirkoohi, D.E. Seivers, H. Garmestani, S.Y. Liang, Heat Source Modeling in Selective Laser Melting, Materials 12(13) (2019) 2052.

[25] E. Neubauer, M. Kitzmantel, M. Hulman, P. Angerer, Potential and challenges of metal-matrix-composites reinforced with carbon nanofibers and carbon nanotubes, Composites Science and Technology 70(16) (2010) 2228-2236.

[26] S.R. Bakshi, D. Lahiri, A. Agarwal, Carbon nanotube reinforced metal matrix composites-a review, International materials reviews 55(1) (2010) 41-64.

[27] T.A. Campbell, O.S. Ivanova, 3D printing of multifunctional nanocomposites, Nano Today 8(2) (2013) 119-120.

[28] X. Zhao, B. Song, W. Fan, Y. Zhang, Y. Shi, Selective laser melting of carbon/AlSi10Mg composites: microstructure, mechanical and electronical properties, Journal of Alloys and Compounds 665 (2016) 271-281.

[29] W. Yu, S. Sing, C. Chua, C. Kuo, X. Tian, Particle-Reinforced Metal Matrix Nanocomposites Fabricated by Selective Laser Melting: A State of the Art Review, Progress in Materials Science (2019).

[30] B. Song, S. Dong, C. Coddet, Rapid in situ fabrication of Fe/SiC bulk nanocomposites by selective laser melting directly from a mixed powder of microsized Fe and SiC, Scripta Materialia 75 (2014) 90-93.

[31] L. Hao, S. Dadbakhsh, O. Seaman, M. Felstead, Selective laser melting of a stainless steel and hydroxyapatite composite for load-bearing implant development, Journal of Materials Processing Technology 209(17) (2009) 5793-5801.

[32] D.E. Cooper, N. Blundell, S. Maggs, G.J. Gibbons, Additive layer manufacture of Inconel 625 metal matrix composites, reinforcement material evaluation, Journal of Materials Processing Technology 213(12) (2013) 2191-2200.

[33] D. Gu, H. Wang, D. Dai, F. Chang, W. Meiners, Y.-C. Hagedorn, K. Wissenbach, I. Kelbassa, R. Poprawe, Densification behavior, microstructure evolution, and wear property of TiC nanoparticle reinforced AlSi10Mg bulk-form nanocomposites prepared by selective laser melting, Journal of Laser Applications 27(S1) (2015) S17003.

[34] D. Gu, H. Wang, D. Dai, Laser additive manufacturing of novel aluminum based nanocomposite parts: tailored forming of multiple materials, Journal of Manufacturing Science and Engineering 138(2) (2016) 021004.

[35] Y. Hu, W. Cong, X. Wang, Y. Li, F. Ning, H. Wang, Laser deposition-additive manufacturing of TiB-Ti composites with novel three-dimensional quasi-continuous network microstructure: effects on strengthening and toughening, Composites Part B: Engineering 133 (2018) 91-100.

[36] H. Attar, M. Bönisch, M. Calin, L.-C. Zhang, S. Scudino, J. Eckert, Selective laser melting of in situ titanium–titanium boride composites: processing, microstructure and mechanical properties, Acta Materialia 76 (2014) 13-22.

[37] B. AlMangour, D. Grzesiak, Selective laser melting of TiC reinforced 316L stainless steel matrix nanocomposites: Influence of starting TiC particle size and volume content, Materials & Design 104 (2016) 141-151.

[38] B. AlMangour, D. Grzesiak, J.-M. Yang, Selective laser melting of TiB 2/H13 steel nanocomposites: Influence of hot isostatic pressing post-treatment, Journal of Materials Processing Technology 244 (2017) 344-353.

[39] B. Zhang, G. Bi, P. Wang, J. Bai, Y. Chew, M.S. Nai, Microstructure and mechanical properties of Inconel 625/nano-TiB 2 composite fabricated by LAAM, Materials & Design 111 (2016) 70-79.

[40] X. Li, G. Ji, Z. Chen, A. Addad, Y. Wu, H. Wang, J. Vleugels, J. Van Humbeeck, J.-P. Kruth, Selective laser melting of nano-TiB 2 decorated AlSi10Mg alloy with high fracture strength and ductility, Acta Materialia 129 (2017) 183-193.

[41] M. Chen, X. Li, G. Ji, Y. Wu, Z. Chen, W. Baekelant, K. Vanmeensel, H. Wang, J.-P. Kruth, Novel composite powders with uniform TiB2 nano-particle distribution for 3D printing, Applied Sciences 7(3) (2017) 250.

[42] W. Zhou, X. Sun, K. Kikuchi, N. Nomura, K. Yoshimi, A. Kawasaki, Carbon nanotubes as a unique agent to fabricate nanoceramic/metal composite powders for additive manufacturing, Materials & Design 137 (2018) 276-285.

[43] H. Tan, D. Hao, K. Al-Hamdani, F. Zhang, Z. Xu, A.T. Clare, Direct metal deposition of TiB 2/AlSi10Mg composites using satellited powders, Materials Letters 214 (2018) 123-126.

[44] C. Ma, L. Chen, C. Cao, X. Li, Nanoparticle-induced unusual melting and solidification behaviours of metals, Nature communications 8 (2017) 14178.

[45] J.H. Martin, B.D. Yahata, J.M. Hundley, J.A. Mayer, T.A. Schaedler, T.M. Pollock, 3D printing of high-strength aluminium alloys, Nature 549(7672) (2017) 365.

[46] M. Xia, A. Liu, Z. Hou, N. Li, Z. Chen, H. Ding, Microstructure growth behavior and its evolution mechanism during laser additive manufacture of in-situ reinforced (TiB+ TiC)/Ti composite, Journal of Alloys and Compounds 728 (2017) 436-444.

[47] D. Gu, P. Yuan, Thermal evolution behavior and fluid dynamics during laser additive manufacturing of Al-based nanocomposites: Underlying role of reinforcement weight fraction, Journal of Applied Physics 118(23) (2015) 233109.

[48] J. Ning, D.E. Sievers, H. Garmestani, S.Y. Liang, Analytical Modeling of In-Process Temperature in Powder Bed Additive Manufacturing Considering Laser Power Absorption, Latent Heat, Scanning Strategy, and Powder Packing, Materials 12(5) (2019) 808.

[49] A.J. Pinkerton, L. Li, Direct additive laser manufacturing using gas-and water-atomised H13 tool steel powders, The International Journal of Advanced Manufacturing Technology 25(5-6) (2005) 471-479.

[50] T. DebRoy, H. Wei, J. Zuback, T. Mukherjee, J. Elmer, J. Milewski, A.M. Beese, A. Wilson-Heid, A. De, W. Zhang, Additive manufacturing of metallic components–process, structure and properties, Progress in Materials Science 92 (2018) 112-224.

[51] J. Muñiz-Lerma, A. Nommeots-Nomm, K. Waters, M. Brochu, A Comprehensive Approach to Powder Feedstock Characterization for Powder Bed Fusion Additive Manufacturing: A Case Study on AlSi7Mg, Materials 11(12) (2018) 2386.

[52] Y. Mahmoodkhani, U. Ali, S. Imani Shahabad, A. Rani Kasinathan, R. Esmaeilizadeh, A. Keshavarzkermani, E. Marzbanrad, E. Toyserkani, On the measurement of effective powder layer thickness in laser powder-bed fusion additive manufacturing of metals, Progress in Additive Manufacturing 4(2) (2019) 109-116.

[53] P. Wang, C. Gammer, F. Brenne, T. Niendorf, J. Eckert, S. Scudino, A heat treatable TiB2/Al-3.5 Cu-1.5 Mg-1Si composite fabricated by selective laser melting: Microstructure, heat treatment and mechanical properties, Composites Part B: Engineering 147 (2018) 162-168.

[54] B. AlMangour, D. Grzesiak, T. Borkar, J.-M. Yang, Densification behavior, microstructural evolution, and mechanical properties of TiC/316L stainless steel nanocomposites fabricated by selective laser melting, Materials & Design 138 (2018) 119-128.

[55] L. Xi, P. Wang, K. Prashanth, H. Li, H. Prykhodko, S. Scudino, I. Kaban, Effect of TiB2 particles on microstructure and crystallographic texture of Al-12Si fabricated by selective laser melting, Journal of Alloys and Compounds 786 (2019) 551-556.

[56] B. AlMangour, Y.-K. Kim, D. Grzesiak, K.-A. Lee, Novel TiB2-reinforced 316L stainless steel nanocomposites with excellent room-and high-temperature yield strength developed by additive manufacturing, Composites Part B: Engineering 156 (2019) 51-63.

[57] L. Takacs, J.S. McHenry, Temperature of the milling balls in shaker and planetary mills, Journal of Materials Science 41(16) (2006) 5246-5249.

[58] H. Retsch Camsizer X2 (Retsch Technology GmbH, Germany), November 2019. https://www.retsch-technology.com/products/dynamic-image-analysis/camsizer-x2/function-features/.

[59] I. ISO, 9276-6 Representation of Results of Particle Size Analysis—Part 6: Descriptive and Quantitative Representation of Particle Shape and Morphology, ISO Geneva:, 2008.

[60] A.B. Spierings, M. Voegtlin, T. Bauer, K. Wegener, Powder flowability characterisation methodology for powder-bed-based metal additive manufacturing, Progress in Additive Manufacturing 1(1-2) (2016) 9-20.

[61] M. Krantz, H. Zhang, J. Zhu, Characterization of powder flow: Static and dynamic testing, Powder Technology 194(3) (2009) 239-245.

[62] Z. Snow, R. Martukanitz, S. Joshi, On the development of powder spreadability metrics and feedstock requirements for powder bed fusion additive manufacturing, Additive Manufacturing 28 (2019) 78-86.

[63] R. Freeman, Measuring the flow properties of consolidated, conditioned and aerated powders—a comparative study using a powder rheometer and a rotational shear cell, Powder Technology 174(1-2) (2007) 25-33.

[64] D. Jeyasimman, S. Sivasankaran, K. Sivaprasad, R. Narayanasamy, R. Kambali, An investigation of the synthesis, consolidation and mechanical behaviour of Al 6061 nanocomposites reinforced by TiC via mechanical alloying, Materials & Design 57 (2014) 394-404.

[65] N. Zhao, P. Nash, X. Yang, The effect of mechanical alloying on SiC distribution and the properties of 6061 aluminum composite, Journal of Materials Processing Technology 170(3) (2005) 586-592.

[66] G. Williamson, W. Hall, X-ray line broadening from filed aluminium and wolfram, Acta metallurgica 1(1) (1953) 22-31.

[67] S. Özbilen, Satellite formation mechanism in gas atomised powders, Powder metallurgy 42(1) (1999) 70-78.

[68] B. Song, S. Dong, P. Coddet, G. Zhou, S. Ouyang, H. Liao, C. Coddet, Microstructure and tensile behavior of hybrid nano-micro SiC reinforced iron matrix composites produced by selective laser melting, Journal of Alloys and Compounds 579 (2013) 415-421.

[69] Q. Wei, S. Li, C. Han, W. Li, L. Cheng, L. Hao, Y. Shi, Selective laser melting of stainless-steel/nano-hydroxyapatite composites for medical applications: Microstructure, element distribution, crack and mechanical properties, Journal of Materials Processing Technology 222 (2015) 444-453.

[70] M. Lorusso, A. Aversa, D. Manfredi, F. Calignano, E.P. Ambrosio, D. Ugues, M. Pavese, Tribological behavior of aluminum alloy AlSi10Mg-TiB 2 composites produced by direct metal laser sintering (DMLS), Journal of Materials Engineering and Performance 25(8) (2016) 3152-3160.

[71] C. Suryanarayana, Mechanical alloying and milling, Progress in materials science 46(1) (2001) 1-184.

[72] B. Prabhu, C. Suryanarayana, L. An, R. Vaidyanathan, Synthesis and characterization of high volume fraction Al–Al2O3 nanocomposite powders by high-energy milling, Materials Science and Engineering: A 425(1-2) (2006) 192-200.

[73] D. Zhang, Processing of advanced materials using high-energy mechanical milling, Progress in Materials Science 49(3-4) (2004) 537-560.

[74] V. Mukhanov, O. Kurakevych, V. Solozhenko, Thermodynamic model of hardness: Particular case of boron-rich solids, Journal of Superhard Materials 32(3) (2010) 167-176.

[75] W. Ji, S.S. Rehman, W. Wang, H. Wang, Y. Wang, J. Zhang, F. Zhang, Z. Fu, Sintering boron carbide ceramics without grain growth by plastic deformation as the dominant densification mechanism, Scientific reports 5 (2015) 15827.

[76] X. Zeng, W. Liu, Aqueous tape casting of B4C ceramics, Advances in Applied Ceramics 115(4) (2016) 224-228.

[77] M. Ghadiri, M. Pasha, W. Nan, C. Hare, V. Vivacqua, U. Zafar, S. Nezamabadi, A. Lopez, M. Pasha, S. Nadimi, Cohesive Powder Flow: Trends and Challenges in Characterisation and Analysis, KONA Powder and Particle Journal (2020) 2020018.

[78] L.J. Jallo, Y. Chen, J. Bowen, F. Etzler, R. Dave, Prediction of inter-particle adhesion force from surface energy and surface roughness, Journal of Adhesion Science and Technology 25(4-5) (2011) 367-384.

[79] J. Yang, A. Sliva, A. Banerjee, R.N. Dave, R. Pfeffer, Dry particle coating for improving the flowability of cohesive powders, Powder Technology 158(1-3) (2005) 21-33.

[80] H.-Y. Xie, The role of interparticle forces in the fluidization of fine particles, Powder Technology 94(2) (1997) 99-108.

[81] M. Ramlakhan, C.Y. Wu, S. Watano, R.N. Dave, R. Pfeffer, Dry particle coating using magnetically assisted impaction coating: modification of surface properties and optimization of system and operating parameters, Powder Technology 112(1-2) (2000) 137-148.

[82] R. Mei, H. Shang, J.F. Klausner, E. Kallman, A contact model for the effect of particle coating on improving the flowability of cohesive powders, KONA Powder and Particle Journal 15 (1997) 132-141.

[83] S. Sivasankaran, K. Sivaprasad, R. Narayanasamy, V.K. Iyer, An investigation on flowability and compressibility of AA 6061100− xx wt.% TiO2 micro and nanocomposite powder prepared by blending and mechanical alloying, Powder technology 201(1) (2010) 70-82.

[84] G. Lumay, F. Boschini, K. Traina, S. Bontempi, J.-C. Remy, R. Cloots, N. Vandewalle, Measuring the flowing properties of powders and grains, Powder technology 224 (2012) 19-27.

[85] S. Ziegelmeier, P. Christou, F. Wöllecke, C. Tuck, R. Goodridge, R. Hague, E. Krampe, E. Wintermantel, An experimental study into the effects of bulk and flow behaviour of laser sintering polymer powders on resulting part properties, Journal of Materials Processing Technology 215 (2015) 239-250.

[86] X. Fu, D. Huck, L. Makein, B. Armstrong, U. Willen, T. Freeman, Effect of particle shape and size on flow properties of lactose powders, Particuology 10(2) (2012) 203-208.

[87] R.U. Din, Q.A. Shafqat, Z. Asghar, G. Zahid, A. Basit, A. Qureshi, T. Manzoor, M.A. Nasir, F. Mehmood, K.I. Hussain, Microstructural Evolution, Powder Characteristics, Compaction Behavior and Sinterability of Al 6061–B 4 C Composites as a Function of Reinforcement Content and Milling Times, Russian Journal of Non-Ferrous Metals 59(2) (2018) 207-222.

[88] J.B. Fogagnolo, F. Velasco, M.H. Robert, J.M. Torralba, Effect of mechanical alloying on the morphology, microstructure and properties of aluminium matrix composite powders, Materials Science and Engineering: A 342(1) (2003) 131-143.

[89] I. Gibson, D.W. Rosen, B. Stucker, Additive manufacturing technologies, Springer2014.

[90] D. Manfredi, F. Calignano, M. Krishnan, R. Canali, E. Ambrosio, E. Atzeni, From powders to dense metal parts: Characterization of a commercial AlSiMg alloy processed through direct metal laser sintering, Materials 6(3) (2013) 856-869.

[91] H. Azizi, R. Ghiaasiaan, R. Prager, M.H. Ghoncheh, K.A. Samk, A. Lausic, W. Byleveld, A.B. Phillion, Metallurgical and mechanical assessment of hybrid additively-manufactured maraging tool steels via selective laser melting, Additive Manufacturing 27 (2019) 389-397.

Chapter 3 Selective laser melting of hybrid ex-situ/in-situ reinforced titanium matrix composites: Laser/powder interaction, reinforcement formation mechanism, and non-equilibrium microstructural evolutions

Complete Citation:

Fereiduni E, Ghasemi A, Elbestawi M. Selective laser melting of hybrid ex-situ/in-situ reinforced titanium matrix composites: Laser/powder interaction, reinforcement formation mechanism, and non-equilibrium microstructural evolutions. Materials & Design. 2019 Dec 15; 184: 108185.

Abstract

Hybrid ex-situ/in-situ reinforced titanium matrix composites (TMCs) were fabricated by selective laser melting (SLM). The optimized pre-processed 5wt.% B_4C/Ti-6Al-4V composite powder feedstock and the un-reinforced Ti-6Al-4V powder were consolidated using energy densities in the range of 50-75 J/mm^3. Despite the full melting of the powder particles in the monolithic Ti-6Al-4V system, complete melting of the host Ti-6Al-4V constituent in the composite case took place by energy densities exceeding 62.5 J/mm^3. Presence of the guest B_4C particles surrounding the un-melted/partially melted host particles gave evidence of the non-efficient guest-to-host heat transfer. In-situ formation of (TiB+TiC) reinforcements was discussed based on a mechanism proposing dissolution rather than melting of the guest particles. The degree of dissolution was a significant function of the energy density and the guest particle size. Microstructural evolutions during SLM of 5wt.% B_4C/Ti64 composite were studied, and the non-equilibrium solidification sequence was suggested based on the microstructural observations and the equilibrium solidification path. High cooling rates during SLM inhibited some of the liquid and solid-state transformations in the TMCs. This was confirmed by microstructural observations of the arc-melted parts fabricated by the same composite feedstock. The SLM processed TMCs showed 30-80% enhancement in microhardness compared to the unreinforced Ti64.

Keywords: Selective laser melting (SLM); Metal matrix composite (MMC); Ti-6Al-4V; In-situ and ex-situ reinforcement; Solidification path

3.1 Introduction

Owing to their high specific strength, adequate stiffness, appropriate high-temperature stability and resistance, good fatigue behavior as well as outstanding corrosion resistance, titanium (Ti) and its alloys are widely used in various industries including chemical, aeronautical and advanced military [1-7]. While having many advantages, the limited wear resistance of Ti alloys is a major concern limiting their utilization in applications demanding high abrasion and erosion resistance [8]. Incorporation of reinforcements (e.g., oxides, intermetallic compounds, nitrides, carbides, and borides) into the metallic matrix leads to the fabrication of outstanding materials known as metal matrix composites (MMCs), which bilaterally benefit from the properties of the reinforcement(s) and the matrix [9, 10]. MMC fabrication is one of the most effective strategies to enhance mechanical properties such as hardness, strength, fatigue life, and wear resistance [11-15].

Because of benefiting from high strength and elastic modulus, excellent thermal and chemical stability as well as close density and coefficient of thermal expansion (CTE) to that of Ti and its alloys, TiB and TiC are known as the most suitable reinforcements for the Ti alloy matrices [16-18]. The extremely low solubility of B and C elements in both α and β phases of the Ti alloy is the other issue introducing TiB and TiC as outstanding reinforcements for these alloys [19]. While the addition of noticeably hard particulate-shape TiC reinforcement enhances the hardness and strength of the fabricated TMCs, the load-bearing capacity and high thermodynamic stability associated with the whisker-shape TiB reinforcement are believed to improve the ductility, strength and creep resistance [20]. Therefore, synergistic effects of both TiB and TiC phases acting as reinforcements for the matrix result in TMC structures with excellent mechanical properties meeting the requirements of various applications [20, 21].

TMCs could have reinforcements incorporated into the matrix in an ex-situ manner or synthesized through in-situ reactions during the composite fabrication process. Moreover, careful control of the chemical reactions in the in-situ reinforced TMCs enables manufacturing of composites benefitting from both ex-situ and in-situ reinforcements, known as hybrid ex-situ/in-situ reinforced TMCs [22, 23]. Compared to the ex-situ reinforced TMCs having the primarily added reinforcing particles as the reinforcement in the final structure, the chemical reactions induced in the in-situ case results in the formation of reinforcements with higher thermodynamic stability within the metallic matrix. Accordingly, stronger reinforcement/matrix interfaces which are free of contamination could be achieved in hybrid and in-situ reinforced TMCs [20, 22, 23]. Therefore, the formation of TiB/TiC reinforcements through the in-situ reaction between the B_4C precursor and Ti alloys is more desired than the ex-situ incorporation of the same reinforcing particles into the system.

Selective laser melting (SLM) is a powder bed fusion (PBF)-AM process which uses a high-intensity laser beam as the energy source to completely melt selected areas of a powder bed [24, 25]. This process is performed within an enclosed chamber that is backfilled with an inert gas such as nitrogen or argon to lower the oxygen level. Once an adequate operating atmosphere is achieved, the first layer of the powder is deposited over the building platform by the recoating unit. The laser beam then scans the pattern defined for that layer based on the CAD model, inducing melting and fusion of the powder particles. Subsequently, the building platform is lowered for an amount which corresponds to the layer thickness, and a new layer of powder is deposited over the previous one. This new layer is then subjected to the laser beam, leading to the melting of powder particles in defined regions of that layer and their fusion to the previously deposited one. This trend is

replicated until the entire component is built [26-28]. The unique characteristics associated with SLM technology have recently opened a new window to fabricate geometrically complex-shaped, custom-designed, and cost-effective TMC parts with the desired functional and mechanical properties [29, 30]. On the other hand, the extremely localized melt pool and the significantly high cooling rates associated with this process has provided the opportunity to mitigate some of the drawbacks involved in conventional manufacturing of TMCs including segregation/agglomeration of reinforcing particles and coarse microstructure [23].

The present research study employs SLM to fabricate TMCs reinforced by TiB/TiC phases by processing 5wt.% B_4C/Ti-6Al-4V (Ti64) powder feedstock having spherical/quasi-spherical host Ti64 particles fully decorated by the guest B_4C particles produced through the ball-milling process. The laser energy densities applied in this study were selected based on the optimum conditions reported in the literature for SLM of Ti64 alloy (the host constituent in the studied TMC) [31-34]. The interaction of the laser beam with the composite powder feedstock was discussed, and the existing mechanisms were identified. Microstructural evolutions were thoroughly analyzed by exploring the guest/host interaction mechanism, following the solidification path, and comparing the microstructures of the SLM fabricated TMCs with those subjected to the arc melting process. Characterizing the nature of the in-situ reaction products formed during SLM through solidification path is of vital importance since the mechanical properties of the SLMed composite parts are directly dictated by the features of the in-situ formed reinforcements. The lessons learned from the solidification sequence can pave the way to manipulate the microstructure to tailor the mechanical properties. On the other hand, enhancing the robustness of the additively manufactured parts via application of a proper

post heat treatment process requires a deep understanding of the microstructural evolutions during SLM which can be enabled by detailed microstructural studies. The level of improvement in mechanical properties was investigated utilizing the microhardness test, and the results were compared with monolithic Ti64 samples SLMed with the same process parameters.

3.2 Materials and Experimental Procedure

3.2.1 Powder Preparation

Figure 3-1 shows the micrographs of the starting Ti64 and B_4C powders used as starting materials in this research study. The Ti64 powder particles are spherical with a smooth surface, which is the characteristic of the gas atomized Ti alloy powder particles. On the other hand, the B_4C powder particles exhibit an irregular shape. The Ti64 and B_4C powders have been named as “host” and “guest” throughout the paper, respectively.

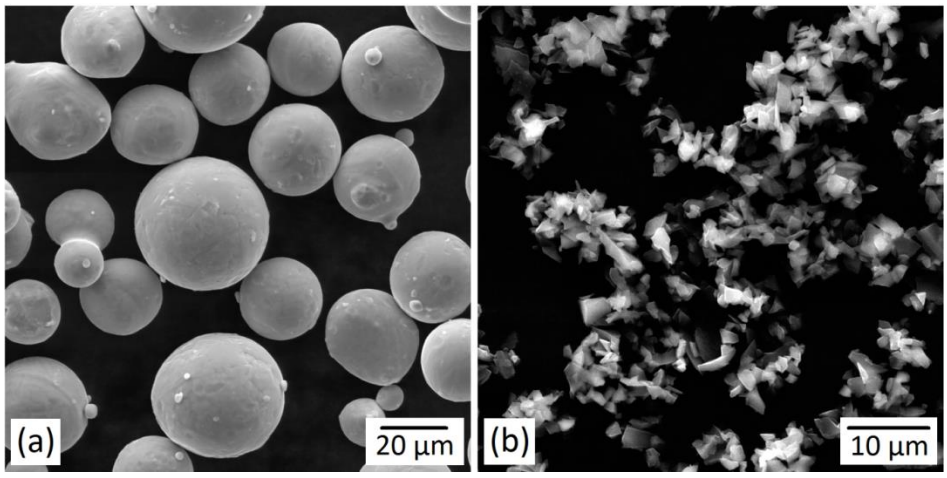

Figure 3-1 SEM micrographs of the starting: (a) Ti-6Al-4V (Ti64) and (b) B4C powder particles.

In order to prepare the TMC powder feedstock, the regular mixing and the ball milling processes as the mechanical methods of MMC powder preparation were used. The mixed powder system contained 5 wt.% B_4C, and the mixing process was performed by a high-

performance planetary Pulverisette 6 ball milling machine at a fixed rotational speed of 200 rpm under the protection of argon atmosphere to avoid oxidation. In the regular mixing case, the powders were mixed without balls. However, stainless steel balls with a diameter of 10 mm were added to the system in the ball milling method. The ball-to-powder ratio was 5:1, and every 30 min. of milling was followed by a 15 min pause to avoid temperature rise. To select the best possible composite powder system, the level of guest/host attachment and the sphericity of the host powder particles were taken into consideration. The guest/host attachment is required in SLM for the following two reasons:

(i) Due to the significant difference between the densities of the two constituents (4.43 g/cm^3 for Ti64 [35] compared to 2.52 g/cm^3 for B_4C [36]), their separation and non-uniform distribution may take place during the powder spreading process.

(ii) The relatively high van der Waals attraction force between the B_4C particles favors their clustering and agglomeration in the non-attached case, leading to the non-homogenous distribution state of the guest powder particles in the composite powder feedstock. The homogenous dispersion state of the guest particles provided by their attachment to the host particles can consequently result in the fabrication of TMCs benefiting from a uniform distribution of reinforcements in the final microstructure.

Another desired feature of the selected composite powder system is the spherical/semi-spherical morphology of the host powder particles. The tremendous energy imparted to the powder particles during the early stages of the ball milling process causes the fracture of the brittle powder particles and the severe plastic deformation of the ductile ones. Depending on the ball milling process parameters (ball-to-powder ratio, rotational speed

and milling time), the induced plastic deformation can cause variable degrees of morphological change, cold-welding or fracture, while the activated collisions may pave the way for guest/host attachment and chemical reactions.

Based on the in-depth analysis of the mixed powder systems produced, 90 min of ball milling led to the desired TMC feedstock, in which the guest B_4C particles were fully decorating the surface of the host spherical-shape Ti64 particles. This composite powder feedstock was utilized for fabricating TMC parts.

3.2.2 SLM processing and arc melting

The SLM machine used in this study was OmniSint-160 having a 400W Yb-fiber laser with a spot size of 100 μm. Cubic parts with the dimensions of 10×10×10 mm^3 were printed on a 160 mm diameter Ti64 build plate under the protection of high-purity argon gas atmosphere. The most important parameters involved in the SLM process include laser power (P), scanning speed (v), hatch spacing (h), layer thickness (t), and scanning strategy. Table 1 lists the process parameters employed to fabricate Ti64 and 5wt.% B_4C/Ti64 parts in this study. The volumetric energy density (E_v), defined as the energy delivered to a unit volume of the powder bed, was 50, 62.5 and 75 J/mm^3 for the processed parts based on Eq. 1 [37-39]:

$$E_v = \frac{P}{vht} \quad [1]$$

As illustrated in Figure 3-2, scanning of layers was conducted using continuous laser mode according to a stripe hatching pattern alternating 67° between each layer, which has been reported to result in the smallest directional stress difference owing to the non-repeated scan vector feature. Moreover, this scanning strategy is believed to alleviate the formation of intense texture since the same pattern is repeated every 180 layers [40, 41].

Table 3-1 The processing parameters employed to fabricate 5wt.% B_4C/Ti64 and Ti64 parts.

Laser Power (P)	Scanning Speed (V)	Layer Thickness (t)	Hatch Spacing (h)
200, 250, 300 (W)	1000 (mm/s)	40 µm	100 µm

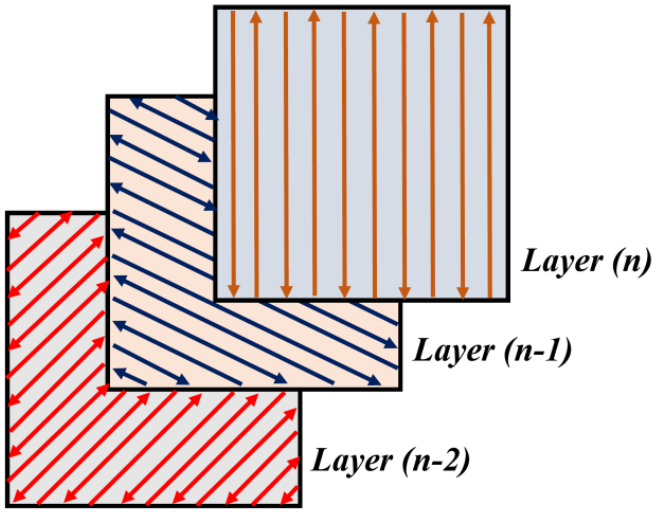

Figure 3-2 Schematic view of the utilized stripe hatching scanning strategy which alternates 67° between the subsequent layers.

Conventional arc melting resembling the quasi-equilibrium solidification condition was also utilized to fabricate parts from the same TMC powder feedstock. For this purpose, the arc melting process was conducted in graphite and water-cooled copper crucibles, indicating two different cooling rates close to the equilibrium and non-equilibrium conditions, respectively.

3.2.3 Powder Characterization

The morphology of the starting Ti64 and B_4C powders, as well as the mixed powder feedstocks, were observed using a Vega Tescan scanning electron microscopy (SEM), operating at an accelerating voltage of 20 kV. The particle size and particle size distribution measurements were performed three times using a Retsch Camsizer X2 machine, which

utilizes a high-resolution dual-camera system to measure fine and agglomerating powders ranging from 800 nm to 8 mm in diameter. The X-ray diffraction (XRD) analysis was also employed for phase analysis both in the starting Ti64 and the developed 5wt.% B_4C/Ti64 powder system. This analysis was performed at ambient temperature over a wide range of $2\theta = 20\text{-}80°$ using a PANalytical X'Pert powder X-ray diffractometer (Cu Kα target, operated at 45 kV and 35 mA with a step size of 0.0167°) equipped with X-ray monochromator.

The sphericity of the starting Ti64 powder particles as well as the 5wt.% B_4C/Ti64 composite powder system was measured using a Retch Camsizer X2 facility based on the following equation suggested by ISO 9276-6 standard [42]:

$$Sphericity = \frac{4\pi A}{P^2} \quad [2]$$

in which P and A are the measured circumference and area covered by a particle projection, respectively. The sphericity of an ideal sphere is unity. However, deviation from the ideal spherical shape leads to lower sphericities.

3.2.4 Microstructural Characterization

The SLM processed parts were sectioned, ground, and polished according to the standard metallography procedure and were etched chemically using Keller's Reagent. Microstructures of the fabricated parts were observed using a Nikon optical microscopy (OM) as well as Vega Tescan SEM operating at an accelerated voltage of 10 kV. The chemical composition of the phases was analyzed using energy-dispersive X-ray spectroscopy (EDS).

3.2.5 Mechanical Properties

The mechanical properties of the SLM processed Ti64 and 5wt.% B_4C/Ti64 parts were evaluated using microhardness test. These measurements were performed by employing a Matsuzawa microhardness testing machine with a load of 500 g being applied for 10 s. The reported microhardness represents the average of at least 5 measurements for each specimen.

3.3 Results and Discussion

3.3.1 B_4C-decorated Ti64 composite powder feedstock

Figure 3-3 shows SEM micrographs of the ball-milled 5wt.% B_4C/Ti64 mixed powder feedstock chosen as the desired TMC powder system for SLM processing. As being observed, the host Ti64 powder particles are fully decorated by the guest B_4C particles.

Referring to Figure 3-3, most of the host powder particles preserved their spherical morphology after relatively short milling time of 90 min. However, some particles were showing spherical to quasi-spherical/flattened morphological change. Moreover, cold welding of the ductile host powder particles occurred for a few particles, as indicated in Figure 3-3(a). The particle size distribution for the starting host powder and the selected 5wt.% B_4C/Ti64 powder feedstock has been provided in Figure 3-4. Besides, the D10, D50, and D90 representing the particle diameters at 10, 50, and 90% in the cumulative distribution (Figure 3-4) are also summarized in Table 2 for both of the powder systems. Referring to Figure 3-4 and Table 3-2, the TMC power system has shown a slight increase in the particle size, which could be attributed to the host decoration and the cold welding of a few particles. The variation in the sphericity of the powder particles as a function of the particle size for both the starting host and the mixed powder feedstock has been shown

in Figure 3-5. The TMC powder particles showed slightly lower sphericity than the starting host system in the whole range of the particle size due to the: (i) surface roughening effects of the guest particles decorating the surface of the host particles, and (ii) the spherical to quasi-spherical morphological change of the host particles. As a result of severe plastic deformation and fracture of the starting host powder particles during the ball milling process, particles less than 20 μm in size with a lower degree of sphericity were introduced into the composite system. On the contrary, cold welding led to the appearance of coarse particles (exceeding 45 μm) deviating from spherical shape, which are responsible for the decreasing trend observed in the upper limit of the TMC sphericity curve provided in Figure 3-5.

Referring to Figure 3-4 and Table 3-2, application of 90 min ball milling led to the fabrication of an MMC powder feedstock with a particle size distribution close to that of the starting Ti64 powder. Moreover, as shown in Figure 3-3, the developed MMC powder system benefits from the host powder particles preserving their spherical shape as well as complete guest/host attachment. These characteristics introduce the selected TMC powder system desired for the SLM process.

The minimized inter-particle friction caused by the low surface area is the main reason behind the high flowability of the spherical-shape powder particles, making them interesting for PBF-AM processes [43]. Although the host powder particles have preserved their spherical shape to a large extent in the developed TMC powder system, the enhanced surface area and the increased inter-particle friction caused by the slight deviation in the particle shape from spherical to quasi-spherical/flattened may lead to lower flowability compared to the starting Ti64 powder [44-46].

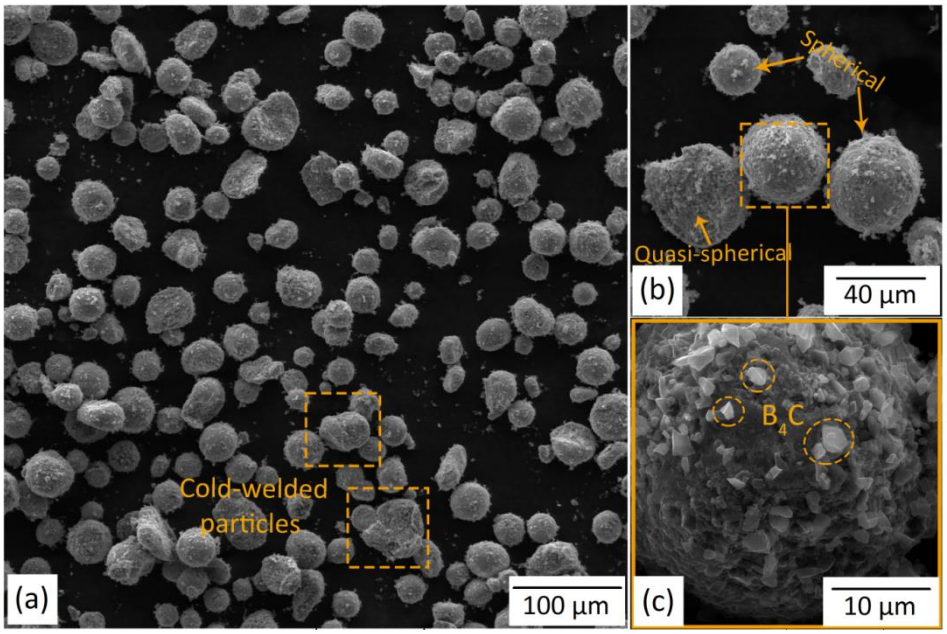

Figure 3-3 SEM micrographs of the B_4C-decorated Ti-6Al-4V powder particles obtained by 90 min of ball milling. (b) Higher magnification micrograph of (a). (c) Enclosed view of the selected region in (b).

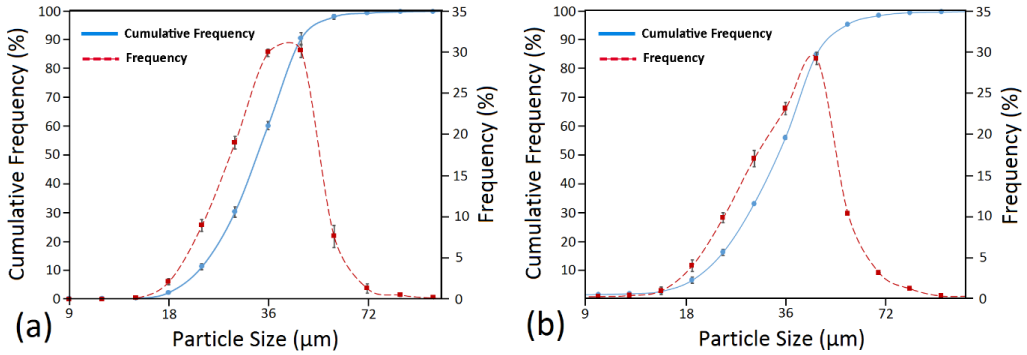

Figure 3-4 The particle size distribution curves of: (a) starting Ti-6Al-4V (Ti64) and (b) 5 wt. % B_4C/Ti64 TMC powder feedstock after 90 min of ball milling.

Table 3-2 The particle size distribution results derived from the data in Figure 3-4, which present the cumulative distribution of D10, D50, and D90.

Powder System	D10 (µm)	D50 (µm)	D90 (µm)
MMC Powder	22.8 ± 0.05	36.6 ± 0.27	50.9 ± 0.19
Ti-6Al-4V Powder	23.4 ± 0.52	35.0 ± 0.36	45.7 ± 0.88

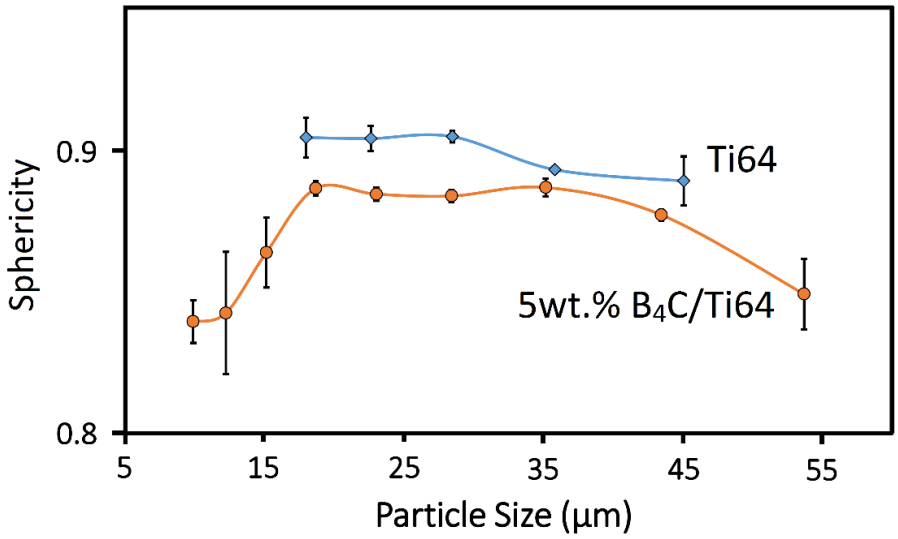

Figure 3-5 The sphericity of the particles as a function of their size for the starting Ti-6Al-4V (Ti64) as well as the 90 min ball-milled 5 wt.%B4C/Ti64 powder feedstock.

The XRD patterns of the starting Ti64 and B_4C powders as well as the developed 5wt.% B_4C/Ti64 powder feedstock have been provided in Figure 3-6. As being observed, the diffraction peaks in the developed TMC powder system correspond to those for the starting materials, revealing that no in-situ reaction has been activated in the system to form new phases during the relatively short milling time of 90 min. Moreover, due to their relatively low content, the diffraction peaks related to the B_4C powder particles in the 5wt.% B_4C/Ti64 powder system showed decreased intensity compared to the starting B_4C powder.

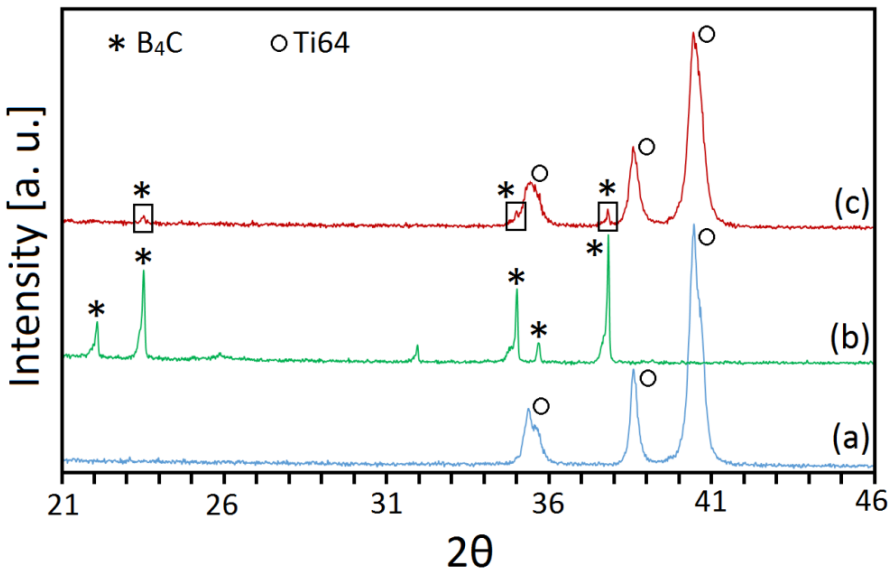

Figure 3-6 XRD patterns of the: (a) Ti-6Al-4V (Ti64), (b) B_4C, and (c) 5 wt.% B_4C/Ti64 systems. The rectangles indicate the diffraction peaks of the B_4C constituent in the TMC powder feedstock.

3.3.2 Laser/composite powder interaction

Due to the noticeably high melting temperature of the guest particles as well as the extremely low laser/powder interaction time during SLM, complete melting of the guest constituent is rather difficult or impossible even at relatively high laser energy densities. Accordingly, fabrication of composite parts by SLM process requires a molten media to interact with the solid guest particles and result in the embedment of the non-reacted (ex-situ), partially reacted (hybrid), or completely reacted (in-situ) reinforcement(s) in the matrix of the final composite. Full melting of the host metallic constituent with a lower melting point compared to the guest particles is essential to provide this molten media in the entire system to produce sound MMC parts. Microstructural observations of the 5wt.% B_4C/Ti64 parts processed with relatively low laser energy densities revealed some host Ti64 particles which were not completely melted (Figure 3-7(a)). These particles were surrounded by the guest B_4C particles to the same feature as the guest-decorated host

particles in the 5wt.% B_4C/Ti64 powder feedstock shown in Figure 3-3. The un-melted/partially melted Ti64 particles can provide valuable information about the mechanism taking place during the interaction of the laser beam with the TMC powder bed. This is an important point which needs to be taken into consideration when fabricating MMCs using PBF-AM processes. Addition of a guest constituent to the host metallic powder has been reported to enhance the laser absorptivity of the system due to the following reasons [22, 47, 48]:

(i) In most cases, the incorporated guest powder particles are ceramics with higher laser absorptivity than the metallic host powder. By replacing a fraction of the metallic constituent, the developed MMC powder benefits from higher laser absorptivity than the individual metallic host powder system.

(ii) The increased surface roughness and consequently the escalated laser/powder interactions caused by the decoration of the host particles by the irregularly-shaped guest particles elevate the laser absorptivity of the MMC powder feedstock.

Despite the higher laser absorptivity of the 5wt.% B_4C/Ti64 powder system than the non-reinforced host Ti64 powder, the SLM fabricated components contained un-melted/partially melted Ti64 powder particles at E_v=50 J/mm^3 (Figure 3-7(a) and (b)). However, the Ti64 parts manufactured with the same process parameters revealed full melting of the powder particles (Figure 3-7(c)). The observed phenomenon can be ascribed to the variations in thermal conductivity (k) and thermal diffusivity (α) of the MMC powder system compared to the non-reinforced case. The thermal conductivity of a composite system (K_{MMC}) containing spherical-shape reinforcing particles dispersed in the matrix can be expressed as [49, 50]:

$$K_{MMC} = \frac{K_m\left[2K_m + K_r^{eff} + 2\left(K_r^{eff} - K_m\right)V_r\right]}{2K_m + K_r^{eff} - \left(K_r^{eff} - K_m\right)V_r} \quad [3]$$

where V_r is the volume fraction of the reinforcing particles in the system, K_m signifies the thermal conductivity of the matrix and K_r^{eff} represents the effective thermal conductivity of the reinforcing particle which is defined as [50]:

$$K_r^{eff} = \frac{K_r}{1 + \frac{K_r}{rh_{rm}}} \quad [4]$$

in which K_r is the intrinsic thermal conductivity of the reinforcing particle, r is the average radius of the reinforcing particles, and h_{rm} stands for the interfacial thermal conductance of the interface between the reinforcing particle and the matrix.

Referring to Eq. 3 and Eq. 4, for a given guest/host MMC powder system, the size of the guest powder particles and the thermal conductivity of the guest/host interface are important factors playing roles in the effective thermal conductivity of the system. As shown in Figure 3-3, the developed TMC powder system in this research has the host Ti64 particles fully decorated by the guest B_4C particles. The higher absorptivity of the laser beam enabled by the guest particles acts to enhance the total laser absorptivity of the TMC powder system and consequently provides the system with more absorbed energy. However, for the developed fully guest-decorated host powder particles, the interaction of the laser with the powder bed starts with the direct exposure of the guest particles to the laser beam. Due to the noticeably high melting point of B_4C (3036 K [51]) as well as the extremely low interaction time associated with the SLM process, these particles do not experience melting. Therefore, the urgent need for the formation of melt during the process takes place if the absorbed heat is effectively transferred from the decorating B_4C particles to the host Ti64 particles with a lower melting point of 1933 K. As the microstructural

observations revealed in Figure 3-7(a) and (b), there were un-melted/partially melted Ti64 particles in some fabricated 5wt.% B_4C/Ti64 parts, confirming the non-efficient transfer of the absorbed energy from B_4C particles to the Ti64 particles. The enclosed view of a partially melted host particle in Figure 3-7(b) clearly shows the guest B_4C particles decorating its outer surface. The interaction of the laser beam with this decorated particle caused partial melting of its surface. The formed melt subsequently came into reaction with the adjacent guest particles, as indicated in Figure 3-7(b). Figure 3-8 illustrates the variation of the thermal diffusivity as a function of temperature for both B_4C and Ti64. Due to its noticeably low thermal diffusivity, B_4C particles seem not to allow the absorbed heat to be easily transferred to the host powder particles. It is worth noting that even if having a guest constituent with a noticeably high thermal diffusivity (much more than the host constituent), full melting of the host powder particles may be a challenge in fully guest-decorated MMC powder systems. The guest particles in such systems act as barriers to the direct interaction of the laser beam with the host powder particles. The elevated heat input provided by higher laser energy densities was found to enhance the melting efficiency of the host power particles, leading to the final TMC microstructures almost free of un-melted/partially melted Ti64 particles. Referring to Eq. 4, the decrease in the size of the guest particles could also be employed as a strategy to enhance the melting efficiency of the host particles by increasing the effective thermal conductivity and thermal diffusivity through the guest particles.

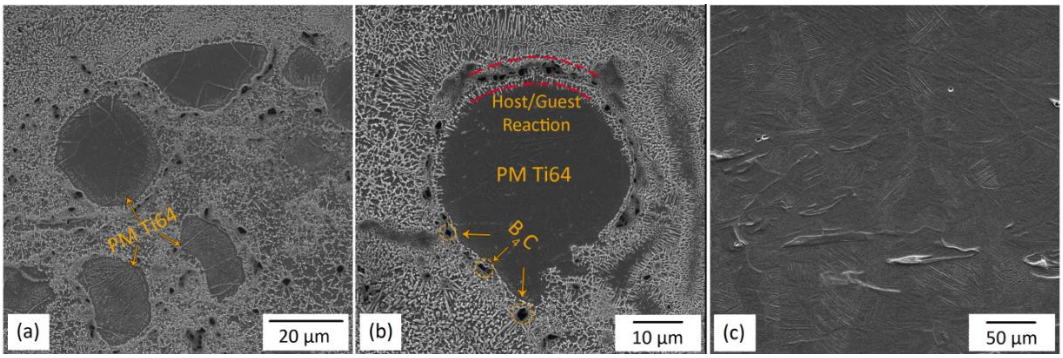

Figure 3-7 SEM micrographs of the SLMed: (a), (b) 5 wt.%B_4C/Ti64, and (c) Ti-6Al-4V (Ti64) systems processed with laser energy density of 50 J/mm^3 (P=200 W, V=1000 mm/s, h=100 µm and t=40 µm). The micrograph in (b) provides an enclosed view of a partially melted Ti64 (PM Ti64) particle surrounded by the partially dissolved B_4C guest particles.

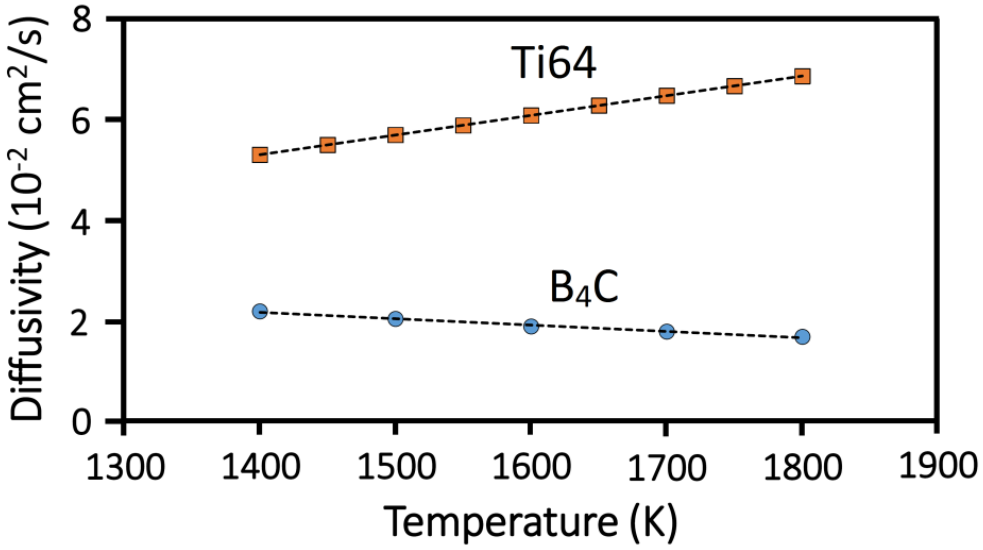

Figure 3-8 Thermal diffusivity of bulk Ti-6Al-4V (Ti64) and B_4C as a function of the temperature [52, 53].

3.3.3 Guest B_4C particles: melting or dissolution?

Figure 3-9(a) schematically shows the thermal cycle of a single track during SLM process, in which T_P represents the peak temperature of the thermal cycle, and λ signifies the period during which the melt pool temperature is higher than the melting point of the host powder. Both T_P and λ play significant roles in evaluating the guest/host interactions during SLM

processing of MMCs. They are directly dictated by the AM process parameters, which can be summarized in terms of volumetric energy density (Eq. 1). According to the microstructural observations provided in Figure 3-10, residual B_4C particles are visible within the composite, regardless of the employed process parameters. However, their volume fraction showed a descending trend with increasing the volumetric energy density. The presence of residual B_4C particles in the final microstructure confirms that T_P is lower than the melting point of B_4C guest particles ($(T_m)_{guest}$= 3036 K) but higher than the liquidus temperature of the host Ti64 alloy ($(T_L)_{host}$= 1933 K). While direct melting of Ti64 particles takes place during the SLM process, the disappearance of B_4C particles occurs through the dissolution mechanism. Due to the large difference between the melting points of the host and the guest constituents (ΔT=1103 K), even high volumetric energy densities employed in this study were not successful in increasing the T_P to the temperatures over the melting point of B_4C particles. Debroy et al. [23] investigated the effect of laser power on T_P of the melt pool during direct laser deposition of 316 stainless steel and reported only 200 K increase in T_P by enhancing the laser power from 150 to 450 W. This can be attributed to the formation of the melt pool within a conductive media (metallic powder), in which the excessive heat provided by the increase in the laser energy density can be sunk by the metallic powder, leading more to the melt pool enlargement rather than the increase in the temperature of the molten material.

Schematic illustration of the thermal cycles induced during SLM processing of the 5wt.% B_4C/Ti64 system using various laser energy densities have been shown in Figure 3-9(b). In zones (I) and (II), the temperature is higher and lower than the melting point of the host constituent, respectively. Therefore, the host powder particles experience direct melting in zone (I) since the temperature exceeds their melting point. As indicated in Figure 3-9(b),

both the T_P and λ follow an ascending trend by increasing the volumetric energy density. However, since the T_P induced in all three cases is less than the melting point of the guest constituent, these particles do not experience direct melting but dissolution.

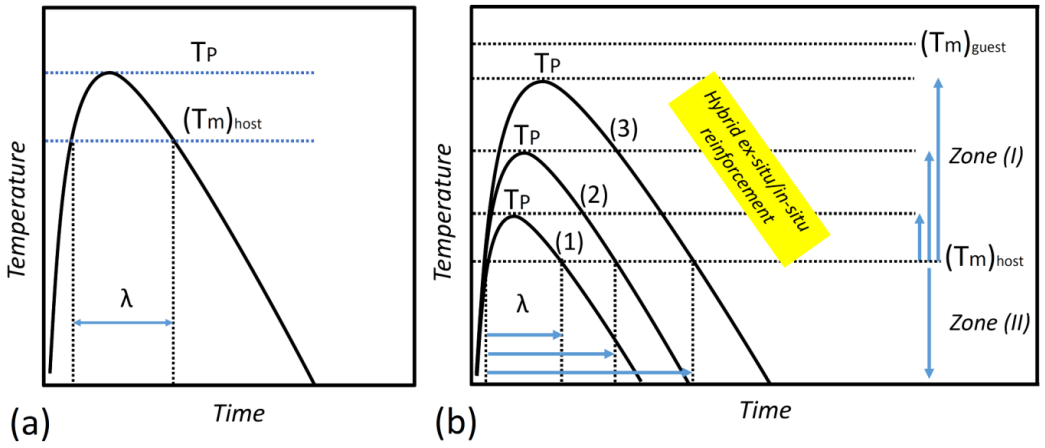

Figure 3-9 (a) Schematic view of the thermal cycle during SLM processing of a single track. T_P, $(T_m)_{host}$ and λ are the maximum temperature of the melt pool, the melting point of the host powder, and the period in which the temperature is higher than the melting point of the host powder, respectively. (b) Schematic illustration of the thermal cycle during SLM of a single track for the 5wt.% B_4C/Ti64 composite system. The temperature in zones (I) and (II) is higher and lower than $(T_m)_{host}$, respectively. The thermal cycles (1), (2), and (3) all lead to the hybrid ex-situ/in-situ reinforced TMCs. $(T_m)_{guest}$ corresponds to the melting point of the guest particles.

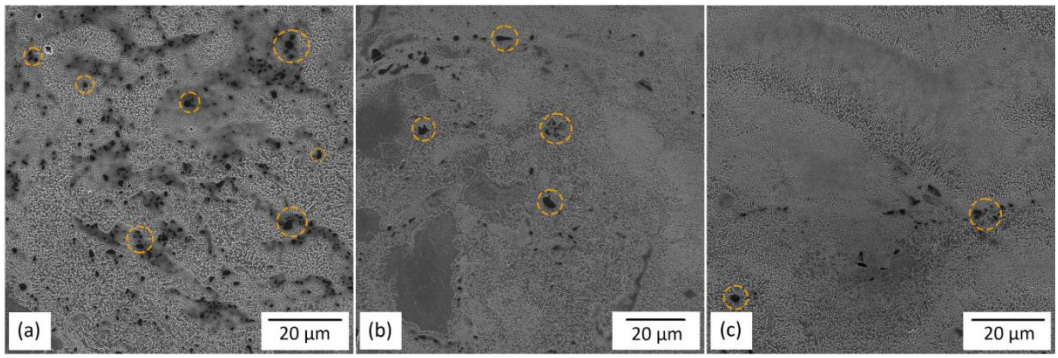

Figure 3-10 SEM micrographs of the 5wt.% B_4C/Ti64 composites SLMed with different laser powers of: (a) 200 W (E_V= 50 J/mm^3), (b) 250 W (E_V= 62.5 J/mm^3), and (c) 300 W (E_V= 75 J/mm^3). The scanning speed, hatch spacing, and layer thickness were 1000 mm/s, 100 µm, and 40 µm, respectively. The volume fraction of the residual B_4C particles (as represented by the dashed circles) decreased with increasing the laser power (volumetric energy density).

3.3.4 Dissolution Mechanism of guest B_4C particles

The fundamental concepts behind the dissolution of the guest powder particles can be discussed based on the schematic illustrations provided in Figure 3-11. Referring to Figure 3-9(b), the temperature of the melt during heating and cooling in zone (I) varies between $(T_m)_{host}$ and T_P. In the following discussion, the liquid phase is assumed to be in a constant temperature of T_{ave} (the average temperature in zone (I)) for a λ period. At the early stage of the host particles melting, the molten Ti64 is in direct contact with the solid guest B_4C powder particles (Figure 3-11(a)). However, the solid and liquid phases are not in equilibrium condition. In order to establish the thermodynamic equilibrium conditions at the solid/liquid interface, the chemical composition of the solid and liquid phases need to be C_S (equilibrium Ti/Al/V/B/C concentrations in the solid phase at the interface) and C_L (equilibrium Ti/Al/V/B/C concentration in the liquid phase at the interface), respectively. Therefore, dissolution of the solid B_4C particles takes place to enrich the adjacent liquid layer by carbon (C) and boron (B) elements (Figure 3-11(b)). On the other hand, the enhanced concentration of Ti/Al/V in the solid phase provided by the diffusion of Ti64 atoms from the liquid phase helps the solid phase to achieve the equilibrium composition at the interface. When the chemical composition of the liquid and solid phases at the interface reaches C_L and C_S, respectively, the interdiffusion between the molten Ti64 and the solid B_4C particles terminates (Figure 3-11(c)). It is noteworthy that the thermodynamic equilibrium is established only at the solid/liquid interface. The achieved thermodynamic equilibrium condition is temporary since the concentration gradients existing between the interface and bulk of the liquid as well as the interface and bulk of the solid provide liquid state and solid-state diffusion of the B/C and Ti/Al/V atoms, respectively. Since the liquid state diffusion is much faster than the solid-state one, and the available time for diffusion

is extremely short during SLM process, the deviation from the thermodynamic equilibrium condition takes place only in the liquid phase. Diffusion of C and B atoms from the interface (with higher C and B concentration) towards the bulk of the liquid (C and B poor region) leads to the deviation from the equilibrium conditions due to the homogenization in the liquid phase (Figure 3-11(d)). In order to re-establish the equilibrium conditions at the solid/liquid interface, the remaining solid B_4C particle again dissolves into the adjacent liquid to enrich the interfacial liquid layer from C and B to achieve C_L (Figure 3-11(e)). To clarify, since the adjacent liquid layer deviated from the equilibrium condition, the solid particle dissolves to re-establish the equilibrium chemical composition (C_L) at the interface. The repeated deviation and re-establishment of the thermodynamic conditions causes the dynamic dissolution of the B_4C particles and is the driving force for the progress of dissolution (Figure 3-11(f)) [54].

Considering the extremely short time available for dissolution during the SLM process with noticeably fast heating and cooling rate, it is interesting that a significant portion of the guest B_4C particles could be dissolved within the molten Ti64. The convective flows in the melt pool, as well as the relatively small size of the guest B_4C particles employed in this study, can explain this fast dissolution. The driving force for the dissolution of the guest particles is the diffusion of the B and C elements from the equilibrium liquid layer towards the bulk of the liquid phase. This results in the deviation from the equilibrium conditions and provides further dissolution of the guest particle to re-establish the equilibrium condition again in the system. The convective flows in the melt pool can significantly increase the dissolution rate of the B_4C particles by (i) offering fresh Ti64 liquid phase at the S/L interface, and (ii) moving elements from the equilibrium liquid layer towards the bulk of the liquid. The degree of dissolution is also a major function of the particle size.

Finer B_4C particles need less interaction time to be completely dissolved into the surrounding melt. In other words, the complete dissolution of small-sized B_4C particles needs less diffusion and a shorter period.

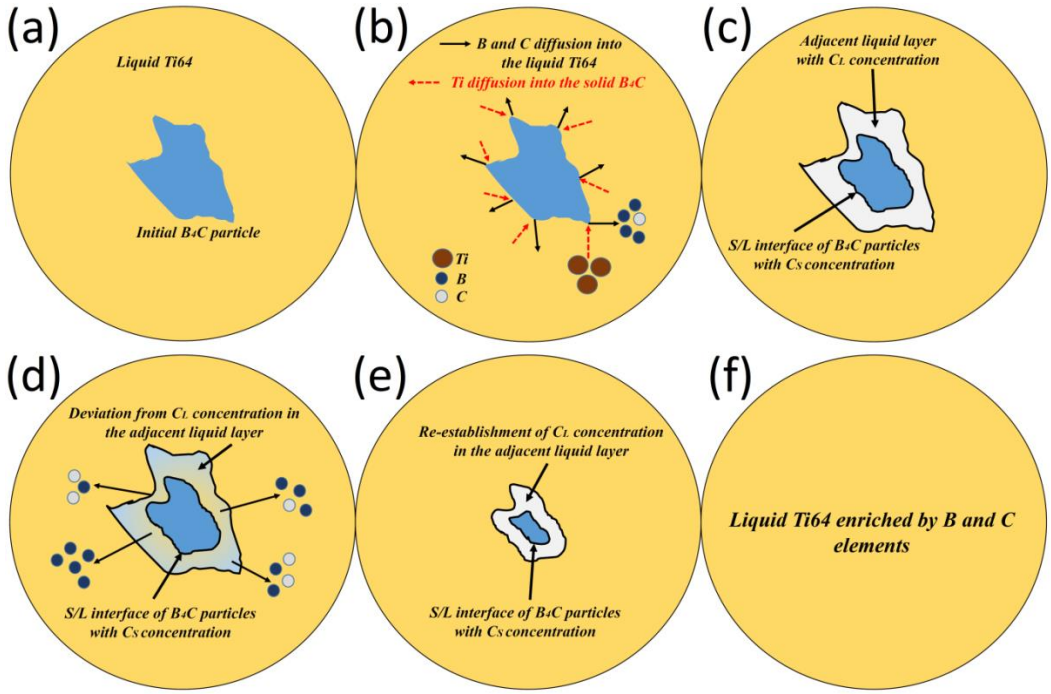

Figure 3-11 The schematic of the solid/liquid interaction between the B_4C particles and the liquid Ti64, representing the mechanism of guest particles dissolution in the molten Ti64 during SLM processing of 5wt.% B_4C/Ti64 powder system with direct melting of the host powder particles: (a) the solid B_4C and the liquid Ti64 phases at the beginning of the host particles melting, (b) interdiffusion between the solid and liquid phases to establish the equilibrium condition at the interface, (c) formation of solid and liquid layers with equilibrium C_S and C_L concentrations, respectively at the solid/liquid interface, (d) deviation from equilibrium conditions caused by the diffusion of B and C atoms from the equilibrium liquid layer surrounding the B_4C particles towards the bulk of the liquid, (e) re-establishment of the equilibrium conditions by further dissolution of the guest particles and enrichment of the adjacent liquid layer by B and C atoms, and (f) progression of the dissolution by deviation and re-establishment of equilibrium conditions at the interface until complete dissolution of guest particles.

According to the dissolution thermodynamics, the guest B_4C particles should be dissolved completely since they are surrounded by an infinite liquid media, in which the full

equilibrium conditions can never be established between the solid B_4C particles and the bulk of the molten Ti64. However, from the kinetics point of view, the dissolution process of the B_4C particles into the surrounding melt needs sufficient time to be accomplished. Therefore, when considering the dissolution of the guest powder particles, three different scenarios of (i) lack of dissolution (ii) partial dissolution, and (iii) complete dissolution may be possible based on the size of the guest powder particles, T_P and λ. Longer λ, higher T_P, and finer guest powder particles are the factors providing the guest powder particles with an increased chance of complete dissolution in the melt pool.

The effect of volumetric energy density and particle size on the dissolution behavior of the B_4C particles in the 5wt.% B_4C/Ti64 composite system can be described based on Figure 3-10 and Figure 3-12. Referring to Figure 3-10, the increase in the volumetric energy density from 50 to 75 J/mm^3 led to a significant decrease in the amount of residual B_4C particles in the final microstructure. This can be attributed to the longer λ and higher T_P, leading to the complete dissolution of a more substantial fraction of the guest particles (Figure 3-9(b)). As shown in Figure 3-12, the size of the guest particles plays a crucial role in their level of dissolution. Microstructural observations revealed that the B_4C particles ranging between 1-3 μm in this study were small enough to be partially or completely dissolved even during the extremely short interaction times provided by the SLM process. As indicated in Figure 3-12, coarse and medium-sized B_4C particles experienced partial dissolution. However, with the same process parameters (the same energy density), the fine particles were able to be completely dissolved. Higher surface to volume ratio and shorter diffusion distance are the main reasons behind the faster dissolution of the fine guest particles.

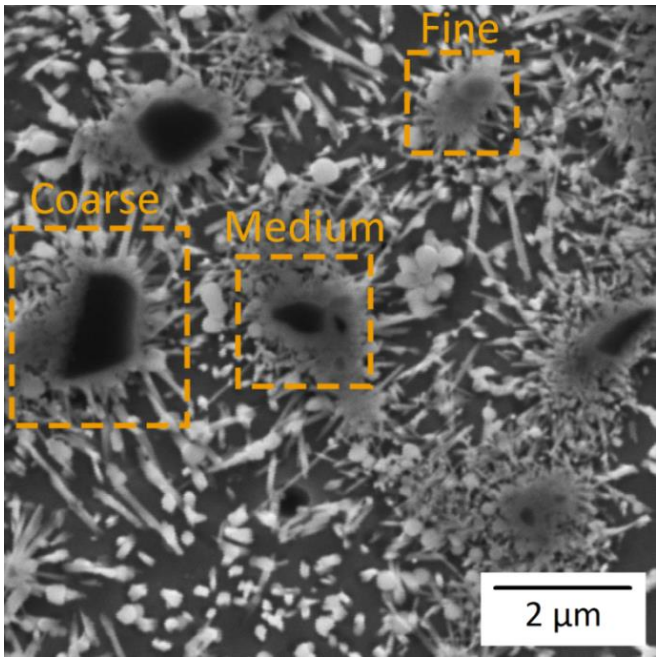

Figure 3-12 The effect of B_4C particle size on its dissolution progression in the 5wt.% B_4C/Ti64 sample processed by the energy density of 62.5 J/mm^3 (P= 250 W, V= 1000 mm/s, h= 100 µm, t= 40 µm). The smaller the size of the guest B_4C particles, the higher the chance of complete dissolution.

3.3.5 Microstructural evolutions and solidification path of the 5wt.% B_4C/Ti64 composite system

Figure 3-13(a) shows the microstructure of the SLM processed 5wt.% B_4C/Ti64 system. The EDS chemical analysis results of the in-situ synthesized phases are provided in Figure 3-13(b) and (c). Based on the morphology of the phases and the EDS results, it can be inferred that the microstructure consists of TiC (particulate-shape) and TiB (hollow whisker-shape) reinforcements synthesized through the in-situ reaction between the guest B_4C particles and the molten Ti64. This is in agreement with the results reported on SLM processing of the same composite system [55]. Boron and carbon could be detected by the EDS analysis, though they could not be quantified due to the inability of the EDS system for the light elements [56-58] as well as their noticeably small size in the SLM fabricated

components. It is worth noting that the reinforcement characterized as TiB contains fine TiC precipitates, as shown in Figure 3-13(d) which resulted in detection of C during EDS analysis of this phase. However, the TiC phase was free from B element. The reaction products (TiB and TiC) with different size and morphology were observed not only in the matrix (Figure 3-13(a)) but also at the interface of the partially dissolved B_4C particles (Figure 3-12). Therefore, the fabricated composite is reinforced by the in-situ synthesized TiB and TiC phases as well as the ex-situ residual B_4C particles which did not find the chance to react with the melt (Figure 3-10 and Figure 3-12). Because of having both ex-situ and in-situ reinforcements in the microstructure, hybrid composites were obtained. The extremely fast cooling rate associated with the SLM process (10^3-10^5 K/s) is much higher than the critical cooling rate for the martensite formation in Ti64 (410 K/s), leading to the martensitic phase transformation of the matrix (α') [2].

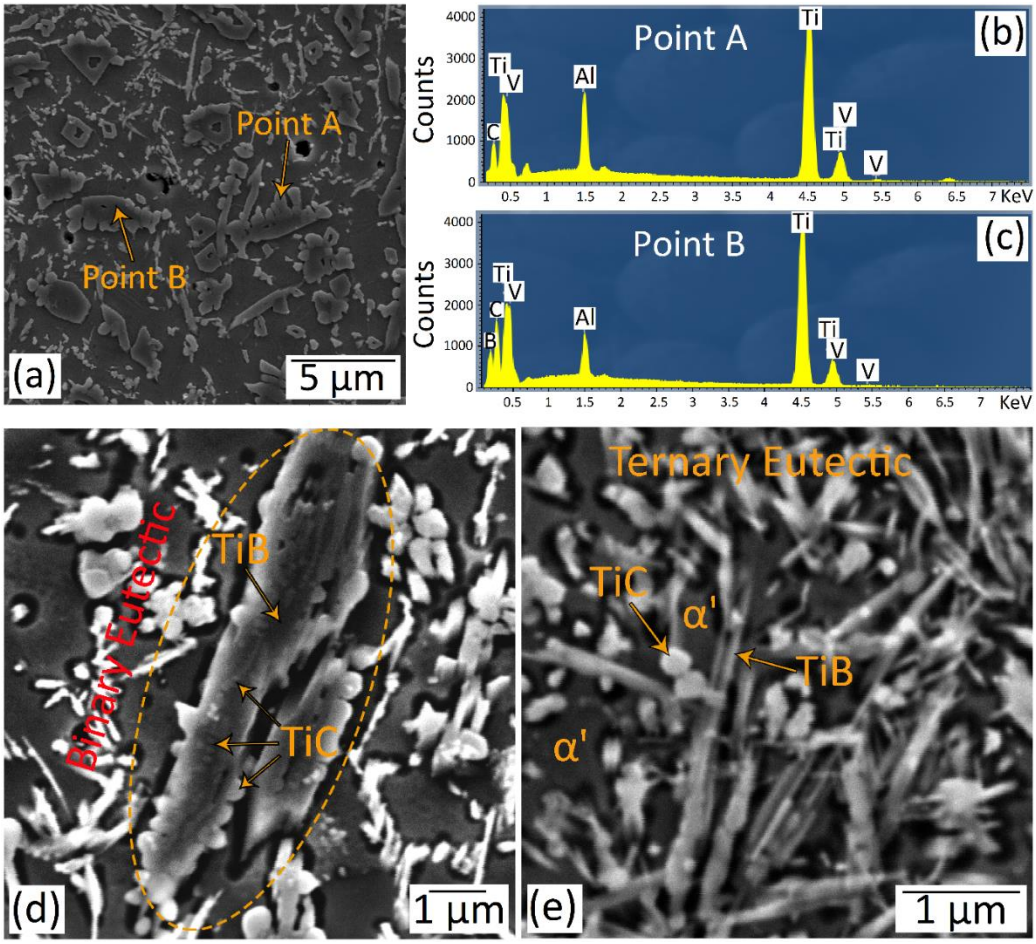

Figure 3-13 (a) Overview of the 5wt.% B_4C/Ti64 composite microstructure, (b) EDS analysis of the Point A, and (c) EDS analysis of point B. The detected phases are believed to be TiC (point A) and TiB (point B) as the products of the in-situ reaction between the solid B_4C and the molten Ti64. Higher magnification micrographs showing the: (d) binary and (e) ternary eutectic reaction products and the martensitic matrix.

In order to have a better understanding of the microstructural evolutions in the TMC structure, the solidification path of the 5wt.% B_4C/Ti64 system was investigated. For this purpose, the multi-component liquid phase consisting of Ti-Al-V-B-C was reduced into a hypothetical Ti-B-C ternary system. In other words, the Al and V atoms were substituted by Ti atoms. Figure 3-14(a) shows the pseudo-binary equilibrium phase diagram of the Ti-B_4C system in the range of 0-10wt.% B_4C. The solidification path of the studied composite

system with 5wt.% B_4C shown in Figure 3-14(a) can be summarized in three stages as follows:

- Stage I (formation of primary (P) TiB phase): The solidification starts with the formation of TiB as the primary phase solidified from the liquid phase: $L \rightarrow (TiB)_P + L$
- Stage II (formation of TiB-TiC binary eutectic (BE)): Formation of the $(TiB)_P$ is accompanied by the reduction of the B concentration and partitioning of C in the remaining liquid phase. The enrichment of the liquid from C shifts the composition of the melt toward the TiB-TiC binary eutectic reaction as: $L \rightarrow (TiB_{BE} + TiC_{BE}) + L$
- Stage III (formation of TiB-TiC-β ternary eutectic (TE)): Depletion of the liquid phase from B and C elements during the formation of primary and binary eutectic products enriches the residual liquid from Ti and subsequently enables the TiB-TiC-β ternary eutectic reaction as: $L \rightarrow (TiB_{TE} + TiC_{TE} + \beta_{TE})$

Based on the above discussions, the equilibrium solidification path in the 5wt.% B_4C/Ti64 system can be summarized as:

$$L \rightarrow (TiB)_P + L \rightarrow (TiB)_P + (TiB_{BE} + TiC_{BE}) + L \rightarrow (TiB)_P + (TiB_{BE} + TiC_{BE}) + (TiB_{TE} + TiC_{TE} + \beta_{TE})$$

The primary β then undergoes an equilibrium solid-state phase transformation to form (α+β) two-phase microstructure at ambient temperature. Accordingly, the final microstructure consists of:

$$(TiB)_P + (TiB_{BE} + TiC_{BE}) + (TiB_{TE} + TiC_{TE} + \alpha + \beta)$$

Figure 3-14(b) schematically shows the microstructural evolutions during equilibrium solidification followed by a diffusion-controlled solid-state transformation. According to the provided equilibrium solidification path, the in-situ precipitated $(TiB)_P$, $(TiB\text{-}TiC)_{BE}$, and $(TiB\text{-}TiC)_{TE}$ phases act as reinforcements to the $(\alpha+\beta)$ matrix of the fabricated composite. Since the formation and growth of the primary and binary eutectic products occurs in the liquid phase, they are larger compared to the ternary eutectic products. The $(TiB)_P$ can be detected as a coarse single phase while the binary and ternary eutectic products can be characterized by the relatively coarse two-phase and fine three-phase microstructures, respectively.

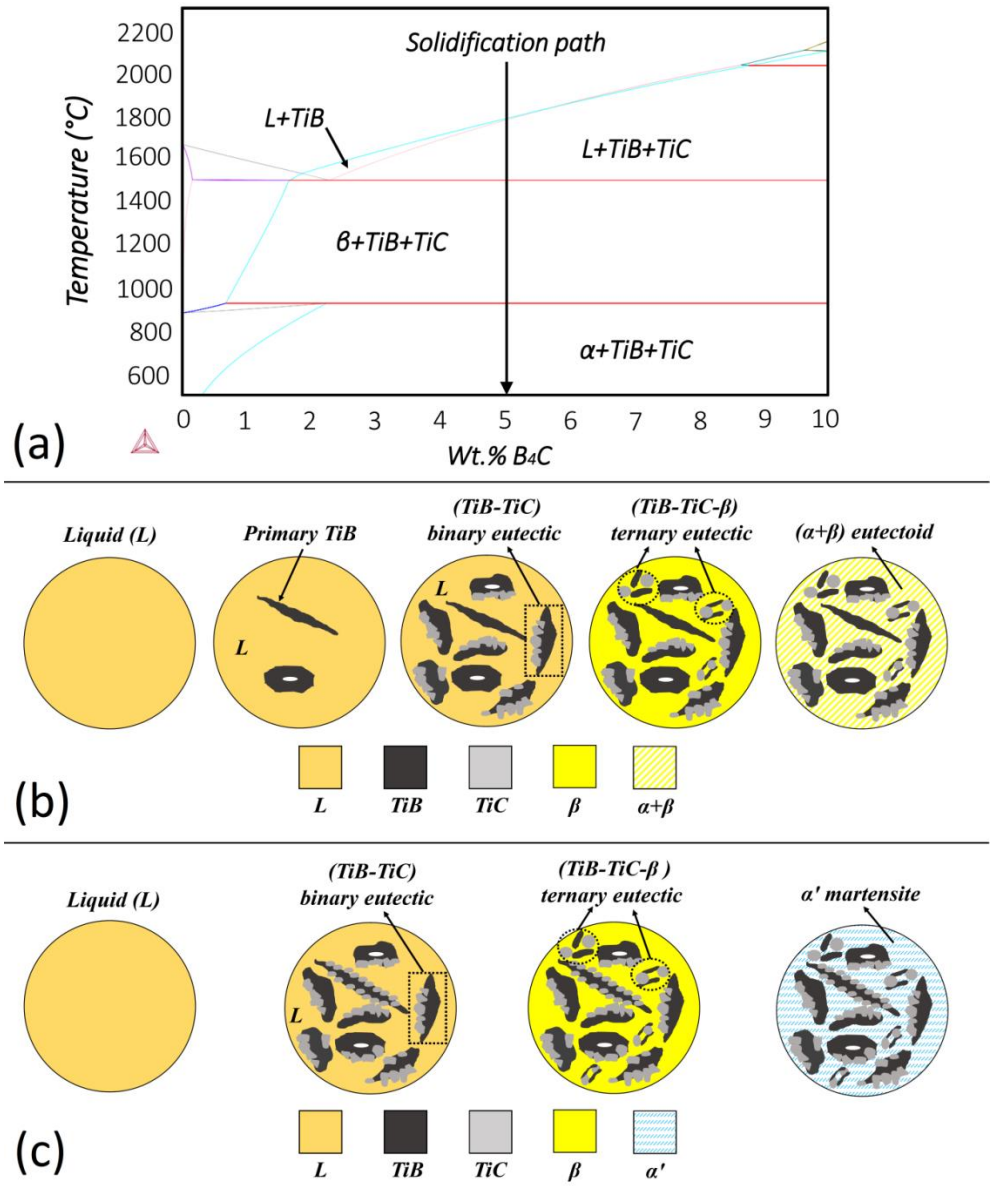

Figure 3-14 (a) Pseudo-binary phase diagram of Ti-B_4C system in the range of 0-10wt.% B_4C [59]; Schematic illustrations of: (b) equilibrium, and (c) non-equilibrium solidification path of the 5wt.% B_4C/Ti64 system.

The microstructural details of the SLM processed 5wt. % B_4C/Ti64 composite are shown in Figure 3-13(d) and (e). The single-phase $(TiB)_P$ was not detected in the microstructure. However, the coexistence of TiB-TiC and β-TiB-TiC is believed to be the result of the binary (Figure 3-13(d)) and ternary (Figure 3-13(e)) eutectic reactions, respectively. The

extremely high cooling rates associated with the SLM process caused the deviation of the solidification path from the proposed equilibrium solidification sequence. In fact, the rapid solidification depressed the appearance of $(TiB)_P$ as the primary solidification phase which was expected to be formed in the extremely narrow solidification range of 12 K based on the equilibrium phase diagram provided in Figure 3-14(a). Moreover, the high cooling rates after the solidification suppressed the diffusion-controlled solid-state transformation of primary β phase and led to the formation of α′ through a diffusionless martensitic transformation. Therefore, the non-equilibrium solidification sequence and solid-state phase transformation during SLM of 5wt. % B_4C/Ti64 can be summarized as:

$$L \rightarrow (TiB_{BE} + TiC_{BE}) + L \rightarrow (TiB_{BE} + TiC_{BE}) + (TiB_{TE} + TiC_{TE} + \beta_{TE}) \rightarrow (TiB_{BE} + TiC_{BE}) + (TiB_{TE} + TiC_{TE} + \alpha')$$

Figure 3-14(c) schematically shows the evolutions of the microstructure for the non-equilibrium scenario. Although the final microstructure is slightly different from the equilibrium microstructure proposed by the phase diagram, the equilibrium solidification sequence could provide valuable insight into the microstructural evolutions of the SLM processed composite parts with much more complex phase transformations.

The microstructure of the graphite crucible-cooled composite revealed the formation of $(TiB)_P$ due to the low cooling rates involved in the solidification process (Figure 3-15(a)). Although still present in the microstructure, the increased cooling rate induced by the water-cooled copper crucible significantly decreased the volume fraction of the $(TiB)_P$ phase and made it rather difficult to find this phase in the microstructure (Figure 3-15(c)). Therefore, the absence of $(TiB)_P$ in the microstructure of the SLM fabricated TMCs is reasonable due to the extremely high cooling rates induced in the process. Regardless of the cooling rate, the arc melted composites contained binary and ternary reaction products,

as shown in Figure 3-15(b) and (d). It is noteworthy that the matrix in the conventional arc melted samples seems to be consisted of (α+β) lamellar microstructure (Figure 3-15(e)). However, the diffusionless transformation induced during the SLM process with extremely high cooling rates led to the formation of a fully martensitic α′ microstructure. Comparison of the microstructures for the arc melted, and SLM processed TMCs also revealed a significant correlation between the size of in-situ formed reinforcements and the cooling rate. The microstructure showed refinement from graphite crucible cooled system to the water-cooled copper crucible case and then to the SLM processed condition (Figure 3-13 and Figure 3-15).

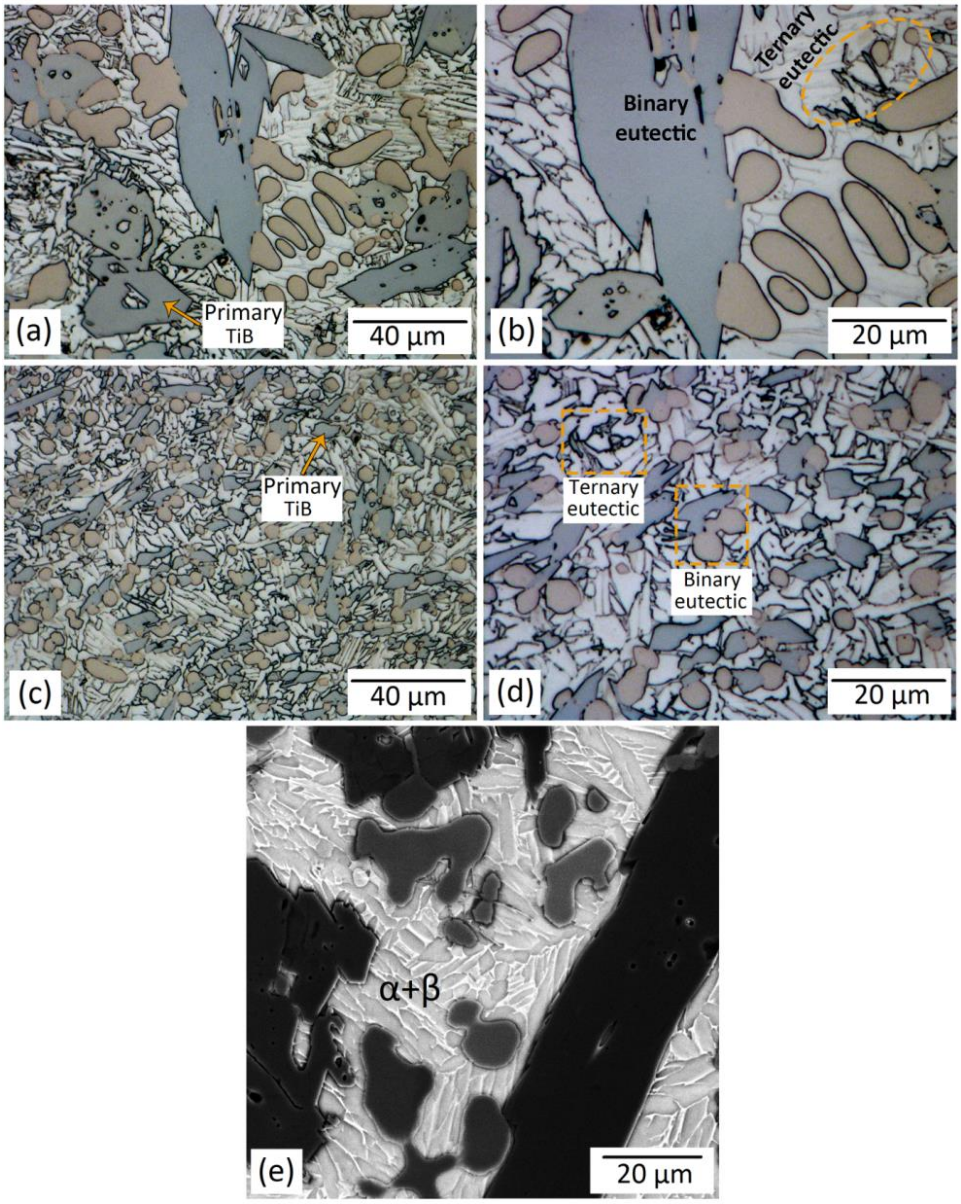

Figure 3-15 The microstructure of the 5wt.% B_4C/Ti64 composite fabricated through conventional arc melting in: (a,b) graphite crucible, and (c,d) water-cooled copper crucible. (e) The microstructure of the matrix in the arc melted composites.

3.3.6 Microhardness

Figure 3-16 compares the microhardness of the SLM fabricated TMCs and the monolithic Ti64 parts generated using the same process parameters. Since the microhardness data are not influenced by the internal defects present in the additively manufactured parts, this test

can provide a useful criterion as a means of comparison of the mechanical properties [60]. The following points can be drawn from the microhardness results:

(1) The microhardness of the TMCs showed a relatively monotonic trend in the applied range of volumetric energy densities. The higher volume fraction of un-dissolved B_4C particles in the E_v= 50 J/mm^3 (587 HV) condition seems to have the same influence on the hardness as the higher volume fraction of in-situ precipitated reinforcements formed in the case of E_v= 75 J/mm^3 (571 HV).

(2) In general, the microhardness of the TMCs was higher than the unreinforced Ti64 samples regardless of the operating process parameters. Incorporation of B_4C particles to the Ti64 matrix resulted in 30-80% improvement in the microhardness, showing an ascending trend with decreasing E_v. By considering the same microhardness values for TMCs under different process parameters, this can be attributed to the significant variation in the microhardness of Ti64 samples (120 HV) for the studied range of E_v.

(3) The microhardness of Ti64 samples was a direct function of E_v, owing to the increase in the martensite lath size [35].

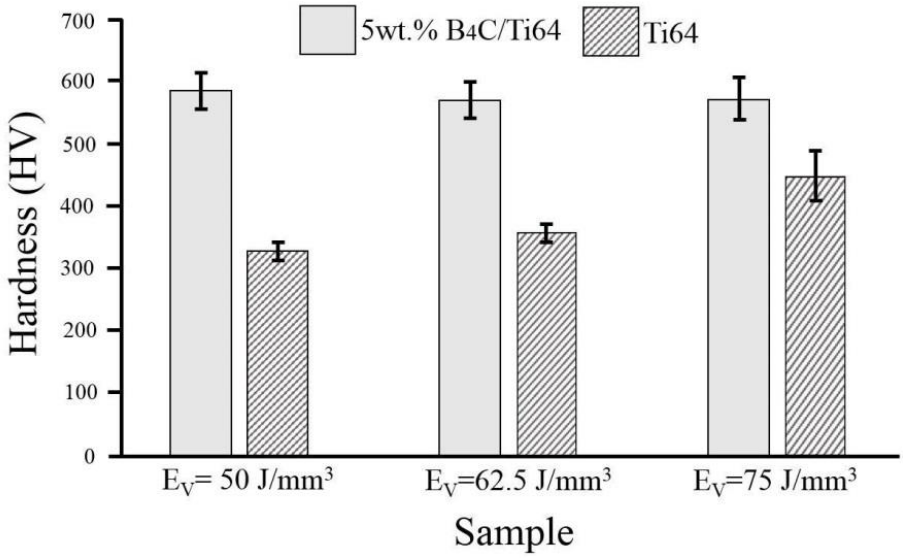

Figure 3-16 The variation of microhardness as a function of the volumetric laser energy density for the SLMed 5wt.% B_4C/Ti64 composite and Ti64 parts fabricated by the same process parameters.

3.4 Conclusions

In this research, selective laser melting (SLM) process was employed to fabricate titanium matrix composites (TMCs) from 5wt.% B_4C/Ti64 powder feedstock prepared by the ball milling process. For a better understanding of the microstructural evolutions in the SLM fabricated TMCs, the same powder system was subjected to the arc melting process with two different cooling rates. The main findings may be summarized as follows:

(i) The powder feedstock developed by 90 min of ball milling was found to meet the characteristics desired for the SLM process. While the guest B_4C particles were fully decorating the surface of the host Ti-6Al-4V (Ti64) particles, the original spherical shape of the Ti64 particles was preserved.

(ii) Microstructural observations revealed the dissolution of B_4C particles rather than melting. Higher laser energy densities led to the enhanced dissolution and elevated in-situ reaction between the B_4C particles and the surrounding molten

Ti64. Moreover, for a given laser energy density, finer B_4C particles experienced faster dissolution rate in the surrounding molten media.

(iii) At relatively low laser energy density of 50 J/mm^3, the TMC microstructure contained un-melted/partially melted host Ti64 particles surrounded by the partially dissolved guest B_4C particles. This was attributed to the limited heat diffusivity from the decorating B_4C particles towards the Ti64 powder particles. The elevated heat input provided by higher energy densities paved the way for the full melting of Ti64 particles.

(iv) Although the arc-melted TMCs cooled in the graphite crucible (near-equilibrium condition) contained coarse primary TiB phase, the SLM processed components were free from this type of TiB. Due to the noticeably narrow solidification range (12 K) for the formation of primary TiB in the full equilibrium condition, the SLM process with non-equilibrium nature inhibited the formation of this phase. The SLM processed microstructure was also extremely finer than the arc-melted cases.

(v) Incorporation of B_4C particles into the Ti64 matrix effectively enhanced the hardness of the fabricated composites through the in-situ formation of TiB and TiC reinforcements. Depending on the applied volumetric energy density, the TMCs showed 30-80% increase in the microhardness compared to the monolithic Ti64 parts processed with the same parameters.

3.5 References

[1] L. Xiao, W. Lu, J. Qin, Y. Chen, D. Zhang, M. Wang, F. Zhu, B. Ji, Creep behaviors and stress regions of hybrid reinforced high temperature titanium matrix composite, Composites Science and Technology 69(11) (2009) 1925-1931.

[2] J. Yang, H. Yu, J. Yin, M. Gao, Z. Wang, X. Zeng, Formation and control of martensite in Ti-6Al-4V alloy produced by selective laser melting, Materials & Design 108 (2016) 308-318.

[3] G. Chen, C. Ren, X. Qin, J. Li, Temperature dependent work hardening in Ti–6Al–4V alloy over large temperature and strain rate ranges: Experiments and constitutive modeling, Materials & Design 83 (2015) 598-610.

[4] M. Galindo-Fernandez, K. Mumtaz, P. Rivera-Diaz-del-Castillo, E. Galindo-Nava, H. Ghadbeigi, A microstructure sensitive model for deformation of Ti-6Al-4V describing Cast-and-Wrought and Additive Manufacturing morphologies, Materials & Design 160 (2018) 350-362.

[5] J.-Y. Xia, L.-J. Chai, H. Wu, Y. Zhi, Y.-N. Gou, W.-J. Huang, N. Guo, EBSD Study of Microstructural and Textural Changes of Hot-Rolled Ti–6Al–4V Sheet After Annealing at 800 °C, Acta Metallurgica Sinica (English Letters) 31(11) (2018) 1215-1223.

[6] T. Wang, L. Zeng, Z. Li, L. Chai, T. Cheng, L. Zhang, V. Fallah, Q. Dong, Z. Yao, Influences of Laser Surface Alloying with Cr on Microstructural Characteristics and Hardness of Pure Ti, Metallurgical and Materials Transactions A 50(8) (2019) 3794-3804.

[7] L. Chai, H. Wu, Z. Zheng, H. Guan, H. Pan, N. Guo, B. Song, Microstructural characterization and hardness variation of pure Ti surface-treated by pulsed laser, Journal of Alloys and Compounds 741 (2018) 116-122.

[8] Y. Feng, K. Feng, C. Yao, Z. Li, J. Sun, Microstructure and properties of in-situ synthesized (Ti3Al+ TiB)/Ti composites by laser cladding, Materials & Design 157 (2018) 258-272.

[9] M. Taya, R.J. Arsenault, Metal matrix composites: thermomechanical behavior, Elsevier2016.

[10] S.C. Tjong, Recent progress in the development and properties of novel metal matrix nanocomposites reinforced with carbon nanotubes and graphene nanosheets, Materials Science and Engineering: R: Reports 74(10) (2013) 281-350.

[11] J. Vreeling, V. Ocelik, J.T.M. De Hosson, Ti–6Al–4V strengthened by laser melt injection of WC p particles, Acta Materialia 50(19) (2002) 4913-4924.

[12] Y. Pei, V. Ocelik, J.T.M. De Hosson, SiC p/Ti6Al4V functionally graded materials produced by laser melt injection, Acta Materialia 50(8) (2002) 2035-2051.

[13] J. Candel, V. Amigó, J. Ramos, D. Busquets, Sliding wear resistance of TiC p reinforced titanium composite coating produced by laser cladding, Surface and Coatings Technology 204(20) (2010) 3161-3166.

[14] F. Wang, J. Mei, X. Wu, Direct laser fabrication of Ti6Al4V/TiB, Journal of materials processing technology 195(1) (2008) 321-326.

[15] S. Wen, K. Chen, W. Li, Y. Zhou, Q. Wei, Y. Shi, Selective laser melting of reduced graphene oxide/S136 metal matrix composites with tailored microstructures and mechanical properties, Materials & Design 175 (2019) 107811.

[16] S. Madtha, C. Lee, K. Ravi Chandran, Physical and mechanical properties of nanostructured titanium boride (TiB) ceramic, Journal of the American Ceramic Society 91(4) (2008) 1319-1321.

[17] J. Li, L. Wang, J. Qin, Y. Chen, W. Lu, D. Zhang, Thermal stability of in situ synthesized (TiB+ La2O3)/Ti composite, Materials Science and Engineering: A 528(15) (2011) 4883-4887.

[18] J. DuttaMajumdar, L. Li, Development of titanium boride (TiB) dispersed titanium (Ti) matrix composite by direct laser cladding, Materials Letters 64(9) (2010) 1010-1012.

[19] K.R. Chandran, K. Panda, S. Sahay, TiB w-reinforced Ti composites: Processing, properties, application prospects, and research needs, Jom 56(5) (2004) 42-48.

[20] S. Li, K. Kondoh, H. Imai, B. Chen, L. Jia, J. Umeda, Y. Fu, Strengthening behavior of in situ-synthesized (TiC–TiB)/Ti composites by powder metallurgy and hot extrusion, Materials & Design 95 (2016) 127-132.

[21] D. Ni, L. Geng, J. Zhang, Z. Zheng, Fabrication and tensile properties of in situ TiBw and TiCp hybrid-reinforced titanium matrix composites based on Ti–B4C–C, Materials Science and Engineering: A 478(1-2) (2008) 291-296.

[22] E. Fereiduni, M. Elbestawi, Process-structure-property relationships in additively manufactured metal matrix composites, Additive Manufacturing of Emerging Materials, Springer2019, pp. 111-177.

[23] E. Fereiduni, M. Yakout, M. Elbestawi, Laser-based additive manufacturing of lightweight metal matrix composites, Additive Manufacturing of Emerging Materials, Springer2019, pp. 55-109.

[24] F. Bartolomeu, M. Buciumeanu, E. Pinto, N. Alves, F. Silva, O. Carvalho, G. Miranda, Wear behavior of Ti6Al4V biomedical alloys processed by selective laser melting, hot pressing and conventional casting, Transactions of Nonferrous Metals Society of China 27(4) (2017) 829-838.

[25] F. Bartolomeu, S. Faria, O. Carvalho, E. Pinto, N. Alves, F.S. Silva, G. Miranda, Predictive models for physical and mechanical properties of Ti6Al4V produced by Selective Laser Melting, Materials Science and Engineering: A 663 (2016) 181-192.

[26] I. Gibson, D.W. Rosen, B. Stucker, Additive manufacturing technologies, Springer2014.

[27] T. DebRoy, H. Wei, J. Zuback, T. Mukherjee, J. Elmer, J. Milewski, A.M. Beese, A. Wilson-Heid, A. De, W. Zhang, Additive manufacturing of metallic components–process, structure and properties, Progress in Materials Science 92 (2018) 112-224.

[28] J. Günther, S. Leuders, P. Koppa, T. Tröster, S. Henkel, H. Biermann, T. Niendorf, On the effect of internal channels and surface roughness on the high-cycle fatigue performance of Ti-6Al-4V processed by SLM, Materials & Design 143 (2018) 1-11.

[29] S. Liu, Y.C. Shin, Additive manufacturing of Ti6Al4V alloy: A review, Materials & Design 164 (2019) 107552.

[30] T. Voisin, N.P. Calta, S.A. Khairallah, J.-B. Forien, L. Balogh, R.W. Cunningham, A.D. Rollett, Y.M. Wang, Defects-dictated tensile properties of selective laser melted Ti-6Al-4V, Materials & Design 158 (2018) 113-126.

[31] S. Pal, G. Lojen, V. Kokol, I. Drstvensek, Evolution of metallurgical properties of Ti-6Al-4V alloy fabricated in different energy densities in the Selective Laser Melting technique, Journal of Manufacturing Processes 35 (2018) 538-546.

[32] B. Jackson, R. Torrens, L. Bolzoni, F. Yang, M. Fry, A. Mukhtar, Additive manufacturing of Ti-6Al-4V with added boron: microstructure and hardness modification, Key Engineering Materials, Trans Tech Publ, 2018, pp. 165-173.

[33] G. Kasperovich, J. Haubrich, J. Gussone, G. Requena, Correlation between porosity and processing parameters in TiAl6V4 produced by selective laser melting, Materials & Design 105 (2016) 160-170.

[34] H. Gong, K. Rafi, H. Gu, G.J. Ram, T. Starr, B. Stucker, Influence of defects on mechanical properties of Ti–6Al–4 V components produced by selective laser melting and electron beam melting, Materials & Design 86 (2015) 545-554.

[35] D.K. Do, P. Li, The effect of laser energy input on the microstructure, physical and mechanical properties of Ti-6Al-4V alloys by selective laser melting, Virtual and Physical Prototyping 11(1) (2016) 41-47.

[36] A. Canakci, F. Arslan, T. Varol, Effect of volume fraction and size of B4C particles on production and microstructure properties of B4C reinforced aluminium alloy composites, Materials Science and Technology 29(8) (2013) 954-960.

[37] L. Thijs, F. Verhaeghe, T. Craeghs, J. Van Humbeeck, J.-P. Kruth, A study of the microstructural evolution during selective laser melting of Ti–6Al–4V, Acta Materialia 58(9) (2010) 3303-3312.

[38] U.S. Bertoli, A.J. Wolfer, M.J. Matthews, J.-P.R. Delplanque, J.M. Schoenung, On the limitations of volumetric energy density as a design parameter for selective laser melting, Materials & Design 113 (2017) 331-340.

[39] W. Xiong, L. Hao, Y. Li, D. Tang, Q. Cui, Z. Feng, C. Yan, Effect of selective laser melting parameters on morphology, microstructure, densification and mechanical properties of supersaturated silver alloy, Materials & Design 170 (2019) 107697.

[40] R. Casati, J. Lemke, M. Vedani, Microstructure and Fracture Behavior of 316L Austenitic Stainless Steel Produced by Selective Laser Melting, Journal of Materials Science & Technology 32(8) (2016) 738-744.

[41] B. Cheng, S. Shrestha, K. Chou, Stress and deformation evaluations of scanning strategy effect in selective laser melting, Additive Manufacturing 12 (2016) 240-251.

[42] I. ISO, 9276-6 Representation of Results of Particle Size Analysis—Part 6: Descriptive and Quantitative Representation of Particle Shape and Morphology, ISO Geneva:, 2008.

[43] N. Karapatis, G. Egger, P. Gygax, R. Glardon, Optimization of powder layer density in selective laser sintering, 1999 International Solid Freeform Fabrication Symposium, 1999.

[44] R.U. Din, Q.A. Shafqat, Z. Asghar, G. Zahid, A. Basit, A. Qureshi, T. Manzoor, M.A. Nasir, F. Mehmood, K.I. Hussain, Microstructural Evolution, Powder Characteristics, Compaction Behavior and Sinterability of Al 6061–B 4 C Composites as a Function of Reinforcement Content and Milling Times, Russian Journal of Non-Ferrous Metals 59(2) (2018) 207-222.

[45] E.C. Abdullah, D. Geldart, The use of bulk density measurements as flowability indicators, Powder Technology 102(2) (1999) 151-165.

[46] S. Sivasankaran, K. Sivaprasad, R. Narayanasamy, V.K. Iyer, An investigation on flowability and compressibility of AA 6061100− xx wt.% TiO2 micro and nanocomposite powder prepared by blending and mechanical alloying, Powder technology 201(1) (2010) 70-82.

[47] X. Li, G. Ji, Z. Chen, A. Addad, Y. Wu, H. Wang, J. Vleugels, J. Van Humbeeck, J.-P. Kruth, Selective laser melting of nano-TiB 2 decorated AlSi10Mg alloy with high fracture strength and ductility, Acta Materialia 129 (2017) 183-193.

[48] M. Chen, X. Li, G. Ji, Y. Wu, Z. Chen, W. Baekelant, K. Vanmeensel, H. Wang, J.-P. Kruth, Novel composite powders with uniform TiB2 nano-particle distribution for 3D printing, Applied Sciences 7(3) (2017) 250.

[49] D. Hasselman, L.F. Johnson, Effective thermal conductivity of composites with interfacial thermal barrier resistance, Journal of Composite Materials 21(6) (1987) 508-515.

[50] S. Polat, Y. Sun, E. Çevik, H. Colijn, Evaluation of thermal conductivity of GNPs-doped B4C/Al-Si composites in terms of interface interaction and electron mobility, Diamond and Related Materials (2019) 107457.

[51] I. Solodkyi, I. Bogomol, P. Loboda, D. Batalu, A.M. Vlaicu, P. Badica, Floating zone partial re-melting of B4C infiltrated with molten Si, Ceramics International 43(17) (2017) 14718-14725.

[52] C. Wood, D. Emin, P.E. Gray, Thermal conductivity behavior of boron carbides, Physical Review B 31(10) (1985) 6811.

[53] M. Boivineau, C. Cagran, D. Doytier, V. Eyraud, M.-H. Nadal, B. Wilthan, G. Pottlacher, Thermophysical properties of solid and liquid Ti-6Al-4V (TA6V) alloy, International journal of thermophysics 27(2) (2006) 507-529.

[54] A. Ghasemi, M. Pouranvari, Fast Isothermal Solidification During Transient Liquid Phase Bonding of a Nickel Alloy Using Pure Copper Filler Metal: Solubility vs Diffusivity, Metallurgical and Materials Transactions A 50(5) (2019) 2235-2245.

[55] M. Xia, A. Liu, Z. Hou, N. Li, Z. Chen, H. Ding, Microstructure growth behavior and its evolution mechanism during laser additive manufacture of in-situ reinforced (TiB+ TiC)/Ti composite, Journal of Alloys and Compounds 728 (2017) 436-444.

[56] A. Ghasemi, M. Pouranvari, Intermetallic phase formation during brazing of a nickel alloy using a Ni–Cr–Si–Fe–B quinary filler alloy, Science and Technology of Welding and Joining 24(4) (2019) 342-351.

[57] S.G. Banadkouki, E. Fereiduni, Effect of prior austenite carbon partitioning on martensite hardening variation in a low alloy ferrite–martensite dual phase steel, Materials Science and Engineering: A 619 (2014) 129-136.

[58] E. Fereiduni, S.G. Banadkouki, Ferrite hardening response in a low alloy ferrite–martensite dual phase steel, Journal of Alloys and Compounds 589 (2014) 288-294.

[59] Thermo-Calc Software, TCS Ti/TiAl-based Alloys Thermodynamic Database, version 2.1.

[60] J. Zuback, T. DebRoy, The hardness of additively manufactured alloys, Materials 11(11) (2018) 2070.

Chapter 4 Laser Powder Bed Fusion Processability of Ti-6Al-4V Powder Decorated by B_4C Particles

Complete Citation:

Fereiduni E, Ghasemi A, Elbestawi M, Jadhav SD, Vanmeensel K. Laser powder bed fusion processability of Ti-6Al-4V powder decorated by B_4C particles. Materials Letters. 2021 Aug 1;296:129923.

Abstract

Understanding the laser-powder interaction during laser powder bed fusion (LPBF) of composite systems is vital in producing robust parts. The currently existing mechanically mixed composite powders are unable to meet the requirements of an ideal powder for the LPBF process, even if the metallic particles remain highly spherical with a second constituent attached to them. It was found that the presence of a reinforcing agent (i.e., B_4C) on the surface of metallic particles (i.e., Ti-6Al-4V), rather than its embedment, hinders the full melting of the metallic constituent and deteriorates the powder flowability by creating inter-particle tangling. Despite the significant improvement in the optical absorption caused by the incorporation of the reinforcing agent, the composite powder showed inferior processability compared to the monolithic system.

Keywords: Laser powder bed fusion (LPBF); Metal matrix composite (MMC); Optical absorption; Unmelted/Partially melted Ti-6Al-4V; Effective powder layer thickness.

4.1 Introduction

Metal matrix composites (MMCs) are known as outstanding engineering materials with tailorable properties, having a huge potential to be used in automotive, aerospace, biomedical, and defence industries [1]. Nevertheless, their application has been overshadowed by alloys and superalloys over the past few decades due to the difficulties associated with the processing of MMCs. Their conventional manufacturing methods including casting, pressure/pressureless infiltration, powder metallurgy, chemical, and physical vapor deposition [2] suffer from the inability to fabricate parts with complex-shaped geometries, intricate features, and functionally graded microstructures and properties, which are of high demand in the abovementioned industries [3]. The emergence of the laser powder bed fusion (LPBF) technique as a promising additive manufacturing (AM) technology has recently resolved the difficulties associated with the fabrication of MMCs and renewed the interest in using them [4]. The main obstacle facing the implementation of this unprecedented technology is the lack of commercially available composite powders serving as the starting material. It has been recently shown that almost ideal composite powders (from the LPBF perspective) having spherical metallic powder particles uniformly decorated by the reinforcing agent are achievable through the ball milling process [5, 6]. However, there might be some other factors that need to be considered in the development of an ideal composite powder for the LPBF.

This study realizes one of the major missing factors in developing ideal composite powders for LPBF process via the ball milling technique. For this purpose, 3wt.%B_4C/Ti-6Al-4V composite powder with almost spherical Ti-6Al-4V (Ti64) particles decorated by irregular-shaped B_4C particles was prepared and subjected to laser processing. The results revealed

that the presence of reinforcing agent (i.e., B_4C) on the surface of the metallic particles (i.e., Ti64), rather than its embedment, led to a significantly reduced melting efficiency of the composite powder compared to the monolithic Ti64. This observation unveils the significant contribution of the location of the reinforcing agent on the LPBF processability of MMCs.

4.2 Materials and experimental procedure

The starting materials were Ti64 and B_4C powders with the morphology shown in Figure 4-1(a,b) and a mean particle size of 35 µm and 2 µm, respectively. A composite powder containing 3wt.%B_4C (Figure 4-1(c)) was developed by ball milling of powders at a rotational speed of 200 rpm and mixing time of 2 h. The optical absorption of Ti64, B_4C, and the composite powder was measured by means of diffuse reflectance spectroscopy (DRS), as thoroughly explained in [7]. The flowability and packing density of Ti64 and the developed composite powders were assessed using the FT4 technique, as explained in [8]. An EOS-M280 machine was utilized to fabricate monolithic Ti64 and composite parts. A wide range of volumetric energy densities ($e_V = \frac{P}{\nu \times h \times t}$) was employed to fabricate test samples on a Ti64 build plate preheated to 200 °C (30-300 J/mm^3). The cut and polished sections were etched chemically using Keller's reagent and characterized by optical microscopy (OM) as well as scanning electron microscopy (SEM) equipped with energy dispersive X-ray spectroscopy (EDS) analysis.

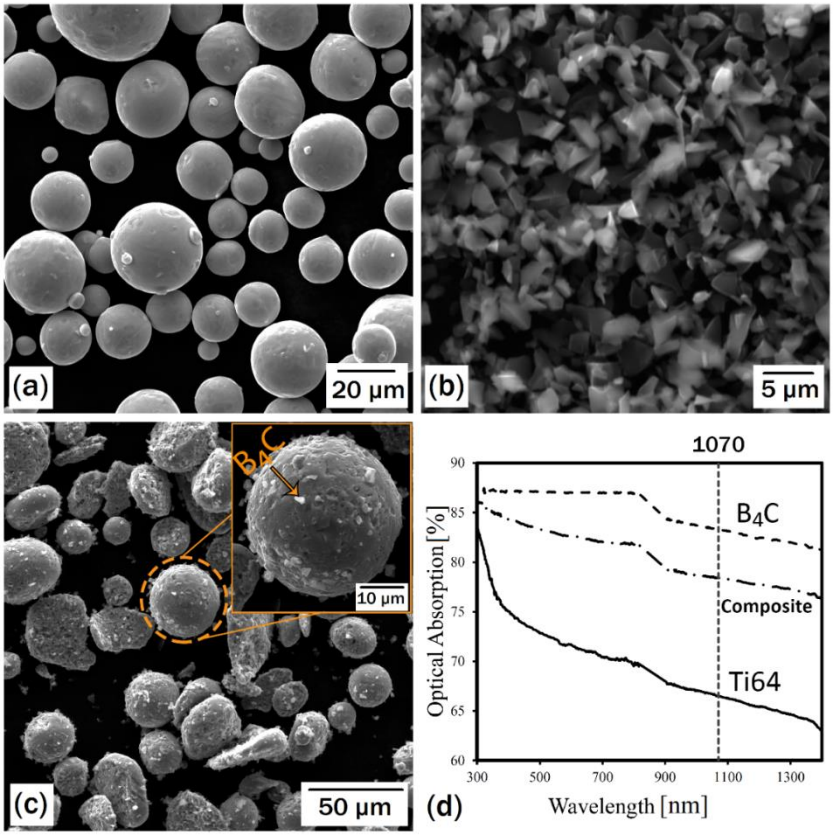

Figure 4-1 SEM micrographs of: (a) Ti64, (b) B_4C, and (c) developed 3wt.%B_4C/Ti64 powders. (d) Optical absorption of powders vs. the wavelength.

4.3 Results and discussions

Referring to Figure 4-1(c), the B_4C constituent has decorated the surface of the Ti64 particles (a surface coverage percentage of ~10%) in the composite powder system. This is inevitably accompanied by the participation of B_4C particles in the laser-powder interactions during the LPBF process. As shown in Figure 4-1(d), this decoration caused a significant increase in optical absorption from 66 to 78%. Although the literature suggests that the enhanced absorption results in better melting kinetics and improved processability [9], the contrary was observed in the 3wt.%B_4C/Ti64 system. As shown in Figure 4-2(a,b), unmelted/partially melted (UM/PM)-Ti64 particles (confirmed by EDS analysis) are

perceptible in the microstructure of composite samples processed with e_V of 33 and 71 J/mm^3. However, these UM/PM particles are absent in monolithic Ti64 samples subjected to the same e_V levels (e.g., e_V of 71 J/mm^3 in Figure 4-2(d)). Microstructural characterization revealed that a noticeably higher e_V (e.g., 297 J/mm^3 in Figure 4-2(c)) is required in the composite scenario for the complete melting of Ti64 particles. Therefore, although the decoration of Ti64 particles by B_4C significantly increases the optical absorption, it surprisingly deteriorates the melting efficiency and processability.

The presence of UM/PM-Ti64 particles in the LPBF-processed composite parts can be traced back to the following factors:

I. *Energy consumption by B_4C particles*: Due to their noticeably higher melting point of 3036 K, B_4C particles do not experience melting but dissolution during the LPBF process [6, 10]. Although the incorporation of B_4C into the Ti64 resulted in the enhanced optical absorption (Figure 4-1(d)) and heat input, a portion of this heat was absorbed by B_4C particles which did not actively participate in the melting (as confirmed by EDS analysis in Figure 4-2(a)). In addition, the dissolution of solid B_4C particles in the molten Ti64 occurs through an endothermic reaction, which further consumes the absorbed energy without assisting the melting. Therefore, higher e_V are required for the complete melting of Ti64 particles and the dissolution of B_4C particles in the composite system.

II. *Different heat inputs under the same process parameters*: Application of $e_V = \frac{P}{\nu \times h \times t}$ for comparing the energy input of two different materials with different optical absorptions and powder bed packing densities can be misleading

since it ignores the effect of these two factors. This equation has been recently modified to take the effect of not only process parameters but also powder properties and laser-powder interactions into consideration. The modified equation is defined as $E_v = \frac{AP}{v \times h \times t_{eff}}$, where A signifies the absorption, and $t_{eff} = \frac{t}{\rho_{bed}}$ denotes the effective powder layer thickness (ρ_{bed} is the powder bed packing density) [7]. A can be found in Figure 4-1(d), and ρ_{bed} is defined as CBD / ρ_{bulk} (ρ_{bulk} signifies the bulk density of the material which is assumed to be 4.43 g/cm^3). According to the modified equation, the energy input in the composite case is slightly lower than that of the monolithic Ti64 under the same process parameters.

The decorating B_4C not only adversely affected the melting efficiency but also deteriorated the flowability of the composite powder by creating mechanical inter-locking among the particles. Referring to Figure 4-1, the composite powder showed ≈ 82% higher specific energy (SE) compared to the monolithic Ti64 powder, meaning a significant decrease in the flowability, and consequently the LPBF processability of the composite system. It is also worth noting that the addition of B_4C to Ti64 has been shown to significantly decrease the fluidity of the melt even if fully dissolved [11]. This can also adversely affect the processability of the fabricated composites.

Table 4-1 Flowability and packing density of powders.

Powder	Powder Flowability	Powder Density
	Specific Energy, SE [mJ/g]	Conditioned Bulk Density, CBD [g/mL]
Ti64	2.1±0.09	2.7±0.02
3wt.%B$_4$C/Ti64	3.8±0.26	2.18±0.00

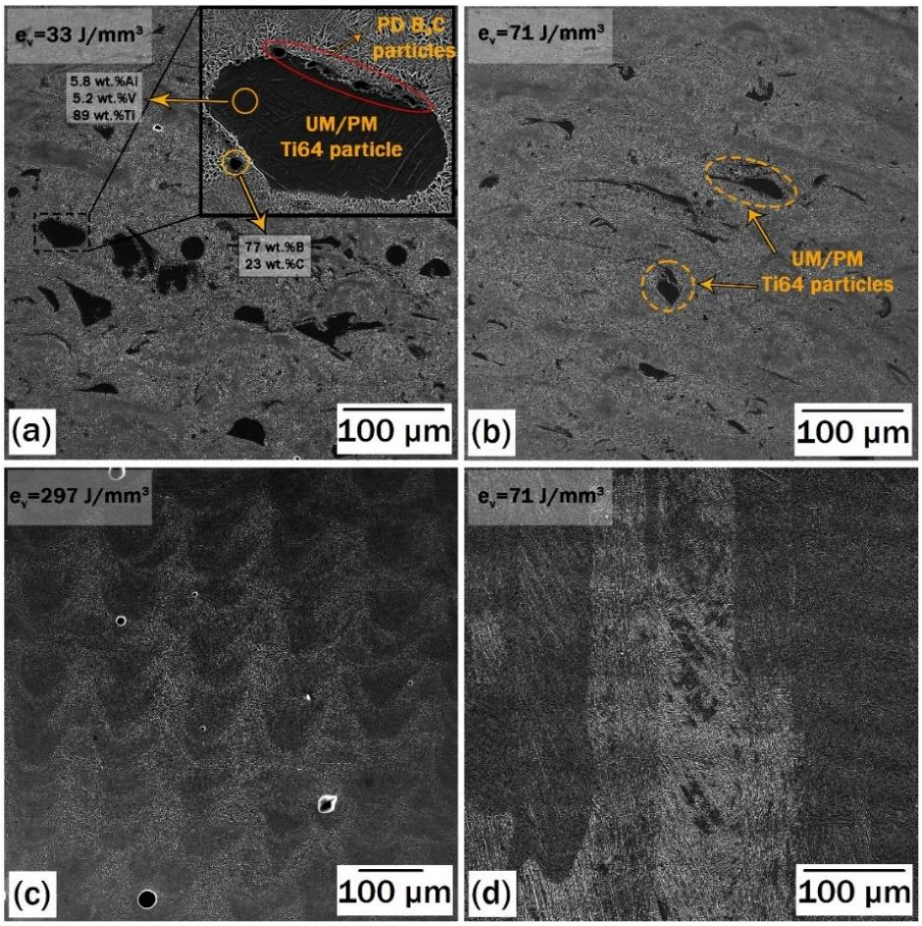

Figure 4-2 SEM micrographs of the LPBF processed: (a-c) 3wt.%B_4C/Ti64 composite powder subjected to various e_V ; and (d) monolithic Ti64 system. "PD" in (a) refers to partially dissolved.

The nature of the matrix and reinforcement(s) in the developed 3wt.%B_4C/Ti64 is significantly dependant on the e_V . As shown in Figure 4-3(a,b), the composites processed at relatively low and medium e_V are both characterized by a cellular/columnar dendritic microstructure. The cores and boundaries are believed to be Ti64 and boron/carbon enriched Ti64, respectively. Although the reaction between the molten Ti64 and the solid B_4C is expected to end up with the formation of TiB and TiC reinforcements [12], such

phases were absent in the microstructure. Since B_4C particles do not find the chance to completely dissolve into the surrounding molten Ti64 in composite systems processed with low and medium e_V , the amounts of boron and carbon are not high enough to cause the formation of TiB and TiC phases. When employing a relatively high e_V of 297 J/mm^3; however, B_4C particles experience a full dissolution into the molten Ti64 during the heating stage. The boron and carbon levels in this scenario are high enough to result in the formation particulate-shape TiC and needle-shape TiB phases from the liquid through eutectic reactions (Figure 4-3(c)) during the cooling stage, as confirmed in [6]. Thus, it is fair to conclude that functionally graded microstructures and properties are achievable through the LPBF process by manipulating process parameters. It is worth noting that cracks were observed in all printed composite parts, examples of such cracks are shown in Figure 4-3(d), and (e). These thermally induced cracks are mainly attributable to the considerably reduced ductility of Ti64 due to the addition of 3wt.%B_4C particles. Nevertheless, the cracking was more severe at low and medium e_V , where UM/PM Ti64 particles existed in the microstructure (Figure 4-3(d)).

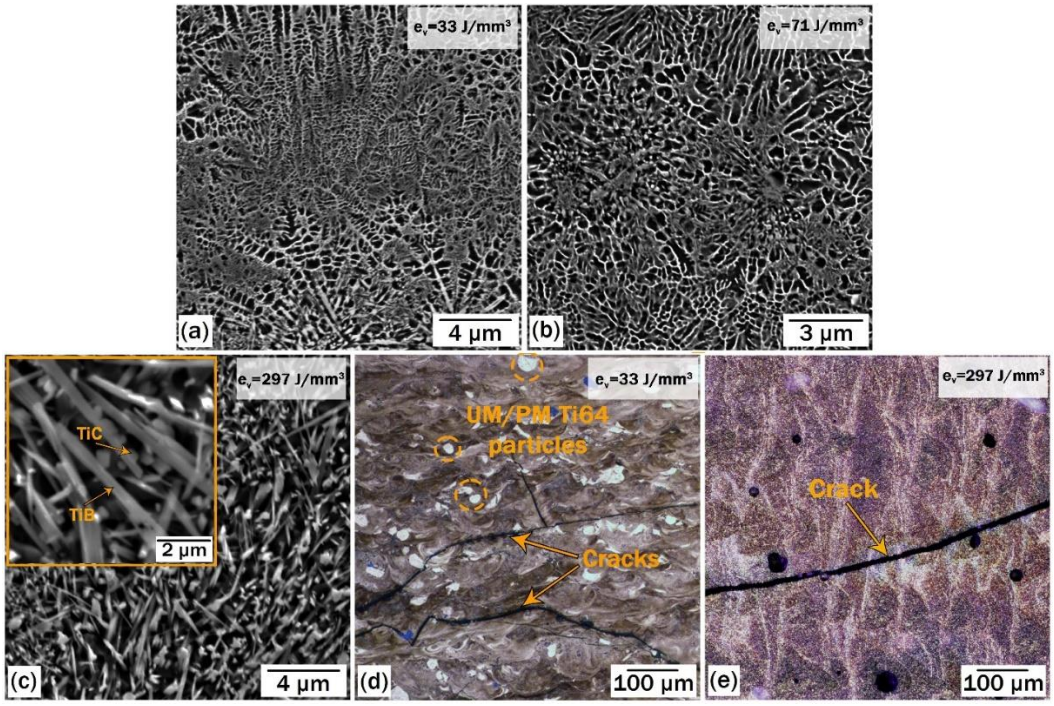

Figure 4-3. SEM micrographs of the LPBF-processed 3wt.%B_4C/Ti64 composite powder subjected to e_V of: (a) 33, (b) 71, and (c) 297 J/mm^3. Optical microscopy images showing cracks in the systems processed by e_V of: (d) 33, and (e) 297 J/mm^3.

4.4 Conclusions

The processability of 3wt.%B_4C/Ti64 composite powder is determined not only by the sphericity of metallic constituent and B_4C-to-Ti64 attachment but also by the location of B_4C particles. Compared to the monolithic Ti64, considerably higher e_V were required in the composite system to completely melt B_4C-decorated Ti64 particles. The detrimental influence of surface-decorating B_4C particles on the processability of the composite system has been attributed to: (i) the dissipation of heat input by B_4C particles, (ii) larger effective powder layer thickness, and (iii) insufficient heat transfer from B_4C to Ti64 particles. To fulfill the existing vacancies and take another step toward finding ideal mechanically-

mixed composite powders, finer reinforcing agents and/or their embedment should be the subject of future studies.

4.5 References

[1] T. Clyne, P. Withers, An introduction to metal matrix composites, Cambridge university press1995.

[2] Y. Nishida, Introduction to Metal Matrix Composites: Fabrication and Recycling, Springer Science & Business Media2013.

[3] P.D. Enrique, Y. Mahmoodkhani, E. Marzbanrad, E. Toyserkani, N.Y. Zhou, In situ formation of metal matrix composites using binder jet additive manufacturing (3D printing), Materials Letters 232 (2018) 179-182.

[4] E. Fereiduni, A. Ghasemi, M. Elbestawi, Selective Laser Melting of Aluminum and Titanium Matrix Composites: Recent Progress and Potential Applications in the Aerospace Industry, Aerospace 7(6) (2020) 77.

[5] E. Fereiduni, A. Ghasemi, M. Elbestawi, Characterization of Composite Powder Feedstock from Powder Bed Fusion Additive Manufacturing Perspective, Materials (Basel) 12(22) (2019) 3673.

[6] E. Fereiduni, A. Ghasemi, M. Elbestawi, Selective laser melting of hybrid ex-situ/in-situ reinforced titanium matrix composites: Laser/powder interaction, reinforcement formation mechanism, and non-equilibrium microstructural evolutions, Materials & Design 184 (2019) 108185.

[7] M. Balbaa, A. Ghasemi, E. Fereiduni, M. Elbestawi, S. Jadhav, J.-P. Kruth, Role of Powder Particle Size on Laser Powder Bed Fusion Processability of AlSi10Mg Alloy, Additive Manufacturing (2020) 101630.

[8] E. Fereiduni, A. Ghasemi, M. Elbestawi, Characterization of composite powder feedstock from powder bed fusion additive manufacturing perspective, Materials 12(22) (2019) 3673.

[9] A. Simchi, The role of particle size on the laser sintering of iron powder, Metallurgical and Materials Transactions B 35(5) (2004) 937-948.

[10] H. Li, Z. Yang, D. Cai, D. Jia, Y. Zhou, Microstructure evolution and mechanical properties of selective laser melted bulk-form titanium matrix nanocomposites with minor B4C additions, Materials & Design 185 (2020) 108245.

[11] J. Wang, X. Guo, L. Wang, W. Lu, The Influence of B4C on the Fluidity of Ti-6Al-4V-xB4C Composites, Materials Transactions (2014) M2014142.

[12] C. Han, R. Babicheva, J.D.Q. Chua, U. Ramamurty, S.B. Tor, C.-N. Sun, K. Zhou, Microstructure and mechanical properties of (TiB+TiC)/Ti composites fabricated in situ via selective laser melting of Ti and B4C powders, Additive Manufacturing 36 (2020) 101466.

Chapter 5 Microstructural characterization and mechanical properties of nano-scale/sub-micron TiB-reinforced titanium matrix composites fabricated by laser powder bed fusion

Abstract

A B_4C/Ti-6Al-4V(Ti64) composite powder containing a minor B_4C content (0.2wt.%) was developed by a novel technique and was subjected to the laser powder bed fusion (L-PBF) process within a wide range of laser powers and scanning speeds to fabricate titanium matrix composite (TMC) parts. The relative density measurement results revealed that almost fully dense TMC parts could be achieved by optimizing the process parameters. Compared to the Ti64 case, slightly higher E_v values were required in the TMC system to achieve the highest relative density. Microstructural characterisation of the TMC parts revealed the formation of large columnar prior β grains containing in-situ formed nano-scale/sub-micron TiB needles homogenously dispersed in a martensitic matrix. While having almost the same ductility, the fabricated TMC parts showed 25, and 8% higher nanohardness, and compressive yield strength, respectively, and 12% lower wear rate than the Ti64 sample. The improved mechanical properties of the TMC part were due to the contribution of several factors including the incorporation of nano-scale/sub-micron TiB reinforcement, the refinement of the martensite α′ laths, and the solid solution strengthening effects of carbon atoms. The contribution of TiB presence and solid solution strengthening was found to be ~87.5%, and ~12.5% in the overall yield strength enhancement of the TMC parts, respectively.

Keywords: Laser powder bed fusion; Titanium matrix composite; Ti-6Al-4V; TiB; Strength; Wear resistance

5.1 Introduction

Ti-6Al-4V (referred to as Ti64 hereafter) is the most widely used titanium alloy with an (α+β) two phase microstructure, which makes of more than half the usage of titanium alloys. This alloy offers a good balance of properties such as high specific strength, adequate stiffness, appropriate high-temperature stability and resistance, good fatigue behavior as well as outstanding corrosion resistance, making it applicable in a wide range of industries such as aerospace, petrochemical, and biomedical [1, 2]. Among these industries, the aerospace sector accounts for >70% of the whole Ti consumption worldwide [3]. Other than these industries, Ti alloys are rarely used in other sectors due to their relatively high cost [4]. Although having numerous benefits, the limited wear resistance of Ti alloys is a major concern when high abrasion and erosion resistance is required [2]. Accordingly, a great deal of attempt has been made in recent decades toward adding alloying elements or incorporating reinforcing particles (ex-situ and in-situ) to/into Ti alloys to improve not only their hardness and strength, but also their wear resistance [5].

In the as-cast condition, the microstructure of Ti64 alloy consists of very coarse prior β grains with sizes in the order of few mm, making it necessary to employ several thermo-mechanical processing steps with the purpose of breaking these coarse grains down to sub-mm or micron length scales [6]. The melting, thermo-mechanical processing and final machining stages employed to produce finished components of Ti alloys have been reported to be very expensive, accounting for approximately 60% of the total cost [7]. A vast majority of research has been carried out in recent decades to reduce the cost of finished Ti products and expand their usage to other industrial sectors. For this purpose, it has been tried out to decrease the number of processing steps of Ti alloys via adding alloying elements which are capable of refining the grain size of the as-cast microstructure.

The refined microstructures will no longer require a number of high-temperature processing steps, leading to a significant drop in the price of manufactured components. Among a wide variety of elements acting as grain refiner in Ti alloys, boron (B) has an incredible grain refining effect and can reduce the as-cast grain size of Ti alloys by an order of magnitude even when existing as minor amounts (e.g., 0.1wt.%) [8]. Although the reduced cost of Ti alloys obtained by the alloy design eliminates the high temperature processing steps, Ti alloy components obtained by conventional manufacturing processes are still expensive. Due to its numerous advantages over traditional manufacturing, additive manufacturing (AM) has become a direct manufacturing technology with applications across a variety of industries [9, 10]. This unprecedented technology provides fabrication of customized and near-net-shape parts with complex shapes, fine features, and unique geometries in one shot, making it economically attractive and of a high interest especially in applications demanding low volume production of relatively expensive materials such as Ti alloys [11-14]. Accordingly, there is a growing global interest in implementing AM technologies providing improved material efficiency and lower cost.

Various AM processes have been emerged in recent decades in which the common theme is the consolidation of the feedstock material in a layer-by-layer manner through the localized melting and subsequent solidification, sharing similarities to the cast microstructures. Direct energy deposition (DED) and powder bed fusion (PBF) are the AM categories most frequently used to fabricate metallic parts. The microstructures of as-deposited Ti64 alloy parts obtained by the DED processes are featured by large columnar prior β grains extended over multiple layers, surrounded by grain boundary α extended along the prior β grain boundaries [15, 16]. The grain boundary α is known as the major

impediment to the ductility by providing a continuous pathway for the crack propagation [17, 18].

Recently, there has been a great interest toward engineering the microstructure via controlling the process parameters during the AM process. Although this strategy has been found to be successful in tailoring the microstructure within a single component in some alloys (e.g. Inconel 718) [19], the low thermal gradients needed for prior β grains of Ti64 alloy to form in an equiaxed morphology is not feasible in the processing space of the DED and PBF techniques [20]. Also, the relatively narrow range of optimum processing window poses a great challenge to the microstructure tailoring through the engineering of process variables. Therefore, researchers have been seeking alternative ways of grain refinement in the AM-fabricated Ti64 alloy. Successful attempts have been made lately to refine the size of prior β grains in AM-fabricated Ti alloys via trace addition of B [16, 20], LaB_6 [21], Si [22], and Be [23]. Due to its significantly high growth restriction factor [24, 25], B has attracted considerable attention for this purpose. In the DED-fabricated B-modified Ti64 alloys, B has been shown to not only refine both the prior β and α grain size, but also eliminate the grain boundary α phase [16]. However, despite these favorable features, the presence of large TiB needles (> 50 μm) textured along the prior β grain boundaries in the B-modified Ti64 alloy subjected to the wire-arc AM process (with relatively lower cooling rate compared to other AM processes) has been shown to increase the anisotropy in the microstructure and mechanical properties, due to the large TiB needles being highly susceptible to cracking under tensile loading [21]. Since the size of TiB needles is dependent on the cooling rate, AM processes with higher cooling rates (e.g., laser powder bed fusion (L-PBF)) can lead to the formation of larger numbers of finer TiB precipitates

with more homogeneous distribution, and consequently reduced anisotropy in the microstructure and mechanical properties.

B and C are known as the most effective grain refiners in Ti alloys. In addition, their presence in Ti alloys can lead to the formation of TiB and TiC phases, which can play a promising role in improving the mechanical properties of Ti alloys [5, 26]. Therefore, minor B_4C (as the source of B and C elements) amount of 0.2wt.% was added to the Ti64 powder in this study to produce the composite powder feedstock. The composite powder was produced by a novel mechanical mixing strategy, causing the flowability and apparent packing to be close to those of the monolithic Ti64 powder. A wide range of process parameters were utilized to fabricate parts out of the composite and monolithic Ti64 powders. The process parameters leading to the highest densification levels were employed to fabricate compression, and wear test specimens. Addition of minor B_4C to the Ti64 was found to improve the hardness, compressive strengths, and wear resistance.

5.2 Materials and Experimental Procedure

5.2.1 Starting materials and preparation of the composite powder feedstock

The starting powders used in this research were gas atomized Ti64 alloy and B_4C with the nominal chemical compositions reported in [27]. A composite powder feedstock containing 0.2 wt.%B_4C (the rest is Ti64) as the starting reinforcing agent was developed using a novel approach benefitting from the advantages of both regular mixing and ball milling processes. Production of each 300 g of composite powder by this technique involved adding 20 g of 2 h-ball milled 3wt.%B_4C/Ti64 composite powder to 280 g of monolithic Ti64 powder, followed by regular mixing for 2 h. The mixing of powders was performed using a high-performance planetary Pulverisette 6 machine operating at a fixed

rotational speed of 200 rpm. The ball-to-powder weight ratio in the ball milling process was set to be 5:1, while the regular mixing was free from balls. The metallic balls added to the system in the ball milling process were made of hardened stainless steel and had a diameter of 10 mm.

5.2.2 Characterization of the powders

The morphology of the starting powders and the produced composite powders were observed using a Vega Tescan scanning electron microscopy (SEM) operating at an accelerating voltage of 20 kV. The optical absorption of Ti64 and B_4C powders as well as the developed composite powder was measured using diffuse reflectance spectroscopy (DRS) technique equipped with an UV-Visible-NIR LAMBDA 950 Perkin Elmer spectrophotometer. The integrating sphere had a diameter of 150 mm and was coated with Spectralon with a spectral resolution of 1 nm. A 100% reflectance standard was used as reference to remove the noise. In order to perform the test, each powder sample was placed in a quartz cuvette and sealed prior to mounting on a Teflon sample holder. The light sources were Deuterium (D2) and Tungsten with the wavelength ranges of 200-320 and 320-2500 nm, respectively. Photon Counting *photomultiplier* tubes (*PMT*) and Lead Sulfide (PbS), applicable in the wavelength ranges of 200-860.8 and 861-2500 nm, respectively were used as detectors. The flowability and packing density of the Ti64 and composite powders were evaluated by the FT4 Freeman powder rheometer with the procedure thoroughly explained in [27, 28].

5.2.3 L-PBF processing

An EOS M280 machine (EOS, Krailling, Germany) equipped with a Yb-fiber laser system delivering power levels of up to 400 W was used in this study. An atmosphere of high

purity Ar gas was applied to reduce the oxygen content in the build chamber and accordingly minimize the oxidation chance. Cubic parts with the dimensions of 10×10×10 mm^3 were printed on a 200 °C-preheated Ti64 build plate (Figure 5-1(a)). Using a fixed layer thickness (t) of 30 µm, and a hatch spacing (h) of 100 µm, varying laser powers (P), and scanning speeds (v) were employed to study the effect of process variables on the quality of the L-PBF fabricated Ti64 and TMC parts (Table 5-1). By considering the process parameters, the volumetric energy density (E_v) is defined as follows [29]:

$$E_v = \frac{P}{vht} \left[\frac{\mathrm{J}}{mm^3}\right] \quad [1]$$

Scanning of layers was conducted using a zigzag scanning strategy, alternating 90° between two successive layers.

Table 5-1 The laser powders and scanning speeds employed to fabricate cubic parts.

Laser Power, P [W]	**Scanning Speed, v [mm/s]**	**E_v [J/mm^3]**
100, 150, 200, 250	400, 600, 800, 1000	33-208

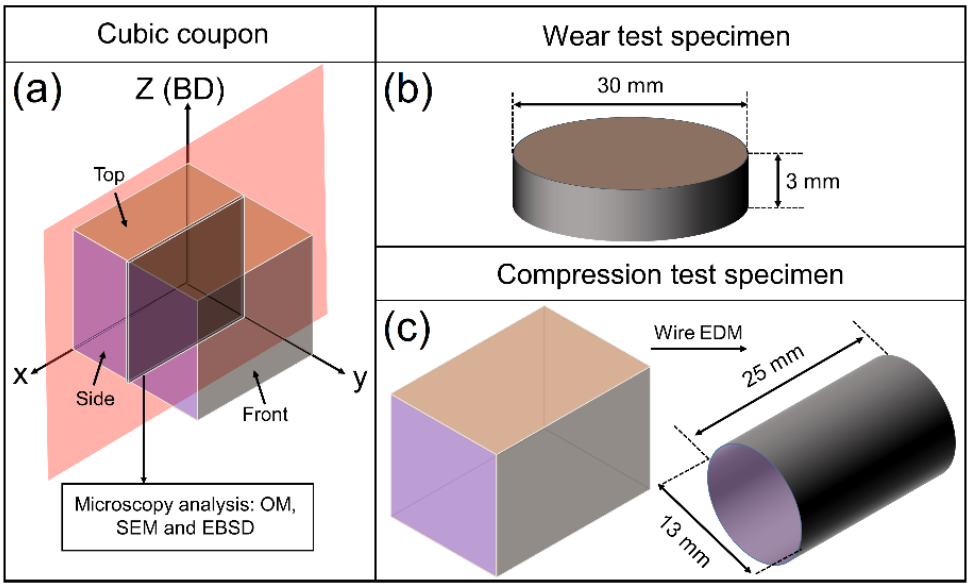

Figure 5-1. Schematic view of the fabricated: (a) cubic samples, (b) wear test specimen, and (c) compression test specimen. As shown in (c), the printed cuboid specimens were subjected to wire electric discharge machining (EDM) to extract cylindrical compression test samples, as per ASTM-E9-09 standard. (Note: The provided dimensions are not proportional to the actual size).

The process parameters leading to the highest relative densities in each case (Ti64 and TMC) were employed to print parts for wear and compression tests (Figure 5-1(b), and (c)). The discs built for the wear test were cut off the plate via wire EDM, ground and then polished according to the standard metallography procedure before testing.

5.2.4 Microstructural observations and oxygen/nitrogen (O/N) analysis

Prior to the microstructural characterization, microhardness measurement and nanoindentation test, the cubic parts sectioned through the front plane (Figure 5-1(a)) were ground and polished according to the standard metallography procedure. The final stage of sample polishing was performed using colloidal silica with an average particle diameter of 0.06 µm. The non-etched sections were observed using a Keyence (Osaka, Japan) VHX digital microscope to compare the defects of the parts qualitatively and quantitatively. The relative density of parts was measured using ImageJ software. The selection of image

analysis technique (instead of Archimedes method) for evaluating the density was due to the fact that the bulk density needed for relative density measurements of the TMC samples was unknown. The reported relative density for each sample represents the average of at least 12 measurements. For microstructural studies, the polished sections were chemically etched using Kroll's Reagent and were observed using a Nikon optical microscopy (OM) as well as a Vega Tescan SEM operating at an accelerated voltage of 10 kV. Electron back-scattered diffraction (EBSD) studies were also carried out to probe the effect of B_4C addition on the grain size, and texture using hardware and software manufactured by FEI. Spatially resolved EBSD maps were acquired at the voltage of 20 keV using a step size of 0.3 µm.

The oxygen/nitrogen (O/N) content of both Ti64 and TMC samples was analyzed using an ON736 model LECO elemental analyzer. Both Ti64 and TMC samples used for this purpose were fabricated using the same process parameters (P=100 W, υ=600 mm/s, h=100 µm, and t=30 µm). Prior to the analysis, calibration was performed using reference specimens.

5.2.5 Mechanical testing

The mechanical properties of fabricated parts were evaluated using microhardness and nanohardness measurements, as well as wear, and room temperature compression tests. Microhardness measurements were conducted using a Matsuzawa microhardness testing machine with a load of 500 g and a dwell time of 10 s. The reported microhardness value for each specimen represents the average of at least 5 distinct measurements. Nanohardness measurements were made using Oliver-Pharr method by utilizing an Anton Paar NHT3 nano-indentation tester (Anton Paar, Graz, Austria) equipped with a Berkovich pyramidal-

shaped indenter tip. Before conducting nanoindentation tests, calibration was performed by using a Fused Silica reference sample. Maximum load of 20 mN, and loading/unloading rate of 40 mN/min were applied on the polished surface of Ti64 and TMC parts in their front view plane. The pause at the maximum load was 10 s for all cases. Compression test was conducted at room temperature using an Instron tensile testing machine as per ASTM E9-19 standard. The strain rate was set to be 0.005 mm/mm/min. The wear performance of samples was evaluated using an Anton Paar standard TRB^3 tribometer in accordance with the ASTM G99-95a standard [30] at room temperature. The employed ball was made of alumina, and had a diameter of 6 mm. The applied normal load was 20 N. The linear speed and acquisition rate were set to be 20 cm/s and 100 Hz, respectively. The tests were performed on three different radii of 4, 6, and 8 mm on the top surface of each sample. Three distinct spots of the worn track at each radius of each sample were analyzed with an Alicona microscope to quantify their depth and width and accordingly calculate the wear rate (W) as follows [31]:

$$W = \frac{V}{F_n \times l} \quad [2]$$

where V is the wear volume, F_n refers to the applied normal force, and l represents the length.

5.3 Results

5.3.1 Composite powder feedstock

Figure 5-2(a) shows the micrograph of the 3wt.%B_4C/Ti64 composite powder prepared by the ball milling of powder constituents for 2 h [32]. As it is evident, Ti64 powder particles in the produced composite powder were either deformed or almost spherical. The morphological change (spherical to quasi-spherical/flattened) of the deformed Ti64

particles occurred during the ball milling process, in which the ductile Ti64 powder particles experienced severe plastic deformation and micro-forging induced by balls [27]. The ball milling process also provided the attachment of irregular-shape B_4C particles to the surface of ductile Ti64 particles, leading to B_4C-decorated Ti64 powder particles. The hard B_4C particles hitting the surface of Ti64 ones during the ball milling stage also caused the roughening of their surface. The 3wt.%B_4C/Ti64 composite powder presented in Figure 5-2(a) was regularly mixed (balls were absent) with the monolithic Ti64 powder (Figure 5-2(b)) to develop the desired composite powder feedstock containing 0.2wt.%B_4C. Figure 5-2(c) presents the micrograph of this composite powder, in which most of the Ti64 powder particles were fully spherical and free from B_4C particles adhered to their surface since:

(i) B_4C particles were well bonded to the surface of Ti64 particles of the ball-milled 3wt.%B_4C/Ti64 composite powder. Accordingly, they did not find the chance to attach to the Ti64 powder particles added to the system in the regular mixing stage (second stage).

(ii) The attachment of B_4C particles to the Ti64 powder particles requires an external load which is the impact energy provided by the balls. Due to the absence of balls and consequently the ball-induced impacts in the regular mixing process, this adherence was not facilitated.

The variation in the optical absorption of the Ti64 and B_4C powders as well as the developed 0.2wt.%B_4C/Ti64 composite powder is given in Figure 5-2(d) as a function of the wavelength. At 1070 nm, which is the wavelength of the L-PBF machine used in this work, Ti64 and B_4C powders had optical absorptions of 66 and 83%, respectively [32]. The composite powder showed a laser absorption of 68%, which was slighly higher than that of the Ti64 powder. This can be ascribed to the contribution of two factors:

(i) Addition of only a low content (0.2wt.%) of a highly absorptive powder (B_4C) to the Ti64 powder to produce the composite powder. Based on the mixture rule principle, this addition enhances the absorption of the composite powder since a fraction of the Ti64 powder constituent is replaced by a higher absorptive material [10, 33].

(ii) The modest change in the morphology (shape and surface roughness) of Ti64 powder particles in the portion of composite powder subjected to the ball milling process. This slight deviation in the morphology acted to increase the frequency of interactions and consequently the optical absorption [34].

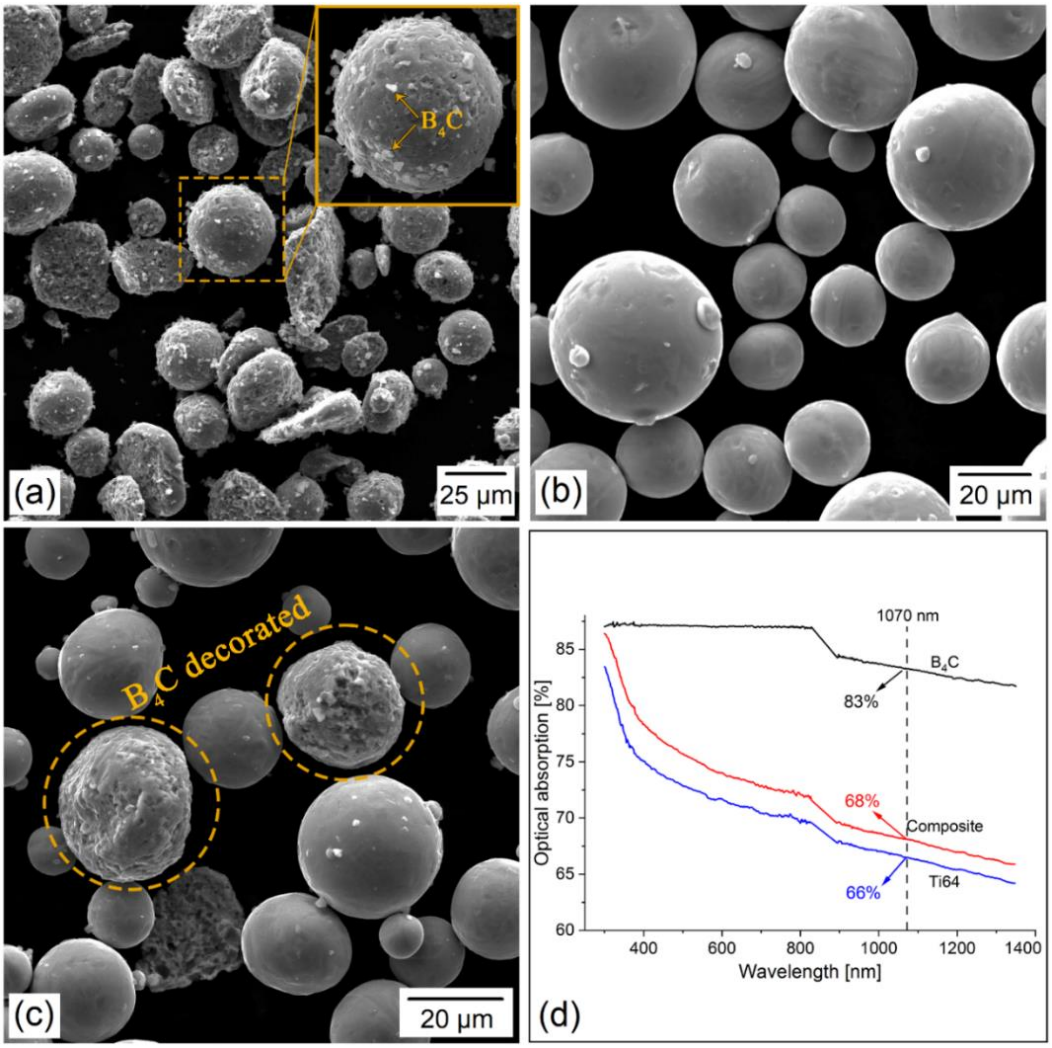

Figure 5-2. SEM micrographs of: (a) 3wt.%B_4C/Ti64 [32], (b) monolithic Ti64 [32], and (c) 0.2wt.%B_4C/Ti64 powders. (d) Optical absorption versus the wavelength for the Ti64 [32] and B_4C [32] powders as well as the developed 0.2wt.%B_4C/Ti64 composite powder. The wavelength of 1070 nm represents the laser wavelength of the L-PBF machine used in this study to fabricate parts.

The results of the FT4 Freeman powder rheometer test for Ti64 and 0.2wt.%B_4C/Ti64 powders are listed in Table 5-2. As can be seen, incorporation of 0.2wt.%B_4C powder to the Ti64 powder led to an increase in the specific energy and adversely affected the flowability (the higher the specific energy, the lower the flowability). Although B_4C particles decorated the surface of only a minor fraction of Ti64 powder particles in the

developed composite powder, they reduced the flowability by increasing the inter-particle friction and acting as mechanical inter-locking sites during the flow of powder particles [27, 32]. However, it should be noted that since most of Ti64 particles maintained their desired spherical shape, the produced composite powder is believed to possess a superior flowability compared to the same composite powder that could be obtained by a single stage of ball milling for 2 h. The developed composite powder also showed a lower conditioned bulk density (CBD) than that of the monolithic Ti64 powder. This can be attributed to two factors: (i) addition of a less-dense material (B_4C) to the Ti64 powder, and (ii) the increased inter-particle friction caused by the presence of irregular-shape B_4C particles [27].

Table 5-2. Flowability and packing density of powders obtained by the FT4 Freeman powder rheometer technique.

Powder	Flowability	Density
	Specific Energy, SE [mJ/g]	Conditioned Bulk Density, CBD [g/mL]
Ti64	2.1 ± 0.09	2.7 ± 0.02
0.2wt.%B_4C/Ti64	3.07 ± 0.05	2.38 ± 0.01

5.3.2 Densification level and processability

Figure 5-3 shows the variation in the density of the L-PBF fabricated Ti64 and TMC parts as a function of the E_v. In both cases, the density first increased, and then followed a decreasing trend by increasing the E_v, leading to the maximum densities being achieved within an optimum range of E_v. The measurements also revealed that a slightly higher E_v was required in the TMC case to obtain the maximum density (50 J/mm^3 for the TMC vs. 42 J/mm^3 for the Ti64 system). To gain a better understanding of the effect of process parameters on the defect formation, non-etched cross-sections of the front view are

provided in Figure 5-4 and Figure 5-5 for Ti64 and TMC samples, respectively. The porosities observed in samples with relatively low E_v are characterized by their irregular shape (Figure 5-4(g) and Figure 5-5(g)), and are known to be caused by the inter-track and/or inter-layer insufficient overlap. At the laser power of 100 W, the decrease in the scanning speed (increase in E_v) led to lower levels of porosity in both Ti64 and TMC parts (Figure 5-4(a), (d) and Figure 5-5(a), (d)). However, compared to the Ti64 case, the TMC system required a lower scanning speed (higher E_v) to yield an almost defect-free part (600 mm/s vs. 800 mm/s in the case of Ti64). Referring to Figure 5-3, the onset of decreasing trend in the density started earlier in Ti64 compared to the TMC scenario (83 vs. 104 J/mm^3). Moreover, a wider range of E_v led to parts with densities>99% in the TMC system. As can be discerned in Figure 5-3, at E_v levels higher than the optimum range for each case, TMCs possessed relative densities higher than those of Ti64 counterparts at any given E_v (see Figure 5-4(f), and Figure 5-5(f)). This suggests that some of the E_v values which are higher than the optimum value for Ti64, are still within the optimum processing window for the TMC system. The porosities formed at relatively high E_v levels featured a spherical/semi-spherical shape (Figure 5-4(c), and Figure 5-5(c)), giving evidence of the keyhole mode as the defect formation mechanism under this condition [35, 36].

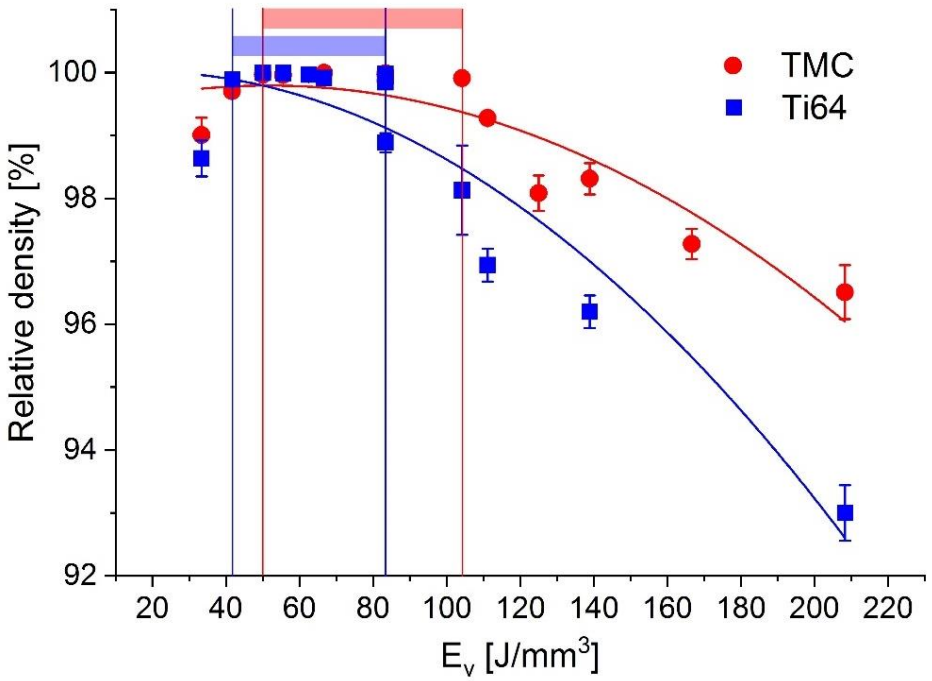

Figure 5-3. The variation of relative density versus the volumetric energy density (E_v) for Ti64 and TMC parts. The designated regions refer to the E_v range in which highly dense samples were achieved.

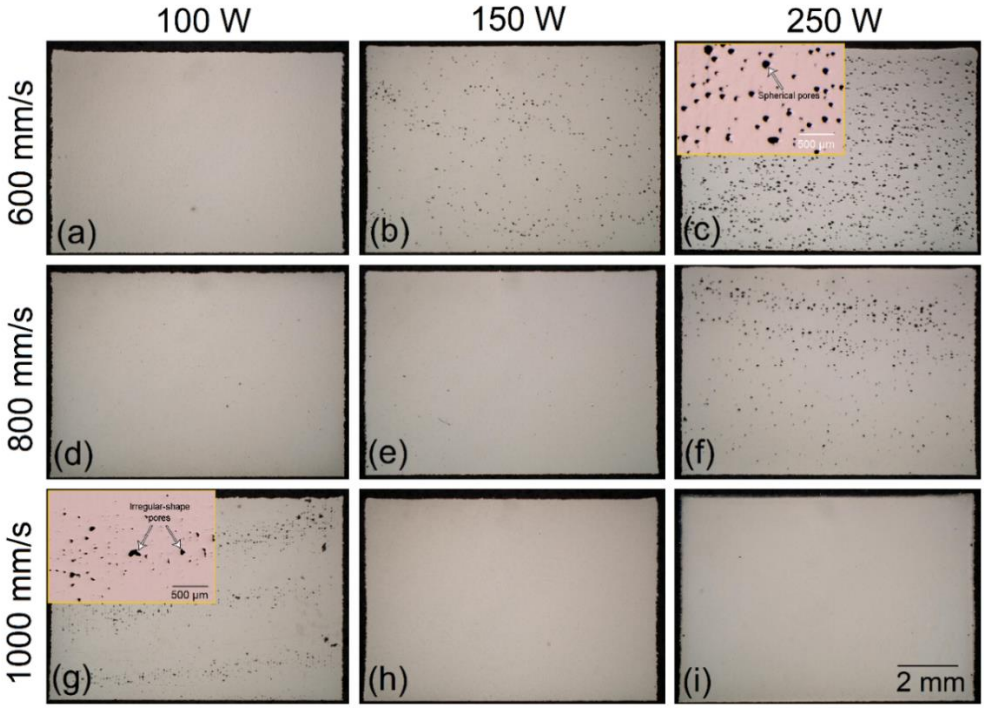

Figure 5-4. Non-etched OM images from the front view cross-sections of Ti64 parts fabricated by different sets of laser powders and scanning speeds.

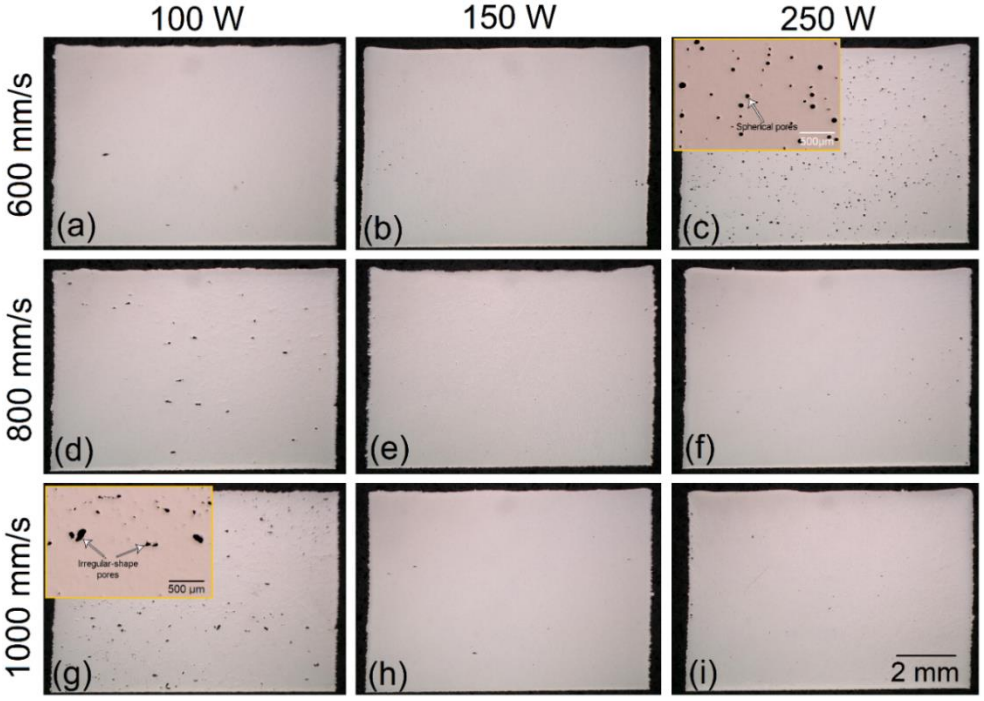

Figure 5-5. Non-etched OM images from the front view cross-sections of TMC parts fabricated by different sets of laser powders and scanning speeds.

5.3.3 Microstructure evolution and phase analysis

Figure 5-6(a), and (f) show 3D view microstructures of the L-PBF processed Ti64 and TMC samples subjected to the same E_v of ~83 J/mm^3, respectively. Higher magnification micrographs of the selected regions from the front and top view sections of Ti64 and TMC parts are also presented in Figure 5-6(b, c), and Figure 5-6(g, h), respectively. Referring to Figure 5-6(a), and (b), the front and top sections revealed the formation of long (several millimeter) prior β grains extended over multiple layers along the building direction. The measurements showed two different size scales for the width of these prior β grains. Accordingly, they were labeled as "wide" and "narrow" prior β grains with a mean width of 86±5.9 µm, and 9.4±3.1 µm, respectively. The narrow grains were located between the wide ones. Microstructural observation of the top view showed that the wide prior β grains had a cubic section and were surrounded by the narrow ones. Figure 5-6(d) shows the EBSD orientation map, while Figure 5-6(e) presents the band contrast image from the front view section of the Ti64 sample. The microstructure was composed of colonies of α′ martensite laths with different inclinations mainly at ~±45° relative to the building direction. Each colony represents several α′ laths having the same variant. Based on the Burgers relationship, twelve different α/α′ variants can be identified for Ti64, accounting for three α/α′ variants for each of the four $<111>_\beta$ directions [37, 38]. The XRD analysis results of the Ti64 sample (Figure 5-7(c)) also featured a fully martensitic microstructure, similar to that of the starting Ti64 powder (Figure 5-7(b)). The formation of a fully martensitic microstructure in the L-PBF processed Ti64 alloy is due to noticeably high cooling rates of the L-PBF process which well exceeds the critical cooling rate for the martensitic phase transformation of this alloy (410 °C/s) [39, 40]. Referring to Figure 5-6(d), the wide and narrow prior β grains were distinguishable since α′ laths transformed

from each narrow prior β grain featured a different orientation and color pattern from those of the neighbor wide grains.

Referring to front and side views of the TMC sample provided in Figure 5-6(f), and (g), typical semi-elliptical shape tracks were perceptible due to the employed scanning strategy alternating 90° between subsequent layers. It is worth noting that although the same etchant was used for both Ti64 and TMC samples, the consolidated tracks were not visible in the Ti64 part. Microstructural characterization of the TMC specimen also revealed the formation of elongated alternate wide and narrow prior β grains (Figure 5-6(f), (g), and (h)). However, compared to the Ti64 sample, narrow prior β grains showed a larger width in the TMC case, and were located along the center of the tracks (Figure 5-6(g)). The mean width for the wide and narrow prior β grains was measured to be 75.5±6.4 μm, and 19.6±4.1 μm, respectively. The sum of the average width of the wide and narrow prior β grains was almost equal to the employed hatch spacing (100 μm) in both Ti64 and TMC cases. However, the narrow prior β grains surrounding the wide ones were more distinctive and had a greater width in the TMC sample compared to the Ti64 one. This can be ascribed to the slight difference between the heat input of the two samples caused by the difference in the optical absorption and the effective powder layer thickness of the powder systems. Referring to the top views presented in Figure 5-6, a chessboard pattern of wide square prior β grains surrounded by narrow β grains along their boundaries was obtained. The same chessboard pattern has been previously observed in several research studies dealing with the L-PBF processing of the Ti64 alloy. The formation of this pattern has been attributed to the employed scanning strategy in which the scan directions rotated 90° between subsequent layers [41, 42].

Similar to the Ti64 sample, a fully martensitic matrix was obtained in the L-PBF fabricated TMC system (Figure 5-6(i), (j)). However, the measurements gave evidence of finer α′ laths in the TMC part. The mean α′ lath width was 0.58±0.14, and 0.48±0.12 μm, while the mean length was 15.6±3.1 and 8.4±7.3 μm for the Ti64 and TMC samples, respectively. The size of the α/α′ laths is an important microstructural feature which governs the mechanical properties of Ti alloys by defining the effective slip length. Smaller α/α′ colonies generally bring about improved mechanical properties [43, 44]. The XRD phase identification of the TMC part indicated no peaks corresponding to the B_4C phase (Figure 5-7(a), (d)). Given the fact that microstructure of L-PBF fabricated TMC was also free from B_4C (Figure 5-6), it can be concluded that these particles have experienced complete melting/dissolution during the process. The XRD analysis of the TMC part also revealed a fully martensitic microstructure, the same as that of the Ti64 sample (Figure 5-7(c), (d)). In addition, no peaks corresponding to the TiB and TiC phases were detected.

Figure 5-8 shows SEM micrographs of the TMC part in which fine features are perceptible in the whole microstructure. Due to their needle-like morphology, these precipitates can be characterized as the TiB phase formed through the reaction between B and Ti elements. Higher magnification micrographs of the track interiors (Figure 5-8(c)) and boundaries (Figure 5-8(d)) revealed that the fine needle-shape TiB precipitates were slightly coarser and had a larger spacing in the boundaries than interiors. This microstructural difference is believed to be the main reason behind observing the tracks in the TMC part, as opposed to the Ti64 counterpart. Within the track interior, TiB needles were mainly oriented toward the center of the melt pool (Figure 5-8(c)). This directionality is known to be due the unidirectional heat flux occurring from center toward the boundaries of the melt pool [59, 73, 74], allowing preferential growth of these needle-shape features opposite to the heat

flux direction. It is noteworthy that the absence of TiB phase in the XRD pattern of the TMC part (Figure 5-7) might be due to its noticeably small size.

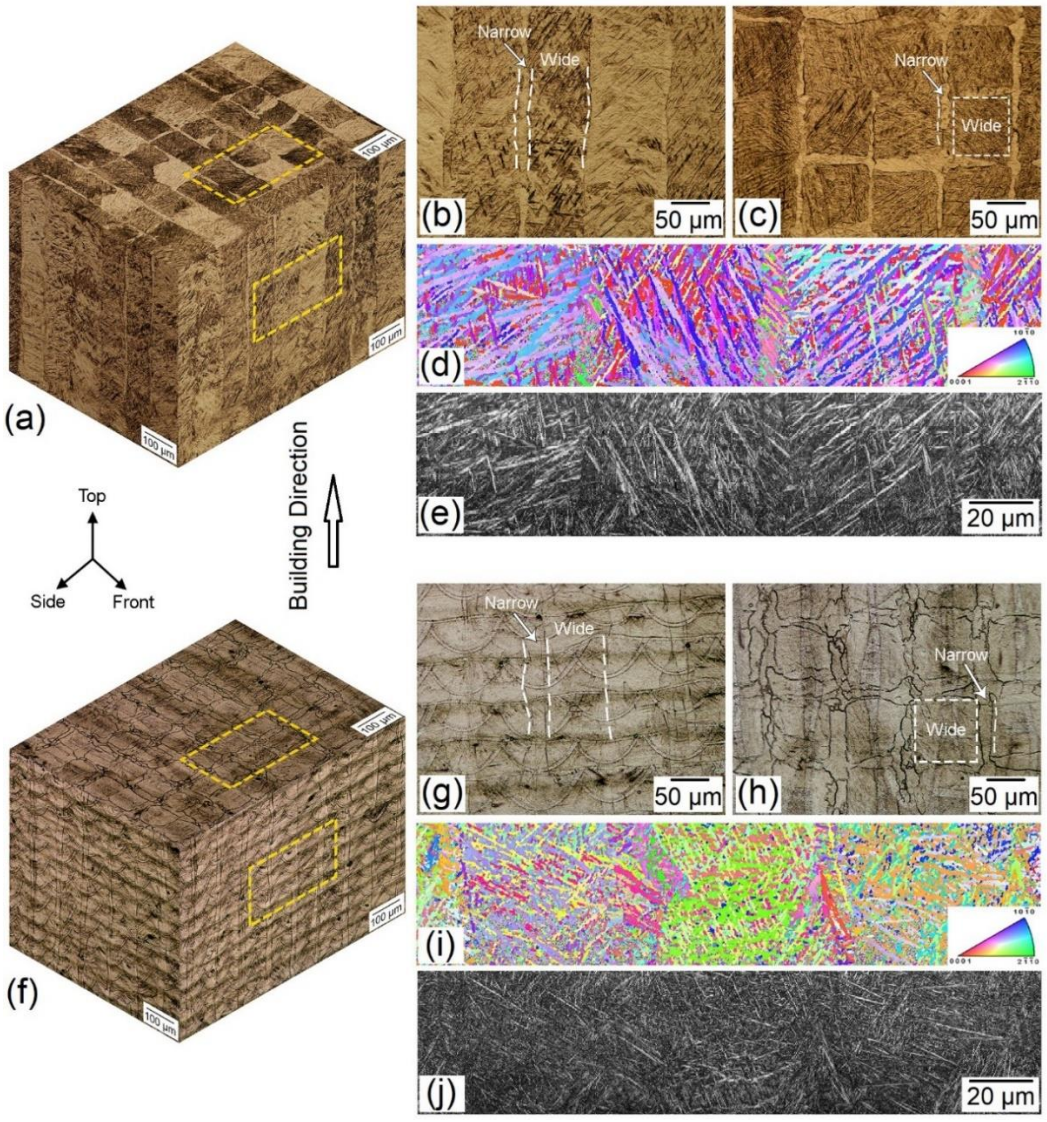

Figure 5-6. (a) OM 3D view of the microstructure of the L-PBF fabricated Ti64; (b), (c) higher magnification OM images of the selected areas of the front and top views shown in (a), respectively; (d) inverse pole figure (IPF-Z), and (e) band contrast EBSD maps of the front view of the Ti64 sample; (f) OM 3D view of the microstructure of the L-PBF fabricated TMC part; (g), (h) higher magnification OM images of the selected areas of the front and top views shown in (f), respectively; (i) inverse pole figure (IPF-Z), and (j) band contrast EBSD maps of the front view of the TMC sample. The employed laser powder, and scanning speed for both Ti64 and TMC samples were 250 W, and 1000 mm/s, respectively.

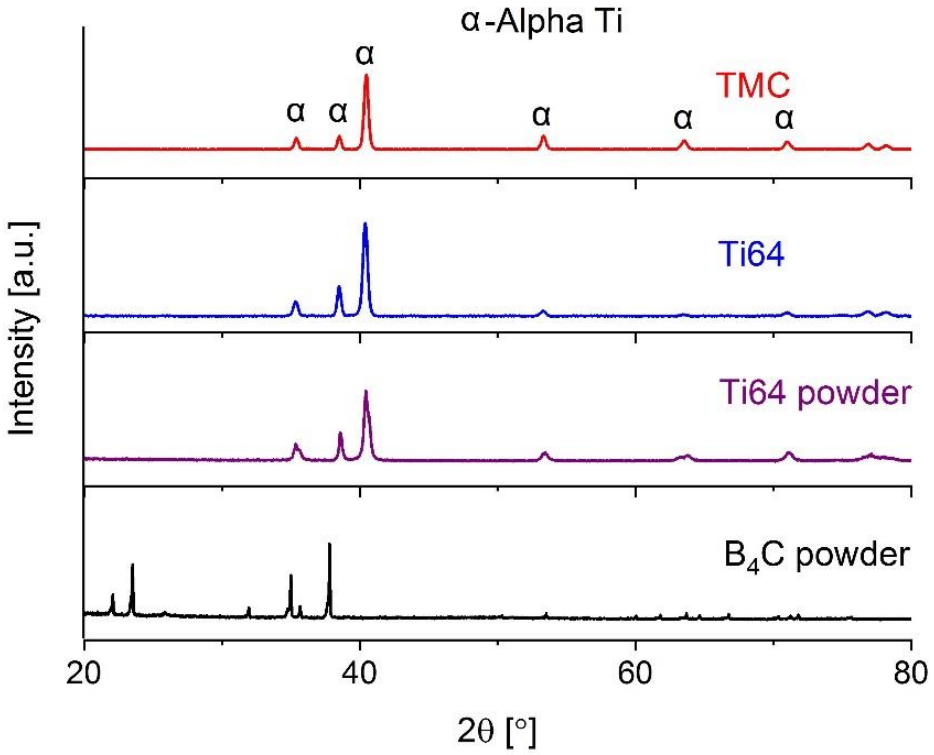

Figure 5-7. XRD patterns of the starting: (a) B_4C, and (b) Ti64 powders, as well as the L-PBF fabricated: (c) Ti64, and (d) TMC parts. Both Ti64 and TMC samples were manufactured using a laser power of 250 W and a scanning speed of 1000 mm/s.

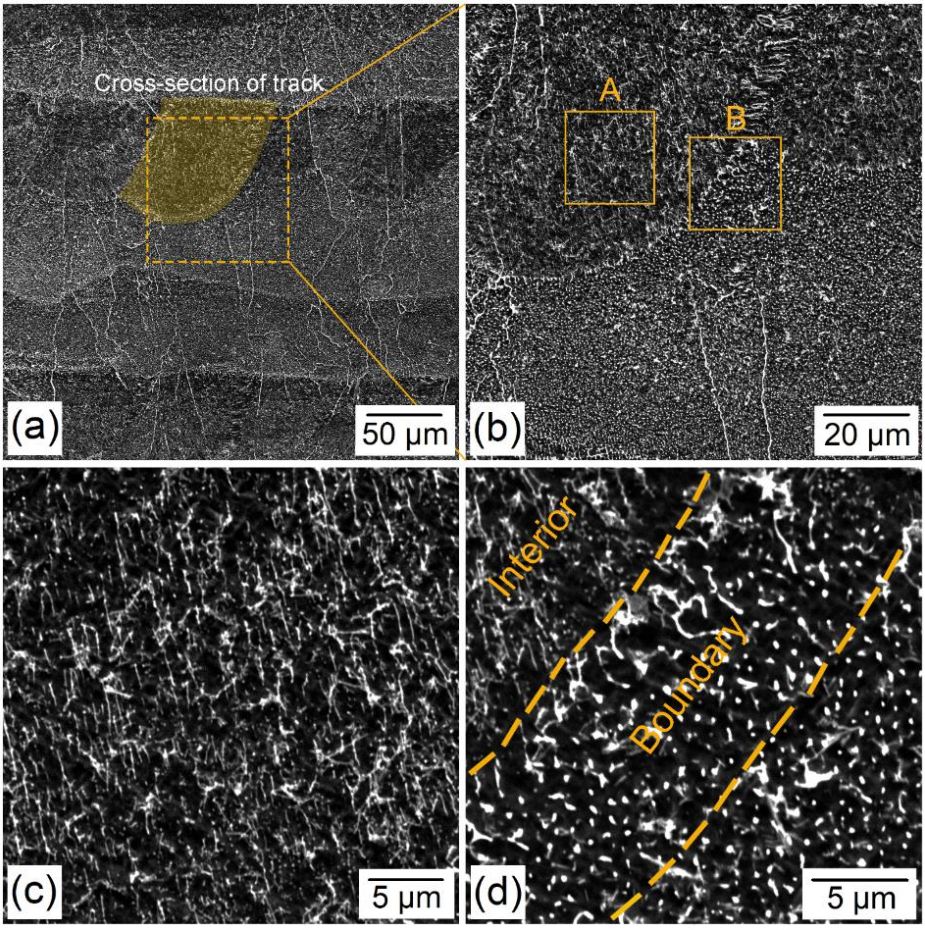

Figure 5-8. Secondary electron (SE)-SEM images from the front view of the L-PBF fabricated TMC part. (a) General view in which the cross-section of a track has been highlighted. Higher magnification micrograph of the selected dashed square in (a) is shown in (b). The square regions marked as "A" and "B" in (b) are shown in a higher magnification in (c) and (d), respectively.

5.3.4 Mechanical Properties

To gain insights into the level of improvement in the mechanical properties caused by the composite fabrication, the hardness, strength, ductility, and wear performance of L-PBF fabricated TMC was evaluated and compared to those of the Ti64 counterpart. As shown in Figure 5-9, the developed TMC showed 5% higher microhardness than that of the Ti64 part. However, nanoindentation measurements revealed a greater difference between the nanohardness values (25%). It is worth noting that compared to the Ti64 part, a smaller

standard deviation was detectable in the nanohardness measurements of the TMC sample. This can be attributed to the enhanced microstructure homogeneity caused by the uniform distribution of fine TiB precipitates in the matrix of the TMC sample.

The typical compressive stress-strain curves of the Ti64 and TMC parts are presented in Figure 5-9(b). Table 5-3 summarizes the most important properties of these two materials obtained from several tests performed on each material. As it is evident, both samples had almost the same ultimate strength (σ_u) and fracture strain (e_f). However, the TMC sample possessed ~8% higher yield strength (σ_y) than the Ti64 counterpart. Therefore, although the incorporation of nano-scale/sub-micron TiB reinforcement into the Ti64 matrix brought about higher hardness, and strength, it did not have an adverse effect on the ductility.

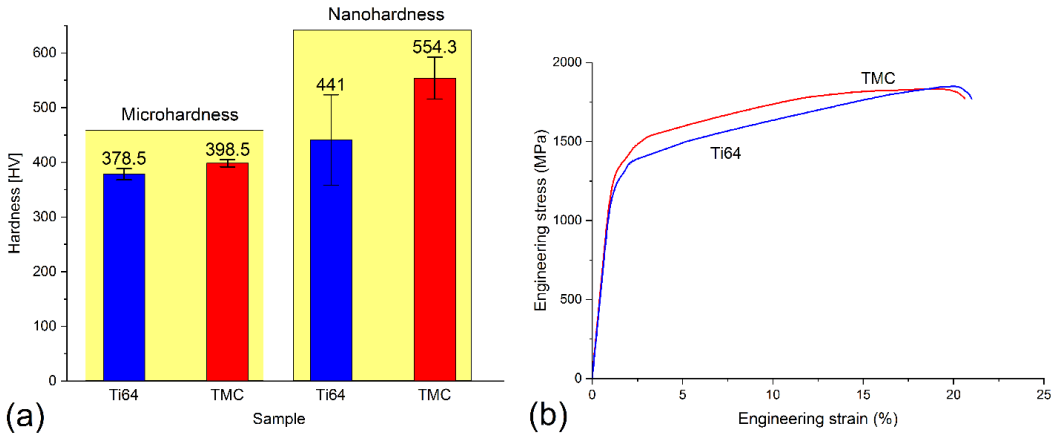

Figure 5-9. (a) The microhardness and nanohardness values, and (b) typical compressive engineering stress-strain curves of the L-PBF fabricated Ti64 and TMC parts.

Table 5-3. Mechanical properties of the L-PBF fabricated Ti64 and TMC parts obtained by compression testing.

Sample	σ_y	σ_u	Young's Modulus, E [GPa]	Fracture Strain, e_f [%]
Ti64	1190	1833	114.4	21
TMC	1284	1850	119.3	20.6

Figure 5-10(a), and (b) shows the variation in the coefficient of friction (COF) for the L-PBF fabricated optimum Ti64 and TMC parts along the sliding distance, respectively. The listed in Table 5-4, there was no significant difference between the COF for the Ti64 and TMC samples. However, the analysis of the wear tested samples revealed a noticable difference between the depth and width of the worn tracks left on the surface of Ti64 and TMC parts. Figure 5-10(c), and (d) illustrates representative depth profiles along the width of the worn tracks for Ti64 and TMC samples across the directions shown in Figure 5-10(d), and (e), respectively. As observed, compared to the Ti64 sample, the TMC featured a shallower depth and a narrower width. The wear rate of samples was calculated by measuring the dimensions of the worn tracks at several spots of each radii and consequently calculating the wear volume. Referring to in Table 5-4, the TMC sample showed 15% lower wear rate than the Ti64 one. This reveals the remarkable influence of incorporated TiB reinforcements on the improved wear resistance of the L-PBF fabricated TMC.

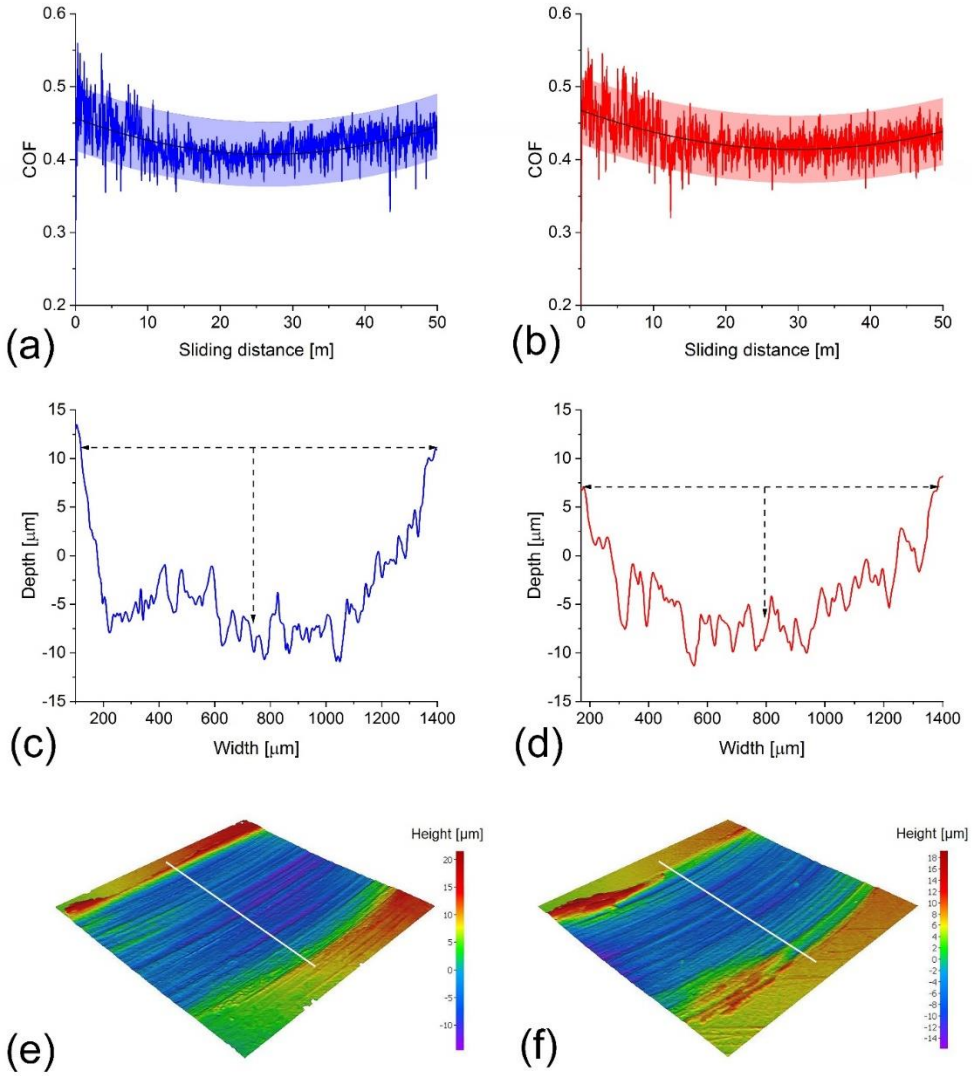

Figure 5-10. (a), (b) the variation of COF versus sliding distance for Ti64 and TMC samples, respectively. Representative depth-width profile of the worn tracks for (c) Ti64, and (d) TMC samples obtained along the paths depicted in the 3D surface topography images in (e), and (f), respectively.

Table 5-4. The coefficient of friction (COF) and wear rate of L-PBF processed Ti64 and TMC samples.

System	COF	Wear rate [$mm^3/(N.m)$]
Ti64	0.4218	1.318×10^{-3}
TMC	0.4314	1.115×10^{-3}

Figure 5-11 shows the SEM micrographs of the wear tracks for Ti64 and TMC samples. The wear tracks of both samples presented wear scars along the sliding direction which is typical of the wear surfaces. In addition, ploughing grooves were observed in both cases. As can be seen in the higher magnification micrographs in Figure 5-11(b), and (d), the wear surface contained delamination cracks in the Ti64 and TMC samples. These cracks are generated as a cause of the high strain levels experienced by the surface of the sample when being in contact with the pin during sliding. As indicated in Figure 5-11(b), and (d), such high strain levels can bring about the delamination of the material during the wear test. A close examination of the wear tracks at several spots of each radii (4, 5, and 8 mm) revealed that compared to the Ti64 sample, the delamination cracks and delamination layers were less intense in the TMC sample. This can be due to the higher hardness and plastic deformation resistivity of the TMC sample caused by the strengthening effects of TiB reinforcements. It has been shown that owing to its high modulus and hardness, incorporation of slight amount of TiB into the Ti alloy matrix can lead to a significant increase in the wear resistance [26].

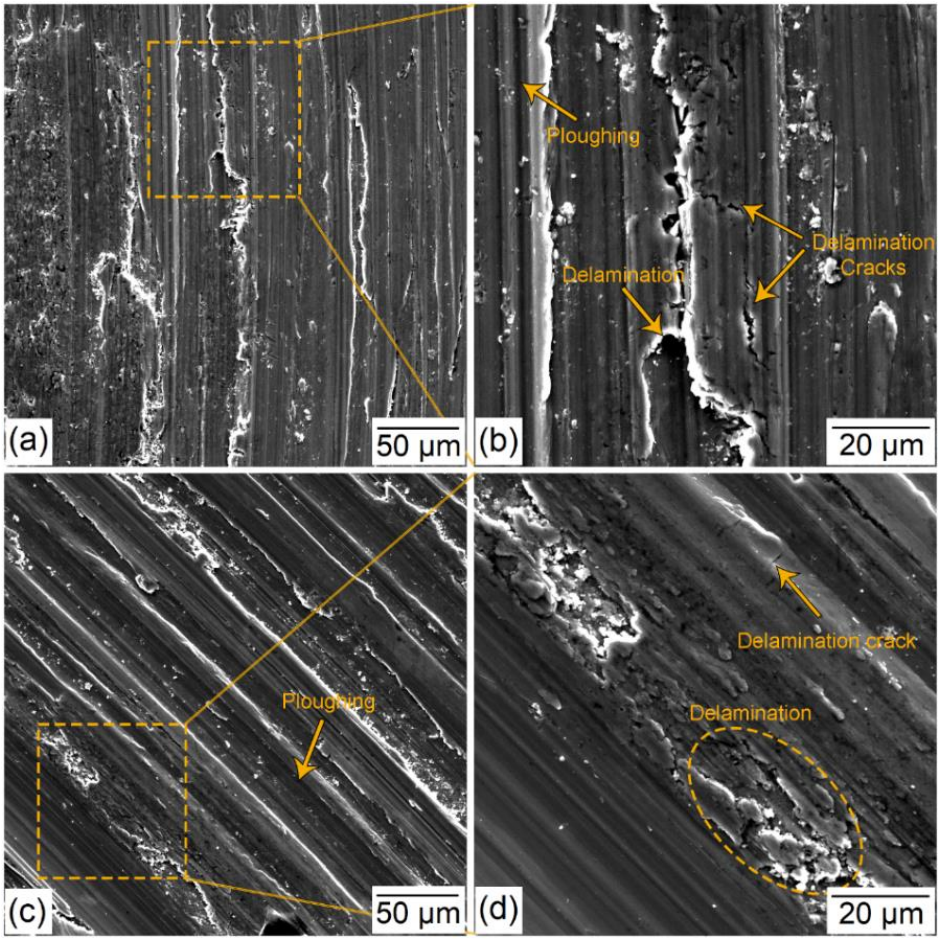

Figure 5-11. SEM images of the wear tracks after the sliding wear test for the L-PBF fabricated: (a), (b) Ti64; and (c), (d) TMC samples. Higher magnification micrographs of the selected regions in (a), and (c) and presented in (b), and (d), respectively.

5.4 Discussions

5.4.1 Processability

As the density measurement results and microstructural observations revealed, addition of a minor amount of B_4C (0.2wt.%) to the Ti64 powder changed its L-PBF processability (Figure 5-3, Figure 5-4, and Figure 5-5). This clearly reveals that not only the process parameters but also the powder characteristics and laser-powder interactions need to be re-examined when dealing with a composite powder system containing even minor amounts

of a second constituent. As proposed in a very recent study on L-PBF processing of VC/H13 system [45], the volumetric energy density calculation equation most frequently used in L-PBF process needs to be revisited for composite powder systems by taking the laser absorptivity (A) and relative powder bed packing density (ρ_{bed}) of the powder also into account as follows:

$$e_v = (A \times \rho_{bed}) E_v \quad [3]$$

where e_v represents the modified volumetric energy density, and ρ_{bed} is defined as CBD/ρ_{bulk} (ρ_{bulk} signifies the bulk density of the material). This equation suggests that powders with higher $(A \times \rho_{bed})$ require lower E_v to yield the optimum e_v. Referring to the CBD measurements results provided in Table 5-2, optical absorption values presented in Figure 5-2(a), and assuming ρ_{bulk} to be 4.43 g/cm^3 for both Ti64 and TMC bulk samples, the $(A \times \rho_{bed})$ term for the Ti64 and 0.2wt.%B_4C/Ti64 systems is 0.4 and 0.36, respectively. This justifies the need for slightly higher E_v in the composite system (compared to the Ti64) to reach the highest densification level.

The observed increasing and then decreasing variation in the density of the Ti64 and TMC samples (Figure 5-3) is in agreement with the results reported in the literature for the L-PBF processing of metallic materials [46, 47]. The decline in the relative density at relatively high E_v values exceeding the optimum value has been well documented in the literature and has been shown to be due to the transition of melting mode from conduction to keyhole [29, 35, 48, 49]. During the keyhole mode of melting, the material evaporation caused by application of high E_v leads to the development of a vapor cavity which further enhances the laser absorption and enables the laser beam to penetrate to a deeper depth. The collapse of the cavity can leave voids in the material which are known as the keyhole

porosities and are spherical in shape [48, 50]. As it is perceptible in Figure 5-3, the decreasing trend in the relative density occurred at a slightly lower E_v in the Ti64 system compared to the TMC case (83 vs. 104 J/mm^3). One of the most effective estimations for the criteria of keyhole threshold has been shown to be based on the normalized enthalpy ($\frac{\Delta H}{h_s}$) as follows [48]:

$$\frac{\Delta H}{h_s} = \frac{AP\sqrt{D}}{kT_m\sqrt{\pi v d^3}} \geq \frac{\pi T_b}{T_m} \quad [4]$$

in which ΔH is the specific enthalpy, h_s is the enthalpy at melting defined as $\frac{kT_m}{D}$, T_m is the melting point, T_b is the boiling point, d is the laser beam size, k is the thermal conductivity, and D is the thermal diffusivity. Eq. 4 takes into account the effect of the applied P, v, and d on the threshold for the formation of keyhole melting mode. However, it fails to consider the influence of layer thickness as one of the important parameters playing role on the melting mode. Eq. 5 provides the modified threshold for keyhole mode of melting by taking the effective layer thickness also into account [51, 52].

$$\frac{\Delta H}{h_s} = \frac{0.865APD}{kT_m\sqrt{\pi}\, dt_{eff} v} \geq \frac{\pi T_b}{T_m} \quad [5]$$

Eq. 5 can be also rewritten as:

$$\frac{P}{v} \geq \frac{kdT_b t_{eff}\sqrt{\pi^3}}{0.865AD} \quad [6]$$

Assuming the same k, and T_b for the Ti64 and TMC systems, and considering $t_{eff} = \frac{t}{\rho_{bed}}$ [32]:

$$\frac{P}{v} \propto \frac{1}{A \times \rho_{bed}} \quad [7]$$

Referring to Eq. 7, the critical $\frac{P}{v}$ for the keyhole threshold in the composite system is expected to be 10% higher than that of the Ti64 case. However, based on the experimental results, this difference was ~25%. Although a portion of this discrepancy may have raised because of assuming the same k, and T_b for both systems, there are still other factors related to the composite systems which have not been considered in the currently existing keyhole threshold models. For instance, given the fact that the dissolution of B_4C particles during the L-PBF processing of the composite system is an endothermic reaction, a part of the energy absorbed by the powder bed is consumed by their dissolution.

5.4.2 Microstructure evolution

As shown in Figure 5-6, the microstructure of both Ti64 and TMC parts contained elongated columnar prior β grains which were extended along the building direction. The formation of such columnar prior β grains is a major characteristic of the L-PBF processed Ti64 alloy parts caused by the combination of epitaxial and competitive growth during the solidification. The epitaxial growth deals with the solidification of the melt pool through the growth (rather than nucleation) of β crystals on the β grains of the adjacent track/underlying layer. Those prior β grains having their easy-growth crystallographic direction (<001> direction in cubic crystal structures) perpendicular to the fusion line (along the heat flux direction) experience a preferential growth, meaning that faster growth of these grains crowds out the β grains oriented in less favorable directions [53-55]. As a result, the final solidification structure consists of columnar prior β grains extended along the building direction.

As the laser beam interacts with the 0.2wt.B_4C/Ti64 composite powder bed, Ti64 powder particles experience melting since their melting temperature is well below the temperature levels induced during the L-PBF process. However, owing to their noticeably high melting point of 3036 K [56] as well as the extremely fast cooling rates associated with the L-PBF process (10^4-10^6 K/s), complete melting of B_4C particles is rather difficult or even impossible. As the microstructural characterizations (Figure 5-6 and Figure 5-8) and XRD analysis results (Figure 5-7) revealed, the fabricated TMC did not contain B_4C constituent in the final microstructure. In fact, B_4C particles fully reacted with the surrounding melt. This reaction is believed to occur through the dissolution of B_4C particles rather than their melting. The full dissolution of B_4C particles in the surrounding molten material is an interesting phenomenon which may not be expected to take place due to the extremely high cooling rate of the L-PBF process and consequently the noticeably short time available for diffusion-based dissolution mechanism. The fast and complete dissolution of high-melting-point B_4C particles in this study can be attributed to: (i) their relatively low fraction and small size, and (ii) convective flows (e.g., Marangoni flow, etc.) active within the melt pool during the L-PBF process which consecutively provide fresh molten material (not enriched from B atoms) adjacent to the solid B_4C particles [40]. Based on the calculations, the molten material formed by complete dissolution of B_4C constituent during the L-PBF processing of the 0.2wt.%B_4C/Ti64 composite powder contains 0.156 and 0.039 wt.% B and C, respectively.

Figure 5-12(a) shows the equilibrium phase diagram of the Ti64-B system where the isopleth for the Ti64-0.156wt.%B system is specified. The schematic illustration of the solidification sequence of this isopleth is also depicted in Figure 5-12(e)-(h), in which the solidification starts with the formation of β phase from the liquid and their subsequent

growth (Figure 5-12(e), and (f)). Due to the extremely low/negligible solubility of B and C in the β phase, they are rejected from the growing solidification interface upon cooling between the liquidus and eutectic temperatures (Figure 5-12(a), (f), and (g)), leading to the progressive enrichment of the liquid from B and C. Since the C in the investigated TMC system is noticeably lower than the equilibrium solubility limit of this element in Ti (0.039 vs. 0.125 wt.%), the C content of the enriched liquid is still below this limit, causing C atoms to exist as solid solution in the Ti64 matrix. At the eutectic temperature, the remaining liquid enriched from B transforms to eutectic $TiB+\beta$ ($TiB_E+\beta_E$) through a pseudo-eutectic reaction (Figure 5-12 (a), (g), and (h)). Therefore, the equilibrium solidification sequence can be summarized as:

$$L \rightarrow \beta + L \rightarrow \beta + (TiB_E + \beta_E)$$

The β phase transforms to (α+β) at the β transus temperature. Therefore, equilibrium microstructure at room temperature consists of lamellar (α+β) islands surrounded by narrow band of $(TiB_E + \beta_E)$.

The isopleth of the Ti64 alloy is presented in Figure 5-12(b), where the solidification starts with the nucleation of β phase from the liquid followed by their growth. Despite the Ti64-0.156wt.%B system with a relatively wide solidification range in the equilibrium state, that of the Ti64 alloy is noticeably narrow. This suggests that no significant partitioning is occurred in the liquid during the solidification of the Ti64 alloy.

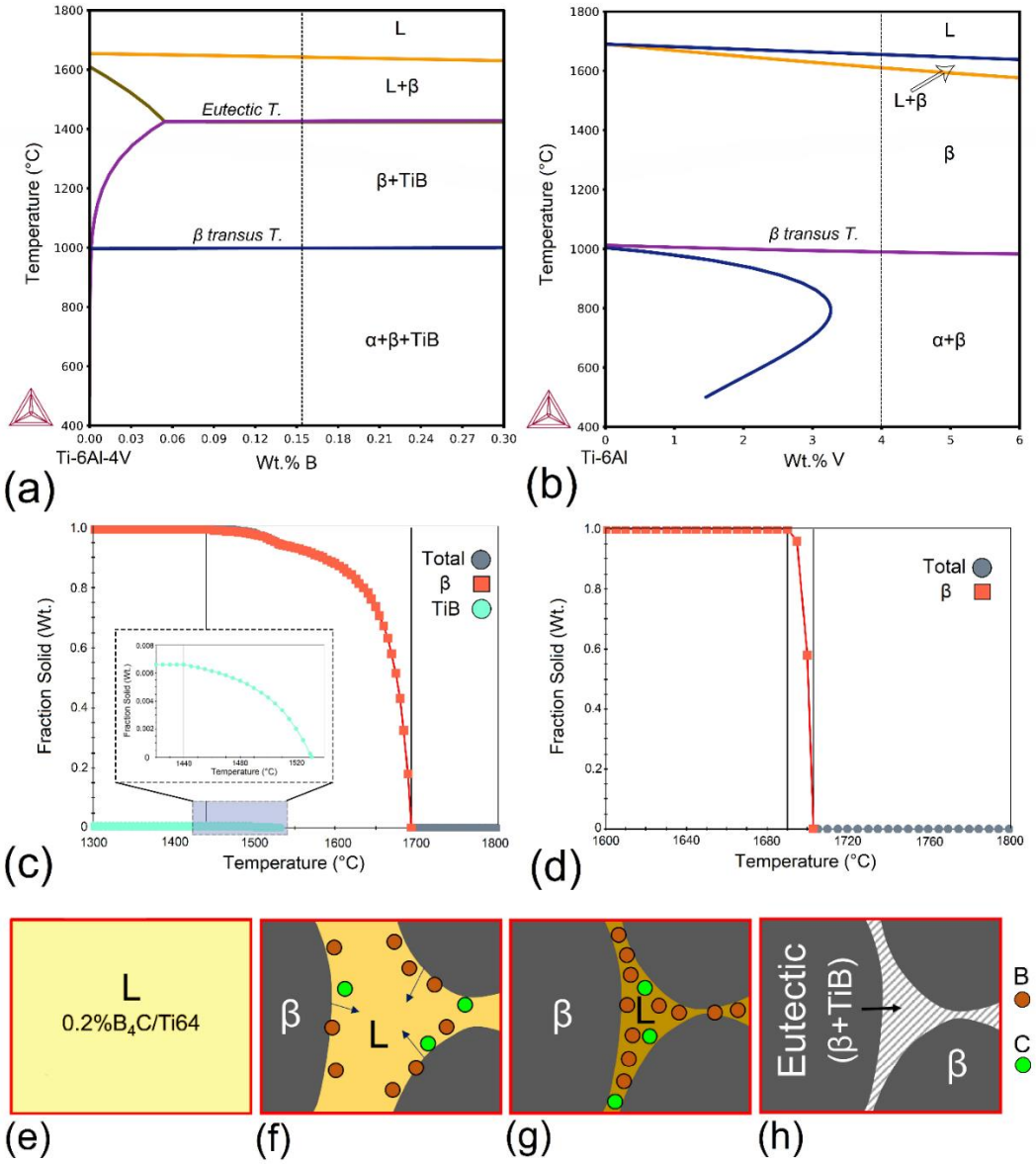

Figure 5-12. (a) Equilibrium phase analysis diagram of the Ti64-B system with the B content in the range of 0-0.3 wt.%. The provided isopleth represents the investigated 0.2wt.%B_4C/Ti64 system which contains 0.156wt.%B. (b) Equilibrium phase analysis diagram of the Ti-6Al-XV, in which the isopleth of the Ti-6Al-4V (Ti64) alloy has been shown. Scheil-Gulliver solidifications models of the: (c) Ti64-0.2wt.%B_4C, and (d) Ti64 systems. The inset in (c) shows the variation of the TiB fraction within the specified temperature range (1530-1420 °C). (e)-(h) Schematic illustration of the solidification sequence of the 0.2wt.%B_4C/Ti64 system in the equilibrium condition. The liquid (L) becomes enriched from B and C as the solidification progresses.

As the microstructural observations revealed, the fabricated TMC contained fine nano-scale/sub-micron TiB needles homogeneously dispersed in the martensitic matrix. This microstructure differs from the microstructure predicted by the equilibrium phase diagram in Figure 5-12(a), where the large prior β grains are surrounded by the pseudo-eutectic reaction products (TiB_E+β_E) along their boundaries (Figure 5-12(h)). Although the formation of a martensitic matrix (rather than the (α+β) two-phase microstructure) in the L-PBF fabricated TMC can be justified based on the extremely fast cooling rates of the process, the reason behind the deviation of the solidification path from the equilibrium condition needs further analysis.

Figure 5-12(c) illustrates the solidification sequence proposed by the non-equilibrium Scheil-Gulliver model for the TMC system investigated in this study. This model accounts for the infinitely fast diffusion in the liquid and no diffusion in the solid. As can be seen, the Scheil-Gulliver model predicts the same solidification sequence as that of the equilibrium condition, revealing that even the non-equilibrium Scheil-Gulliver solidification model fails to predict the solidification sequence of the TMC system subjected to the L-PBF process. However, unlike the equilibrium condition in which the TiB phase is formed at a specific temperature (Eutectic temperature of 1440 °C), the Scheil-Gulliver model predicts the formation of TiB to occur within a relatively wide range starting at 1530 °C and finishing at 1440 °C. This can be ascribed to the lack of solute diffusion in the solid based on the Scheil-Gulliver model which provides the liquid with the B content required for the formation of TiB at higher temperatures.

Figure 5-13(a), and (b) shows the microstructure of the last solidified layer of the fabricated TMC part, which is composed of the TiB needles homogeneously dispersed in a martensitic matrix. The microstructure evolution of the last layer is schematically illustrated in Figure

5-13(c)-(g). Although B has a negligible solubility in the equilibrium condition in the high-temperature β phase (a maximum of ~0.05 wt.% (Figure 5-13(a))), the extremely fast cooling rate associated with the L-PBF process can significantly diminish the rejection of B atoms into the liquid during the solidification (Figure 5-13(d), and (e)). For instance, rapid solidification of the Ti-B systems has been shown to cause supersaturation of B in the matrix up to 10 at.% (2.5 wt.%B) [57], which is noticeably higher than the B content of the TMC system in this study (0.156 wt.%). Accordingly, the high-temperature prior β phase is supersaturated from B. Due to the decreased solubility limit during the cooling stage, a portion of the supersaturated B tends to precipitate out as the TiB phase from both the β and the later transformed B-supersaturated martensite (M) phases (Figure 5-13(f), and (g)). Compared to the bulk of the TMC sample shown in Figure 5-8, lower volume fraction of TiB phase was perceptible in the last layer. This clearly reveals the significant role of the subsequent thermal cycles (caused by the heat conduction from the melt pool to the previously deposited tracks or layers) on the precipitation of TiB from the B-supersaturated matrix. The same phenomenon has been also observed in the powder metallurgy-processed 1.7wt.%B/Ti64 alloy, where the exposure of the material to elevated temperatures during the thermo-mechanical processing led to the increase in the volume fraction of the TiB phase in the microstructure [58].

Both the equilibrium and Scheil-Gulliver non-equilibrium solidification models are based on the scenario where the temperature gradient is low enough to allow the formation of a constitutionally undercooled zone in front of the solidification interface, favoring the nucleation of new prior β grains. However, when an extremely steep temperature gradient exists (e.g., such as that of the L-PBF process), very limited or even no nucleation events would occur ahead of the solidification interface. This explains the observation that the

TMC part also featured columnar prior β grains with almost the same size as those of the Ti64 alloy (Figure 5-6). It is worth noting that the inability of the minor B amounts in avoiding the formation of columnar prior β grains has been also reported in B-modified Ti64 alloys subjected to the AM processes with thermal gradients noticeably lower than that of the L-PBF process (WAAM) [59].

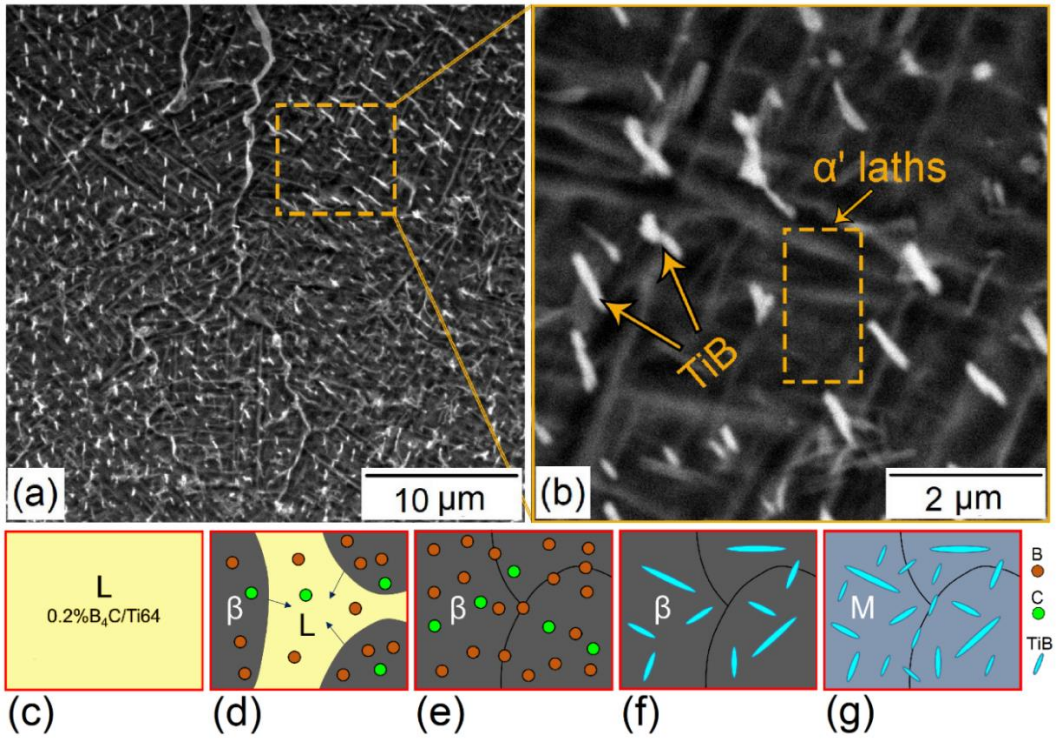

Figure 5-13. (a), and (b) SEM micrographs of the last layer of the L-PBF fabricated TMC part. Higher magnification micrograph of the selected region in (a) is shown in (b). (c)-(g) Schematic illustration of the microstructure evolution of the last layer of the L-PBF fabricated TMC part during cooling. "M" in (g) refers to martensite.

As observed in Figure 5-8 and Figure 5-13, TiB reinforcements had a needle-like shape and were uniformly dispersed in the martensitic matrix. The reason behind such a morphology has been traced back to the strong preferential growth along the $[010]_{27}$ direction compared to the other directions [60]. The average length and width of TiB needles were 1.6 µm and 260 nm, respectively, being significantly smaller than those

formed in Ti-B systems with trace B content subjected to the DED [61], direct laser deposition (DLD) [62], and wire-arc AM (WAAM) [21] processes, which usually have a length in the order of several microns. This corresponds to the noticeably higher cooling rates associated with the L-PBF process. The relatively large TiB needles have been reported to be detrimental to the mechanical properties since they can act as crack nucleation sites during loading [16, 21, 61]. Therefore, the L-PBF fabricated TiB reinforced TMCs are more favorable since they benefit from greater number of finer TiB reinforcements with smaller inter-reinforcement spacing uniformly dispersed in the matrix (as opposed to fewer numbers of TiB reinforcements with a larger spacing).

5.4.3 Mechanical Properties

Based on the hardness measurements, compression test results, and wear test, the TMC sample benefitted from a higher hardness, yield strength, and wear resistance than the Ti64 counterpart. The improvement in the mechanical properties of the TMC over the Ti64 can be ascribed to the contribution of several strengthening mechanisms, including the grain refinement, second constituent, dislocation, and solid solution. In the following, the level of enhancement in the yield strength caused by each mechanism is discussed.

Grain refinement: The increased fraction of boundaries obtained by grain refinement elevates the plastic deformation resistivity and consequently improves the strength of the material [63, 64]. Based on the Hall-Petch relationship, the increase in the yield strength of the TMC caused by the grain refinement can be expressed as follows [63]:

$$\Delta\sigma_{HP} = k_{HP}\left(\frac{1}{\sqrt{d_2}} - \frac{1}{\sqrt{d_1}}\right) \quad [8]$$

in which k_{HP} is the Hall-Petch coefficient for Ti64; while d_2, and d_1 are the mean grain sizes of the TMC and Ti64 samples, respectively. Eq. 8 is typically used for the equiaxed microstructures whereas the Ti64 and TMC samples featured martensitic microstructures characterized by α′ laths. Therefore, the average width of α′ laths in each material was taken into account [65].

Second constituent strengthening: The strength improvement caused by the presence of TiB reinforcements in the TMC part is defined as [66]:

$$\Delta\sigma_{TiB} = \frac{1}{2}\sigma_{ym} \times V_{TiB} \times \frac{l_{TiB}}{d_{TiB}}\omega_0 \quad [9]$$

where σ_{ym} is the yield strength of the Ti64 matrix, V_{TiB} is the volume fraction of TiB, $(\frac{l_{TiB}}{d_{TiB}})$ refers to the aspect ratio of TiB (treated as cylinders with the average length and width of l_{TiB}, and d_{TiB}, respectively), and ω_0 is the orientation factor which has a value between 0 and 1. Due to the random distribution of TiB whiskers in the matrix of the TMC part, ω_0 is equal to 0.125 or 0.27 based on the 3D or 2D random array model, respectively [67].

Dislocation strengthening: The increment in the strength originated from the dislocation strengthening can be estimated as follows [68]:

$$\Delta\sigma_{dis} = \sqrt{(\Delta\sigma_{oro})^2 + (\Delta\sigma_{the})^2 + \left(\Delta\sigma_{geo}\right)^2} \quad [10]$$

in which $\Delta\sigma_{oro}$ is the strength improvement by the Orowan mechanism, $\Delta\sigma_{the}$ represents the stress enhancement caused by the thermal expansion mismatch between the TiB and the Ti64 matrix, and $\Delta\sigma_{geo}$ signifies the stress increment due to the geometrically necessary dislocations (GNDs).

In the composites containing reinforcements not exceeding 1 μm in size (e.g. TiB needles with nano-scale/sub-micron width in this study), the reinforcements can act as strong obstacles to the movement of dislocations and impede their motion on the matrix's slip plane [69]. The strengthening effect caused by this phenomenon is known as the Orowan mechanism, in which the shear component of the applied stress bows out the dislocation between reinforcements. This produces a back stress which in turn prevents the migration of further dislocations and consequently enhances the yield strength [70]. The Orowan stress can be described by the Orowan-Ashby equation as [71]:

$$\Delta\sigma_{oro} = \frac{0.13\ G_m b_m}{\lambda} \ln \frac{D_{TiB}}{2b_m} \quad [11]$$

where G_m is the shear modulus of the Ti64 matrix, b_m is the Burgers vector of the Ti64 matrix, D_{TiB} is the equivalent diameter of the TiB reinforcement, and λ is the interparticle spacing. D_{TiB} and λ can be calculated as [68, 72]:

$$D_{TiB} = \sqrt[3]{1.5 d_{TiB}^2 l_{TiB}} \quad [12]$$

$$\lambda \approx D_{TiB}\left[(2V_{TiB})^{-\frac{1}{3}} - 1\right] \quad [13]$$

Since the thermal expansion coefficients of TiB and Ti64 are very close to each other, $\Delta\sigma_{the}$ can be neglected.

$\Delta\sigma_{geo}$ deals with the strength improvement caused by the GNDs required to accommodate the plastic deformation mismatch between the TiB reinforcement and the matrix, and is expressed as follows [73]:

$$\Delta\sigma_{geo} = 0.4 G_m \sqrt{\frac{\varepsilon_{T-m} b_m V_{TiB}}{D_{TiB}}} \quad [14]$$

in which ε_{T-m} is the compressive true strain of the matrix at the yield point.

Solid solution strengthening: As the microstructural observations and phase analysis results revealed, the TiC phase was not detected in the fabricated TMC part. Since the C content in the studied TMC is less than the solid solubility limit of C in Ti, C atoms have been entrapped in the matrix as solid solution. Given the fact that C is an interstitial alloying element, it can generate a significantly strong obstacle (compared to the substitutional elements) for the movement of dislocations in the matrix and consequently lead to higher levels of solid solution strengthening [74]. The solid solution strengthening caused by the interstitial solutes is generally proportional to the square root of the concentration as [75]:

$$\Delta\sigma_{ss} = 0.002G_m c^{1/2} \quad [15]$$

where c is the carbon concentration in at.%.

By taking all the strengthening mechanisms into account, the yield strength of the TMC component (σ_{y-TMC}) can be calculated as [76]:

$$\sigma_{y-TMC} = \sigma_{y-m} + \Delta\sigma_{HP} + \Delta\sigma_{TiB} + \Delta\sigma_{dis} + \Delta\sigma_{ss} \quad [16]$$

Table 5-6 summarizes the contribution of each strengthening mechanism in the yield strength increment of the TMC sample over the Ti64 counterpart. While the $\Delta\sigma_{TiB}$ is the direct strengthening mechanism originating from the incorporated TiB reinforcement, $\Delta\sigma_{HP}$, and $\Delta\sigma_{dis}$ are the indirect strengthening mechanisms activated due to the presence of this phase in the microstructure. Therefore, taking both direct and indirect strengthening mechanisms into consideration, 87.5% of the total yield strength enhancement in the TMC is caused by the presence of TiB phase. This is attributable to the high volume fraction (0.218) of the nano-scale/sub-micron TiB needles in the microstructure of the TMC caused

by the extremely high cooling rates of the L-PBF process along with the solid-state nature of the TiB formation. On the other hand, the remaining 12.5% is linked to the solid solution strengthening of the matrix induced by C atoms. The improved hardness and wear resistance of the TMC parts can be also attributed to the same strengthening mechanisms discussed above for the strength. It is worth noting that Eq. 16 overestimates the yield strength of the TMC sample by 15%. The research studies conducted on the DED processing and investment casting of the TiB reinforced TMCs have reported a great agreement (error <5%) between the experimental and predicted yield strength values. Although it has not been mentioned in these studies, the volume fraction of the TiB phase seems to be determined based on the lever rule for their investigated chemical composition rather than the microstructural analysis [68, 77]. By following the same approach, a volume fraction of 0.0082 was obtained for the 0.156wt.%B-Ti system, resulting in a predicted σ_y of 1282 MPa, which is a perfect agreement with the experimental value (Table 5-3).

Table 5-5. The properties and parameters used in obtaining the contribution of different strengthening mechanisms.

Properties and Parameters	**Value**	**Source**
k_{HP}	300 MPa.μm$^{1/2}$	[78]
d_2	0.48 μm	Measured
d_1	0.58 μm	Measured
b_m	0.295 nm	[79]
G_m	45 GPa	[80]
ω_0	0.125	[67]
V_{TiB}	0.218	Measured
l_{TiB}	990 nm	Measured
d_{TiB}	150 nm	Measured
ε_{T-m}	0.0094	Measured
D_{TiB}	0.32 μm	Measured

Table 5-6. The calculated values of strengthening mechanisms in the TMC part along with their contribution in the enhancement of the yield strength over the Ti64 counterpart.

Strengthening Mechanism	**Value [MPa]**	**Proportion in the total** $\Delta\sigma$ [%]
$\Delta\sigma_{HP}$	39.1	13.4
$\Delta\sigma_{TiB}$	107	36.6
$\Delta\sigma_{dis}$	109.5	37.5
$\Delta\sigma_{ss}$	36.6	12.5

To confirm whether the proposed mechanisms are the only strengthening mechanisms governing the yield strength improvement in the TMC, the contribution of the most predominant interstitial impurities in Ti alloys needs to be also determined. The literature lacks investigating the role that these elements (i.e., oxygen and nitrogen) might play in strengthening of L-PBF fabricated Ti alloys and TMCs. To embrace the discussion on the strengthening caused by oxygen/nitrogen elements, their contribution in the yield strength improvement was calculated using Eq. 15. For this purpose, the oxygen/nitrogen content in the L-PBF fabricated Ti64 and TMC samples was measured (Error! Reference source n ot found.). Results revealed the nitrogen content to be negligible in both samples (6 and 7 ppm for Ti64 and TMC, respectively). The oxygen level was 20, and 36 ppm for the Ti64, and TMC samples, respectively. Such oxygen contents are noticeably low and do not provide a notable strengthening based on Eq. 15 (~6 MPa increase in the $\boldsymbol{\sigma_y}$). This reveals that the interstitial solid solution strengthening by oxygen/nitrogen has a negligible effect on enhancing the $\boldsymbol{\sigma_y}$ of the TMC.

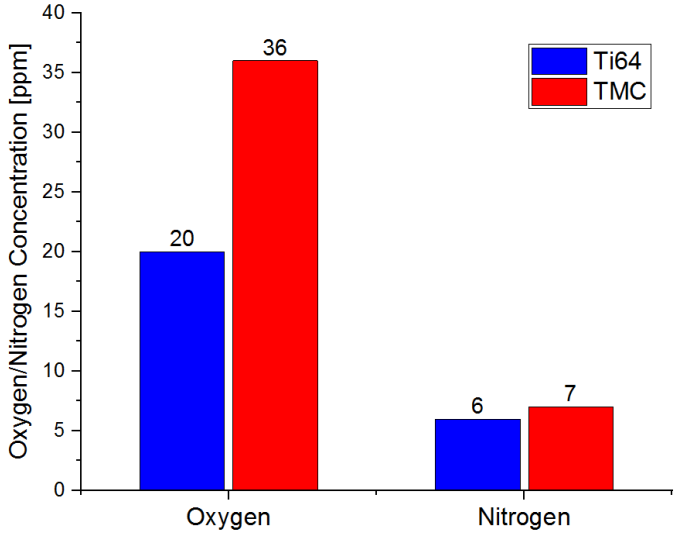

Figure 5-14. The oxygen/nitrogen concentration in the L-PBF fabricated Ti64 and TMC samples.

5.5 Conclusions

In this study, the laser powder bed fusion (L-PBF) process was implemented to fabricate high performance titanium matrix composite (TMC) parts using a composite powder feedstock produced by a novel technique. The main conclusions of this research study can be summarized as follows:

1- The proposed composite powder preparation technique benefiting from the advantages of both regular mixing and ball milling was found to yield a 0.2wt.%B_4C/Ti64 composite powder having the flowability and apparent packing density close to those of the monolithic Ti64 powder.

2- In both Ti64 and TMC cases, an increasing and then decreasing trend in the relative density of parts was achieved by enhancing the volumetric energy density. Compared to the Ti64 case, slightly higher energy densities were needed in the

TMC to achieve almost fully dense samples. Moreover, the decline in the relative density took place at higher energy densities in TMC than Ti64.

3- Microstructural characterizations revealed the formation of large columnar prior β grains in both Ti64 and TMC samples which were elongated along the building direction. The TMC sample featured nano-scale/sub-micron TiB needles homogeneously dispersed in a fully martensitic matrix.

4- The equilibrium and Scheil-Gulliver non-equilibrium solidification models were found not to be able to predict the microstructure evolution experienced by the L-PBF fabricated TMC parts. This was attributed to the extremely high cooling rates of the L-PBF process which led to the supersaturation of B atoms in the β grains during solidification.

5- The TMC part possessed 25% higher nanohardness, 8% higher yield strength, and 12% lower wear rate. The improved yield strength of the TMC was justified by calculating the contribution of different strengthening mechanisms involved. While ~87.5% of this improvement was due to the direct and indirect strengthening effects caused by the TiB phase, the remaining ~12.5% was originating from the solid solution strengthening of the matrix by C atoms.

5.6 References

[1] D. Miracle, Metal matrix composites–from science to technological significance, Composites science and technology 65(15-16) (2005) 2526-2540.

[2] S.C. Tjong, Recent progress in the development and properties of novel metal matrix nanocomposites reinforced with carbon nanotubes and graphene nanosheets, Materials Science and Engineering: R: Reports 74(10) (2013) 281-350.

[3] C. Cui, B. Hu, L. Zhao, S. Liu, Titanium alloy production technology, market prospects and industry development, Materials & Design 32(3) (2011) 1684-1691.

[4] M.J. Donachie, Titanium: a technical guide, ASM international2000.

[5] Y. Jiao, L. Huang, L. Geng, Progress on discontinuously reinforced titanium matrix composites, Journal of Alloys and Compounds 767 (2018) 1196-1215.

[6] M.G. Glavicic, P.A. Kobryn, F. Spadafora, S.L. Semiatin, Texture evolution in vacuum arc remelted ingots of Ti-6Al-4V, Materials Science and Engineering: A 346(1) (2003) 8-18.

[7] G. Singh, U. Ramamurty, Boron modified titanium alloys, Progress in Materials Science 111 (2020) 100653.

[8] S. Tamirisakandala, R.B. Bhat, J.S. Tiley, D.B. Miracle, Grain refinement of cast titanium alloys via trace boron addition, Scripta materialia 53(12) (2005) 1421-1426.

[9] E. Fereiduni, M. Yakout, M. Elbestawi, Laser-based additive manufacturing of lightweight metal matrix composites, Additive Manufacturing of Emerging Materials, Springer2019, pp. 55-109.

[10] E. Fereiduni, M. Elbestawi, Process-structure-property relationships in additively manufactured metal matrix composites, Additive Manufacturing of Emerging Materials, Springer2019, pp. 111-177.

[11] R.R. Sélo, S. Catchpole-Smith, I. Maskery, I. Ashcroft, C. Tuck, On the thermal conductivity of AlSi10Mg and lattice structures made by laser powder bed fusion, Additive Manufacturing 34 (2020) 101214.

[12] A. Salmi, F. Calignano, M. Galati, E. Atzeni, An integrated design methodology for components produced by laser powder bed fusion (L-PBF) process, Virtual and Physical Prototyping 13(3) (2018) 191-202.

[13] E. Fereiduni, A. Ghasemi, M. Elbestawi, Selective Laser Melting of Aluminum and Titanium Matrix Composites: Recent Progress and Potential Applications in the Aerospace Industry, Aerospace 7(6) (2020) 77.

[14] M. Narvan, A. Ghasemi, E. Fereiduni, S. Kendrish, M. Elbestawi, Part deflection and residual stresses in laser powder bed fusion of H13 tool steel, Materials & Design 204 (2021) 109659.

[15] S.M.J. Razavi, F. Berto, Directed energy deposition versus wrought Ti-6Al-4V: a comparison of microstructure, fatigue behavior, and notch sensitivity, Advanced Engineering Materials 21(8) (2019) 1900220.

[16] K. Zhang, X. Tian, M. Bermingham, J. Rao, Q. Jia, Y. Zhu, X. Wu, S. Cao, A. Huang, Effects of boron addition on microstructures and mechanical properties of Ti-6Al-4V manufactured by direct laser deposition, Materials & Design 184 (2019) 108191.

[17] C. Liu, Y. Lu, X. Tian, D. Liu, Influence of continuous grain boundary α on ductility of laser melting deposited titanium alloys, Materials Science and Engineering: A 661 (2016) 145-151.

[18] B.E. Carroll, T.A. Palmer, A.M. Beese, Anisotropic tensile behavior of Ti–6Al–4V components fabricated with directed energy deposition additive manufacturing, Acta Materialia 87 (2015) 309-320.

[19] W.J. Sames, K.A. Unocic, R.R. Dehoff, T. Lolla, S.S. Babu, Thermal effects on microstructural heterogeneity of Inconel 718 materials fabricated by electron beam melting, Journal of materials research 29(17) (2014) 1920-1930.

[20] Z. Mahbooba, H. West, O. Harrysson, A. Wojcieszynski, R. Dehoff, P. Nandwana, T. Horn, Effect of hypoeutectic boron additions on the grain size and mechanical properties of Ti-6Al-4V manufactured with powder bed electron beam additive manufacturing, Jom 69(3) (2017) 472-478.

[21] M. Liu, S. Liu, W. Chen, C. Chen, Y. Lv, X. Zhang, P. Lei, Y. Lin, K. Zhou, Effect of trace lanthanum hexaboride on the phase, grain structure, and texture of electron beam melted Ti-6Al-4V, Additive Manufacturing 30 (2019) 100873.

[22] S. Mereddy, M.J. Bermingham, D.H. StJohn, M.S. Dargusch, Grain refinement of wire arc additively manufactured titanium by the addition of silicon, Journal of Alloys and Compounds 695 (2017) 2097-2103.

[23] M.J. Bermingham, S.D. McDonald, D.H. StJohn, M.S. Dargusch, Beryllium as a grain refiner in titanium alloys, Journal of Alloys and Compounds 481(1) (2009) L20-L23.

[24] H. Okamoto, Desk handbook: phase diagrams for binary alloys, ASM international2000.

[25] M. Bermingham, S. McDonald, K. Nogita, D.S. John, M. Dargusch, Effects of boron on microstructure in cast titanium alloys, Scripta Materialia 59(5) (2008) 538-541.

[26] S.C. Tjong, Y.-W. Mai, Processing-structure-property aspects of particulate- and whisker-reinforced titanium matrix composites, Composites Science and Technology 68(3) (2008) 583-601.

[27] E. Fereiduni, A. Ghasemi, M. Elbestawi, Characterization of composite powder feedstock from powder bed fusion additive manufacturing perspective, Materials 12(22) (2019) 3673.

[28] M.A. Balbaa, A. Ghasemi, E. Fereiduni, M.A. Elbestawi, S.D. Jadhav, J.P. Kruth, Role of powder particle size on laser powder bed fusion processability of AlSi10mg alloy, Additive Manufacturing 37 (2021) 101630.

[29] U. Scipioni Bertoli, A.J. Wolfer, M.J. Matthews, J.-P.R. Delplanque, J.M. Schoenung, On the limitations of Volumetric Energy Density as a design parameter for Selective Laser Melting, Materials & Design 113 (2017) 331-340.

[30] ASTM, G99-95a (2000) e1, Standard Test Method for Wear Testing with a Pin-on-Disk Apparatus, (2000).

[31] D. Odabas, Effects of load and speed on wear rate of abrasive wear for 2014 Al alloy, IOP Conference Series: Materials Science and Engineering, IOP Publishing, 2018, p. 012008.

[32] E. Fereiduni, A. Ghasemi, M. Elbestawi, S. Dinkar Jadhav, K. Vanmeensel, Laser powder bed fusion processability of Ti-6Al-4V powder decorated by B4C particles, Materials Letters 296 (2021) 129923.

[33] A. Grabowski, M. Nowak, J. Śleziona, Optical and conductive properties of AlSi-alloy/SiCp composites: application in modelling CO2 laser processing of composites, Optics and Lasers in Engineering 43(2) (2005) 233-246.

[34] W. Zhou, X. Sun, K. Kikuchi, N. Nomura, K. Yoshimi, A. Kawasaki, Carbon nanotubes as a unique agent to fabricate nanoceramic/metal composite powders for additive manufacturing, Materials & Design 137 (2018) 276-285.

[35] W. Liu, C. Chen, S. Shuai, R. Zhao, L. Liu, X. Wang, T. Hu, W. Xuan, C. Li, J. Yu, J. Wang, Z. Ren, Study of pore defect and mechanical properties in selective laser melted Ti6Al4V alloy based on X-ray computed tomography, Materials Science and Engineering: A 797 (2020) 139981.

[36] H. Salem, L.N. Carter, M.M. Attallah, H.G. Salem, Influence of processing parameters on internal porosity and types of defects formed in Ti6Al4V lattice structure fabricated by selective laser melting, Materials Science and Engineering: A 767 (2019) 138387.

[37] J. Lin, Y. Lv, D. Guo, X. Wu, Z. Li, C. Liu, B. Guo, G. Xu, B. Xu, Enhanced strength and ductility in thin Ti-6Al-4V alloy components by alternating the thermal cycle strategy during plasma arc additive manufacturing, Materials Science and Engineering: A 759 (2019) 288-297.

[38] Z. Zhao, J. Chen, X. Lu, H. Tan, X. Lin, W. Huang, Formation mechanism of the α variant and its influence on the tensile properties of laser solid formed Ti-6Al-4V titanium alloy, Materials Science and Engineering: A 691 (2017) 16-24.

[39] J. Yang, H. Yu, J. Yin, M. Gao, Z. Wang, X. Zeng, Formation and control of martensite in Ti-6Al-4V alloy produced by selective laser melting, Materials & Design 108 (2016) 308-318.

[40] E. Fereiduni, A. Ghasemi, M. Elbestawi, Selective laser melting of hybrid ex-situ/in-situ reinforced titanium matrix composites: Laser/powder interaction, reinforcement formation mechanism, and non-equilibrium microstructural evolutions, Materials & Design 184 (2019) 108185.

[41] S. Cao, Z. Chen, C.V.S. Lim, K. Yang, Q. Jia, T. Jarvis, D. Tomus, X. Wu, Defect, Microstructure, and Mechanical Property of Ti-6Al-4V Alloy Fabricated by High-Power Selective Laser Melting, JOM 69(12) (2017) 2684-2692.

[42] M. Neikter, A. Huang, X. Wu, Microstructural characterization of binary microstructure pattern in selective laser-melted Ti-6Al-4V, The International Journal of Advanced Manufacturing Technology 104(1) (2019) 1381-1391.

[43] M.J. Bermingham, L. Nicastro, D. Kent, Y. Chen, M.S. Dargusch, Optimising the mechanical properties of Ti-6Al-4V components produced by wire + arc additive manufacturing with post-process heat treatments, Journal of Alloys and Compounds 753 (2018) 247-255.

[44] B. Baufeld, O.V.d. Biest, R. Gault, Additive manufacturing of Ti–6Al–4V components by shaped metal deposition: Microstructure and mechanical properties, Materials & Design 31 (2010) S106-S111.

[45] M. Narvan, A. Ghasemi, E. Fereiduni, M. Elbestawi, Laser powder bed fusion of functionally graded bi-materials: Role of VC on functionalizing AISI H13 tool steel, Materials & Design (2021) 109503.

[46] H. Shipley, D. McDonnell, M. Culleton, R. Coull, R. Lupoi, G. O'Donnell, D. Trimble, Optimisation of process parameters to address fundamental challenges during selective laser melting of Ti-6Al-4V: A review, International Journal of Machine Tools and Manufacture 128 (2018) 1-20.

[47] C.Y. Yap, C.K. Chua, Z.L. Dong, Z.H. Liu, D.Q. Zhang, L.E. Loh, S.L. Sing, Review of selective laser melting: Materials and applications, Applied physics reviews 2(4) (2015) 041101.

[48] W.E. King, H.D. Barth, V.M. Castillo, G.F. Gallegos, J.W. Gibbs, D.E. Hahn, C. Kamath, A.M. Rubenchik, Observation of keyhole-mode laser melting in laser powder-bed fusion additive manufacturing, Journal of Materials Processing Technology 214(12) (2014) 2915-2925.

[49] T. Qi, H. Zhu, H. Zhang, J. Yin, L. Ke, X. Zeng, Selective laser melting of Al7050 powder: Melting mode transition and comparison of the characteristics between the keyhole and conduction mode, Materials & Design 135 (2017) 257-266.

[50] C. Teng, D. Pal, H. Gong, K. Zeng, K. Briggs, N. Patil, B. Stucker, A review of defect modeling in laser material processing, Additive Manufacturing 14 (2017) 137-147.

[51] D. Hann, J. Iammi, J. Folkes, A simple methodology for predicting laser-weld properties from material and laser parameters, Journal of Physics D: Applied Physics 44(44) (2011) 445401.

[52] J. Yang, J. Han, H. Yu, J. Yin, M. Gao, Z. Wang, X. Zeng, Role of molten pool mode on formability, microstructure and mechanical properties of selective laser melted Ti-6Al-4V alloy, Materials & Design 110 (2016) 558-570.

[53] T. Wang, Y. Zhu, S. Zhang, H. Tang, H. Wang, Grain morphology evolution behavior of titanium alloy components during laser melting deposition additive manufacturing, Journal of Alloys and Compounds 632 (2015) 505-513.

[54] M.J. Bermingham, D.H. StJohn, J. Krynen, S. Tedman-Jones, M.S. Dargusch, Promoting the columnar to equiaxed transition and grain refinement of titanium alloys during additive manufacturing, Acta Materialia 168 (2019) 261-274.

[55] F. Wang, S. Williams, P. Colegrove, A.A. Antonysamy, Microstructure and mechanical properties of wire and arc additive manufactured Ti-6Al-4V, Metallurgical and materials transactions A 44(2) (2013) 968-977.

[56] I. Solodkyi, I. Bogomol, P. Loboda, D. Batalu, A. Vlaicu, P. Badica, Floating zone partial re-melting of B4C infiltrated with molten Si, Ceramics International 43(17) (2017) 14718-14725.

[57] S.H. Whang, Rapidly solidified titanium alloys for high-temperature applications, Journal of materials science 21(7) (1986) 2224-2238.

[58] S. Tamirisakandala, R. Bhat, D. Miracle, S. Boddapati, R. Bordia, R. Vanover, V. Vasudevan, Effect of boron on the beta transus of Ti–6Al–4V alloy, Scripta Materialia 53(2) (2005) 217-222.

[59] M.J. Bermingham, D. Kent, H. Zhan, D.H. StJohn, M.S. Dargusch, Controlling the microstructure and properties of wire arc additive manufactured Ti–6Al–4V with trace boron additions, Acta Materialia 91 (2015) 289-303.

[60] S. Sahay, K. Ravichandran, R. Atri, B. Chen, J. Rubin, Evolution of microstructure and phases in in situ processed Ti–TiB composites containing high volume fractions of TiB whiskers, Journal of Materials Research 14(11) (1999) 4214-4223.

[61] A. Xue, X. Lin, L. Wang, J. Wang, W. Huang, Influence of trace boron addition on microstructure, tensile properties and their anisotropy of Ti6Al4V fabricated by laser directed energy deposition, Materials & Design 181 (2019) 107943.

[62] R.R. Rashid, S. Palanisamy, H. Attar, M. Bermingham, M. Dargusch, Metallurgical features of direct laser-deposited Ti6Al4V with trace boron, Journal of Manufacturing Processes 35 (2018) 651-656.

[63] N. Hansen, Hall–Petch relation and boundary strengthening, Scripta Materialia 51(8) (2004) 801-806.

[64] J. Wyrzykowski, M. Grabski, The Hall–Petch relation in aluminium and its dependence on the grain boundary structure, Philosophical Magazine A 53(4) (1986) 505-520.

[65] M. Galindo-Fernandez, K. Mumtaz, P. Rivera-Diaz-del-Castillo, E. Galindo-Nava, H. Ghadbeigi, A microstructure sensitive model for deformation of Ti-6Al-4V describing Cast-and-Wrought and Additive Manufacturing morphologies, Materials & Design 160 (2018) 350-362.

[66] X. Guo, L. Wang, M. Wang, J. Qin, D. Zhang, W. Lu, Effects of degree of deformation on the microstructure, mechanical properties and texture of hybrid-reinforced titanium matrix composites, Acta Materialia 60(6) (2012) 2656-2667.

[67] H. Fukuda, T.-W. Chou, A probabilistic theory of the strength of short-fibre composites with variable fibre length and orientation, Journal of materials science 17(4) (1982) 1003-1011.

[68] Y. Hu, W. Cong, X. Wang, Y. Li, F. Ning, H. Wang, Laser deposition-additive manufacturing of TiB-Ti composites with novel three-dimensional quasi-continuous network microstructure: effects on strengthening and toughening, Composites Part B: Engineering 133 (2018) 91-100.

[69] E. Orowan, Zur Kristallplastizität. III, Zeitschrift für Physik 89(9) (1934) 634-659.

[70] R. George, K. Kashyap, R. Rahul, S. Yamdagni, Strengthening in carbon nanotube/aluminium (CNT/Al) composites, Scripta Materialia 53(10) (2005) 1159-1163.

[71] G.E. Dieter, D.J. Bacon, Mechanical metallurgy, McGraw-hill New York1986.

[72] M.A. Meyers, K.K. Chawla, Mechanical behavior of materials, Cambridge university press2008.

[73] L. Brown, W. Stobbs, The work-hardening of copper-silica v. equilibrium plastic relaxation by secondary dislocations, Philosophical Magazine 34(3) (1976) 351-372.

[74] S. Schmauder, C. Kohler, Atomistic simulations of solid solution strengthening of α-iron, Computational Materials Science 50(4) (2011) 1238-1243.

[75] P. Luo, D. McDonald, W. Xu, S. Palanisamy, M. Dargusch, K. Xia, A modified Hall–Petch relationship in ultrafine-grained titanium recycled from chips by equal channel angular pressing, Scripta Materialia 66(10) (2012) 785-788.

[76] J. Keist, S. Nayir, T. Palmer, Impact of hot isostatic pressing on the mechanical and microstructural properties of additively manufactured Ti–6Al–4V fabricated using directed energy deposition, Materials Science and Engineering: A 787 (2020) 139454.

[77] J. Wang, X. Guo, J. Qin, D. Zhang, W. Lu, Microstructure and mechanical properties of investment casted titanium matrix composites with B4C additions, Materials Science and Engineering: A 628 (2015) 366-373.

[78] K.D. Rekedal, Investigation of the high-cycle fatigue life of selective laser melted and hot isostatically pressed Ti-6Al-4V, (2015).

[79] A. Muiruri, M. Maringa, W. du Preez, Evaluation of Dislocation Densities in Various Microstructures of Additively Manufactured Ti6Al4V (Eli) by the Method of X-ray Diffraction, Materials 13(23) (2020) 5355.

[80] W.D. Callister, D.G. Rethwisch, Materials science and engineering, John wiley & sons NY2011.

Chapter 6 Unique opportunities for microstructure engineering via trace B_4C addition to Ti-6Al-4V through laser powder bed fusion process: As-built and heat-treated scenarios

Abstract

This research study examines the role of minor B_4C addition (0.2 wt.%) in improving the mechanical properties of the laser powder bed fusion (L-PBF) fabricated Ti-6Al-4V (Ti64) alloy in the as-built and heat-treated conditions. The fabricated titanium matrix composites (TMCs) were subjected to two different heat treatment scenarios, i.e., subtransus and supertransus, and were compared to the Ti64 counterparts exposed to the same thermal cycles. Both the as-built and heat-treated Ti64 and TMC samples were characterized in terms of the grain structure, and microstructure within the grains as well as the size, morphology, volume fraction and crystallographic orientation of the phases. The knowledge gained from the microstructural investigations were correlated with the mechanical behavior of components, including compressive strength and ductility, microhardness, and scratch resistance. The governing strengthening mechanisms were identified, and the contribution of each mechanism in the overall yield strength was explored. Results revealed that TMCs possessed higher yield and ultimate compressive strengths than their Ti64 counterparts owing to the hard TiB needles homogeneously dispersed in the microstructure. However, except for the supertransus heat-treated condition, the TMCs showed slightly lower fracture strain than the Ti64 samples. The elimination of GB-α in the supertransus heat-treated TMC sample caused by the TiB needles led to a higher fracture strain than the corresponding Ti64 case. While the mechanical properties could be tailored by the implemented heat treatment strategies, the optimum thermal cycles for Ti64 were not necessarily applicable to TMC components.

Keywords: Laser powder bed fusion (L-PBF), Ti-6Al-4V (Ti64), Titanium matrix composite (TMC), TiB, mechanical properties.

6.1 Introduction

Additive manufacturing (AM) refers to a group of advanced manufacturing techniques in which an object is produced in a layer-by-layer fashion using a sliced computer aided design (CAD) model [1]. Laser powder bed fusion (L-PBF) is one of the most promising AM processes which utilizes a high-intensity laser beam as the heat source to selectively fuse powder layers in pre-defined regions through a stepwise additive process [2-4]. The L-PBF process has expanded the freedom in design since no tools, molds, and other auxiliaries are required to produce components with complex geometries and intricate features [5-7]. Besides, the parts manufactured by this unparalleled technology possess higher strength that their conventionally manufactured counterparts owing to the microstructural refinement caused by the noticeably high cooling rates associated with the process [8-10]. Moreover, since powder serves as the feedstock material in the L-PBF process, different alloys and composite systems can be easily developed through powder mixing routes and subsequently utilized to fabricate different materials using this process [11-14].

Despite the aforementioned advantages, the L-PBF fabricated parts generally suffer from anisotropy in microstructure and mechanical properties along with the residual stresses originating from the directional heat flow opposite to the building direction and temperature gradients induced by the layer-wise nature of the process, respectively [15-18]. In addition, the metastable microstructure of the L-PBF processed parts in the as-built condition caused by the non-equilibrium phase transformation(s) during solidification and/or cooling stages adversely affects the high-temperature stability and therefore, the service temperature of the material [19-21]. For instance, the L-PBF fabricated Ti-6A-4V (Ti64) alloy components have shown to contain columnar prior β grains (PBGs) elongated

along the building direction (causing anisotropy), high levels of residual stresses, and a fully martensitic metastable microstructure [22-24]. In view of these facts, the as-built parts need to be subjected to an appropriate post processing heat treatment to mitigate the anisotropy through generation of equiaxed grains, alleviate the residual stresses by annealing, and eliminate the microstructural non-equilibrity.

Although appropriate heat treatment strategies have been well established for some of the alloys widely used in the L-PBF process (e.g., Ti64, and AlSi10Mg, and Inconel 718), these heat-treating cycles are still unknown for newly designed alloys and composites. For instance, a minor B_4C content was added to the Ti64 alloy in this study to explore the possibility of enhancing the hardness, wear resistance, and compressive strength of the Ti64 alloy. Due to the fact that post processing heat treatments should be also carried out on these L-PBF fabricated composites, it needs to be explored whether the heat treatment cycles proposed for the Ti64 alloy can be successfully applied to these composites to obtain the desired properties. By considering the formation of TiB phase through an in-situ reaction between the Ti and B elements in the B_4C/Ti64 composite system, the optimum heat treatment for the composite is expected to be different from that of the Ti64 alloy since a new phase having a different response to the employed heat treatment has been incorporated into the material. Moreover, TiB phase can play a crucial role in the microstructural evolutions during the heat treatment by affecting the nucleation and growth of the grains in the matrix.

In this study, highly dense titanium matrix composite (TMC) parts were fabricated by L-PBF processing of the 0.2wt%B_4C/Ti64 composite powder. For the sake of comparison, defect-free monolithic Ti64 alloy parts were also manufactured. The microstructure of the as-built TMC sample was investigated to realize if the addition of B_4C can mitigate the

degree of anisotropy and alter the solidification path. As-built TMC and Ti64 samples were subjected to two different heat treatment scenarios, namely subtransus and supertransus. The β transus temperature in each system was identified by the differential scanning calorimetry (DSC) test. The microstructure of the as-built and heat treated TMCs was characterized and compared to their corresponding Ti64 counterparts. The microstructural features such as the nature, morphology, size, and volume fraction of phases were assessed and correlated to the microhardness, scratch, and compression properties. The strengthening mechanisms were explored, and the contribution of each mechanism in the overall compressive yield strength was identified by employing analytical models. Based on different criteria such as (i) the degree of anisotropy mitigation, (ii) combination of strength and ductility, and (iii) combination of hardness and scratch resistance, the optimum heat treatments were introduced for the TMCs. Results revealed that the optimum heat treatment in the Ti64 alloy could not be applied to the fabricated TiB reinforced TMCs.

6.2 Materials and Experimental Procedure

6.2.1 Fabrication

Ti64 alloy and 0.2 wt%B_4C/Ti64 composite powders were subjected to the laser processing using an EOS M280 DMLS machine. The starting Ti64 and B_4C powders had the mean particle size of 35 and 2 μm, respectively, and the chemical compositions provided in [25]. The 0.2 wt.%B_4C composite powder was produced by adding a 2 h-ball milled 3 wt.%B_4C/Ti64 composite powder to the Ti64 powder, followed by regular mixing for 2 h. The ball-to-powder weight ratio and the ball diameter in the ball milling were 5:1 and 10 mm, respectively. Steel balls did not exist in the regular mixing stage. The rotational speed in both ball milling and regular mixing was set to be 200 rpm. The optimum process

parameters used to fabricate Ti64 and TMC parts with densification levels exceeding 99.5% are listed in Table 6-1. These parameters were utilized to print 10 mm×10 mm×10 mm cubic coupons for microstructural investigations, as well as scratch and compression test specimens for the assessment of mechanical properties (Figure 6-1).

Table 6-1. The optimum set of process parameters used to print Ti64 and TMC parts.

Process variable	Material	
	Ti64	TMC
Laser power, P [W]	200	250
Scan speed, v [mm/s]	1000	1000
Hatch spacing, h [μm]	100	100
Nominal powder layer thickness, t [μm]	30	30
Preheating temperature, $T_{preheat}$ [$°C$]	200	200

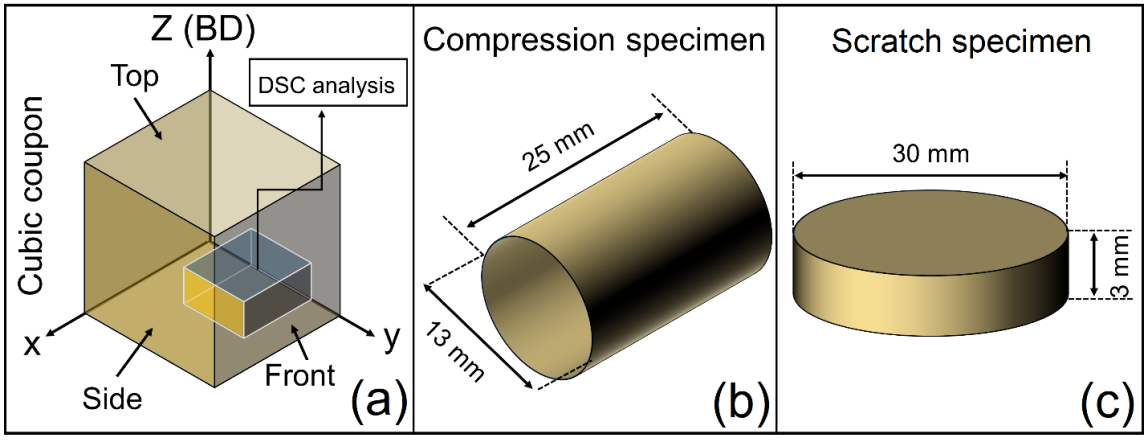

Figure 6-1. Schematic illustration of (a) cubic coupon, (b) compression test specimen, and (c) wear test specimen. “BD” in (a) refers to the building direction.

6.2.2 Heat Treatment

The as-built Ti64 and TMC samples were heat treated through two different strategies, namely, subtransus and supertransus heat treatments. The β transus temperature was measured for both Ti64 and TMC samples using a NETZSCH-DSC 404F1 differential scanning calorimetry (DSC) device, within the temperature range of 250-1200 °C with

heating and cooling rates of 20, and 40 °C/min, respectively. The DSC samples with dimensions of 4×4×1 mm^3 (~70 mg) were cut from the as-built coupons (Figure 6-1(a)). For supertransus heat treatment, Ti64 and TMC cubic coupons and mechanical test specimens experienced a thermal cycle of 1050 °C/2 h. For the subtransus heat treatment on the other hand, three different temperatures of 850 and 950 °C and the same holding time of 2 h was used. In all heat treatment cycles, the heating rate was set to be 10 °C/min, and the cooling was performed in the furnace.

6.2.3 Microstructural Characterization

The overview of the microstructure was studied by a Nikon LV100 optical microscopy (OM). Samples for microstructural characterization were prepared as per the standard metallography procedure for Ti alloys and were etched using Kroll's reagent (6 ml HNO_3, 2 ml HF in 92 ml H_2O). High magnification imaging of the microstructure was conducted using a Vega Tescan scanning electron microscope (SEM), operating at an accelerating voltage of 10 keV. The microscope was equipped with an energy dispersive X-ray spectroscopy (EDS) detector to identify the elemental chemical composition of micro-constituents in the material. The phase analysis was performed using X-ray Diffraction (XRD) on a Bruker D8 DISCOVER with a DAVINCI design diffractometer equipped with a copper sealed tube source and a VANTEC-500 area detector.

The electron backscatter diffraction (EBSD) analysis was performed to obtain texture, grain size/morphology, and inter-phase orientation relationship information. For EBSD analysis, an FEI, Versa 3D field-emission scanning electron microscope (FE-SEM) was utilized, operating at an accelerating voltage of 20 keV, and a tilt angle of 70° with a step size in the range of 0.05-0.5 μm. The EBSD data were collected using the TSL OIM 7 software and were analyzed using the HKL Channel 5 software package. To assess the

texture of samples, this software indexes Kikuchi bands, assigns a spatial orientation to each scanned point and reconstructs them to create a crystallographic orientation map of the scanned area through pole figures (PFs) and inverse pole figures (IPFs). The reconstruction of PBGs was performed using MTEX, which is a free MATLAB-based toolbox for analysing the crystallographic textures using EBSD or PF data [26]. The PBGs were reconstructed from the indexed orientations using misorientation angles higher than 2.5°.

6.2.4 Mechanical Properties Investigation

Microhardness test was carried on the cubic coupons with the load of 500 g and dwell time of 10 s using a Matsuzawa microhardness tester. The reported microhardness values are the average of five distinct measurements. For compression test, specimens were cut out of the printed cuboids shown in Figure 6-1(b) with dimensions as per ASTM E9-19 standard. An Instron tensile testing machine was used to perform the compression test at room temperature with the fixed strain rate of 0.005 mm/mm/s. The test was stopped when a sharp drop in the load-displacement curve was observed. For scratch test, disk specimens were printed with dimensions shown in Figure 6-1(c). The scratch test was performed using an Anton-Paar Revetest scratch tester with a tip radius of 200 µm, under a constant load of 10 N, a scratch rate of 2 mm/min, and a scratch length of 3 mm, as per ASTM C1624-05 standard [27]. The sliding contact response was analysed in terms of the penetration depth-scratch length profile.

6.3 Results and Discussion

6.3.1 Heat treatment cycle selection

To select the subtransus and supertransus heat treatment temperatures, the β transus temperature of the as-built Ti64 and TMC samples need to be first determined. For this purpose, the as-built samples were subjected to the DSC analysis in which the phase transformations are investigated during a heating/cooling cycle. Figure 6-2 shows the DSC analysis results for the as-built Ti64 and TMC samples. As shown in Figure 6-2(a), the DSC thermogram of the Ti64 sample during heating showed an exothermic peak at 490 °C, and an endothermic peak at 960 °C. The exothermic peak for the TMC sample was observed at a higher temperature of 530 °C (Figure 6-2(c)). However, compared to the Ti64, the endothermic peak for the TMC sample was shifted to the higher temperature of 1025 °C. This peak was not sharp and covered a wider temperature range than that of the Ti64 counterpart. The temperatures at which the endothermal effects terminated were 1000 and 1040 °C for the Ti64 and TMC samples, respectively (Figure 6-2(a) and (c)). The exothermic peaks observed during heating are caused by the martensite (α') decomposition into β and α phases, as explained in Section 6.3.2.1.2. The observed exothermal events are in a good agreement with the DSC analysis results of a water quenched Ti64 sample with the martensitic microstructure, showing an exothermic peak at ~500 °C [28]. The endothermal effects occurred at noticeably higher temperatures correspond to the β transus temperature, where the $\alpha + \beta \rightarrow \beta$ transition takes place. The β transus temperature observed during heating of the Ti64 sample (960 °C) well conforms to those of the gas atomized Ti64 powder (950 °C) [29], and water quenched Ti64 sample (930 °C) [30] both with a fully martensitic microstructure. In light of the foregoing, the subtransus and supertransus heat treatment temperatures selected in this study were below 960 °C and above 1040 °C, respectively, for both Ti64 and TMC parts.

It is worth noting that the subtransus heat treatment temperatures were selected to be higher than the martensitic decomposition temperature ranges to ensure that the microstructure evolves during the post processing of the printed parts.

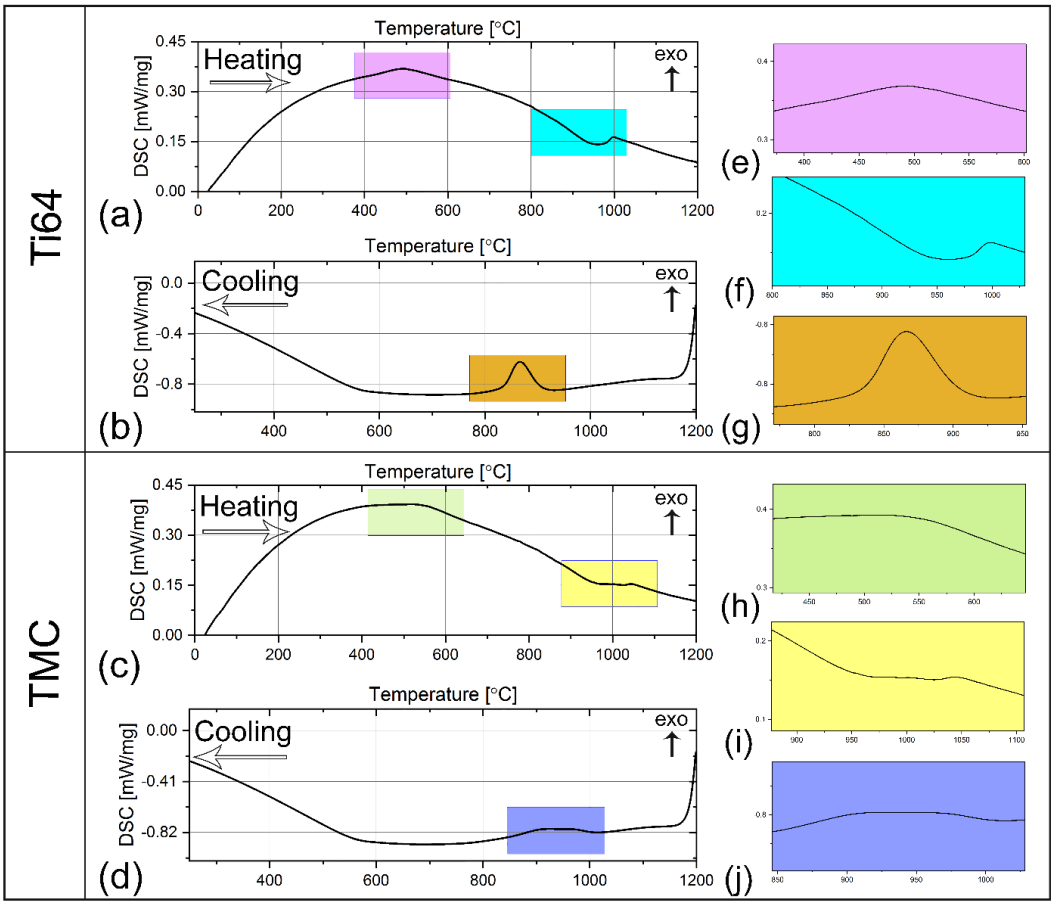

Figure 6-2. Differential scanning calorimetry (DSC) analysis results for the as-built Ti64 and TMC parts in heating (a, c) and cooling (b, d) stages. Higher magnification views of the selected regions in (a-d) are shown in (e-j) with the same background color.

The DSC thermograms of the cooling stage for both samples are provided in Figure 6-2(b) and (d). The temperature ranges of the phase transformations during the cooling stage provide valuable information which can be utilized to predict the size of the micro-constituents in both Ti64 and TMC parts, especially for the supertransus heat-treated scenario (Section 6.3.2.2). As can be seen in Figure 6-2(b), the Ti64 sample featured a

sharp exothermic peak at ~870 °C. This peak started at 925 and ended at 825 °C. Compared to the Ti64 sample, the exothermic peak of the TMC sample was less intense and covered a wide temperature range from 1010 to 850 °C (Figure 6-2(d)). Although it seems rather difficult to assign a specific temperature to the exothermic peak of the TMC sample, it is obvious that its β transus temperature is noticeably higher than that of the Ti64 specimen. The occurrence of $\beta \rightarrow \alpha$ transformation at higher temperatures in the TMC than the Ti64 sample can be ascribed to the role that TiB needles play in this transformation. Since the $\beta \rightarrow \alpha$ transformation is of a nucleation and growth type, TiB needles homogenously dispersed in the microstructure can act as heterogeneous nucleation sites for this transformation [31-34] in addition to the PBG boundaries. This consequently facilitates the $\beta \rightarrow \alpha$ transformation at higher temperatures.

6.3.2 Microstructural Characterization

The mechanical response of the L-PBF processed parts is governed by several factors among which the microstructure plays a significant role. In this section, the microstructure of the as-built samples along with the microstructural evolutions during the heat treatment cycles are thoroughly investigated from different perspectives including: (i) grain structure, (ii) phases within the grains, (iii) volume fraction of the phases, and (iv) size of the micro-constituents. The influence of each microstructural feature on the mechanical properties is discussed in Section 6.3.3.

6.3.2.1 Grain structure and analysis of phases within the grains

The L-PBF processed Ti64 is characterized by a fully martensitic microstructure with low ductility in tandem with anisotropic properties. To understand whether the addition of minor B_4C amounts can mitigate the anisotropy and affect the phase transformations during

solidification and subsequent cooling, the microstructure of the as-built TMC samples needs be analyzed. On this account, the grain structure and microstructure within the grains are assessed in the as-built Ti64 and TMC parts.

6.3.2.1.1 As-built

As-built Ti64: Figure 6-3 shows the optical micrograph of the front view of the as-built Ti64 sample, in which large PBGs are elongated along the building direction. Based on their width, these prior β grains can be categorized as wide and narrow, as shown in Figure 6-3(a) and (b). The length of the PBGs was several times of the nominal power layer thickness, revealing that each PBG extends over multiple layers and causes microstructural anisotropy due to the preferential growth of the $\langle 100 \rangle$ direction of the β phase in the building direction during solidification [23, 35].

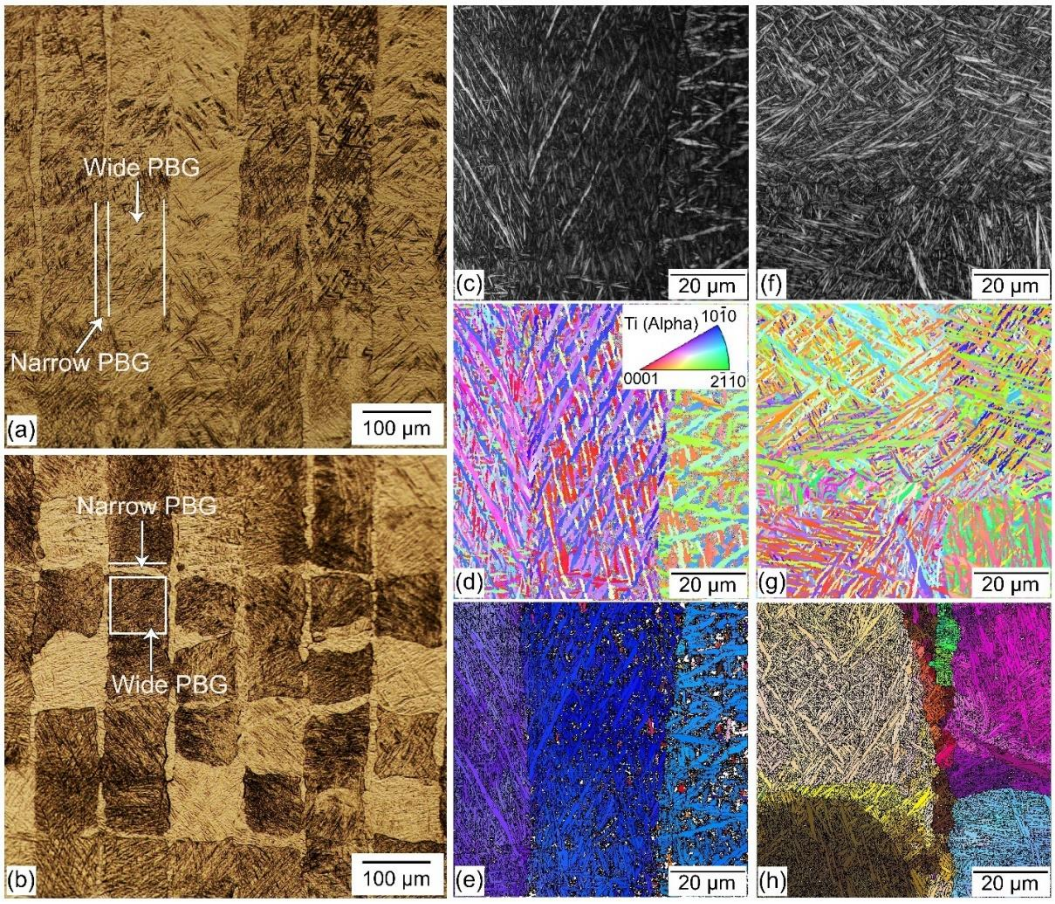

Figure 6-3. Optical micrographs of the: (a) front and (b) top view sections of the as-built Ti64 sample. The band contrast, IPF-Z and reconstructed PBGs EBSD maps of the front and top views are shown in (c-e) and (f-h), respectively. The EBSD analysis was performed with a step size of 0.15 µm.

Referring to the EBSD maps shown in Figure 6-3(c), and (d), the prior β grains contained α' laths with random orientations, giving evidence of a fully martensitic microstructure. The transformation of the PBGs to the martensite originated from the extremely high cooling rates associated with the L-PBF process [36]. Figure 6-3(e) presents PBG orientation maps reconstructed from the IPF map in Figure 6-3(d), in which the PBGs can be distinguished. The optical micrograph from the top view of the as-built Ti64 coupon is shown in Figure 6-3(b). As observed, the elongated PBGs have a square section, and the

wide PBGs are surrounded by narrow ones. The martensitic microstructure is also evident based on the α' laths in the EBSD maps provided in Figure 6-3(f) and (g). The reconstructed PBG orientation map illustrated in Figure 6-3(h) clearly distinguishes the PBGs, where both the wide grains and the narrow ones surrounding them are visible.

As-built TMC: Microstructural characterization of the as-built TMC sample also indicated large columnar PBGs (Figure 6-4(a)). The top view of the as-built TMC specimen also showed a chessboard pattern, like that of the as-built Ti64 counterpart (Figure 6-4(g), and Figure 6-3(b)). The columnar PBGs observed in the as-built TMC can be also classified into two different categories, i.e., wide and narrow. SEM micrograph of the front view showed the cross-section of the tracks which were distinguishable by their boundaries (Figure 6-4(b)). The microstructural examination at higher magnification revealed a needle-like phase homogenously dispersed in the microstructure (Figure 6-4(c)), which can be characterized as the TiB phase due to its morphology. As shown in the inset of Figure 6-4(c), the TiB needles were oriented perpendicular to the track's boundary. This originates from the directionality of the heat flux from the center toward the boundary of the track [37]. Since the nanoscale/micron-sized TiB phase forms through a solid-state transformation from the B-supersaturated matrix, it cannot act as inoculant during the solidification to yield a microstructure with equiaxed PBGs. As confirmed by the EBSD analysis results, the microstructure of the matrix was fully martensitic, characterized by randomly oriented α' laths (Figure 6-4(d), (e), (h) and (i)). This indicates that the incorporation of 0.2 wt.%B_4C into the Ti64 could not avoid the martensitic phase transformation of the matrix. The reconstructed PBG orientation maps of the front and top views of the as-built TMC sample are also shown in Figure 6-4(f) and (j), respectively, to distinguish the wide and narrow PBGs.

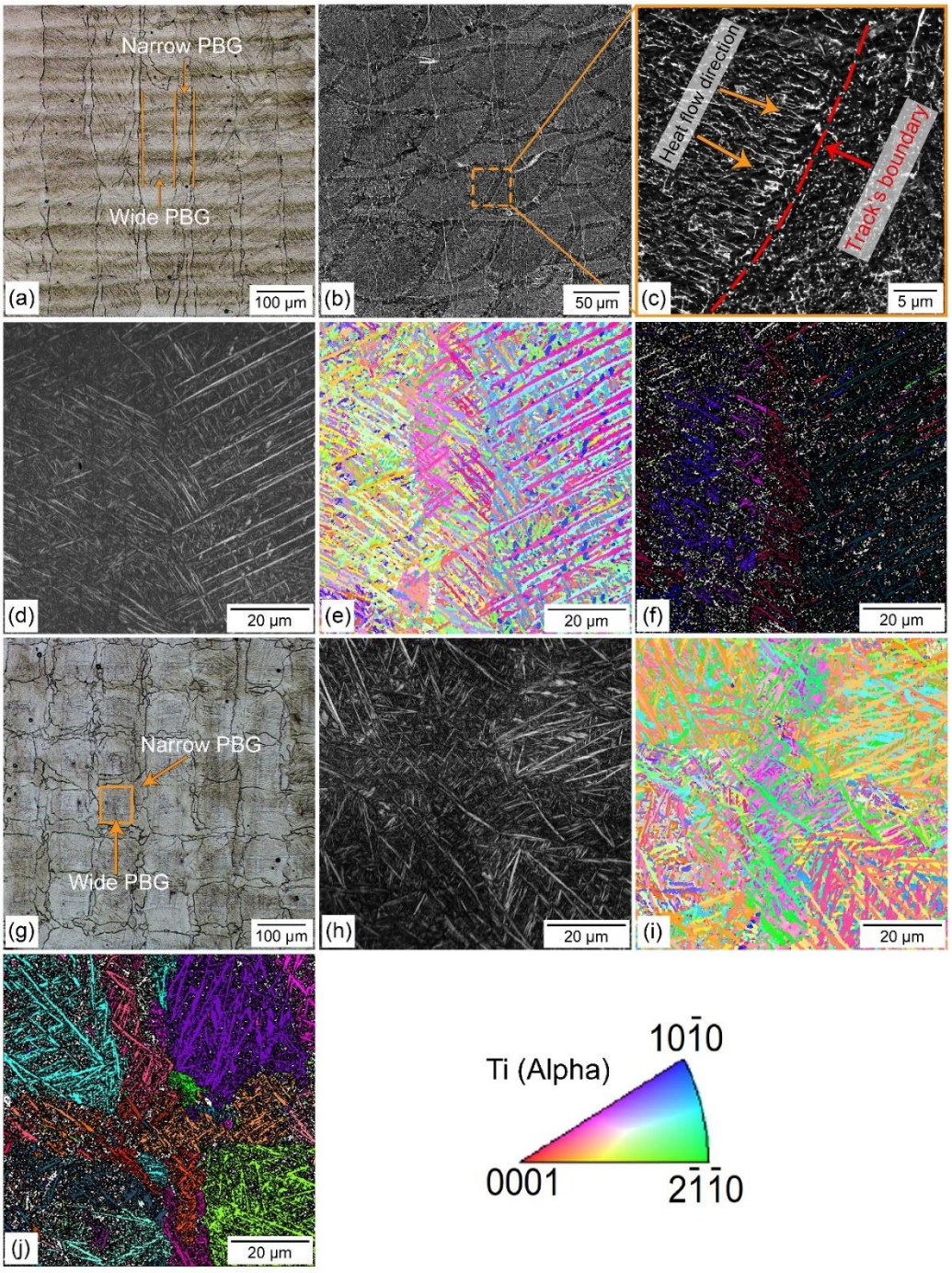

Figure 6-4. (a) Optical micrograph, (b) and (c) SEM micrographs, (d) band contrast EBSD map, (e) IPF-Z EBSD map, and (f) reconstructed PBGs of the front view of the as-built TMC sample. (g) Optical micrograph, (h) band contrast EBSD map, (i) the IPF-Z EBSD map, (j) and reconstructed PBGs of the top view of the as-built TMC sample, respectively. The EBSD analysis was performed with a step size of 0.15 µm.

6.3.2.1.2 Heat-treated

According to the microstructural investigations, the as-built Ti64 and TMC samples suffer from microstructural anisotropy caused by the elongated PBGs. Besides, the fully martensitic microstructure can adversely affect the ductility of the fabricated parts. Moreover, since being metastable, the as-built parts cannot be used in applications where the decomposition of the martensite phase occurs. Therefore, heat treatment of the as-built parts is inevitable to obtain parts with tailored mechanical properties meeting the requirements of medium and high temperature applications.

Subtransus heat-treated Ti64: Figure 6-5(a) and (b) show optical micrographs from the front and top views of the Ti64-850 sample, in which the footprints of the PBGs are detectable. The same pattern was also observed in other subtransus heat-treated samples, confirming that the subtransus heat treatment cycles fail to eliminate the microstructural anisotropy. As shown in Figure 6-5(c-f), a lamellar $\alpha+\beta$ microstructure is discernible in Ti64-850, meaning that the initial α' martensitic microstructure of the as-built Ti64 was fully decomposed. This is in line with the DSC results shown in Figure 6-2, where the martensite decomposition occurred well below 850 °C. It is worth noting that the heat treatment temperatures higher than ~750 °C are known to completely relieve the residual stresses of the as-built Ti64 components [38, 39]. Microstructural characterization of the Ti64 samples subjected to higher subtransus temperature (i.e., Ti64-950) also revealed the same but coarser microstructure. According to Figure 6-6, the XRD pattern of the Ti64-850 sample revealed α peaks, and a very weak peak corresponding to the β phase, also affirming the formation of a minor amount of β phase in the microstructure. The XRD patterns of the as-built Ti64 sample are also presented in Figure 6-6, depicting only peaks

corresponding to the α/α' phase. Therefore, the β phase detected in the Ti64-850 sample has been formed as a result of the heat treatment.

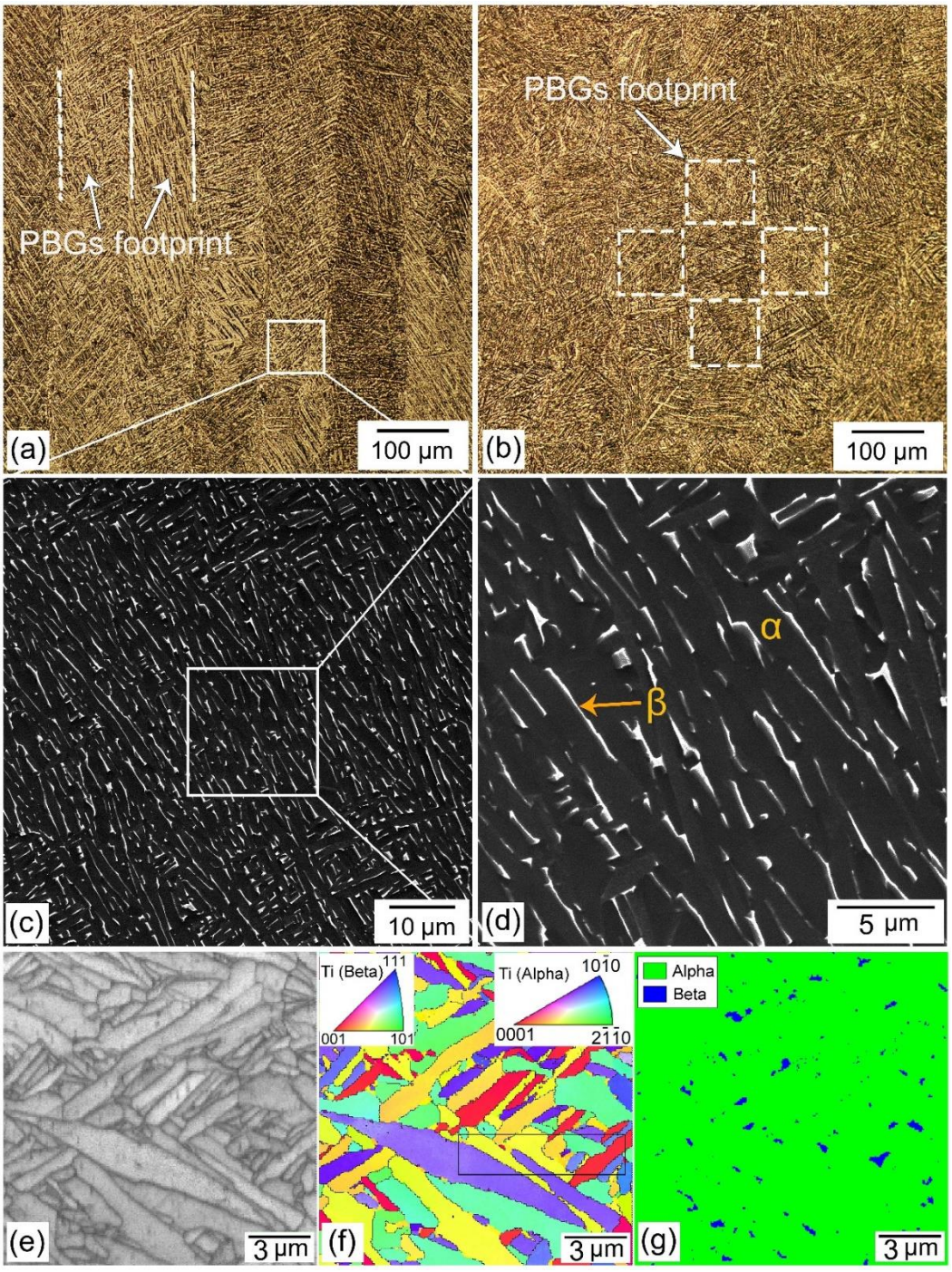

Figure 6-5. Optical micrographs of the: (a) front and (b) top views of the Ti64-850 sample. (c) and (d) SEM micrographs of the front view. (c) shows higher magnification view of the designated zone in (a), and (d) presents higher magnification of the selected region in (c). The band contrast, IPF-Z and phase EBSD maps of the front view are shown in (e-g), respectively. The EBSD analysis was performed with a step size of 0.05 µm.

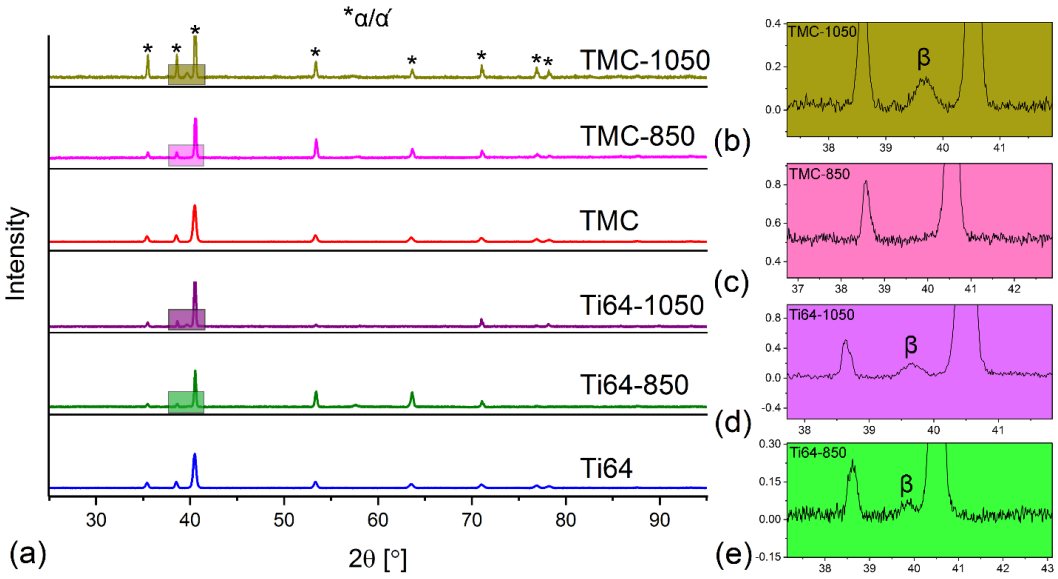

Figure 6-6. (a) XRD patterns of the as-built and heat-treated Ti64 and TMC samples. Higher magnification view of the designated colored box in each pattern is shown in (b-e).

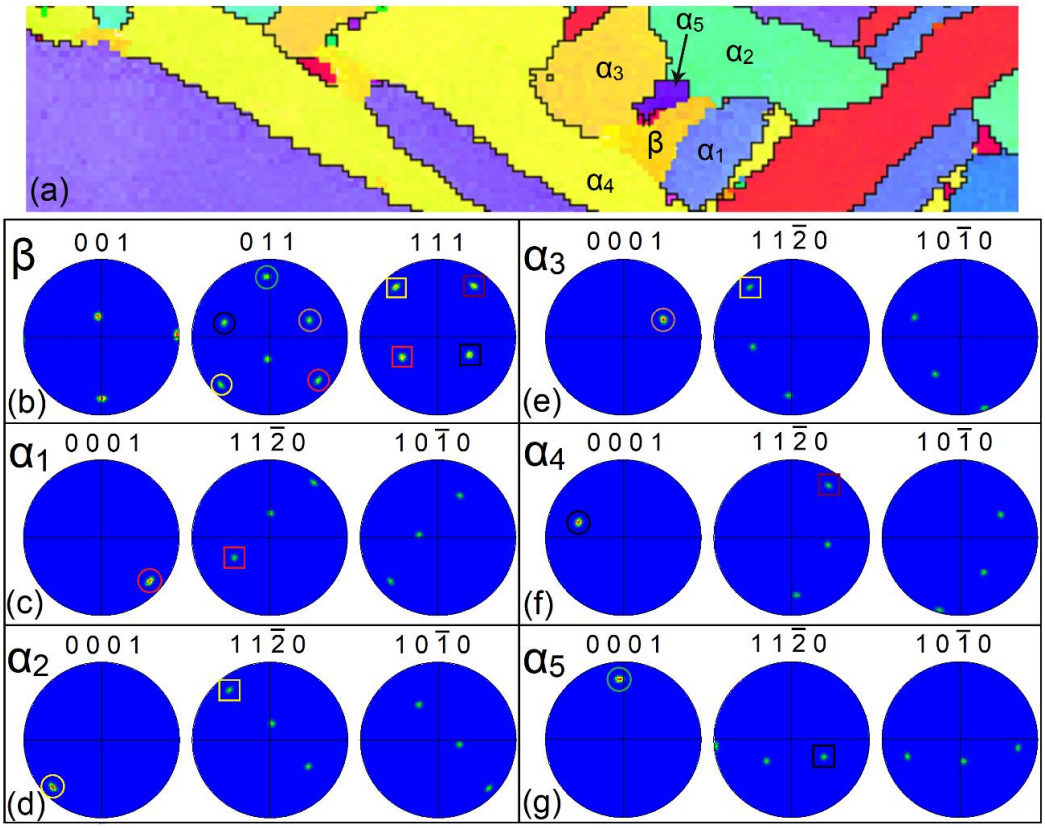

Figure 6-7. (a) Higher magnification IPF-Z EBSD map of the region designated in Figure 6-5(f). (b-g) PFs of a β grain and five different α grains adjacent to it, as marked in (a).

To understand whether there is an orientation relationship between the α and β phases in the subtransus heat-treated Ti64 samples (e.g., Ti64-850), PFs of a β grain and its five neighbour α grains were acquired. As shown in Figure 6-7, there is an orientation relationship between the specified β grain and all α grains in its vicinity. These Burgers relationships are as follows:

$$\begin{aligned} &(011)_{\beta} // (0001)_{\alpha} \\ &\langle 111 \rangle_{\beta} // \langle 11\bar{2}0 \rangle_{\alpha} \end{aligned} \qquad \text{Eq. 1}$$

Referring to the Burgers relations given in Eq. 1, the preferential growth of the α phase parallel to the (011) family of the crystallographic planes of the β phase leads to a Widmanstätten structure when intermediate or slow cooling rates are applied. In fact, the long dimension of the α grain extends parallel to the (011) planes of the β phase since the growth along these planes is faster [40, 41].

Supertransus heat-treated Ti64: As shown in Figure 6-8(a), the Ti64-1050 sample is characterized by equiaxed PBGs, as opposed to the as-built Ti64 and the subtransus heat-treated samples (Figure 6-3, and Figure 6-5). The supertransus temperatures can shatter the columnar PBGs of the as-built Ti64 parts into an equiaxed morphology by providing the condition for the nucleation of new β grains from the boundaries of the existing columnar PBGs [22, 42, 43]. The average size of these newly formed equiaxed PBGs was 250 μm, being remarkably larger than the average width of the columnar PBGs of the as-built Ti64 part (Figure 6-3). This clearly reveals the severe coarsening of PBGs of the Ti64 alloy caused by isothermal holding at this supertransus temperature. The equiaxed PBGs were surrounded by a continuous network of thick GB- α and contained packets of lamellar ($\alpha+\beta$) structure, each presenting a distinct orientation (Figure 6-8(a) and (b)). The EBSD maps of the Ti64-1050 sample are presented in Figure 6-8(c)-(e). Figure 6-8(d) shows a few of these packets, where each individual packet is characterized by large aspect ratio α lamellae belonging to the same crystallographic variant. The XRD analysis of the Ti64-1050 sample confirmed the presence of β phase in the microstructure with a more intense peak than the Ti64-850 case, suggesting a higher volume fraction of this phase in the former (Figure 6-6).

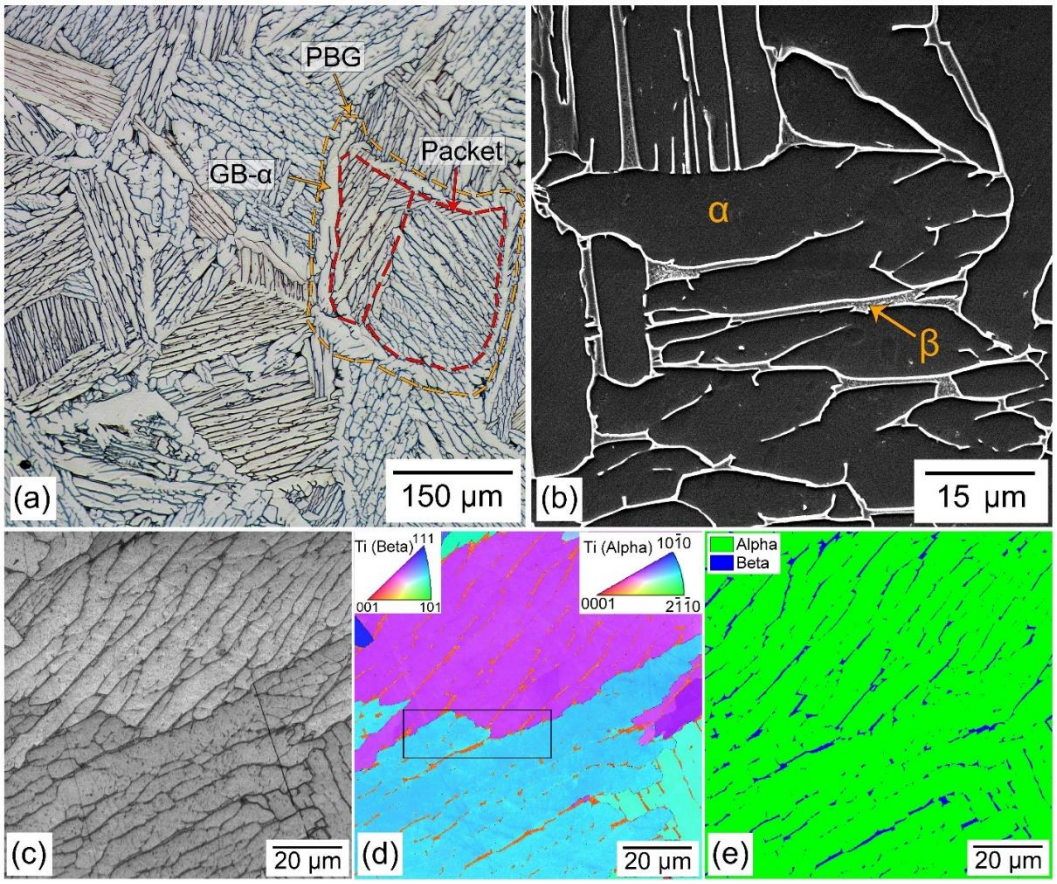

Figure 6-8. (a) Optical and (b) SEM micrographs of the front view of the Ti64-1050 sample. The band contrast, IPF-Z and phase EBSD maps of the front view are shown in (c-e), respectively. The EBSD analysis was performed with a step size of 0.1 µm.

The PFs of α and β phases existing in two adjacent packets are provided in Figure 6-9. As it is evident, the β phase in both packets shares the exact same crystallographic variant, confirming that both packets are formed from the same PBG. Moreover, the α phase within each packet has an orientation relationship with the β phase, like those in Eq. 1.

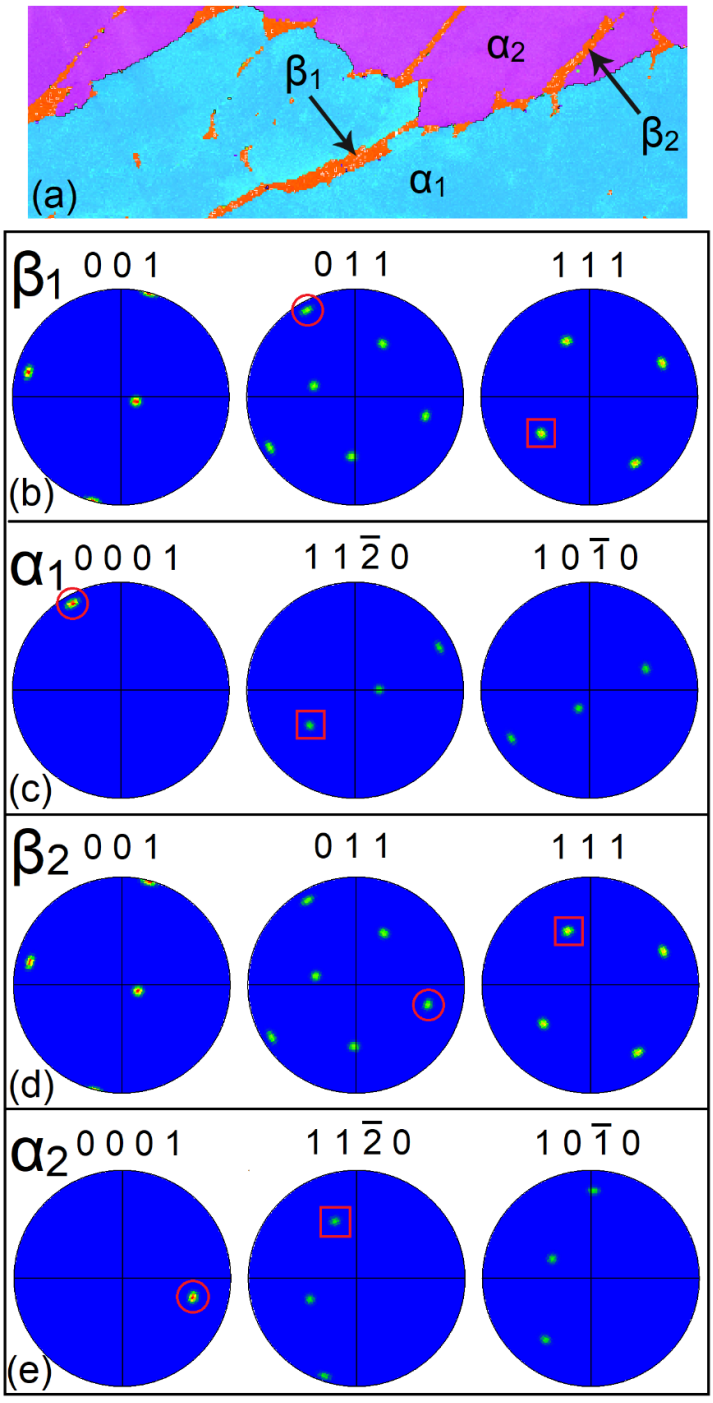

Figure 6-9. (a) Higher magnification IPF-Z EBSD map of the region designated in Figure 6-8(d). (b-e) PFs of the α and β grains marked in (a).

Subtransus heat-treated TMC: Microstructural characterizations of the TMC-850 sample revealed the inability of this subtransus temperature in eliminating the footprint of the tracks and columnar PBGs (Figure 6-10(a) and (b)). Higher magnification SEM micrographs indicated the decomposition of the α' phase to α and β phases. As shown in Figure 6-10(c) and (d), the track boundaries contained a higher frequency of TiB needles than the interior locations. Although the microstructural analysis of the TMC-850 part confirmed the presence of TiB needles and the β phase, no peaks referring to these two phases were detected in the XRD pattern (Figure 6-6), probably due to their low content and significantly small size. It is worth noting that in the as-built TMC sample, only peaks corresponding to the α / α' phase were detected, and no peaks referring to the TiB phase were observed, as opposed to the microstructural characterizations confirming the formation of nano-scale/sub-micron TiB needles (Figure 6-4(c)). Similar to the Ti64-850 sample (Figure 6-7), an obvious orientation relationship was detected between the adjacent α and β phases of the TMC-850 sample (Figure 6-11). These Burgers relations were the same as those observed in the Ti64-850 and Ti64-1050 samples (Eq. 1). Microstructural characterizations revealed (not shown here) that even the subtransus temperature of 950 °C could not eliminate the trace of scan tracks and the footprints of PBGs. As expected, the α and β phases also experienced coarsening due to the application of a higher temperature.

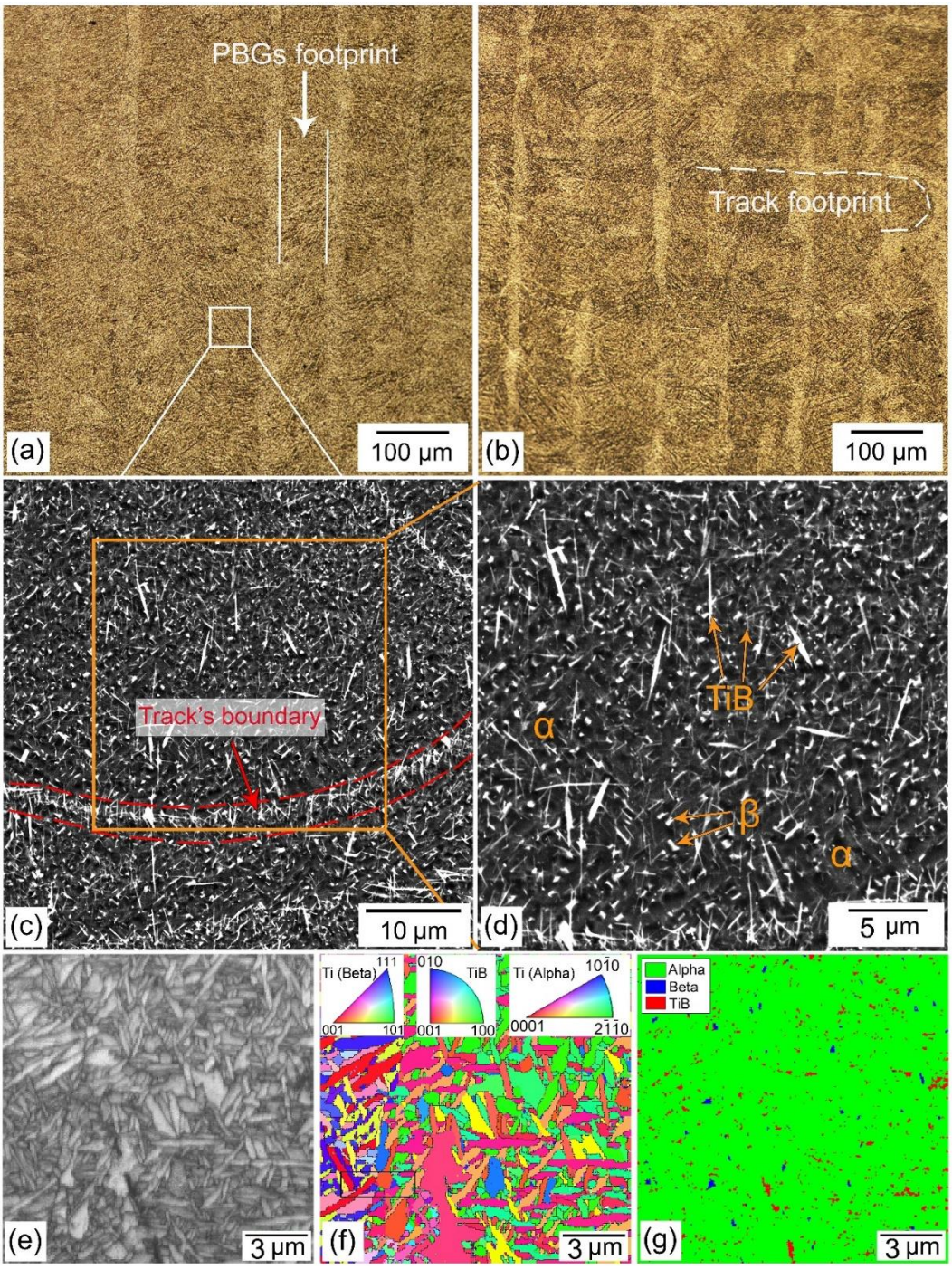

Figure 6-10. Optical micrographs of the: (a) front and (b) top views of the TMC-850 sample. (c) and (d) SEM micrographs of the front view. (c) shows higher magnification view of the designated zone in (a), and (d) presents higher magnification view of the selected region in (c). The band contrast, IPF-Z, and phase EBSD maps of the front view are shown in (e-g), respectively. The EBSD analysis was performed with a step size of 0.05 µm.

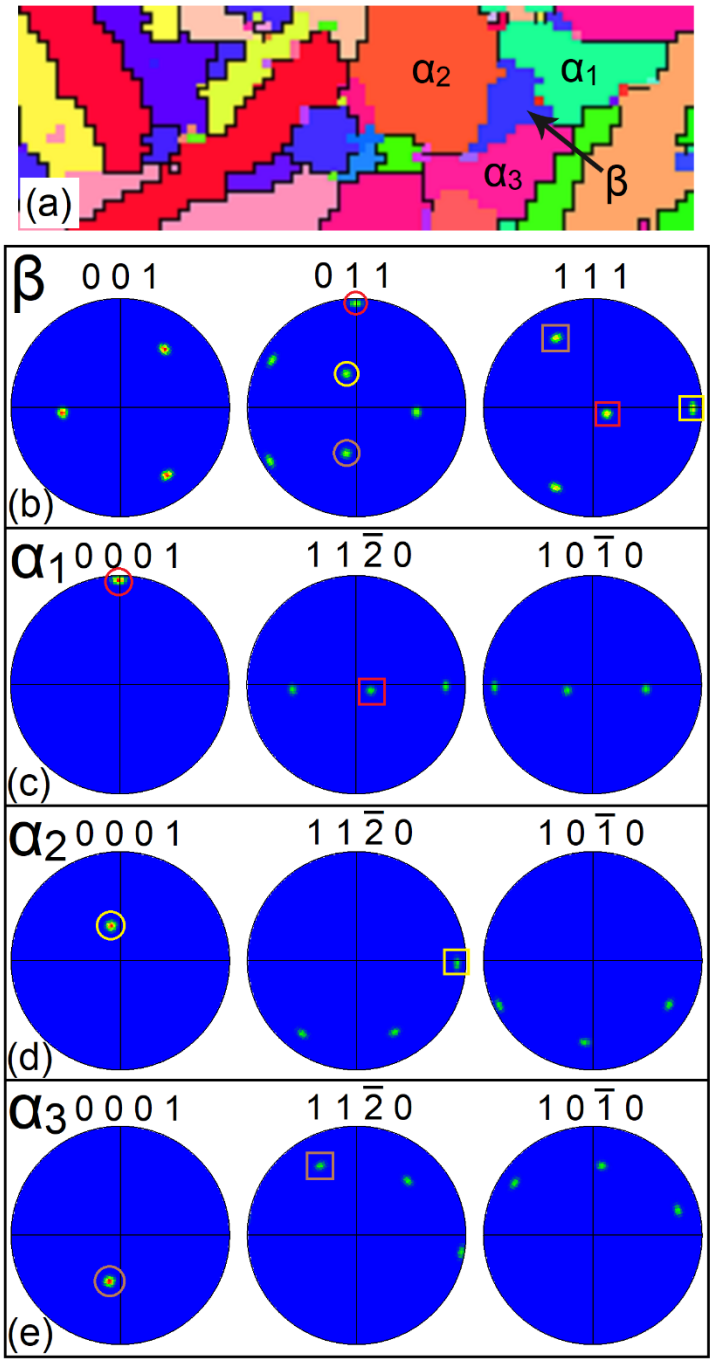

Figure 6-11. (a) Higher magnification IPF-Z EBSD map of the region designated in Figure 6-10(f). (b-e) PFs of the α and β grains marked in (a).

Supertransus heat-treated TMC: Figure 6-12(a) shows optical micrograph of the TMC-1050 sample, in which the columnar PBGs are removed, and a fully isotropic

microstructure is obtained. The XRD analysis of the TMC-1050 sample confirmed the presence of β phase in the microstructure, owing to the higher volume fraction of this phase than that existing in the TMC-850 case (Figure 7). However, despite the significant coarsening of the TiB phase, this phase was still not detectable with the performed XRD analysis possibly due to its low volume fraction. Moreover, unlike the Ti64-1050 counterpart (Figure 6-8(a)), the GB-α was absent in the microstructure. Contrary to the lamellar morphology of the α phase in the subtransus heat-treated TMC-850 sample (Figure 6-10), this phase featured an equiaxed morphology in the supertransus heat-treated TMC-1050 sample (Figure 6-12). To understand the reason behind such a morphological change, the crystallographic orientation of α , β , and TiB phases were analysed.

Figure 6-13 shows PFs for a TiB needle as well as the β phase and several α grains existing in its immediate vicinity. As observed, the β phase had orientation relationships with three of the adjacent α grains, namely α_1 , α_3, and α_4. These Burgers relations were $(011)_\beta // (0001)_\alpha$ and $\langle 111 \rangle_\beta // \langle 11\bar{2}0 \rangle_\alpha$. Comparison of the PFs of the α_2 grain (Figure 6-13(e)) with those of the β grain (Figure 6-13(b)) clearly revealed the absence of any Burgers relations between them. The analysis of PFs also indicated no orientation relationships between the β phase and its neighbour TiB needle. Although the detailed microstructural observation and EBSD analysis of the wire arc additive manufacturing (WAAM) processed 0.1 wt.%B/Ti64 system has recently shown orientation relationships between the TiB needles and the β grains [44], such relationships were not observed in this study. This can be ascribed to the differences between the solidification path and subsequent microstructural evolutions of the WAAM and L-PBF processed TiB reinforced

TMCs. As opposed to the L-PBF fabricated TMCs in this study in which the TiB phase is formed through a solid state reaction from the B-supersaturated β phase ($\beta \rightarrow (\beta + TiB)$), the formation of TiB phase in the WAAM processed TMC occurs through a eutectic reaction ($L \rightarrow (\beta + TiB)$). That is why an orientation relationship was observed between the β and TiB products in the WAAM fabricated TiB reinforced TMCs. Referring to the PFs provided in Figure 6-13, there exists no Burgers relation between the investigated TiB needle and the adjacent α grains. It has been reported in the literature that TiB is a potent nucleant for the heterogenous nucleation of the α phase due to the identified specific orientation relationships of $(001)_{TiB} // (0001)_{\alpha}$, $(001)_{TiB} // \{11\bar{2}0\}_{\alpha}$ and $(100)_{TiB} // \{10\bar{1}0\}_{\alpha}$ as well as excellent lattice matches between them [32, 44]. However, at least for the investigated TiB needle, such orientation relationships were not identified. This observation is in agreement with the results reported in [45], where orientation relationships were not found between some of the TiB reinforcements and their adjacent α grains. The EBSD analysis results reported recently by Cui et al. [46] also revealed no TiB/α orientation relationships in electron beam powder bed fusion (EB-PBF) fabricated TiB reinforced TMCs. However, the same composite system in the hot-forged state showed the common TiB/α orientation relationships. The absence of TiB/α orientation relationships in the EB-PBF fabricated TMCs has been ascribed to the possibility of the nucleation of α phase on other planes of the TiB phase in addition to the $(100)_{TiB}$ plane [46, 47]. Therefore, the absence of TiB/α orientation relationships between the investigated TiB needle and the α grains in this study does not necessarily mean that such orientation relationships do not exist in the whole microstructure.

As microstructural characterizations revealed, the morphology of α grains changed from lamellar in the Ti64-1050 sample to equiaxed in the TMC-1050 one (Figure 6-8, and Figure 6-12). The equiaxed morphology of α grains has been also reported in other research studies dealing with the heat treatment of TiB-reinforced TMCs at supertransus temperatures [31-34]. Such a morphological change could be ascribed to the role that TiB needles played in the: (i) growth of prior β grains, and (ii) $\beta \rightarrow \alpha + \beta$ phase transformation. The TiB needles homogeneously dispersed in the matrix can effectively restrict the growth of PBGs and consequently bring about finer PBGs than the non-reinforced Ti64-1050 counterpart [32, 48]. This refinement is caused by TiB needles acting as pinning points for the grain boundaries of the PBGs [49]. Since PBG boundaries act as nucleation sites for the α grains during cooling below the β transus temperature, higher frequency of α nucleation sites and consequently finer α grains are formed. Moreover, as the maximum length of α lamellae is limited to the size of the PBG accommodating them, finer PBGs generally lead to shorter α lamellae. When nucleated from the PBG boundaries, TiB needles act as effective grain growth inhibitors and confine the growth of the long dimension of the α grain [40, 41], leading to a more equiaxed morphology. The absence of the continuous GB-α network in the TMC-1050 sample can be also discussed based on the same mechanism. It is worth noting that although the orientation relationship between a representative TiB needle and its surrounding α grains was not found (Figure 6-13), the possible existence of such relationship for some other TiB needles can be also a reason behind the formation of fine equiaxed α grains in the TMC-1050 sample. As reported in [33, 50, 51], the TiB/α orientation relationships in B-modified Ti alloys justify that TiB needles provide heterogeneous nucleation sites for the α phase and favor equiaxed morphology.

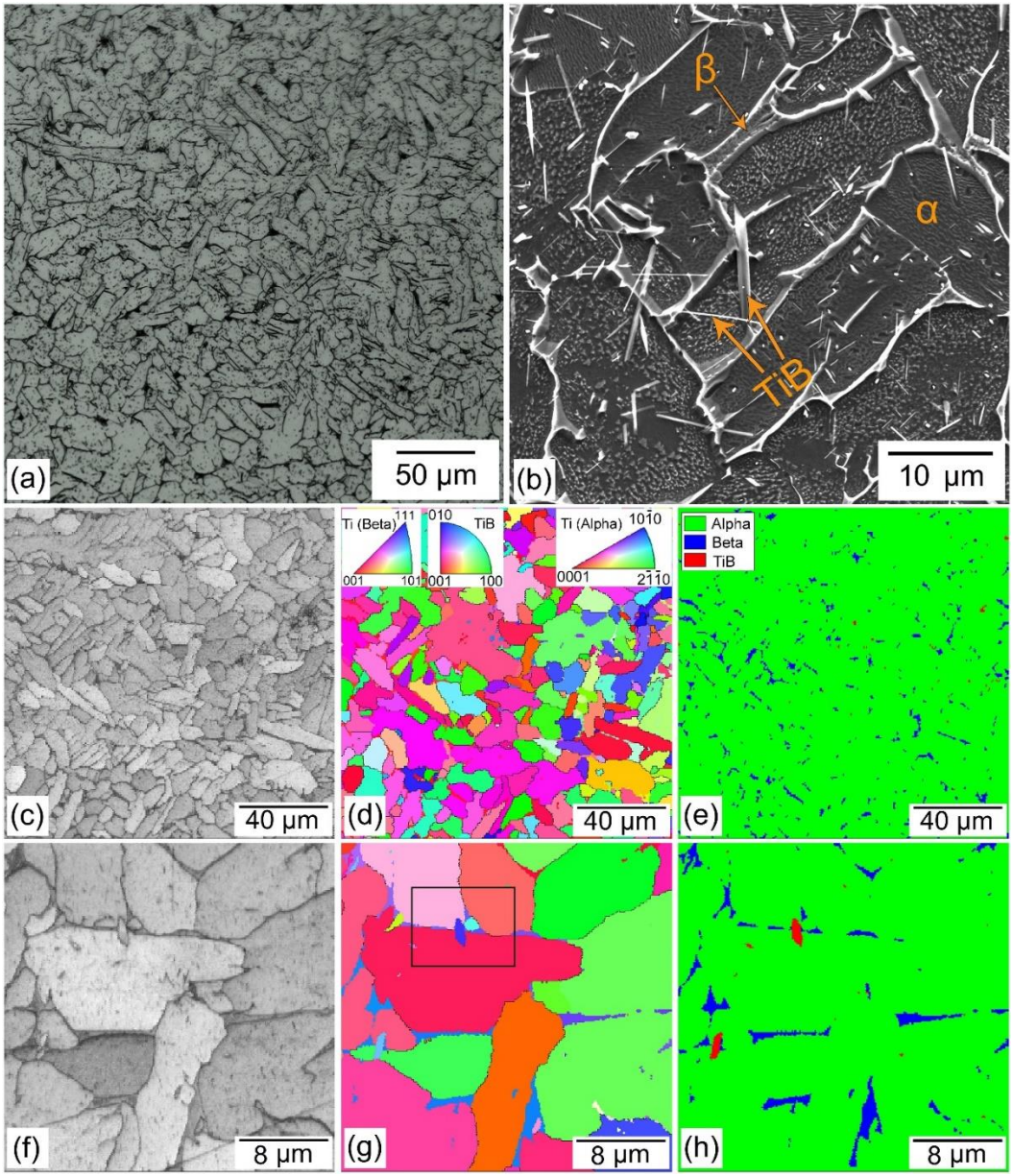

Figure 6-12. (a) Optical and (b) SEM micrographs of the front view of the TMC-1050 sample. The band contrast, IPF-Z and phase EBSD maps of the front view are shown in (c, f), (d, g) and (e, h), respectively. The EBSD analysis was performed with a step size of: (c-e) 0.5 µm, and (f-h) 0.1 µm.

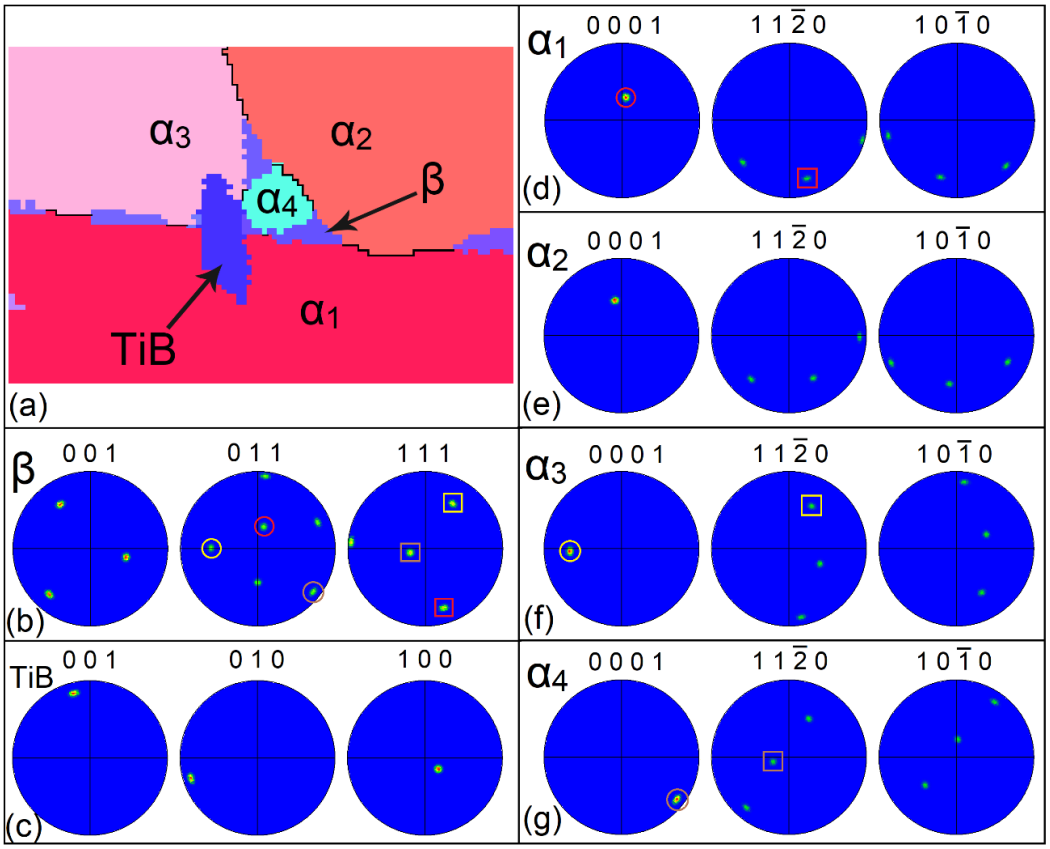

Figure 6-13. (a) Higher magnification IPF-Z EBSD map of the region designated in Figure 6-12(g). (b-g) PFs of the TiB needle, and α and β grains adjacent to it, as marked in (a).

6.3.2.2 Size and volume fraction of micro-constituents- Ti64 vs. TMC

The mechanical properties of the as-built and heat-treated Ti64 and TMC parts are dictated not only by the grain structure and the nature of the phases within the grains, but also by the size and volume fraction of the micro-constituents. In this respect, microstructures were subjected to the statistical analysis, the results of which are listed in Table 6-2 and Table 6-3 for the as-built and heat-treated samples, respectively.

According to Table 6-2, the width and length of α' laths in the as-built TMC sample were smaller than those of the as-built Ti64 owing to the presence of nanoscale/micron-sized TiB needles homogeneously dispersed in the matrix of the TMC sample. It is of note that

compared to the width, the length of α' lath was more affected by the presence of TiB needles. The average width of the α lamellae in the Ti64-850 sample was higher than that of the α' laths in the as-built Ti64 counterpart (Table 6-3). The measurements indicated that the size of the lamellar structure follows an increasing trend by increasing the heat treatment temperature. As shown in Figure 6-14(a), the increase in the temperature from 850 to 1050 °C led to a significant increase in the width of α phase from 0.58±0.14 to 7.5±2.3 µm in the Ti64 samples. The average width of α lamellae in the Ti64-1050 specimen was noticeably higher than those of the subtransus heat-treated counterparts (Table 6-3). The α/α' width in all of the as-built and heat-treated TMCs was lower than their corresponding Ti64 counterparts, revealing that TiB needles actively restricted the α growth kinetic (Figure 6-14(a)).

Table 6-2. The size and volume fraction of microstructural features of the as-built Ti64 and TMC samples.

Sample	**Microstructural Feature**								
	Prior β width (wide), µm	Prior β width (Narrow), µm	α′ lath length, µm	α′ lath width, µm	TiB length, µm	TiB diameter, nm	TiB aspect ratio	α′ Vol. %	TiB Vol.%
As-built Ti64	86±5.9	9.4±3.1	15.6±3.1	0.58±0.14	-	-	-	100	-
As-built TMC	75.5±6.4	19.6±4.1	8.4±7.3	0.48±0.12	0.99±0.31	150±50	~6.6	78.2	21.8

Table 6-3. The size and volume fraction of microstructural features of the heat-treated Ti64 and TMC samples.

Sample	Microstructural Feature							
	α width (diameter), μm	TiB length, μm	TiB diameter, nm	TiB aspect ratio	β Vol.%	α Vol.%	TiB Vol.%	β width
Ti64-850	1.09±0.38	-	-	-	10.9	89.1	-	0.292±0.093
TMC-850	0.44±0.18	1.3±0.72	210±72	6.2	6.4	75.1	18.5	0.207±0.064
Ti64-950	3.54±1.04	-	-	-	11.2	88.8	-	0.836±0.256
TMC-950	1.66±0.57	2.87±1.24	306±155	9.4	7.2	78.3	14.5	0.462±0.176
Ti64-1050	7.5±2.3	-	-	-	13.2	86.8	-	1.357±0.743
TMC-1050	5.75±1.6	6.3±4.22	381±151	~16.5	9.2	84.7	6.1	0.85±0.454

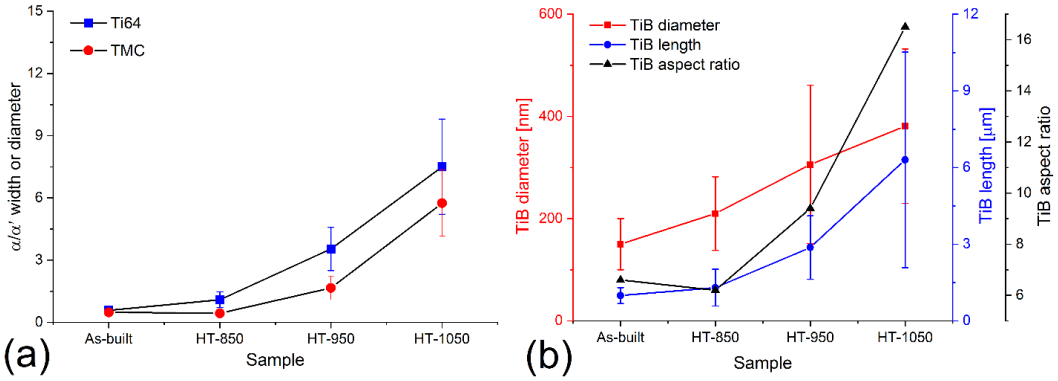

Figure 6-14. (a) The α/α′ width of the Ti64 and TMC samples, and (b) the length, width, and aspect ratio of the TiB needles in the TMC samples in the as-built and heat-treated conditions.

To justify the measured values and explore the role of TiB on impeding the growth of α lamellae, the size of α phase in Ti64 needs to be analytically calculated at different temperatures. As mentioned earlier, the α' decomposition occurs through a diffusion-controlled solid-state transformation, leading to the formation of α and β phases, the

size of which is dictated by the thermal cycle experienced during the heat treatment. The variations observed in the size of α phase (Figure 6-14(a)) can be analytically modeled using the self-diffusion equations available for Ti in the α phase (for subtransus heat treatment) and the β phase (for supertransus heat treatment), as expressed by Eq. 2, and Eq. 3, respectively [52]:

$$D_{Ti}^{\alpha} = 1.527\times10^{-9}\exp(\frac{-150700}{RT}) \quad [2]$$

$$D_{Ti}^{\beta} = 5.381\times10^{-6}\exp(\frac{-188400}{RT}) \quad [3]$$

where D_{Ti}^{α}, and D_{Ti}^{β} are the self-diffusion coefficients of Ti in α and β phases, respectively, T is the absolute temperature, and R is the gas constant. The Ti diffusion path for the subtransus (d_{Ti}^{α}) heat-treated Ti64 samples and supertransus (d_{Ti}^{β}) heat-treated Ti64 and TMC samples can be calculated using Eq. 4 and Eq. 5, respectively:

$$d_{Ti}^{\alpha} = 2\sqrt{D_{Ti}^{\alpha}\times t_{holding}} \quad [4]$$

$$d_{Ti}^{\beta} = 2\sqrt{D_{Ti}^{\beta}\times t_{cooling}} \quad [5]$$

in which $t_{holding}$ is the holding time at each subtransus temperature (i.e., 2 h), and $t_{cooling}$ is the period during which the $\beta\rightarrow\alpha$ transformation takes place during the cooling stage in the supertransus heat-treated Ti64. Since $\alpha'\rightarrow\alpha$ transformation occurs during holding at the subtransus heat treatment temperature, the Ti self-diffusion needs to be calculated in α' rather than β. As α and α' phases have the same crystal structure and almost similar lattice parameters, the Ti self-diffusion in α' is assumed to be the same as the α phase

(Eq. 4). In the supertransus heat treatment, on the other hand, the formation of α from β phase during the cooling stage necessitates using the Ti self-diffusion equation in the β phase (Eq. 5). In the subtransus heat-treated sample of Ti64-950, the d_{Ti}^{α} predicted by Eq. 4 was 4 µm, which is in a good agreement with the measured α width (Figure 6-14(a)). This approach was also utilized to predict the α width in the supertransus heat-treated Ti64-1050 and TMC-1050 samples using Eq. 5. Referring to the DSC test results shown in Figure 6-2, the $\beta \rightarrow \alpha$ phase transformation during the cooling stage occurs in the temperature ranges of 925-825 °C for Ti64 and 1010-850 °C for TMC. Since samples were furnace cooled with the cooling rates of 10 and 15 °C/min within the respective temperature ranges, $t_{cooling}$ was ~10 min for both Ti64-1050 and TMC-1050 samples. An equivalent diffusion coefficient ($D_{eq,Ti}^{\beta}$) was defined for each temperature range using the following equation:

$$D_{eq,Ti}^{\beta} = \frac{\int_{T_s}^{T_f} D_{Ti}^{\beta} dT}{T_s - T_f} \quad [6]$$

By substituting the calculated $D_{eq,Ti}^{\beta}$ in Eq. 5, the d_{Ti}^{β} was found to be 6.5 and 13.5 µm for Ti64-1050 and TMC-1050 samples, respectively. Although the predicted α width in Ti64-1050 is in a good agreement with the measured value, the α width is significantly overestimated in the TMC-1050 case. Despite having a considerably higher T_s and a wider ($T_s - T_f$) in which the β phase transforms to α, the measured α width in the TMC-1050 sample was lower than that of the Ti64-1050 counterpart. This clearly reveals the remarkable role of TiB needles in refining the microstructure of supertransus heat-treated

TMCs, caused by the growth restricting effects of the TiB phase as well as the potential nucleation of α grains from the TiB needles.

The employed heat treatments also affected the fraction of phases in the final microstructure. As listed in Table 6-3, the volume fraction of α phase decreased from 89.1 to 86.8% as the temperature increased from 850 to 1050 °C in Ti64 case. The same trend was observed for the TMC samples, the only difference being that the volume fraction of α phase was lower at any given temperature. Based on the size measurements, the length, and diameter of TiB needle were ~1 μm, and 150 nm, respectively, yielding an aspect ratio of ~6.6 in the as-built TMC. As illustrated in Figure 6-14(b), both the length and diameter of TiB needles followed an increasing trend due to higher diffusion rates induced at higher temperatures. The coarsening of TiB needles in TMCs has been reported to follow the Ostwald ripening principle, in which the large TiB needles grow at the expense of small ones [38]. The aspect ratio of TiB needles also followed an increasing trend by increasing the heat treatment temperature.

6.3.3 Mechanical Properties

In this section, the grain and phase analysis results in Section 6.3.2.1 as well as the size and volume fraction of the micro-constituents in Section 6.3.2.2 are implemented to discuss the mechanical properties of the as-built and heat-treated Ti64 and TMC components in terms of the compressive strength, fracture strain, microhardness, and scratch resistance.

6.3.3.1 Compression

The typical true stress-true stain curves of the as-built and heat-treated Ti64 and TMC samples are shown in Figure 6-15(a) and (b), respectively. The mean yield strength (σ_y),

ultimate strength (σ_u) and fracture strain (ε_f) of all samples are depicted in Figure 6-16. In the case of Ti64, the maximum σ_y and σ_u values and the minimum ε_f correspond to the as-built sample. This is attributable to the fully martensitic microstructure of this sample (Figure 6-3). By heat treating the sample at 850 °C (Ti64-850), a sharp drop of 16.8 and 8.3% was observed in the σ_y and σ_u, respectively. However, the increase in the heat treatment temperature to 950 °C led to only a negligible decrease in these values compared to the Ti64-850 sample. Further increase of the temperature to 1050 °C again resulted in a considerable drop in the σ_y but slightly affected the σ_u. The ductility of the heat-treated Ti64 samples in the subtransus region showed an ascending trend with a sharp increase of 44 and 65.3% in Ti64-850 and Ti64-950 samples, respectively, compared to the as-built Ti64. Although the ductility of the Ti64-1050 sample was still higher than that of the as-built Ti64, it was lower than the ductility of the subtransus heat-treated samples.

The observed trend in the σ_y of the Ti64 samples can be justified by taking the role of different strengthening mechanisms into account. In the absence of reinforcements, the grain boundary (Hall-Petch), and solid solution strengthening are the major mechanisms governing the variations in the σ_y. In this study, only the α/α' phase was considered in the grain boundary strengthening mechanism since being the dominant phase. According to the Hall-Petch equation [53], the σ_y can be predicted for the heat-treated Ti64 samples with a lamellar ($\alpha+\beta$) microstructure using the following equation:

$$\sigma_y = \sigma_0^{\alpha+\beta} + \frac{K_{HP}}{\sqrt{d_\alpha}} \quad [7]$$

where $\sigma_0^{\alpha+\beta}$ is the friction stress, K_{HP} is the Hall-Petch coefficient, and d_α is the mean width of α lamellae. Given that the $\sigma_0^{\alpha+\beta}$ for Ti64 has not been reported in the literature, this term was calculated using the mixture rule as follows:

$$\sigma_0^{\alpha+\beta} = \sigma_\alpha V_\alpha + \sigma_\beta V_\beta \quad [8]$$

in which σ_α, and σ_β are the friction stresses, and V_α and V_β are the volume fraction of α, and β phases, respectively. σ_α and σ_β are both unknown and can be calculated by considering the friction stress of Ti for α (σ_0^α) and β (σ_0^β) phases as well as the solid solution strengthening of Al as α -stabilizer ($\sigma_{SS,Al}^\alpha$) and V as β -stabilizer ($\sigma_{SS,V}^\beta$) in Ti. On this account, σ_α is defined as [54]:

$$\sigma_\alpha = \sigma_0^\alpha + \sigma_{SS,Al}^\alpha = \sigma_0^\alpha + (0.8 G_m \delta_{Al}^{Ti} C_{Al}^\alpha) \quad [9]$$

in which G_m, δ_{Al}^{Ti}, and C_{Al}^α are the shear modulus, misfit strain of Al in Ti, and atomic fraction of Al in the α phase, respectively. The misfit strain of each solute in Ti matrix can be obtained using the following equation [55]:

$$\delta_{solute}^{Ti} = \frac{|r_{Ti} - r_{solute}|}{r_{Ti}} \quad [10]$$

where r_{Ti} and r_{solute} are the atomic radius of Ti and solute, respectively.

σ_β is defined as [56]:

$$\sigma_\beta = \sigma_0^\beta + \sigma_{SS,V}^\beta = \sigma_0^\beta + V_\beta \times \left[34 \times (100 \times C_V^\beta)^{0.765}\right]^{1.075} \quad [11]$$

where C_V^{β} is the atomic fraction of V in the β phase. By substituting the calculated σ_{α} and σ_{β} values in Eq. 8, the resultant $\sigma_0^{\alpha+\beta}$ can then be used to predict the σ_y based on Eq. 7. The data required to calculate σ_y are summarized in Table 6-4.

The procedure mentioned above for the lamellar ($\alpha+\beta$) microstructure of the heat-treated Ti64 samples is not valid for the as-built Ti64 with a fully martensitic microstructure. σ_y of such microstructure can be predicted using the following equation:

$$\sigma_y = \sigma_0^{\alpha'} + \frac{K_{HP}}{\sqrt{d_{\alpha'}}} \quad [12]$$

in which $\sigma_0^{\alpha'}$ is the friction stress of the α' phase and $d_{\alpha'}$ is the mean width of α' laths. $\sigma_0^{\alpha'}$ is defined as:

$$\sigma_0^{\alpha'} = \sigma_0^{\alpha} + \sigma_{SS,Al}^{Ti} + \sigma_{SS,V}^{Ti} = \sigma_0^{\alpha} + 0.8G(\delta_{Al}^{Ti} C_{Al}^{Ti} + \delta_V^{Ti} C_V^{Ti}) \quad [13]$$

where $\sigma_{SS,Al}^{Ti}$ and $\sigma_{SS,V}^{Ti}$ are the solid solution strengthening caused by Al and V in Ti, respectively, and C_{Al}^{Ti} and C_V^{Ti} are the atomic fraction of Al, and V in Ti, respectively. The data required to calculate the σ_y of the as-built Ti64 using Eq. 12 and 13 are listed in Table 6-4.

Table 6-4. The properties and parameters used in obtaining the contribution of different strengthening mechanisms.

Properties and Parameters	Value	Source
K_{HP}	300 MPa.μm$^{1/2}$	[57]
b_m	0.295 nm	[58]
G_m	45 GPa	[59]
ω_0	0.125	[60]
ε_m	0.00944	Measured
σ_0^{α}	80 MPa	[56]
σ_0^{β}	4.5 MPa	[56]
r_{Ti}	1.36 Å	[61]
r_{Al}	1.18 Å	[61]
r_V	1.25 Å	[61]
δ_{Al}^{Ti}	0.132	Calculated
δ_V^{Ti}	0.081	Calculated
C_{Al}^{α}	0.115	Measured
C_V^{β}	0.238	Measured
C_{Al}^{Ti}	0.102	Measured
C_V^{Ti}	0.036	Measured
E	124 GPa	Measured

The σ_y values predicted for Ti64 samples are also provided in Figure 6-16(a). As can be seen, there is a good match between the calculated and measured values. The contribution of each strengthening mechanism, namely, friction stress, substitutional solid solution (i.e., by Al and/or V), and Hall-Petch in the overall σ_y of the as-built and heat-treated Ti64

samples are depicted in Figure 6-17(a). The major strengthening mechanism in all samples was substitutional solid solution. A monotonic increase ranging from 55 to 75% was observed in the contribution of this strengthening mechanism with respect to the increase in the heat treatment temperature. In the as-built Ti64 sample with the lowest α' width, the highest contribution by the Hall-Petch mechanism was perceptible (37%). Since the heat treatment of the Ti64 samples is accompanied by the growth of the α lamellae, the Hall-Petch mechanism became less effective in the strengthening of these samples. The minimum strengthening caused by the Hall-Petch mechanism was observed in the Ti64-1050 sample (15%) with the largest α width. Friction stress had the minimum impact on the σ_y of all samples with a contribution in the range of 7.5-11%.

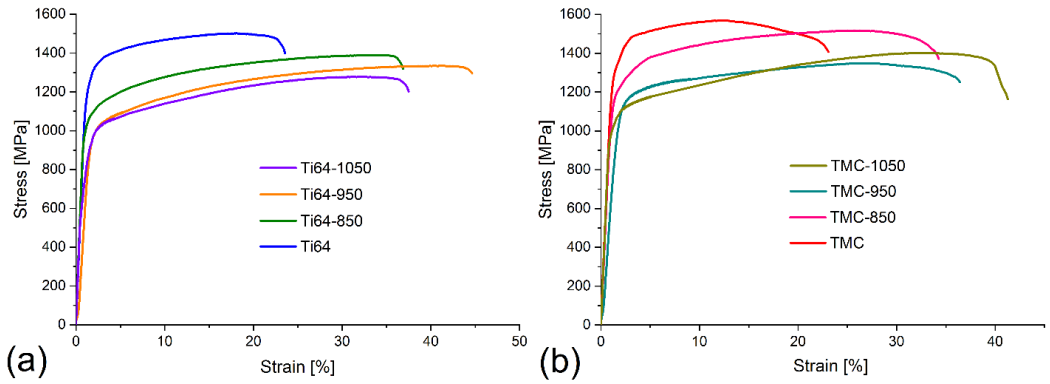

Figure 6-15. The true stress-true strain curves of the: (a) Ti64 and (b) TMC samples in the as-built and heat-treated conditions.

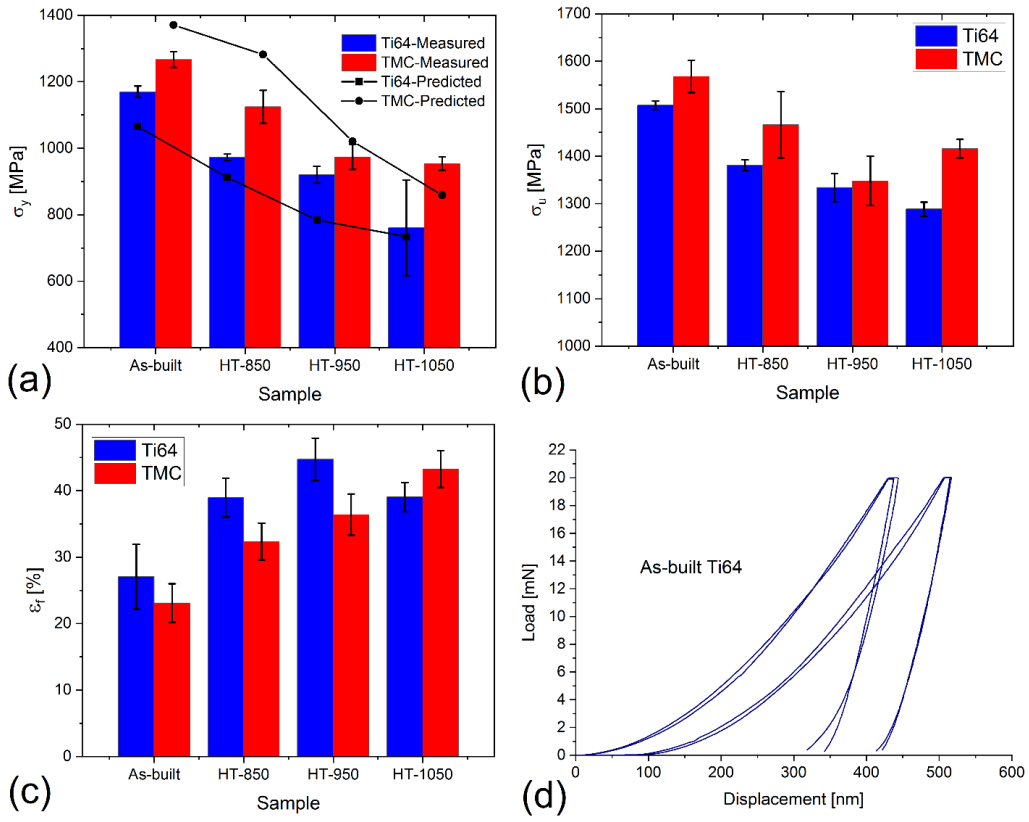

Figure 6-16. Compressive (a) yield strength, (b) ultimate strength, and (c) elongation % at break of the Ti64 and TMC samples in the as-built and heat-treated conditions. The nanoindentation load-displacement curves of the as-built Ti64 sample are presented in (d).

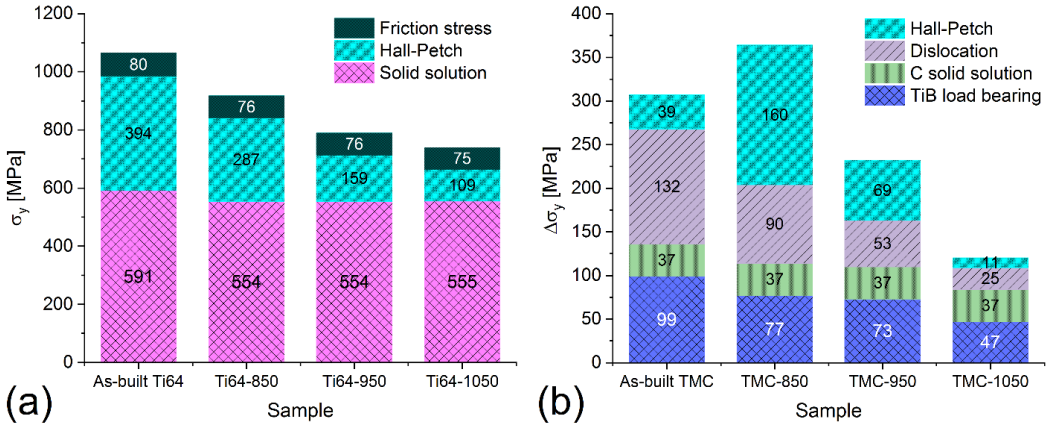

Figure 6-17. (a) The contribution of each strengthening mechanism in the overall compressive yield strength of the Ti64 samples, and (b) the increment in the compressive yield strength of TMC samples over the non-reinforced counterparts caused by different strengthening mechanisms.

Referring to Figure 6-16(a), TMCs possessed a higher σ_y than their corresponding Ti64 counterpart ($\sigma_{y,m}$). This increase in the σ_y is attributable to four distinct strengthening mechanisms, namely, grain refinement ($\Delta\sigma_{HP}$), TiB load bearing ($\Delta\sigma_{TiB}$), dislocation ($\Delta\sigma_{dis}$), and interstitial solid solution of carbon ($\Delta\sigma_{SS}^{C}$). By taking the effect of these strengthening mechanisms into account, the σ_y of the TMCs can be predicted as follows [62, 63]:

$$\sigma_{y,TMC} = \sigma_{y,m} + \Delta\sigma_{HP} + \Delta\sigma_{TiB} + \Delta\sigma_{dis} + \Delta\sigma_{SS}^{C} \quad [14]$$

As listed in Table 6-2 and

Table 6-3, the presence of TiB caused finer α/α' than the monolithic Ti64 counterparts. The effect of such a refinement on the σ_y increment can be determined using the following equation [53]:

$$\Delta\sigma_{HP} = K_{HP}\left(\frac{1}{\sqrt{d_2}} - \frac{1}{\sqrt{d_1}}\right) \quad [15]$$

where d_1 and d_2 denote the α/α' width in a Ti64 sample and its corresponding TMC counterpart, respectively.

TiB needles can also enhance the σ_y by acting as load-bearing sites, the magnitude of which can be estimated as [64]:

$$\Delta\sigma_{TiB} = \frac{1}{2}\sigma_{ym} V_{TiB} \frac{L_{TiB}}{d_{TiB}} \omega_0 \quad [16]$$

where V_{TiB}, L_{TiB}, and d_{TiB} signify the volume fraction, length and diameter of TiB needles, respectively. ω_0 is the orientation factor with a value between 0 and 1. The σ_y increment caused by dislocations consists of Orowan ($\Delta\sigma_{oro}$), thermal mismatch ($\Delta\sigma_{the}$), and geometrically necessary dislocation ($\Delta\sigma_{geo}$) mechanisms as follows [65]:

$$\Delta\sigma_{dis} = \sqrt{(\Delta\sigma_{oro})^2 + (\Delta\sigma_{the})^2 + (\Delta\sigma_{geo})^2} \quad [17]$$

$\Delta\sigma_{oro}$ can be calculated by the Orowan-Ashby equation as [66]:

$$\Delta\sigma_{oro} = \frac{0.13 G_m b_m}{\lambda} Ln\left(\frac{D_{TiB}}{2b_m}\right) \quad [18]$$

in which b_m is the Burgers vector, λ is the inter-particle spacing, and D_{TiB} is the equivalent TiB diameter. D_{TiB} and λ can be calculated by applying the following formulas [65, 67]:

$$D_{TiB} = \sqrt[3]{1.5 d_{TiB}^2 L_{TiB}} \quad [19]$$

$$\lambda \approx D_{TiB}[(2V_{TiB})^{-1/3} - 1] \quad [20]$$

Since TiB and Ti64 have very close thermal expansion coefficients, the $\Delta\sigma_{the}$ is negligible. The term $\Delta\sigma_{geo}$ is defined as [68]:

$$\Delta\sigma_{geo} = 0.4 G_m \sqrt{\frac{\varepsilon_m b_m V_{TiB}}{D_{TiB}}} \quad [21]$$

where ε_m is the compressive true strain of the matrix at the yield point:

$$\varepsilon_m = \frac{\sigma_{y,m}}{E} \quad [22]$$

in which E is the elastic modulus of the matrix, measured by the nanoindentation of the as-built Ti64 sample (Figure 6-16(d)). The role of carbon solid solution strengthening mechanism can be estimated as follows [69]:

$$\Delta\sigma_{SS}^{C} = 0.002 G_m C_c^{1/2} \quad [23]$$

where C_c represents the atomic percent of carbon in the matrix. The data required to calculate the contribution of each strengthening mechanism in the σ_y increment of the TMCs are listed in Table 6-4, and the predicted σ_y values are depicted in Figure 6-16(a). As it is evident, there is a good agreement between the experimental and analytical results for the σ_y of TMCs. In all cases, ~5-14% difference was observed between the predicted

and measured σ_y values. The contribution of each strengthening mechanism in the improvement of the σ_y of the TMCs over the $\sigma_{y,m}$ is shown in Figure 6-17(b). The major strengthening mechanism was not the same for different samples. The $\Delta\sigma_{dis}$ and $\Delta\sigma_{TiB}$ were dominant strengthening mechanisms in the as-built TMC, originating from the high volume fraction and aspect ratio of TiB needles in this sample. In TMC-850, $\Delta\sigma_{HP}$ accounted for 45% of the total σ_y improvement due to the noticeable difference between the α width of the Ti64-850 and TMC-850 samples. $\Delta\sigma_{TiB}$ and $\Delta\sigma_{HP}$ in TMC-950, and $\Delta\sigma_{SS}^{C}$ and $\Delta\sigma_{TiB}$ in TMC-1050 were the governing strengthening mechanisms in the σ_y enhancement of the matrix.

The same discussion can be also applied to the σ_u since the same strengthening mechanisms mentioned for the σ_y improvement are active in impeding the dislocation movement in the plastic deformation region. That is why the same trend as the σ_y was observed in the σ_u (Figure 6-16(a) and (b)). It is worth noting that for both Ti64 and TMC parts, heat-treated samples showed lower strength and higher ductility compared to the as-built condition. Except for the Ti64-1050, the increase in the heat treatment temperature resulted in higher ductility (Figure 6-16(c)). It is also of note that the ductility of TMCs were slightly lower than their corresponding Ti64 samples, with the only exception being the TMC-1050. This can be rationalized based on the presence of hard and brittle TiB phase which acts to enhance the strength and decrease the ductility.

Figure 6-18 shows SEM micrographs taken from the cross-section of the compression test specimens adjacent to the fracture location. As shown in Figure 6-18(a) and (b), the Ti64-950 specimen featured a noticeable deformation of the lamellar ($\alpha+\beta$) microstructure near the fracture path. Examination of the microstructure revealed the formation of micro-cracks at the α/β interface of the deformed region as well as the decohesion of the α/β interface at locations farther from the fracture site. The α/β interfaces in the Ti64 alloy act to hinder the dislocation motion and lead to the dislocation pile-up. The localization of deformation and stress concentration at these interfaces makes them potential sites for the formation of micropores [70]. The elongation and coalescence of these micro-voids during further deformation may result in the formation of micro-cracks, as shown in Figure 6-18(a). Microstructural observation of the TMC-950 specimen revealed multiple cracking of TiB needles, specifically the coarse ones (Figure 6-18(c), and (d)). In addition, the deformation of the lamellar ($\alpha+\beta$) matrix was less prevalent compared to the Ti64-950 counterpart. Examination of the Ti64-1050 specimen disclosed the formation of long cracks elongated along the GB-α (Figure 6-18(e)), justifying the detrimental effect of the GB-α network on both strength and ductility of the supertransus heat-treated Ti64 alloy (Figure 6-16(a), (b), and (c)). The unexpectedly low ductility of Ti64-1050 sample is attributed to the GB-α network acting as a potential site for the propagation of cracks during loading. As indicated in Figure 6-18(f), the Ti64-1050 specimen featured another type of elongated cracks which were not originating from the GB-α. The microstructure clearly showed a shift in the position of α and β phases existing in each side of the cracks. The orientation of these cracks (~45° relative to the loading direction) clearly reveals that they have been formed due to the shear stress, which is in its maximum value at this angle. The Ti64-1050 sample contained other defects such as small cracks caused

by the β phase failure and voids originated form the α / β interface decohesion (Figure 6-18(f)).

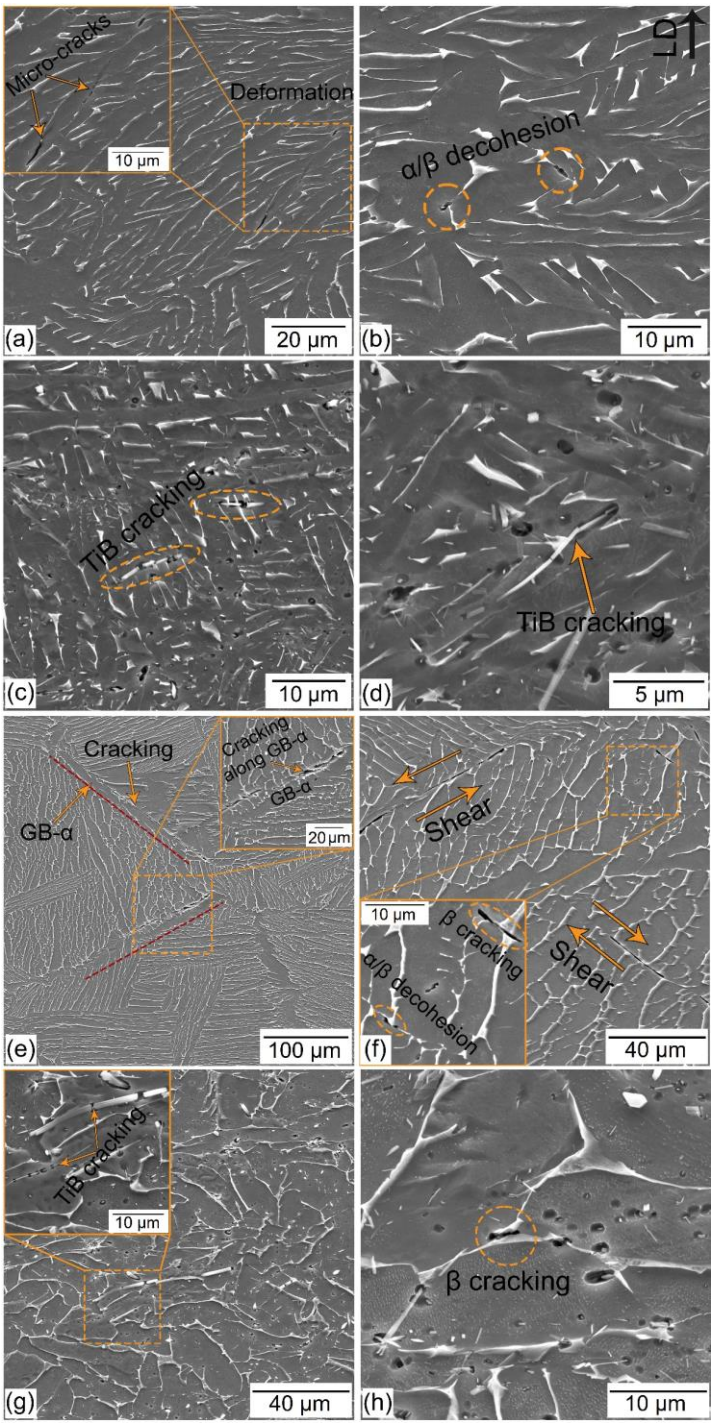

Figure 6-18. SEM micrographs from the cross-section of the: (a, b) Ti64-950, (c, d) TMC-950, (e, f) Ti64-1050, and (g, h) TMC-1050 samples after the compression test. The inset in each micrograph shows higher magnification view of the selected region in the same micrograph. “LD” refers to loading direction.

Microstructural characterization of the TMC-1050 specimen adjacent to the fracture path showed multiple cracking for a high frequency of large-sized TiB needles (Figure 6-18(g)). Due to the significant coarsening of TiB needles in the TMC-1050 sample and their higher tendency to failure, the TiB cracking was much more prevalent than the subtransus heat-treated TMC counterparts (e.g., TMC-950). The strong interfacial bonding between TiB needles and the matrix is the main reason behind their multiple cracking. This allows the failed needles to further undertake the load transferred from the matrix and experience more fracture [71]. The load bearing capacity of the TiB needles is one of the main strengthening mechanisms in the fabricated TMCs. Referring to Figure 6-18(h), the failure of β phase was also less frequently observed beside the fracture site of the TMC-1050 sample. Given the fact that the TMC-1050 sample was free from the detrimental GB-α phase, the ductility of this sample followed the general increasing trend observed in the heat-treated TMC samples.

6.3.3.2 Microhardness and scratch resistance

Figure 6-19 shows the microhardness of Ti64 and TMC specimens. In the as-built state, the TMC specimen was ~5% harder that the Ti64 counterpart due to two factors: (i) the second constituent strengthening caused by the hard and stiff nanoscale/sub-micron TiB needles, and (ii) the decreased width of α' laths. The subtransus heat treatment temperature of 850 °C did not have a noticeable effect on the hardness compared to the as-built conditions. This can be attributed to the limited growth of α laths at such relatively low temperatures (Table 6-2, and

Table 6-3). The subtransus temperature of 950 °C led to a remarkable drop in the hardness of the Ti64 sample due to the significant microstructural coarsening. However, due to the

growth restricting effects caused by TiB needles, the TMC-950 specimen featured only a slight decrease in the hardness compared to the TMC-850 case. Ti64-1050 specimen showed higher hardness than Ti64-950 case. Moreover, due to the presence of TiB needles and finer α grains, the TMC-1050 possessed a higher hardness than the Ti64-1050 specimen. The gradual decreasing trend in the microhardness of heat-treated TMCs caused by the increase in the heat treatment temperature can be rationalized by the coarsening of α laths and TiB needles, as shown in Figure 6-14.

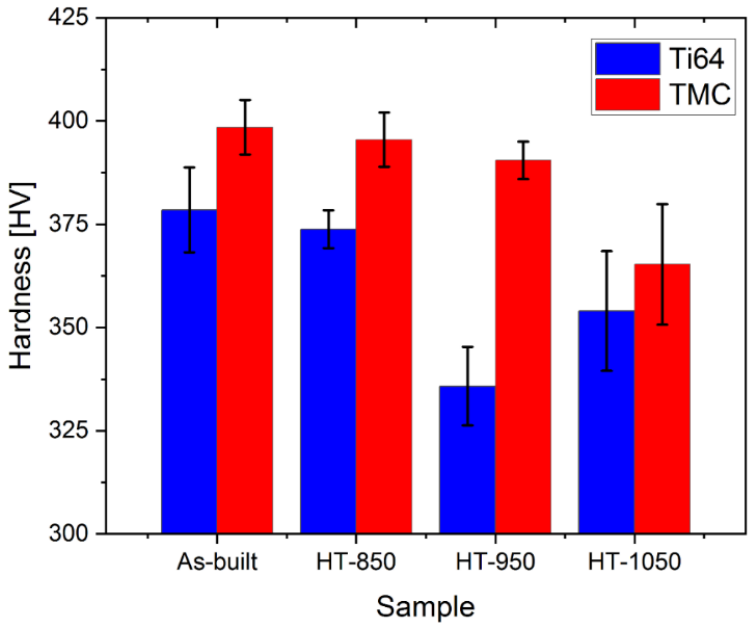

Figure 6-19. The microhardness of the Ti64 and TMC samples in the as-built and heat-treated conditions.

Figure 6-20(a) shows the variation in the penetration depth along the scratch length of Ti64 samples. The Ti64-950 and Ti64-1050 samples featured lower scratch resistances than the as-built Ti64 sample. This well conforms to the microhardness measurement results in Figure 6-19, where these two samples showed the lowest microhardness among all Ti64 samples. The best Ti64 sample in terms of the scratch resistance was Ti64-850. The scratch

profiles of the TMCs are provided in Figure 6-20(b), in which the TMC-950 sample featured the highest scratch resistance while the other samples showed almost the same penetration depth profiles. The observed scratch resistance behaviors can be explained based on the ductility and microhardness results shown in Figure 6-16(c) and Figure 6-19, respectively. Although having almost the same microhardness as that of their corresponding as-built counterparts, the relatively higher ductility of the Ti64-850 and TMC-950 samples is believed to be the main reason behind their enhanced scratch resistance. Despite the high hardness of the as-built samples favoring their scratch resistance, the low ductility of these samples results in cracking and delamination of the material and consequently yields deeper scratch profile. Ti64-850 and TMC-950 samples with almost the same hardness and higher ductility than the as-built ones benefit from deformation rather than cracking and delamination during the scratch test, leading to the reduced penetration depth.

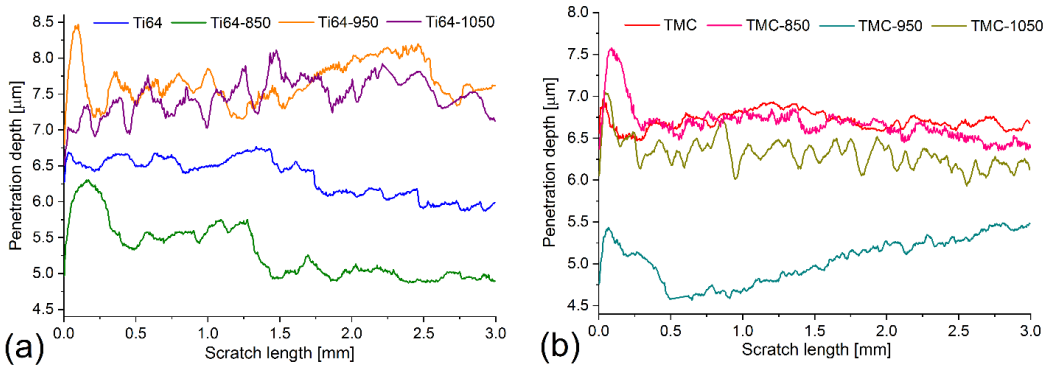

Figure 6-20. The penetration depth-scratch length profiles of the: (a) Ti64, and (b) TMC samples in the as-built and heat-treated conditions.

6.3.4 Selection of the optimum heat treatment cycle

As the results in Section 6.3.3 revealed, mechanical properties of the Ti64 and TMC parts could be tailored by employing heat treatment cycles. The question that has remained

unanswered is “what is the optimum heat treatment cycle?” To answer this question, it should be noted that the optimum heat treatment cycle depends on the application and the service requirements as follows:

- *Isotropy in microstructure and mechanical properties*: The columnar PBGs are indicative of the anisotropy in microstructure and mechanical properties of the as-built Ti64 and TMC samples. Only the supertransus heat treatment strategy could successfully eliminate these columnar grains (Figure 6-8, and Figure 6-12). Although being isotropic, the Ti64-1050 sample suffered from relatively low strength, ductility and scratch resistance, owing to the GB-α phase. The presence of TiB reinforcement in the TMC-1050 not only hindered the formation of GB-α but also led to the formation of fine equiaxed α grains.
- *Combination of strength and ductility*: The combination of these two mechanical properties represents the toughness of the material, which can be obtained by calculating the area under the stress-strain curve. On this account, Ti64-950 and TMC-1050 are introduced as the optimum samples since having the highest toughness among all samples in their category.
- *Combination of hardness and scratch resistance*: By considering this criterion, the optimum samples are Ti64-850 and TMC-950, yielding the highest hardness and superior scratch resistance.

6.4 Conclusions

This research study offers an insight into the improvement of mechanical properties of the laser powder bed fusion (L-PBF) fabricated Ti-6Al-4V (Ti64) alloy via incorporation of minor B_4C content. The as-built titanium matrix composite (TMC) and the reference Ti64

samples were subjected to the subtransus and supertransus heat treatment cycles. Results revealed that the optimum heat treatment cycles for Ti64 alloy cannot be necessarily applied to the TiB reinforced TMCs owing to the role that TiB needles play in restricting the growth of the prior β grains (PBGs) and the nucleation/growth of α phase formed by the $\beta \rightarrow \alpha$ transformation. The subtransus heat treatments led to full decomposition of the α' phase into the ($\alpha + \beta$) lamellar microstructure for both Ti64 and TMC samples. However, they failed to eliminate the footprints of the laser scan tracks as well as the anisotropy caused by the elongated PBGs. The presence of TiB led to 100 °C shift in the subtransus heat treatment temperature required to obtain optimum set of microhardness and scratch resistance properties (Ti64-850 vs. TMC-950). The supertransus heat treatment cycle altered the morphology of PBGs from elongated to equiaxed in both Ti64-1050 and TMC-1050 samples. However, contrary to the lamellar morphology of α phase in the Ti64-1050 sample, this phase featured an equiaxed morphology in the TMC-1050 counterpart owing to the role that TiB needles played in restricting their growth. The TiB needles also avoided the formation of the detrimental grain boundary α (GB-α) network which was perceptible in the Ti64-1050 sample. Therefore, the presence of TiB made it possible to achieve a fully isotropic microstructure without being concerned about the detrimental GB-α phase. In applications demanding combination of high strength and ductility, supertransus heat treatment was found to be the optimum cycle for TMCs.

6.5 References

[1] A. International, F2792-12a-Standard Terminology for Additive Manufacturing Technologies, Rapid Manuf. Assoc. (2013) 10-12.

[2] H.R. Kotadia, G. Gibbons, A. Das, P.D. Howes, A Review of Laser Powder Bed Fusion Additive Manufacturing of Aluminium Alloys: Microstructure and Properties, Additive Manufacturing (2021) 102155.

[3] S.A. Tofail, E.P. Koumoulos, A. Bandyopadhyay, S. Bose, L. O'Donoghue, C. Charitidis, Additive manufacturing: scientific and technological challenges, market uptake and opportunities, Materials today 21(1) (2018) 22-37.

[4] D. Herzog, V. Seyda, E. Wycisk, C. Emmelmann, Additive manufacturing of metals, Acta Materialia 117 (2016) 371-392.

[5] A. Ghasemi, E. Fereiduni, M. Balbaa, S.D. Jadhav, M. Elbestawi, S. Habibi, Influence of alloying elements on laser powder bed fusion processability of aluminum: A new insight into the oxidation tendency, Additive Manufacturing 46 (2021) 102145.

[6] M. Attaran, The rise of 3-D printing: The advantages of additive manufacturing over traditional manufacturing, Business Horizons 60(5) (2017) 677-688.

[7] E. Fereiduni, A. Ghasemi, M. Elbestawi, Selective Laser Melting of Aluminum and Titanium Matrix Composites: Recent Progress and Potential Applications in the Aerospace Industry, Aerospace 7(6) (2020) 77.

[8] D.-H. Lee, B. Sun, S. Lee, D. Ponge, E.A. Jägle, D. Raabe, Comparative study of hydrogen embrittlement resistance between additively and conventionally manufactured 304L austenitic stainless steels, Materials Science and Engineering: A 803 (2021) 140499.

[9] M. Schmitt, T. Kamps, F. Siglmüller, J. Winkler, G. Schlick, C. Seidel, T. Tobie, K. Stahl, G. Reinhart, Laser-based powder bed fusion of 16MnCr5 and resulting material properties, Additive Manufacturing 35 (2020) 101372.

[10] J. Pelleg, Additive and Traditionally Manufactured Components: A Comparative Analysis of Mechanical Properties, Additive Manufacturing Materia2020.

[11] S. Dadbakhsh, R. Mertens, G. Ji, B. Vrancken, K. Vanmeensel, H. Fan, A. Addad, J.-P. Kruth, Heat treatment possibilities for an in situ βTi-TiC composite made by laser powder bed fusion, Additive Manufacturing 36 (2020) 101577.

[12] H. Chen, D. Gu, K. Kosiba, T. Lu, L. Deng, L. Xi, U. Kühn, Achieving high strength and high ductility in WC-reinforced iron-based composites by laser additive manufacturing, Additive Manufacturing 35 (2020) 101195.

[13] W.H. Yu, S.L. Sing, C.K. Chua, C.-N. Kuo, X.L. Tian, Particle-reinforced metal matrix nanocomposites fabricated by selective laser melting: A state of the art review, Progress in Materials Science 104 (2019) 330-379.

[14] E. Fereiduni, A. Ghasemi, M. Elbestawi, S. Dinkar Jadhav, K. Vanmeensel, Laser powder bed fusion processability of Ti-6Al-4V powder decorated by B4C particles, Materials Letters 296 (2021) 129923.

[15] Y. Kok, X.P. Tan, P. Wang, M. Nai, N.H. Loh, E. Liu, S.B. Tor, Anisotropy and heterogeneity of microstructure and mechanical properties in metal additive manufacturing: A critical review, Materials & Design 139 (2018) 565-586.

[16] M. Narvan, A. Ghasemi, E. Fereiduni, S. Kendrish, M. Elbestawi, Part deflection and residual stresses in laser powder bed fusion of H13 tool steel, Materials & Design 204 (2021) 109659.

[17] M. Salem, S. Le Roux, A. Hor, G. Dour, A new insight on the analysis of residual stresses related distortions in selective laser melting of Ti-6Al-4V using the improved bridge curvature method, Additive Manufacturing 36 (2020) 101586.

[18] M. Carraturo, S. Kollmannsberger, A. Reali, F. Auricchio, E. Rank, An immersed boundary approach for residual stress evaluation in selective laser melting processes, Additive Manufacturing 46 (2021) 102077.

[19] Z. Zhu, W. Li, Q.B. Nguyen, X. An, W. Lu, Z. Li, F.L. Ng, S.M. Ling Nai, J. Wei, Enhanced strength–ductility synergy and transformation-induced plasticity of the selective laser melting fabricated 304L stainless steel, Additive Manufacturing 35 (2020) 101300.

[20] S.-B. Sun, L.-J. Zheng, J.-H. Liu, H. Zhang, Selective Laser Melting of an Al–Fe–V–Si Alloy: Microstructural Evolution and Thermal Stability, Journal of Materials Science & Technology 33(4) (2017) 389-396.

[21] W.-C. Lin, Y.-J. Chang, T.-H. Hsu, S. Gorsse, F. Sun, T. Furuhara, A.-C. Yeh, Microstructure and tensile property of a precipitation strengthened high entropy alloy processed by selective laser melting and post heat treatment, Additive Manufacturing 36 (2020) 101601.

[22] T. Vilaro, C. Colin, J.-D. Bartout, As-fabricated and heat-treated microstructures of the Ti-6Al-4V alloy processed by selective laser melting, Metallurgical and materials transactions A 42(10) (2011) 3190-3199.

[23] L. Thijs, F. Verhaeghe, T. Craeghs, J.V. Humbeeck, J.-P. Kruth, A study of the microstructural evolution during selective laser melting of Ti–6Al–4V, Acta Materialia 58(9) (2010) 3303-3312.

[24] B. Ahmad, S.O. van der Veen, M.E. Fitzpatrick, H. Guo, Residual stress evaluation in selective-laser-melting additively manufactured titanium (Ti-6Al-4V) and inconel 718 using the contour method and numerical simulation, Additive Manufacturing 22 (2018) 571-582.

[25] E. Fereiduni, A. Ghasemi, M. Elbestawi, Characterization of composite powder feedstock from powder bed fusion additive manufacturing perspective, Materials 12(22) (2019) 3673.

[26] F. Bachmann, R. Hielscher, H. Schaeben, Texture analysis with MTEX–free and open source software toolbox, Solid State Phenomena, Trans Tech Publ, 2010, pp. 63-68.

[27] A. C-05, Standard test method for adhesion strength and mechanical failure modes of ceramic coatings by quantitative single point scratch testing, (2005).

[28] P. Homporova, C. Poletti, M. Stockinger, F. Warchomicka, Dynamic phase evolution in titanium alloy Ti-6Al-4V, Proc. 12th World Conference on Titanium, 2011, pp. 19-42.

[29] A. Neira-Arce, Thermal Modeling and Simulation of Electron Beam Melting for Rapid Prototyping on Ti6Al4V Alloys, (2012).

[30] M. Motyka, A. Baran-Sadleja, J. Sieniawski, M. Wierzbinska, K. Gancarczyk, Decomposition of deformed α′(α ″) martensitic phase in Ti–6Al–4V alloy, Materials Science and Technology 35(3) (2019) 260-272.

[31] D. Hill, R. Banerjee, D. Huber, J. Tiley, H. Fraser, Formation of equiaxed alpha in TiB reinforced Ti alloy composites, Scripta Materialia 52(5) (2005) 387-392.

[32] Y.F. Yang, M. Yan, S.D. Luo, G.B. Schaffer, M. Qian, Modification of the α-Ti laths to near equiaxed α-Ti grains in as-sintered titanium and titanium alloys by a small addition of boron, Journal of Alloys and Compounds 579 (2013) 553-557.

[33] A. Xue, X. Lin, L. Wang, J. Wang, W. Huang, Influence of trace boron addition on microstructure, tensile properties and their anisotropy of Ti6Al4V fabricated by laser directed energy deposition, Materials & Design 181 (2019) 107943.

[34] D.J. McEldowney, S. Tamirisakandala, D.B. Miracle, Heat-treatment effects on the microstructure and tensile properties of powder metallurgy Ti-6Al-4V alloys modified with boron, Metallurgical and Materials Transactions A 41(4) (2010) 1003-1015.

[35] P.A. Kobryn, S. Semiatin, Microstructure and texture evolution during solidification processing of Ti–6Al–4V, Journal of Materials Processing Technology 135(2-3) (2003) 330-339.

[36] E. Fereiduni, A. Ghasemi, M. Elbestawi, Selective laser melting of hybrid ex-situ/in-situ reinforced titanium matrix composites: Laser/powder interaction, reinforcement formation mechanism, and non-equilibrium microstructural evolutions, Materials & Design 184 (2019) 108185.

[37] W.E. Frazier, Metal additive manufacturing: a review, Journal of Materials Engineering and performance 23(6) (2014) 1917-1928.

[38] H. Li, D. Jia, Z. Yang, X. Liao, H. Jin, D. Cai, Y. Zhou, Effect of heat treatment on microstructure evolution and mechanical properties of selective laser melted Ti–6Al–4V and TiB/Ti–6Al–4V composite: A comparative study, Materials Science and Engineering: A 801 (2021) 140415.

[39] X.-Y. Zhang, G. Fang, S. Leeflang, A.J. Böttger, A.A. Zadpoor, J. Zhou, Effect of subtransus heat treatment on the microstructure and mechanical properties of additively manufactured Ti-6Al-4V alloy, Journal of Alloys and Compounds 735 (2018) 1562-1575.

[40] F.J. Gil, M.P. Ginebra, J.M. Manero, J.A. Planell, Formation of α-Widmanstätten structure: effects of grain size and cooling rate on the Widmanstätten morphologies and on the mechanical properties in Ti6Al4V alloy, Journal of Alloys and Compounds 329(1) (2001) 142-152.

[41] G. Welsch, R. Boyer, E. Collings, Materials properties handbook: titanium alloys, ASM international1993.

[42] Q. Huang, X. Liu, X. Yang, R. Zhang, Z. Shen, Q. Feng, Specific heat treatment of selective laser melted Ti–6Al–4V for biomedical applications, Frontiers of Materials Science 9(4) (2015) 373-381.

[43] B. Vrancken, L. Thijs, J.-P. Kruth, J. Van Humbeeck, Heat treatment of Ti6Al4V produced by Selective Laser Melting: Microstructure and mechanical properties, Journal of Alloys and Compounds 541 (2012) 177-185.

[44] R. Chen, C. Tan, Y. Yu, M. Zhang, X. Yu, C. Liu, W. Ye, S. Hui, Y. Jiang, Modification of α-phase of wire + arc additive manufactured Ti-6Al-4 V alloy with boron addition, Materials Characterization 169 (2020) 110616.

[45] R. Sarkar, P.S. Karamched, P. Ghosal, K.S. Prasad, T.K. Nandy, K.K. Ray, Crystallographic orientation relationships of boride and carbide particles with α and β phases in a β-Ti alloy, Journal of Alloys and Compounds 612 (2014) 435-442.

[46] Y. Cui, K. Aoyagi, Y. Zhao, K. Yamanaka, Y. Hayasaka, Y. Koizumi, T. Fujieda, A. Chiba, Manufacturing of a nanosized TiB strengthened Ti-based alloy via electron beam powder bed fusion, Additive Manufacturing 36 (2020) 101472.

[47] T. Sasaki, B. Fu, K. Torres, G. Thompson, R. Srinivasan, B. Cherukuri, J. Tiley, Nucleation and growth of α-Ti on TiB precipitates in Ti–15Mo–2.6 Nb–3Al–0.2 Si–0.12 B, Philosophical Magazine 91(6) (2011) 850-864.

[48] Z. Mahbooba, H. West, O. Harrysson, A. Wojcieszynski, R. Dehoff, P. Nandwana, T. Horn, Effect of hypoeutectic boron additions on the grain size and mechanical properties of Ti-6Al-4V manufactured with powder bed electron beam additive manufacturing, Jom 69(3) (2017) 472-478.

[49] S. Roy, S. Suwas, S. Tamirisakandala, D.B. Miracle, R. Srinivasan, Development of solidification microstructure in boron-modified alloy Ti–6Al–4V–0.1 B, Acta Materialia 59(14) (2011) 5494-5510.

[50] K. Zhang, X. Tian, M. Bermingham, J. Rao, Q. Jia, Y. Zhu, X. Wu, S. Cao, A. Huang, Effects of boron addition on microstructures and mechanical properties of Ti-6Al-4V manufactured by direct laser deposition, Materials & Design 184 (2019) 108191.

[51] M. Liu, S. Liu, W. Chen, C. Chen, Y. Lv, X. Zhang, P. Lei, Y. Lin, K. Zhou, Effect of trace lanthanum hexaboride on the phase, grain structure, and texture of electron beam melted Ti-6Al-4V, Additive Manufacturing 30 (2019) 100873.

[52] C. Leyens, M. Peters, Titanium and titanium alloys: fundamentals and applications, Wiley Online Library2006.

[53] N. Hansen, Hall–Petch relation and boundary strengthening, Scripta Materialia 51(8) (2004) 801-806.

[54] H. Rosenberg, W. Nix, Solid solution strengthening in Ti-Al alloys, Metallurgical Transactions 4(5) (1973) 1333-1338.

[55] E. Fereiduni, M. Elbestawi, Process-structure-property relationships in additively manufactured metal matrix composites, Additive Manufacturing of Emerging Materials, Springer2019, pp. 111-177.

[56] I. Ghamarian, B. Hayes, P. Samimi, B. Welk, H. Fraser, P.C. Collins, Developing a phenomenological equation to predict yield strength from composition and microstructure in β processed Ti-6Al-4V, Materials Science and Engineering: A 660 (2016) 172-180.

[57] K.D. Rekedal, Investigation of the high-cycle fatigue life of selective laser melted and hot isostatically pressed Ti-6Al-4V, (2015).

[58] A. Muiruri, M. Maringa, W. du Preez, Evaluation of Dislocation Densities in Various Microstructures of Additively Manufactured Ti6Al4V (Eli) by the Method of X-ray Diffraction, Materials 13(23) (2020) 5355.

[59] W.D. Callister, D.G. Rethwisch, Materials science and engineering, John wiley & sons NY2011.

[60] H. Fukuda, T.-W. Chou, A probabilistic theory of the strength of short-fibre composites with variable fibre length and orientation, Journal of materials science 17(4) (1982) 1003-1011.

[61] U.o.S. Mark Winter, UK, WebElements.

[62] I. Ghamarian, P. Samimi, V. Dixit, P.C. Collins, A constitutive equation relating composition and microstructure to properties in Ti-6Al-4V: as Derived using a novel integrated computational approach, Metallurgical and Materials Transactions A 46(11) (2015) 5021-5037.

[63] J. Keist, S. Nayir, T. Palmer, Impact of hot isostatic pressing on the mechanical and microstructural properties of additively manufactured Ti–6Al–4V fabricated using directed energy deposition, Materials Science and Engineering: A 787 (2020) 139454.

[64] X. Guo, L. Wang, M. Wang, J. Qin, D. Zhang, W. Lu, Effects of degree of deformation on the microstructure, mechanical properties and texture of hybrid-reinforced titanium matrix composites, Acta Materialia 60(6) (2012) 2656-2667.

[65] Y. Hu, W. Cong, X. Wang, Y. Li, F. Ning, H. Wang, Laser deposition-additive manufacturing of TiB-Ti composites with novel three-dimensional quasi-continuous

network microstructure: effects on strengthening and toughening, Composites Part B: Engineering 133 (2018) 91-100.

[66] G.E. Dieter, D.J. Bacon, Mechanical metallurgy, McGraw-hill New York1986.

[67] M.A. Meyers, K.K. Chawla, Mechanical behavior of materials, Cambridge university press2008.

[68] L. Brown, W. Stobbs, The work-hardening of copper-silica v. equilibrium plastic relaxation by secondary dislocations, Philosophical Magazine 34(3) (1976) 351-372.

[69] P. Luo, D. McDonald, W. Xu, S. Palanisamy, M. Dargusch, K. Xia, A modified Hall–Petch relationship in ultrafine-grained titanium recycled from chips by equal channel angular pressing, Scripta Materialia 66(10) (2012) 785-788.

[70] X. Ma, Z. Xiang, M. Ma, C. Tan, Z. Yang, G. Shen, Z. Chen, Q. Shu, Effect of trace boron addition on microstructures, textures, mechanical properties and fracture behaviors of near α titanium alloy, Materials Science and Engineering: A 772 (2020) 138749.

[71] Z. Yang, L. Fu, S. Wang, M. Zhang, Y. Wang, Z. Ma, D. Wang, Balance of strength and plasticity of additive manufactured Ti-6Al-4V alloy by forming TiB whiskers with cyclic gradient distribution, Additive Manufacturing 39 (2021) 101883.

Chapter 7 TiB reinforced Ti-6Al-4V matrix composites with improved short-term creep performance fabricated by laser powder bed fusion

Complete Citation: Fereiduni E, Ghasemi A, Elbestawi M. TiB reinforced Ti-6Al-4V matrix composites with improved short-term creep performance fabricated by laser powder bed fusion. Journal of Manufacturing Processes. 2021 Oct 1;70:593-607.

Abstract

This study investigates the short-term creep performance of laser powder bed fusion (L-PBF) fabricated Ti-6Al-4V (Ti64) and TiB-reinforced Ti64 matrix composite (TMC) parts. The TMCs were fabricated by L-PBF processing of 0.2wt.%B_4C/Ti64 composite powder. The optimum set of process parameters was used to manufacture creep test specimens. In addition to the as-built scenario, supertransus heat treatment was conducted to eliminate the microstructural anisotropy. Creep testing of the as-built and heat treated samples was performed at 600 °C under a constant tensile stress of 200 MPa. Microstructural evolutions were scrutinized before and after the creep test. Results revealed a slightly longer rupture time for Ti64 than the TMC part in the as-built state. Although the boundaries of prior β grains were detected as the preferential void nucleation sites in both as-built samples, the TMC part featured a significantly higher frequency of smaller voids near the fracture site. The heat-treated Ti64 sample showed the most inferior creep performance with a premature failure due to continuous networks of grain boundary α (GB-α). However, the heat-treated TMC counterpart showed a noticeably improved creep performance with a rupture time of 5.8 h owing to the absence of GB-α, presence of hard and stiff TiB reinforcements, and the increased fraction of interfaces.

Keyword: Ti-6Al-4V; Titanium matrix composite (TMC); Laser powder bed fusion (L-PBF); Short-term creep

7.1 Introduction

Titanium (Ti) and its alloys are used in a wide variety of low- and medium-temperature applications in different industries such as aerospace, biomedical, and petrochemical due to their high specific strength and good corrosion resistance [1, 2]. Among all industries, the aerospace sector is the most compelling one, accounting for more than 70% of the whole Ti consumption [3]. The Ti alloys used in the aerospace sector contain both α and β stabilizing elements in various proportions depending on the application and the required combination of mechanical properties [4]. Ti-6Al-4V (Ti64) is the most famous Ti alloy with an (α+β) two-phase microstructure, which plays a significant role in the manufacturing of components in the aerospace industry, such as disks and blades for aircraft turbines as well as steam turbines [5]. Creep resistance is one of the main criteria in such applications and is often the limiting parameter when designing structural components to be used in different temperature-stress domains [6].

The challenges involved in refining, casting, forming, and machining Ti alloys have made them very expensive compared to other metallic counterparts such as steel and Al alloys [7]. Given this fact, there has been a great deal of research in recent years to produce net- or near-net-shape Ti alloy parts that require minimum post-processing steps [8, 9]. Laser powder bed fusion (L-PBF) is a near-net-shape additive manufacturing (AM) process in which a component is built by melting successive layers of a powder feedstock onto a build plate using a focused laser beam as the heat source [10-12]. Since providing fabrication of custom-designed parts with complex geometries, and fine features in a single shot, this unprecedented technology has become economically attractive and of high interest, especially in applications demanding low volume production of relatively expensive materials (e.g., Ti alloys) [5, 13-15]. In the as-built condition, the L-PBF fabricated Ti64

parts are characterized by large columnar prior β grains, elongated along the building direction, and contain fine α′ laths featuring a martensitic microstructure [16-18]. Although the fully martensitic microstructure of the L-PBF fabricated Ti64 components brings about a noticeably high strength which well exceeds the minimum requirements of the ASTM standard for forged (ASTM F1472) and cast (ASTM F1108) products, it generally renders a low ductility [19, 20]. In addition, since the martensitic microstructure is metastable, the fabricated parts cannot be used in the as-built form in medium- and high-temperature applications. Moreover, the as-built parts have been shown to suffer from a high degree of anisotropy in the mechanical properties due to the microstructural anisotropy caused by the elongated prior β grains [21, 22].

Therefore, the L-PBF fabricated Ti64 parts need to be subjected to the post-processing heat treatments. The heat treatment of the as-built Ti64 alloy at temperatures below the β transus temperature (subtransus) is one of the strategies which has been employed in recent years to enhance the ductility (at the expense of strength) by relieving the residual stress and decomposing the martensite to (α+β) phases [23-25]. However, such heat treatment cycles are not able to eliminate microstructural/mechanical anisotropy. By providing the nucleation of new prior β grains with an equiaxed morphology, supertransus heat treating is capable of eliminating the microstructural anisotropy [26]. However, the extensive growth of the prior β grains at such high temperatures is the major concern associated with the supertransus heat treatment, adversely affecting mechanical properties. In addition, supertransus heat treatment of the Ti64 alloy leads to the formation of grain boundary alpha (GB-α) along the boundaries of prior β grains, which unfavorably affects the ductility by providing a continuous pathway for the nucleation and propagation of cracks during loading [24, 26, 27].

Although the creep behavior and mechanism of Ti matrix composites (TMCs), especially TiB, TiC, and hybrid (TiB+TiC) reinforced composites fabricated by conventional manufacturing processes have hitherto been extensively investigated [4, 28-30], the literature lacks research studies dealing with the evaluation of the creep performance of TMCs fabricated by AM processes, especially PBF ones. This might be because the research field concerning the fabrication of metal matrix composites (MMCs) by AM technology is relatively new and has yet to be explored. Moreover, due to the unique microstructural features associated with the AM fabricated MMCs, a deep understanding of the microstructural evolutions during their creep testing is needed for an improved understanding of the creep mechanisms.

The focus domain of this study is to improve the creep performance of the L-PBF fabricated Ti64 alloy by engineering the microstructure via incorporating ceramic reinforcing particles into the matrix and employing appropriate post-processing heat treatment cycles. For this purpose, a minor amount of B_4C powder (0.2wt.%) was added to the Ti64 powder to produce a composite powder as the feedstock material for fabricating TMC parts via the L-PBF process. The selection of B_4C as the starting reinforcing agent was on account of the fact that B can lead to a significant improvement in mechanical properties and high-temperature durability through the in-situ formation of TiB reinforcement with noticeably high hardness and stiffness [7, 31-33]. Since having almost the same coefficient of thermal expansion as that of Ti, minimum thermal residual stresses are generated at the TiB/matrix interface during cooling in TiB-reinforced TMCs [34]. The presence of B element/TiB phase in Ti alloys brings about a remarkable grain refinement and improves the strength of the TMCs [35, 36]. Moreover, the highly stable TiB whiskers in TMCs restrict the mobility

of grain boundaries at high temperatures and act as strong barriers for mobile dislocations, leading to a profound effect on the elevated-temperature performance [37, 38].

Following the L-PBF processing within a wide range of volumetric energy densities, the optimum set of process parameters leading to the highest relative density in both monolithic Ti64 and TMC cases were employed to manufacture creep test specimens. The as-built samples were heat treated at a supertransus temperature to explore whether such a heat treatment cycle can improve the creep performance. The results of the short-term creep testing indicated a slightly longer rupture time for Ti64 than the TMC counterpart in the as-built condition (3.4 vs. 2.9 h). However, compared to the heat-treated Ti64 sample, which experienced premature failure only after 0.6 h, the heat-treated TMC featured a significantly longer rupture time of 5.9 h. This was discussed based on the stiffness of TiB reinforcement, the density of interfaces, and the load transfer from the matrix to the reinforcement. The findings of this research study reveal that the service temperature of the L-PBF fabricated Ti64 alloy can be elevated by incorporating suitable reinforcements and employing appropriate post-processing heat treatment cycles. The fabricated TMC parts can be considered for fracture-critical members (e.g., in the aerospace sector), especially at elevated temperatures.

7.2 Materials and experimental procedure

The starting materials were Ti64 and B_4C powders with a mean particle size of 35 and 2 μm, respectively, and the chemical composition reported in [39]. A composite powder containing 0.2wt.%B_4C as the starting reinforcing agent was produced by adding a 2 h-ball milled 3wt.%B_4C/Ti64 composite powder to the monolithic Ti64 powder, followed by regular mixing for 2 h. The ball-to-powder weight ratio and the ball diameter in the ball

milling were 5:1 and 10 mm, respectively, and the rotational speed in the ball milling was set to be 200 rpm. The regular mixing process was also conducted with the same rotational speed without balls. A wide range of process parameters was employed to fabricate cubic test coupons, and the optimum set of process parameters leading to the highly dense (>99.5% densification level based on the image analysis by the ImageJ software) Ti64 and TMC samples were utilized to manufacture creep test specimens. The shared optimum process parameters were scanning speed of 2000 mm/s, hatch spacing of 100 µm, and nominal powder layer thickness (platform displacement) of 30 µm. However, the optimum laser power was 200 and 250 W for Ti64 and TMC samples, respectively. The samples were printed using an EOS M280 machine (EOS, Krailling, Germany) equipped with a Yb-fiber laser system providing power levels of up to 400 W. The build plate was Ti64, heated to 200 °C prior to the L-BPF processing of both Ti64 and TMC parts. The geometry and dimensions of the fabricated creep test specimen are schematically illustrated in Figure 7-1. The as-built cubic and creep test samples were cut from the build plate via wire electric discharge machining (EDM). Heat treatment of specimens was performed at 1050 °C for 2 h, with a heating rate of 10 °C/min followed by furnace cooling. The heat-treated Ti64 and TMC samples are referred to as HT-Ti64 and HT-TMC, respectively. The top and bottom surfaces of the as-built and HT creep test samples were ground to achieve a smooth surface finish.

The cross-sections of the as-built and HT cubic samples were ground and polished according to the standard metallography procedure and were chemically etched using Kroll's Reagent. For microstructural characterizations, Nikon optical microscopy (OM), as well as a Vega Tescan scanning electron Microscopy (SEM) equipped with energy dispersive X-ray spectroscopy (EDS), were used. Determination of the size of phases was

performed using ImageJ software. Electron backscatter diffraction (EBSD) technique was carried out using an FEI, Versa 3D SEM, and the data collection and analysis was performed using the TSL OIM 7 software to address the grain size and crystal orientation in the as-built and HT samples. Prior to the EBSD analysis, the aforementioned sample preparation procedure was followed by 5 minutes of polishing on a chemical-resistant cloth with a 0.04 μm colloidal silica suspension. The spatially resolved EBSD maps were acquired at 20 keV using step sizes in the range of 0.1 to 4 μm.

The elastic modulus (E) of the as-built Ti64 and TMC samples was assessed using nanoindentation measurements. The employed method was Oliver-Pharr, and the utilized device was an Anton Paar NHT3 nano-indentation tester (Anton Paar, Graz, Austria) equipped with a Berkovich pyramidal-shaped indenter tip. The calibration process was performed using a Fused Silica reference sample. The maximum load, the loading/unloading rate, and the pause at the maximum load were 10 mN, 40 mN/min, and 10 s, respectively.

Constant-load creep tensile-test experiments were carried out at the temperature of 600 °C, and the applied nominal stress of 200 MPa on vertical load frames using a SATEC creep rupture machine, Model M-3, with a total capacity of 3000 kg, and a lever arm ratio of 16:1. The dimensions of the printed creep test specimens (Figure 7-1(a)) were selected as per the ASTM-E139 standard. The creep strain-life behavior was recorded during the experiments. The creep strain was measured using a linear variable differential transform (LVDT) assembly with an accuracy of 0.1% on a 5D original gauge length of 29.46 mm. The heating of test specimens was performed in a resistance heating furnace with a temperature control within ± 5 °C. The temperature monitoring was implemented by three K-type thermocouples attached to each specimen within the reduced section. Prior to the

creep testing, samples were soaked at the desired creep test temperature for 90 minutes to ensure a uniform testing temperature throughout the specimen and minimize the thermal stresses. All creep tests were carried out in air according to the ASTM E139-11 standard [40]. Following each creep test, the fracture surfaces were observed via SEM (Figure 7-1(b)). The fractured specimens were also sectioned parallel to the loading direction (Figure 7-1(b)), and the top views were subjected to the standard metallography procedure to investigate the creep failure mechanism.

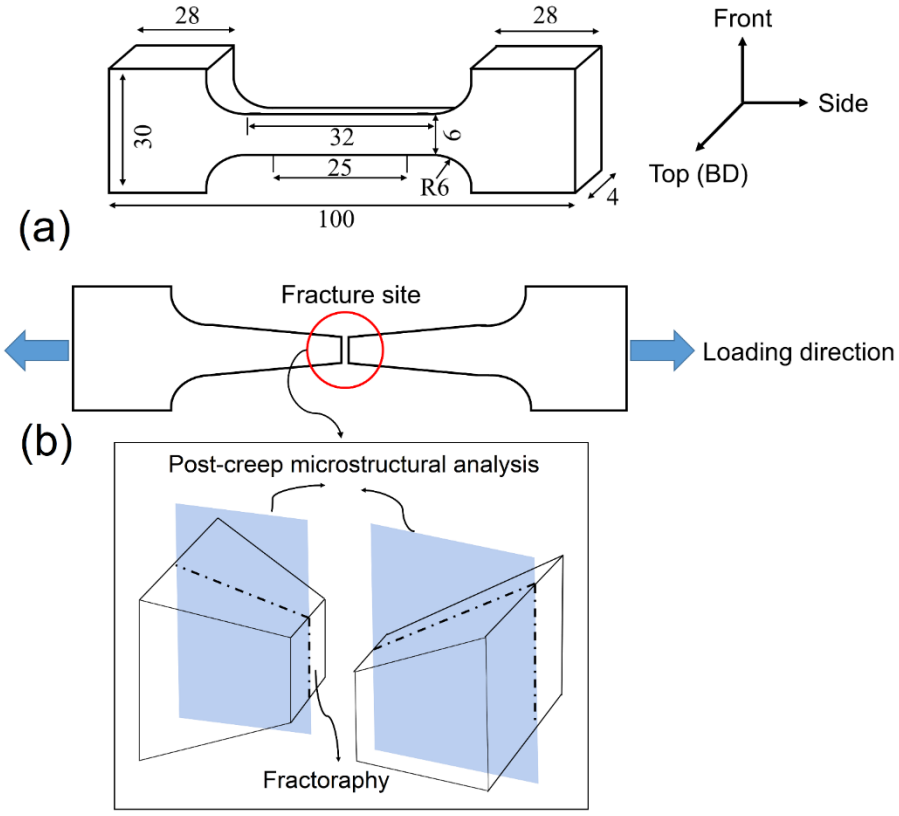

Figure 7-1. (a) General and (b) top views of the L-PBF fabricated creep test samples. The inset in (b) illustrates the locations where the post-creep microstructural characterization and fracture surface analysis were performed.

7.3 Results

7.3.1 Creep properties

7.3.1.1 Creep strain-time curves

Figure 7-2 shows the variation in the creep strain versus time for the as-built and HT specimens. The creep parameters derived from the creep tests are also listed in Table 7-1. As observed in Figure 7-2, the Ti64 sample showed a slightly longer rupture time in the as-built condition compared to the TMC counterpart (3.4 vs. 2.9 h). The heat-treated Ti64 sample showed a rupture time of only 0.6 h. However, the TMC part with the same heat treatment history endured a noticeably longer time of 5.8 h. The highest steady-state creep rate ($\dot{\varepsilon}_{ss}$) among all specimens was for the as-built Ti64 part (5.9 %/h). This was slightly lower for the as-built TMC specimen (4.5 %/h). The lowest $\dot{\varepsilon}_{ss}$ was discerned in the heat-treated TMC case (0.84 %/h), being significantly lower than those of the as-built Ti64 and TMC counterparts. Although the HT-Ti64 sample featured a lower $\dot{\varepsilon}_{ss}$ than the as-built Ti64 and TMC samples, its premature failure led to a rupture time being remarkably shorter than the other two. Figure 7-2(b) illustrates the load-displacement curves during nanoindentation of the as-built samples. As observed, the as-built TMC sample benefits from higher nanohardness and elastic modulus (E) than the as-built Ti64 counterpart. Due to the significantly higher stiffness of TiB than α′/α and β phases, incorporation of TiB into the Ti alloy matrix leads to a TMC with higher hardness and E [41].

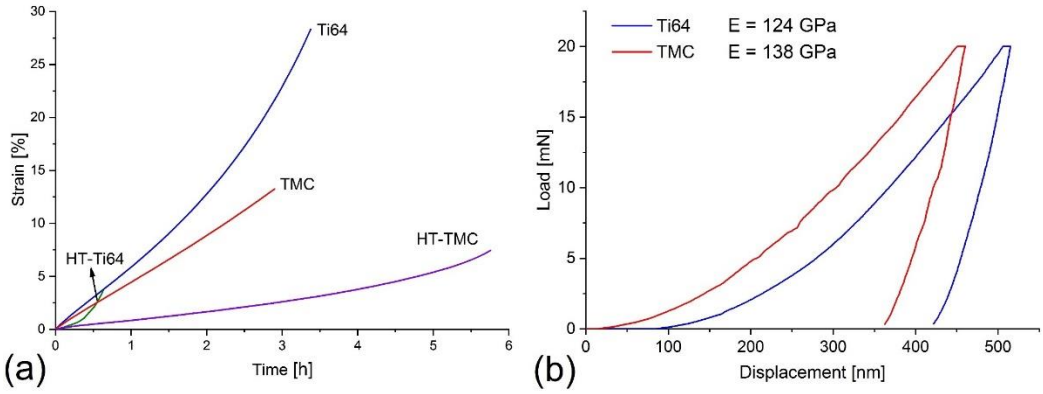

Figure 7-2. (a) Creep strain versus time curves for the as-built and heat-treated (HT) Ti64 and TMC samples, and (b) typical nanoindentation load-displacement curves of the as-built Ti64 and TMC samples.

Table 7-1. The creep parameters of the as-built and HT specimens tested at 600 °C under a stress of 200 MPa.

Sample	**Parameter**			
	t_r [h]	$\dot{\varepsilon}_{ss}$ [%/h]	Total Strain [%]	5D Elongation [%]
As-built Ti64	3.4	5.93	28.3	53.3
As-built TMC	2.9	4.48	13.26	66.7
HT-Ti64	0.6	2.16	3.6	-
HT-TMC	5.8	0.84	7.46	12.5

7.3.1.2 Post-creep microstructural characterization

To better understand the creep fracture mechanism, the top view cross-sections of the creep test specimens after fracture were subjected to microstructural characterization. Figure 7-3 shows these microstructures for the as-built Ti64 and TMC specimens close to the fracture site and along the loading direction. As observed in Figure 7-3(a), the region beside the fracture site of the Ti64 specimen was characterized by large voids which were elongated along the loading direction. The final fracture is believed to have occurred by the coalescence of these elongated voids. Although the voids were also visible at a greater

distance from the fracture site, they were noticeably smaller in size compared to ones existing in its vicinity. As can be seen in Figure 7-3(b), the neighborhood of the fracture site of the as-built TMC specimen was heavily populated by tiny voids. The density of these voids decreased as moving further away from the fracture location. As opposed to the as-built Ti64 counterpart, the large elongated voids were not perceptible in the as-built TMC case. Close examination of both as-built Ti64 and TMC specimens revealed that although there were a few voids at the prior β grain boundaries parallel to the loading direction, they were not as prevalent as voids located at the prior β grain boundaries perpendicular to the loading direction. Referring to the square section of the prior β grains observed from the top view micrographs in Figure 6-3(b) and Figure 6-4(g), it is clear that the prior β grains have experienced elongation along the loading direction during the creep testing. The degree of this elongation showed a gradual decrease farther from the fracture site.

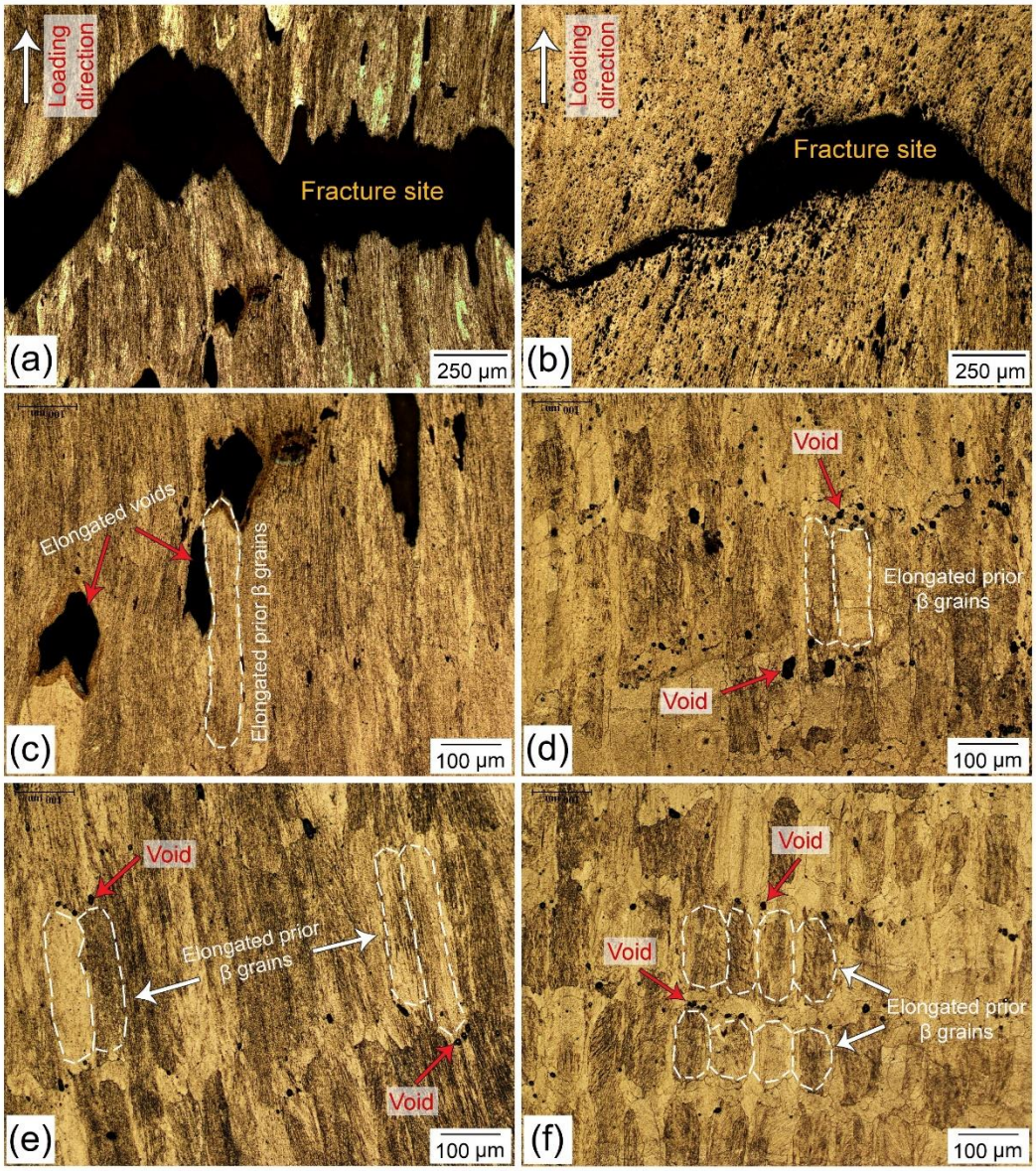

Figure 7-3. Optical micrographs of the top view section of the as-built: (a), (c), (e) Ti64; and (b), (d), (f) TMC creep test samples after failure. (a), and (b) show the fracture sites, while (c), (d), (e), and (f) refer to locations further away from them. (e), and (f) present the microstructures of regions having a greater distance from the fracture site than (c) and (d), respectively.

Figure 7-4(a) shows the top view optical micrograph beside the fracture location of the HT-Ti64 creep test sample after failure. Figure 8(b) and (c) show higher magnification SEM micrographs of this region. As observed in Figure 7-4(a) and (b), the fracture of this

specimen occurred predominantly from the boundaries of the equiaxed prior β grains where GB-α is located. These GB-α networks acted as potential sites for crack nucleation during the creep test. The nucleated cracks then propagated along the GB-α due to their continuous morphology and low ductility, leading to an intergranular fracture mode. Microstructural characterizations revealed that the α/β interfaces were also potential sites for the nucleation of voids during the creep test. Moreover, local cracking of β lamella was evident in the microstructure (Figure 7-4(c)). However, due to the extremely fast growth of cracks along the GB-α, the other two cracking and void nucleation sites could not play a significant role in the creep performance of the HT-Ti64 sample. The EDS analysis results provided in Figure 7-4(e) and (f) also clearly confirmed the microstructure of the HT-Ti64 creep sample to be composed of α and β phases. As can be seen, the α and β phases are characterized by their higher Al and V content as α- and β-stabilizer elements in Ti alloys, respectively.

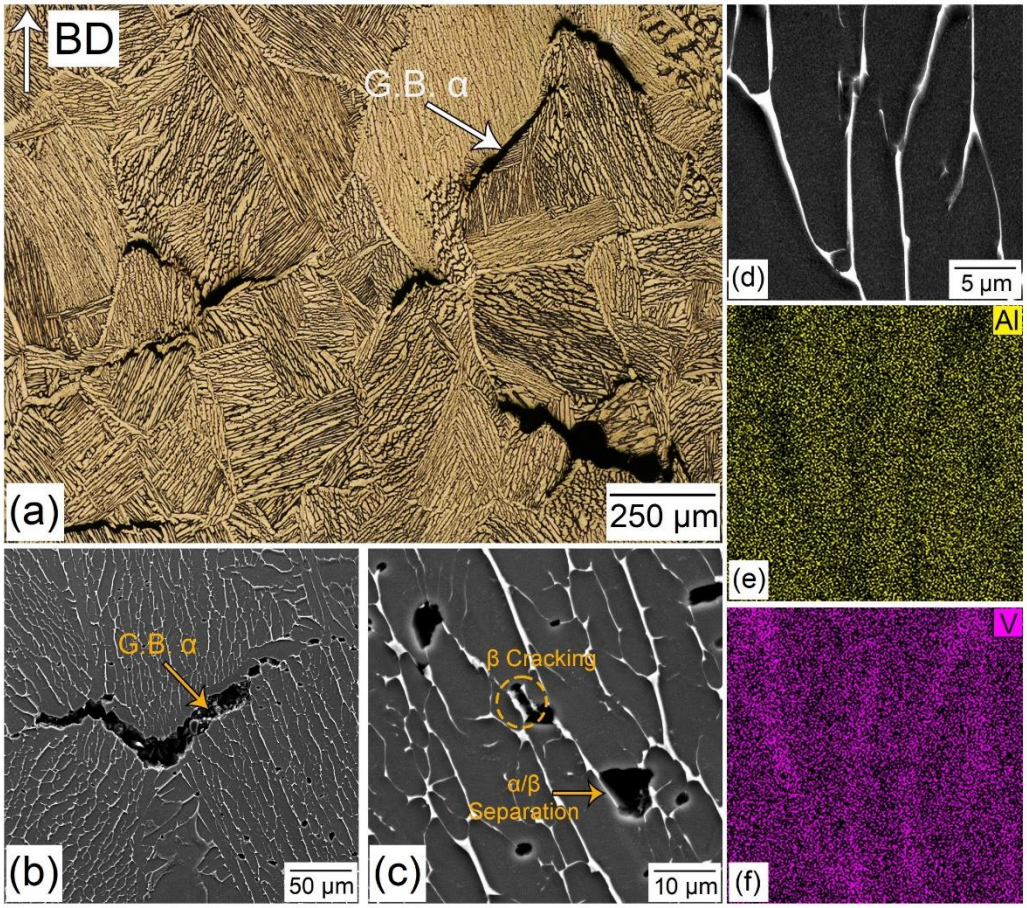

Figure 7-4. (a) Optical micrograph, (b), and (c) SEM images of the top view section of the failed HT-Ti64 creep test sample adjacent to the fracture site. (e), and (f) are the EDS maps showing the elemental distribution of Al and V in the SEM image presented in (d).

Figure 7-5(a) presents the optical micrograph of the region beside the fracture site of the HT-TMC creep specimen. Compared to the heat-treated Ti64 specimen, the voids and cracks observed adjacent to the fracture location were significantly smaller. Higher magnification SEM micrographs of the fracture location neighborhood indicated the formation of a high frequency of cracks and voids. As shown in Figure 7-5(b), the cracking of TiB needles, especially the large-sized ones, was perceptible in the microstructure. In addition, as specified in Figure 7-5(b), some TiB needles experienced debonding from the matrix due to the deformation incompatibility between the matrix and the TiB

reinforcement [42]. The same as the HT-Ti64 creep specimen, the cracking of the β lamellae and the decohesion of α/β interfaces (especially those oriented perpendicular to the loading direction) were evident in the microstructure. The EDS maps in Figure 7-5(e), (f), and (g) illustrate the distribution of Al, V, and B elements in Figure 7-5(d), respectively, and confirm that the microstructure consists of TiB needles acting as reinforcements in an α+β matrix.

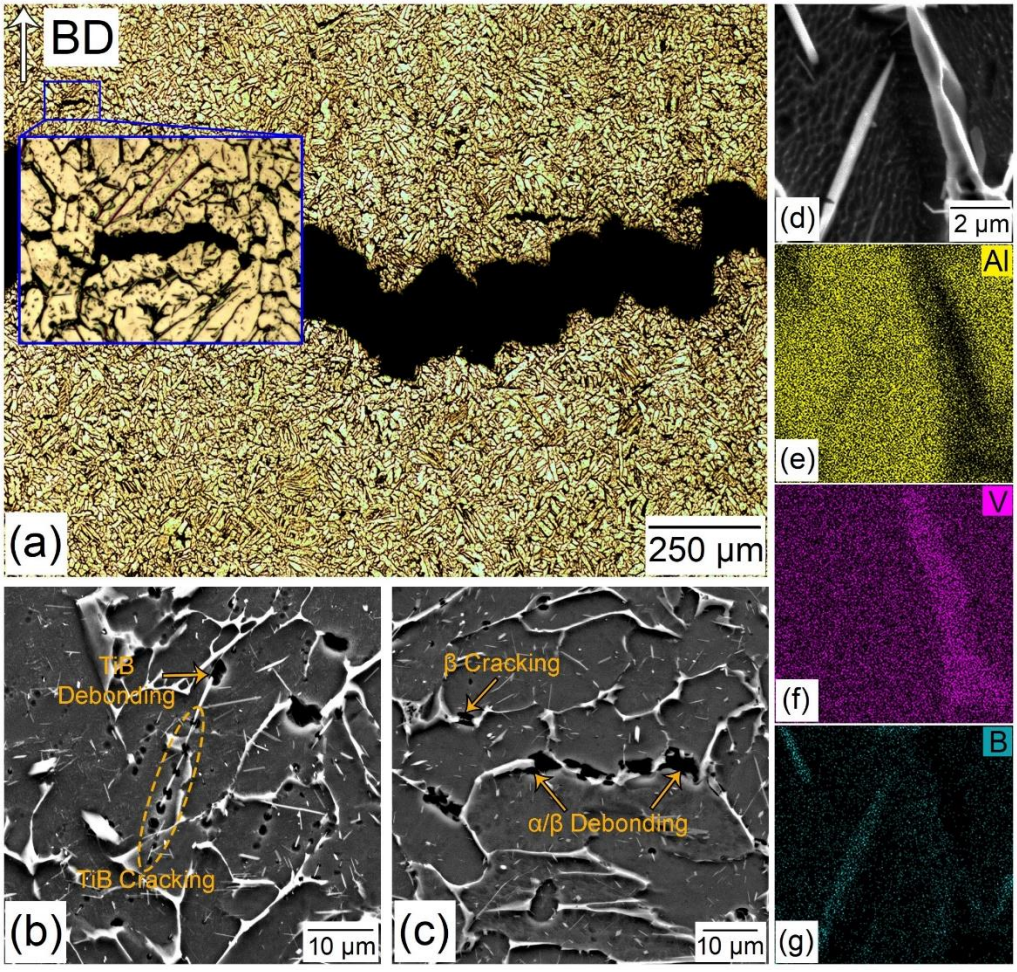

Figure 7-5. (a) Optical micrograph, (b), and (c) SEM images of the top view section of the failed HT-TMC creep test sample adjacent to the fracture site. (e), (f), and (g) are the EDS maps showing the elemental distribution of Al, V, and B in the SEM image presented in (d).

7.3.1.3 Fractography of the creep samples

Figure 7-6 shows SEM micrographs of the fracture surfaces for creep tested as-built and HT samples. Except for the HT-Ti64 case, all samples featured a ductile mode characterized by dimples on the fracture surface. However, the size of dimples was found to be different among the samples. As observed in Figure 7-6(a), the fracture surface of the as-built Ti64 sample contained dimples with two different scales, i.e., large and small. Compared to the small-sized dimples, the large-sized ones were noticeably deeper and less frequent on the surface. These deep dimples can also be observed in the top view cross-section of the fractured creep test specimen (Figure 7-3(a)). In general, the fracture surfaces with small numbers of relatively large-sized dimples represent a highly ductile material, while those containing larger number of finer and shallower dimples give evidence of a material with a lower ductility [43]. Accordingly, the presence of large-sized and deep dimples along with the fine ones on the fracture surface of the as-built Ti64 specimen unveils its relatively high ductility and justifies its higher total strain to fracture compared to other specimens. The creep fracture surface of the as-built TMC sample also featured dimples. However, the large-sized and deep dimples were absent. The fracture surface of the HT-Ti64 specimen displayed an intergranular fracture mode, representing a weak grain boundary cohesion (Figure 7-3(c)). This can be ascribed to the presence of continuous GB-α network along the prior β grain boundaries which provided pathways for the nucleation and then propagation of the cracks (Figure 7-4(a), and (b)). As provided in Figure 7-3(d), the fracture surface of the HT-TMC specimen featured a ductile mode. In addition to the round shape dimples which were also observed in the as-built specimens, the fracture surface of the heat-treated TMC sample exhibited cylindrical-shape dimples containing TiB needles. These dimples are caused by the deboning of the TiB whiskers from the matrix

during the creep loading. Transverse cracking of the TiB whiskers was another phenomenon observed on the fracture surface of this specimen (Figure 7-6(d)). The TiB cracking as well as the debonding of TiB needles from the matrix of the HT-TMC creep test specimen are the microstructural features which were also observed adjacent to the fracture site (Figure 7-5(b), and (c)).

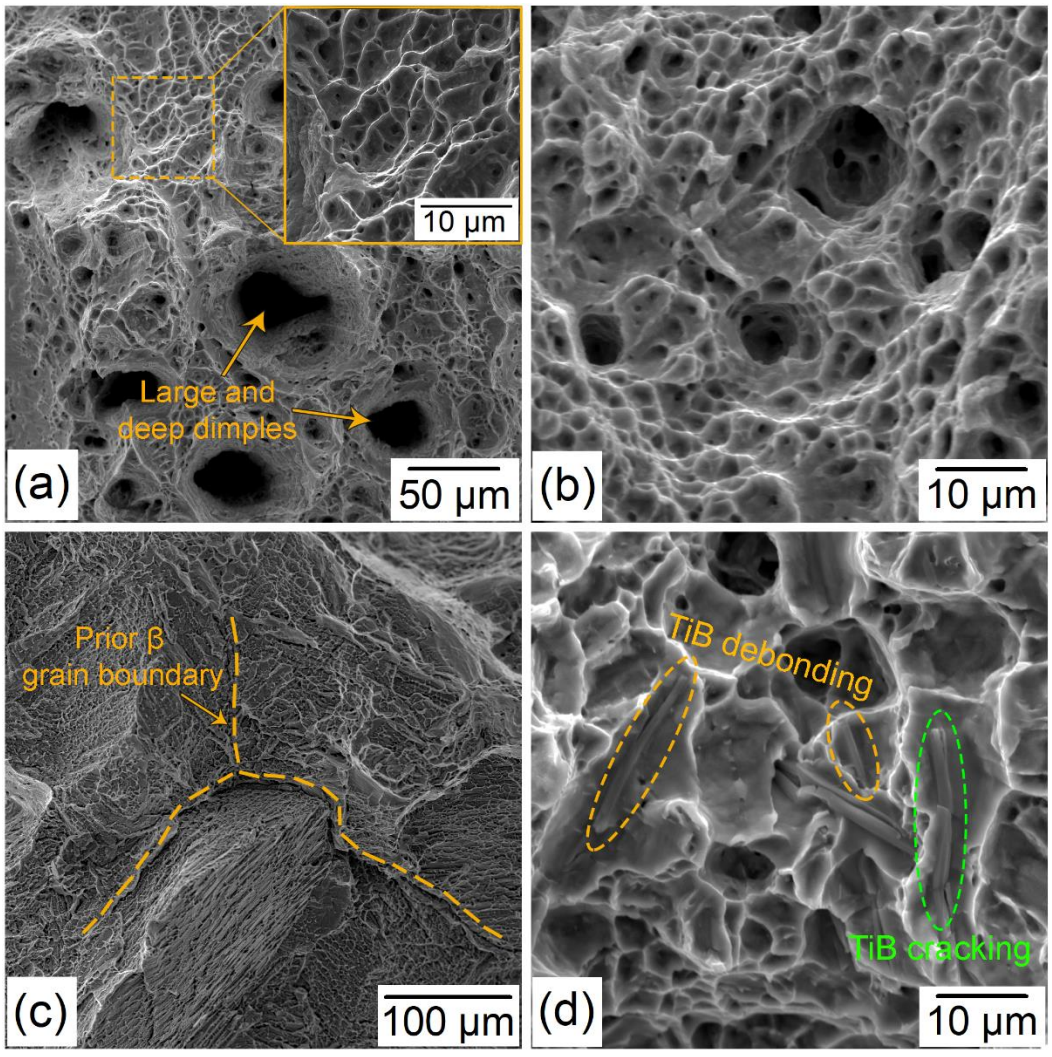

Figure 7-6. SEM micrographs of the fracture surface of: (a) as-built Ti64, (b) as-built TMC, (c) HT-Ti64, and (d) HT-TMC creep test samples after failure. The inset in (a) shows a higher magnification image of the region selected by the dashed square.

7.4 Discussion

As microstructural observations revealed, the as-built Ti64 and TMC parts contained large prior β grains elongated along the building direction (Figure 5-6). This structure is formed due to the combination of epitaxial and competitive growth during the solidification, where faster growth of those prior β grains having their easy-growth crystallographic direction perpendicular to the fusion line crowds out the β grains oriented in less favorable directions [44, 45].

The TMC sample contained nanoscale/sub-micron TiB whiskers homogeneously dispersed in the microstructure (Figure 5-8). The obtained dispersion state of TiB whiskers is quite different from the microstructure of the TiB reinforced TMC systems with minor B content subjected to other manufacturing processes with relatively lower cooling rates than the LPBF process (e.g., conventional processes such as casting [35], or AM processes such as direct energy deposition [31], electron beam melting [46], and wire-arc AM [47]). The solidification in these processes starts with the formation and growth of the β phase and the rejection of B from the growing solidification interface into the liquid. The B-enriched liquid then transforms to (β+TiB) through a eutectic reaction, leading to the β grains surrounded by TiB whiskers. The extremely high cooling rate of the LPBF process hinders the rejection of B into the liquid during the solidification, leading to the supersaturation of the β phase from B [48]. Due to the decreased solubility of B in the β phase during the cooling stage, the supersaturated B precipitates out as noticeably fine and homogeneously dispersed TiB whiskers through a solid-state transformation. The formation of a fully martensitic matrix, rather than an α+β two-phase microstructure, is another consequence of the extremely high cooling of the LPBF process which well surpasses the critical cooling rate for the martensitic phase transformation in Ti64 alloy [49-51].

Referring to Figure 6-8, the HT-Ti64 sample contained a continuous network of GB-α surrounding the equiaxed prior β grains. The change in the morphology of prior β grains from columnar to equiaxed is due to applying a supertransus heat treatment temperature, which leads to the nucleation and subsequent growth of new prior β grains from the boundaries of the columnar β grains of the as-built Ti64 sample. During cooling from the supertransus temperature in an equilibrium condition (i.e., furnace cooling in this study), the GB-α is the first transformation product that forms at the prior β grain boundaries of the Ti64 sample with a thick plate-like morphology [52, 53]. At the β transus temperature, the α phase (which is enriched from Al as an α-stabilizer element) starts to form from prior β grains. This leads to the rejection of V (as a β-stabilizer element) into the remaining β directly adjacent to the formed α lamellae and makes it stable. The local variation of Al and V causes packets of lamellar (α+β) microstructure to be formed in each prior β grain. As opposed to the HT-Ti64 sample, the HT-TMC did not contain the GB-α phase with a continuous morphology owing to the TiB precipitates acting as effective heterogeneous nucleation sites [54]. The evolution of α grains with an equiaxed morphology in the HT-TMC sample (rather than the lamellar morphology of this phase in the HT-Ti64 counterpart (Figure 7-4)) can be ascribed to the effect of TiB precipitates on the β→(α+β) transformation kinetics (Figure 7-5). Given that the phase transformation from β to α is of a nucleation and growth type, TiB precipitates can provide heterogeneous nucleation sites for this transformation and bring about an equiaxed morphology [31, 37, 55]. It is worth noting that the kinetics of this transformation depends on some variables such as the solutionizing temperature, cooling rate, as well as the size and volume fraction of TiB precipitates [56]. Compared to the TiB needles existing in the as-built TMC sample, those in the microstructure of the HT-TMC component were coarser (both length and width) with

larger spacing. The coarsening of TiB reinforcements in the heat-treated TMC compared to the as-built TMC part is due to the Ostwald Ripening mechanism during which larger TiB needles get bigger at the expense of smaller ones [57].

As the microstructural observation of the near-fracture sites for the as-built Ti64 and TMC parts revealed (Figure 7-3), voids were found to be much more prevalent at the prior β grain boundaries perpendicular to the loading direction. This can be ascribed to the normal force being maximum at these boundaries, making the formation of voids more probable and tends to open voids [58]. As the comparison of the as-built samples indicated, the TMC sample featured noticeably higher numbers and smaller voids directly adjacent to the fracture site. This gives evidence that the cracking of nanoscale/sub-micron TiB whiskers or their separation from the matrix might have played a role in forming such a high frequency of fine voids in the as-built TMC creep specimen. The slightly shorter rupture time and the significantly lower total creep strain of the as-built TMC than those of the Ti64 can be attributed to these fine and closely spaced voids, which can experience an easier and faster coalescence up to the final fracture. The presence of noticeably fine dimples on the fracture surface of the as-built TMC (Figure 7-6(b)) also confirms that the final fracture has occurred by the growth and the coalescence of these microvoids.

The creep performance of the specimens can be rationalized based on the following discussion:

(i) The dependence of $\dot{\varepsilon}_{ss}$ on the applied stress (σ), temperature (T), and E is described by the following power-law for metal matrix composites [59]:

$$\dot{\varepsilon}_{ss} = A\left(\frac{\sigma-\sigma_{th}}{E}\right)^{n} \exp\left(-\frac{Q_c}{RT}\right) \quad [1]$$

where A is the creep constant, n is the stress exponent, R is the universal gas constant, T is the absolute temperature, Q is the activation energy for creep, and σ_{th} is the threshold stress. As confirmed by nanoindentation measurements, the TMC possessed higher E than the Ti64 sample (Figure 7-2(b)). Referring to Eq. 1, the increase in E results in the improved creep performance by reducing the $\dot{\varepsilon}_{ss}$. Moreover, the ceramic reinforcing particles existing in the MMCs are known to act as effective barriers to the mobile dislocations and consequently give rise to the σ_{th} for creep, below which the strain rate and hot deformation are assumed to be negligible [60-62]. This justifies the noticeably lower $\dot{\varepsilon}_{ss}$ of the HT-TMC sample than the as-built and HT-Ti64 counterparts. It is also worth noting that while both Ti64 and TMC samples featured the same fully martensitic microstructure in the as-built state, the TMC sample showed a lower $\dot{\varepsilon}_{ss}$ partly due to the presence of TiB whiskers in its microstructure.

(ii) As microstructural characterizations and EBSD analysis results revealed (Figure 6-8 and Figure 6-12), the HT-TMC sample benefitted from a noticeably finer microstructure compared to the HT-Ti64 counterpart. The increased density of interfaces (α-α, α-β, and α-TiB) caused by this microstructure refinement leads to the improved creep resistance since these interfaces provide obstacles to the movement of dislocations during the creep [60, 63]. The lower $\dot{\varepsilon}_{ss}$ of the as-built TMC than the Ti64 counterpart is also partially related to the higher density of interfaces caused by smaller size of α′ needles and the presence of TiB in the TMC part (Figure 6-12).

(iii) Owing to their significantly higher strength and stiffness than the α and β phases, much of the load placed on the TMC is gradually transferred from the (α+β) matrix

to the TiB needles [64]. The TiB reinforcement is generally known to possess a high load-bearing capability due to the high adhesion strength of the semi-coherent interfaces between the TiB whiskers and the Ti alloy matrix [59, 65]. The load bearing by TiB whiskers has been reported to cause stress relaxation in the α and β phases of the matrix [28, 66]. As microstructural characterizations of the creep specimens after fracture revealed, TiB whiskers (especially larger ones) experienced fracture during the test (Figure 7-5). This clearly shows that TiB whiskers bore the load that was transferred from the matrix. During the creep test, microcracks start to form on TiB whiskers at locations where the maximum stresses are induced or flaws are accumulated [28]. The stress concentration at these sites can exceed the ultimate strength of the TiB whiskers and consequently cause their cracking. Referring to Figure 7-5(b), the microstructure of the HT-TMC after the creep test contained TiB whiskers that experienced multiple cracking. This phenomenon reveals the high potential of TiB whiskers in undertaking the transferred load even after cracking. The strong interfacial bonding between the in-situ synthesized TiB whiskers and the Ti matrix is the main reason behind the multiple cracking of the TiB whiskers, allowing the failed whiskers to further undertake the load transferred from the matrix and experience more fracture [30]. After experiencing multiple cracking, the TiB whiskers no longer participate in the load bearing since experiencing debonding from the matrix. As microstructural characterizations revealed (Figure 7-5(b)), in addition to the cracking, TiB whiskers (specifically the larger ones) experienced debonding from the matrix. This phenomenon is due to the concentration of the shear stresses at the end of the TiB whiskers which can locally exceed the strength of the TiB/matrix interface.

After the debonding of TiB from the matrix, further creep deformation in the TMC sample will be facilitated [28, 66]. The significant contribution of TiB whiskers in load bearing during the creep test justifies the noticeably higher rupture time of the HT-TMC part.

Figure 7-7 illustrates $\dot{\varepsilon}_{ss}$ for the conventionally manufactured pure Ti, Ti64 alloy and their composites with relatively the same σ and T conditions. As observed, the highest $\dot{\varepsilon}_{ss}$ corresponds to the pure Ti, being in the range of 1-10 h^{-1}. Incorporation of TiB or (TiB+TiC) reinforcement(s) into the pure Ti matrix has been reported to decrease the $\dot{\varepsilon}_{ss}$ by 3 orders of magnitude, confirming the significant role that TiB and TiC reinforcements can play on the creep performance improvement. Alloying of pure Ti with Al and V elements (i.e., Ti64) has been shown to yield the same $\dot{\varepsilon}_{ss}$ (or even lower) as that of the pure Ti matrix composites. By adding TiB and/or TiC reinforcements to the Ti64 alloy matrix, the developed material benefits simultaneously from both the alloying and reinforcing strengthening mechanisms, leading to $\dot{\varepsilon}_{ss}$ values up to four orders of magnitude lower than those of pure Ti. The $\dot{\varepsilon}_{ss}$ of the as-built and heat treated Ti64 and TMC samples fabricated by the L-PBF process in this study is also shown in Figure 7-7 for the sake of comparison. In the as-built Ti64 case, the $\dot{\varepsilon}_{ss}$ was higher than the conventionally manufactured counterparts. This might originate from the metastable martensitic microstructure of the as-built Ti64 sample, as opposed to the (α+β) two-phase microstructure of the conventionally manufactured ones (Figure 6-3). Although the heat treatment of the as-built Ti64 sample slightly reduced the $\dot{\varepsilon}_{ss}$, it significantly deteriorated the rupture time due to the GB-α acting as crack propagation sites (Figure 7-2 and Figure 7-4). The as-built TMC showed a slightly lower $\dot{\varepsilon}_{ss}$ than the as-built Ti64, but higher than the conventionally manufactured TMCs. In the HT-TMC sample, the $\dot{\varepsilon}_{ss}$ is ~80% lower

than that of the as-built TMC, confirming the remarkable influence of the selected heat treatment on improving the creep performance of the L-PBF fabricated TMCs. To further enhance the creep durability of the L-PBF fabricated TMCs, other heat treatment strategies with different supertransus temperatures need to be explored.

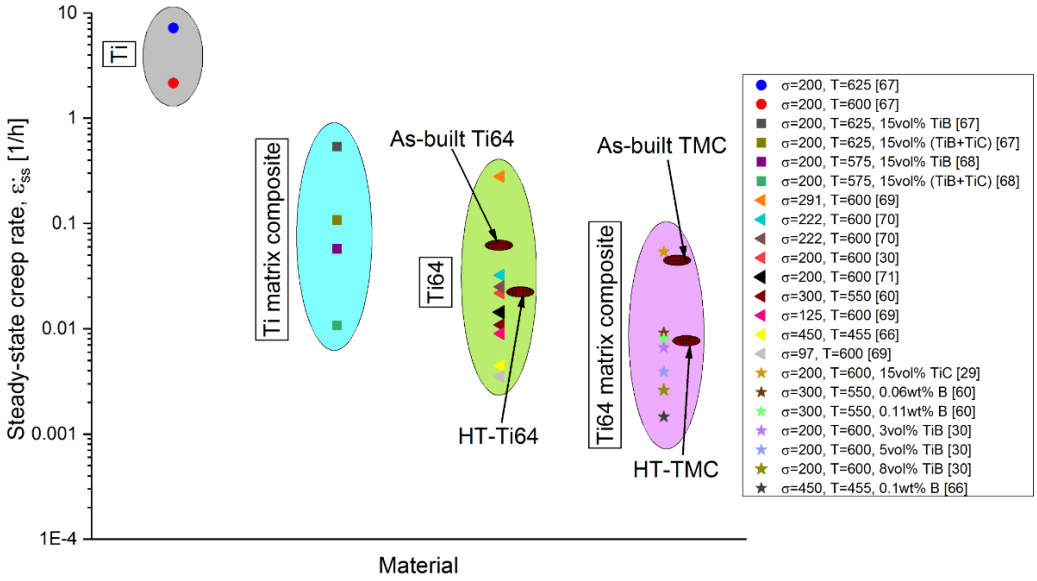

Figure 7-7. The steady-state creep rate of the conventionally manufactured pure Ti, and Ti64 alloy, as well as the TiB/TiC/(TiB+TiC)-reinforced pure Ti, and Ti64 matrix composites compared with the as-built and heat treated Ti64 and TMC samples in this study fabricated by the L-PBF process. The temperature (T) and stress (σ) under which the creep test has been performed are listed. ([67] [68] [69] [70] [30] [71] [60] [66] [29])

7.5 Conclusions

This research study aimed at improving the creep performance of laser powder bed fusion (L-PBF) fabricated Ti64 parts via incorporating in-situ synthesized ceramic reinforcements and employing appropriate post-processing heat treatment. For this end, highly dense monolithic Ti64 and TiB reinforced Ti64 matrix composite (TMC) parts were fabricated using the L-PBF process. The parts were also subjected to the supertransus heat treatment to eliminate the microstructural anisotropy of the as-built samples. The creep performance

of the as-built and heat treated (HT) components was assessed. The main conclusions can be drawn as follows:

1- In the as-built condition, the Ti64 sample showed a slightly longer rupture time than the TMC counterpart (3.4 vs. 2.9 h). Microstructural characterization of the cross-section adjacent to the fracture site revealed voids formed at the prior β grain boundaries in both cases. These voids were much more prevalent at the grain boundaries perpendicular to the loading direction, where the induced normal force is in its maximum magnitude. Compared to the Ti64, the TMC sample contained a remarkably higher frequency of small-size voids.

2- Although showing 60% and 50% lower steady-state creep rate ($\dot{\varepsilon}_{ss}$) than those of the as-built Ti64 and TMC cases, the HT-Ti64 creep test specimen featured a premature failure only after 0.6 h. The relatively poor creep performance of the HT-Ti64 specimen was due to grain boundary α (GB-α) as a continuous network around the prior β grains, acting as preferential crack nucleation and propagation sites during loading, leading to an intergranular fracture mode.

3- The TiB whiskers in the HT-TMC specimen not only hindered the formation of GB-α but also changed the morphology of α grains from lamellar (in the HT-Ti64 sample) to equiaxed. This morphological change originates from the TiB precipitates acting as heterogeneous nucleation sites for the transformation of β to α.

4- The highest short-term creep performance (the longest rupture time and the lowest $\dot{\varepsilon}_{ss}$) was achieved for the HT-TMC specimen. This superior creep performance was due to the contribution of several factors including: (i) the higher elastic modulus and threshold stress, (ii) the finer microstructure and higher density of

interfaces (α-α, α-β, and α-TiB) which can act as obstacles to the movement of dislocations, and (iii) the load transfer from the matrix to the stiff TiB whiskers.

7.6 References

[1] V.A. Joshi, Titanium alloys: an atlas of structures and fracture features, Crc Press2006.

[2] J. Liu, K. Guo, J. Sun, Q. Sun, L. Wang, H. Li, Compressive behavior and vibration-damping properties of porous Ti-6Al-4V alloy manufactured by laser powder bed fusion, Journal of Manufacturing Processes 66 (2021) 1-10.

[3] C. Cui, B. Hu, L. Zhao, S. Liu, Titanium alloy production technology, market prospects and industry development, Materials & Design 32(3) (2011) 1684-1691.

[4] M. Barboza, E. Perez, M. Medeiros, D. Reis, M. Nono, F.P. Neto, C. Silva, Creep behavior of Ti–6Al–4V and a comparison with titanium matrix composites, Materials Science and Engineering: A 428(1-2) (2006) 319-326.

[5] E. Fereiduni, A. Ghasemi, M. Elbestawi, Selective Laser Melting of Aluminum and Titanium Matrix Composites: Recent Progress and Potential Applications in the Aerospace Industry, Aerospace 7(6) (2020) 77.

[6] R.W. Evans, B. Wilshire, Introduction to creep, Institute of Materials London1993.

[7] G. Singh, U. Ramamurty, Boron modified titanium alloys, Progress in Materials Science 111 (2020) 100653.

[8] E. Fereiduni, M. Elbestawi, Process-structure-property relationships in additively manufactured metal matrix composites, Additive Manufacturing of Emerging Materials, Springer2019, pp. 111-177.

[9] B. Dutta, F.H. Froes, 24 - The additive manufacturing (AM) of titanium alloys, in: M. Qian, F.H. Froes (Eds.), Titanium Powder Metallurgy, Butterworth-Heinemann, Boston, 2015, pp. 447-468.

[10] E. Fereiduni, M. Yakout, M. Elbestawi, Laser-based additive manufacturing of lightweight metal matrix composites, Additive Manufacturing of Emerging Materials, Springer2019, pp. 55-109.

[11] I. Gibson, D. Rosen, B. Stucker, M. Khorasani, Additive manufacturing technologies, Springer2014.

[12] N. Ahmed, Direct metal fabrication in rapid prototyping: A review, Journal of Manufacturing Processes 42 (2019) 167-191.

[13] I. Gibson, D. Rosen, B. Stucker, M. Khorasani, Design for Additive Manufacturing, in: I. Gibson, D. Rosen, B. Stucker, M. Khorasani (Eds.), Additive Manufacturing Technologies, Springer International Publishing, Cham, 2021, pp. 555-607.

[14] E. Fereiduni, A. Ghasemi, M. Elbestawi, S. Dinkar Jadhav, K. Vanmeensel, Laser powder bed fusion processability of Ti-6Al-4V powder decorated by B4C particles, Materials Letters 296 (2021) 129923.

[15] A.A. Akilan, A. Gökçe, S.D. Nath, V.K. Balla, K.H. Kate, S.V. Atre, Laser powder bed fusion of in-situ composites using dry-mixed Ti6Al4V and Si3N4 powder, Journal of Manufacturing Processes 59 (2020) 43-50.

[16] L. Thijs, F. Verhaeghe, T. Craeghs, J.V. Humbeeck, J.-P. Kruth, A study of the microstructural evolution during selective laser melting of Ti–6Al–4V, Acta Materialia 58(9) (2010) 3303-3312.

[17] C. Qiu, N.J.E. Adkins, M.M. Attallah, Microstructure and tensile properties of selectively laser-melted and of HIPed laser-melted Ti–6Al–4V, Materials Science and Engineering: A 578 (2013) 230-239.

[18] W. Xu, M. Brandt, S. Sun, J. Elambasseril, Q. Liu, K. Latham, K. Xia, M. Qian, Additive manufacturing of strong and ductile Ti–6Al–4V by selective laser melting via in situ martensite decomposition, Acta Materialia 85 (2015) 74-84.

[19] H.K. Rafi, N.V. Karthik, H. Gong, T.L. Starr, B.E. Stucker, Microstructures and Mechanical Properties of Ti6Al4V Parts Fabricated by Selective Laser Melting and Electron Beam Melting, Journal of Materials Engineering and Performance 22(12) (2013) 3872-3883.

[20] X. Zhao, S. Li, M. Zhang, Y. Liu, T.B. Sercombe, S. Wang, Y. Hao, R. Yang, L.E. Murr, Comparison of the microstructures and mechanical properties of Ti–6Al–4V fabricated by selective laser melting and electron beam melting, Materials & Design 95 (2016) 21-31.

[21] G.M. Ter Haar, T.H. Becker, The influence of microstructural texture and prior beta grain recrystallisation on the deformation behaviour of laser powder bed fusion produced Ti–6Al–4V, Materials Science and Engineering: A 814 (2021) 141185.

[22] C.M. Cepeda-Jiménez, F. Potenza, E. Magalini, V. Luchin, A. Molinari, M.T. Pérez-Prado, Effect of energy density on the microstructure and texture evolution of Ti-6Al-4V manufactured by laser powder bed fusion, Materials Characterization 163 (2020) 110238.

[23] M.-T. Tsai, Y.-W. Chen, C.-Y. Chao, J.S.C. Jang, C.-C. Tsai, Y.-L. Su, C.-N. Kuo, Heat-treatment effects on mechanical properties and microstructure evolution of Ti-6Al-4V alloy fabricated by laser powder bed fusion, Journal of Alloys and Compounds 816 (2020) 152615.

[24] B. Vrancken, L. Thijs, J.-P. Kruth, J. Van Humbeeck, Heat treatment of Ti6Al4V produced by Selective Laser Melting: Microstructure and mechanical properties, Journal of Alloys and Compounds 541 (2012) 177-185.

[25] X.-Y. Zhang, G. Fang, S. Leeflang, A.J. Böttger, A.A. Zadpoor, J. Zhou, Effect of subtransus heat treatment on the microstructure and mechanical properties of additively manufactured Ti-6Al-4V alloy, Journal of Alloys and Compounds 735 (2018) 1562-1575.

[26] T. Vilaro, C. Colin, J.-D. Bartout, As-fabricated and heat-treated microstructures of the Ti-6Al-4V alloy processed by selective laser melting, Metallurgical and materials transactions A 42(10) (2011) 3190-3199.

[27] Q. Huang, X. Liu, X. Yang, R. Zhang, Z. Shen, Q. Feng, Specific heat treatment of selective laser melted Ti–6Al–4V for biomedical applications, Frontiers of Materials Science 9(4) (2015) 373-381.

[28] C. Boehlert, The creep behavior of powder-metallurgy processed Ti–6Al–4V–1B (wt.%), Materials Science and Engineering: A 510 (2009) 434-439.

[29] Z. Ma, R.S. Mishra, S. Tjong, High-temperature creep behavior of TiC particulate reinforced Ti–6Al–4V alloy composite, Acta materialia 50(17) (2002) 4293-4302.

[30] S. Wang, L. Huang, L. Geng, F. Scarpa, Y. Jiao, H. Peng, Significantly enhanced creep resistance of low volume fraction in-situ TiBw/Ti6Al4V composites by architectured network reinforcements, Scientific reports 7(1) (2017) 1-13.

[31] A. Xue, X. Lin, L. Wang, J. Wang, W. Huang, Influence of trace boron addition on microstructure, tensile properties and their anisotropy of Ti6Al4V fabricated by laser directed energy deposition, Materials & Design 181 (2019) 107943.

[32] C. Han, R. Babicheva, J.D.Q. Chua, U. Ramamurty, S.B. Tor, C.-N. Sun, K. Zhou, Microstructure and mechanical properties of (TiB+ TiC)/Ti composites fabricated in situ via selective laser melting of Ti and B4C powders, Additive Manufacturing 36 (2020) 101466.

[33] Y. Feng, J. Hou, L. Gao, G. Cui, W. Zhang, Research on the inhomogeneity and joint interface of in situ oriented TiBw/TA15 composites fabricated by vacuum hot-pressing sintering and canned extrusion, Journal of Manufacturing Processes 59 (2020) 791-800.

[34] K.R. Chandran, K. Panda, S. Sahay, TiB w-reinforced Ti composites: Processing, properties, application prospects, and research needs, Jom 56(5) (2004) 42-48.

[35] S. Tamirisakandala, R.B. Bhat, J.S. Tiley, D.B. Miracle, Grain refinement of cast titanium alloys via trace boron addition, Scripta materialia 53(12) (2005) 1421-1426.

[36] V. Chandravanshi, R. Sarkar, P. Ghosal, S. Kamat, T. Nandy, Effect of minor additions of boron on microstructure and mechanical properties of as-cast near α titanium alloy, Metallurgical and Materials Transactions A 41(4) (2010) 936-946.

[37] D.J. McEldowney, S. Tamirisakandala, D.B. Miracle, Heat-treatment effects on the microstructure and tensile properties of powder metallurgy Ti-6Al-4V alloys modified with boron, Metallurgical and Materials Transactions A 41(4) (2010) 1003-1015.

[38] H. Feng, D. Jia, Y. Zhou, Spark plasma sintering reaction synthesized TiB reinforced titanium matrix composites, Composites Part A: Applied Science and Manufacturing 36(5) (2005) 558-563.

[39] E. Fereiduni, A. Ghasemi, M. Elbestawi, Characterization of composite powder feedstock from powder bed fusion additive manufacturing perspective, Materials 12(22) (2019) 3673.

[40] E. ASTM, 139," Standard test methods for conducting creep, creep-rupture, and stress-rupture tests of metallic materials 3 (2010).

[41] S. Gorsse, D.B. Miracle, Mechanical properties of Ti-6Al-4V/TiB composites with randomly oriented and aligned TiB reinforcements, Acta Materialia 51(9) (2003) 2427-2442.

[42] Y. Jiao, L.J. Huang, S. Wang, X.T. Li, Q. An, X.P. Cui, L. Geng, Effects of first-scale TiBw on secondary-scale Ti5Si3 characteristics and mechanical properties of in-situ (Ti5Si3+TiBw)/Ti6Al4V composites, Journal of Alloys and Compounds 704 (2017) 269-281.

[43] W. Qin, J. Li, Y. Liu, J. Kang, L. Zhu, D. Shu, P. Peng, D. She, D. Meng, Y. Li, Effects of grain size on tensile property and fracture morphology of 316L stainless steel, Materials Letters 254 (2019) 116-119.

[44] T. Wang, Y. Zhu, S. Zhang, H. Tang, H. Wang, Grain morphology evolution behavior of titanium alloy components during laser melting deposition additive manufacturing, Journal of Alloys and Compounds 632 (2015) 505-513.

[45] F. Wang, S. Williams, P. Colegrove, A.A. Antonysamy, Microstructure and mechanical properties of wire and arc additive manufactured Ti-6Al-4V, Metallurgical and materials transactions A 44(2) (2013) 968-977.

[46] X. Tao, Z. Yao, S. Zhang, M. Yao, S. Sun, M. Oleksandr, Effect of beam power on the distribution statues of aligned TiBw and tensile behavior of trace boron-modified Ti6Al4V alloy produced by electron beam freeform fabrication, Vacuum 172 (2020) 109070.

[47] M.J. Bermingham, D. Kent, H. Zhan, D.H. StJohn, M.S. Dargusch, Controlling the microstructure and properties of wire arc additive manufactured Ti–6Al–4V with trace boron additions, Acta Materialia 91 (2015) 289-303.

[48] S.H. Whang, Rapidly solidified titanium alloys for high-temperature applications, Journal of materials science 21(7) (1986) 2224-2238.

[49] J. Yang, H. Yu, J. Yin, M. Gao, Z. Wang, X. Zeng, Formation and control of martensite in Ti-6Al-4V alloy produced by selective laser melting, Materials & Design 108 (2016) 308-318.

[50] E. Fereiduni, A. Ghasemi, M. Elbestawi, Selective laser melting of hybrid ex-situ/in-situ reinforced titanium matrix composites: Laser/powder interaction, reinforcement formation mechanism, and non-equilibrium microstructural evolutions, Materials & Design 184 (2019) 108185.

[51] S. Pal, G. Lojen, V. Kokol, I. Drstvensek, Evolution of metallurgical properties of Ti-6Al-4V alloy fabricated in different energy densities in the Selective Laser Melting technique, Journal of Manufacturing Processes 35 (2018) 538-546.

[52] R. Pederson, Microstructure and phase transformation of Ti-6Al-4V, Luleå tekniska universitet, 2002.

[53] I. Drstvenšek, F. Zupanič, T. Bončina, T. Brajlih, S. Pal, Influence of local heat flow variations on geometrical deflections, microstructure, and tensile properties of Ti-6Al-4 V products in powder bed fusion systems, Journal of Manufacturing Processes 65 (2021) 382-396.

[54] R. Chen, C. Tan, Y. Yu, M. Zhang, X. Yu, C. Liu, W. Ye, S. Hui, Y. Jiang, Modification of α-phase of wire + arc additive manufactured Ti-6Al-4 V alloy with boron addition, Materials Characterization 169 (2020) 110616.

[55] Y.F. Yang, M. Yan, S.D. Luo, G.B. Schaffer, M. Qian, Modification of the α-Ti laths to near equiaxed α-Ti grains in as-sintered titanium and titanium alloys by a small addition of boron, Journal of Alloys and Compounds 579 (2013) 553-557.

[56] D. Hill, R. Banerjee, D. Huber, J. Tiley, H. Fraser, Formation of equiaxed alpha in TiB reinforced Ti alloy composites, Scripta Materialia 52(5) (2005) 387-392.

[57] H. Jeong, S. Kim, Y. Hyun, Y. Lee, Densification and compressive strength of in-situ processed Ti/TiB composites by powder metallurgy, Metals and Materials International 8(1) (2002) 25-35.

[58] T. Lillo, J. Cole, M. Frary, S. Schlegel, Influence of grain boundary character on creep void formation in alloy 617, Metallurgical and Materials transactions A 40(12) (2009) 2803.

[59] R. Fernández, G. González-Doncel, Threshold stress and load partitioning during creep of metal matrix composites, Acta Materialia 56(11) (2008) 2549-2562.

[60] G. Singh, D. Satyanarayana, R. Pederson, R. Datta, U. Ramamurty, Enhancement in creep resistance of Ti–6Al–4V alloy due to boron addition, Materials Science and Engineering: A 597 (2014) 194-203.

[61] R. Fernández, G. González-Doncel, Creep behavior of ingot and powder metallurgy 6061Al, Journal of Alloys and Compounds 440(1) (2007) 158-167.

[62] K.E. Knipling, D.C. Dunand, Creep resistance of cast and aged Al–0.1Zr and Al–0.1Zr–0.1Ti (at.%) alloys at 300–400°C, Scripta Materialia 59(4) (2008) 387-390.

[63] J. Lu, L. Dong, Y. Liu, Y. Fu, W. Zhang, Y. Du, Y. Zhang, Y. Zhao, Simultaneously enhancing the strength and ductility in titanium matrix composites via discontinuous network structure, Composites Part A: Applied Science and Manufacturing 136 (2020) 105971.

[64] L. Xiao, W.J. Lu, J.N. Qin, Y.F. Chen, D. Zhang, M.M. Wang, F. Zhu, B. Ji, Steady state creep of in situ TiB plus La2O3 reinforced high temperature titanium matrix composite, Materials Science and Engineering: A 499(1) (2009) 500-506.

[65] X. Guo, L. Wang, M. Wang, J. Qin, D. Zhang, W. Lu, Effects of degree of deformation on the microstructure, mechanical properties and texture of hybrid-reinforced titanium matrix composites, Acta Materialia 60(6) (2012) 2656-2667.

[66] W. Chen, The elevated-temperature creep behavior of boron-modified Ti-6Al-4V alloys, Materials transactions 50(7) (2009) 1690-1703.

[67] Z. Ma, S. Tjong, X. Meng, Creep behavior of in situ dual-scale particles-TiB whisker and TiC particulate-reinforced titanium composites, Journal of materials research 17(9) (2002) 2307-2313.

[68] B. Xiao, Z. Ma, J. Bl, Creep behavior of TiBw/Ti and (TiBw+ TiCp)/Ti in situ composite, Journal of materials science letters 21(11) (2002) 859-861.

[69] M. Barboza, C.M. Neto, C. Silva, Creep mechanisms and physical modeling for Ti–6Al–4V, Materials Science and Engineering: A 369(1-2) (2004) 201-209.

[70] V.M.C.A. de Oliveira, M.C.L. da Silva, C.G. Pinto, P.A. Suzuki, J.P.B. Machado, V.M. Chad, M.J.R. Barboza, Short-term creep properties of Ti-6Al-4V alloy subjected to surface plasma carburizing process, Journal of Materials Research and Technology 4(4) (2015) 359-366.

[71] L. Badea, M. Surand, J. Ruau, B. Viguier, Creep behavior of Ti-6Al-4V from 450 C to 600 C, University Polytechnica of Bucharest Scientific Bulletin, Series B 76(1) (2014) 185-196.

Chapter 8 Summary, Strength, Limitations, and Future Work

8.1 Summary and conclusive remarks

Ti-6Al-4V (Ti64) is the most widely used titanium alloy which provides a good balance of mechanical properties such as high specific strength, adequate stiffness, good fatigue behavior and outstanding corrosion resistance. Combination of these properties makes this material applicable in a wide range of industries including aerospace, petrochemical, and biomedical industries. However, the limited wear resistance and creep performance of the Ti64 alloy are major concerns in applications demanding high abrasion and erosion resistance as well as acceptable creep durability at medium service temperatures. Incorporation of ceramic reinforcing particles into the Ti64 matrix is known as one of the most effective strategies to develop new materials which offer an improvement not only in the hardness and strength but also in the wear and creep performance. These outstanding materials are called "metal matrix composite (MMC)" and bilaterally benefit from the properties of hard reinforcements and the ductile matrix in a single structure.

Additive manufacturing (AM) is a direct manufacturing technology which provides near-net-shape fabrication of metal and MMC parts with complex shapes, fine features, and unique geometries. Accordingly, it has gained a considerable attention in recent years to manufacture not only metallic materials but also MMCs. Laser powder bed fusion (L-PBF) is one of the most promising AM techniques which can be utilized to fabricate MMC components through processing of a composite powder. Since the composite powders meeting the requirements of the L-PBF process are not commercially available, they need to be produced by using appropriate techniques.

In this study, 5wt.%B_4C/Ti64 powder system was considered as a model to explore the effect of mixing type and process variables on the characteristics and behaviors of the

composite powder and develop a composite powder meeting the requirements of the L-PBF process. For this purpose, regular mixing and ball milling methods were employed with different mixing times to prepare a wide variety of mixed powder systems. The effects of the mixing method and the mixing time on size, size distribution, sphericity, shape, distribution state of guest particles, phase formation, plastic deformation, apparent density, and flow behavior of the prepared composite powder systems were studied. Moreover, the mechanisms involved in the flow behavior of the developed feedstocks were identified. Results revealed that the ideal mixed powder system needs to have: (i) non-free guest powder particles which are uniformly and homogeneously distributed throughout the system, (ii) host powder particles which have preserved their desired spherical shape, and (iii) the same flow behavior and apparent packing density as the starting host powder constituent.

The ideal 5wt.%B_4C/Ti64 composite powder was subjected to the L-PBF processing within a wide range of volumetric energy densities to fabricate TMC parts. For a better understanding of the microstructural evolutions in the L-PBF fabricated TMCs, the same powder system was subjected to the arc melting process with two different cooling rates. It is worth noting that regardless of the employed energy density, all parts fabricated by the L-PBF process experienced cracking and failure during the process due to the: (i) high content of hard and brittle TiB and TiC reinforcements in the microstructure, and (ii) high levels of thermal residual stresses induced by extremely fast cooling rates associated with the L-PBF process. However, microstructural characterization of the fabricated parts provided valuable information regarding the interaction of the laser beam with the composite powder and consequently increased our understanding of the microstructural evolutions during the L-PBF processing of composite powder systems. Microstructural

observations revealed that higher laser energy densities led to more intensified dissolution of B_4C particles into the matrix. As opposed to the arc-melted samples, the L-PBF fabricated TMCs did not contain primary TiB phase in their microstructure due to the non-equilibrium nature of the process caused by the extremely fast cooling rates. In addition, the L-PBF fabricated TMCs featured significantly higher hardness than the non-reinforced Ti64 counterparts.

The main focus domain of this research was fabricating high-performance TMCs with improved hardness, strength, wear resistance and creep performance than the non-reinforced Ti64 counterparts. For this purpose, a composite powder containing a minor B_4C content (0.2wt.%B_4C/Ti64) was developed by a novel technique benefitting from the advantages of both regular mixing and ball milling methods. This composite powder was subjected to a wide range of process parameters, and the optimum set of process parameters leading to the highly dense parts were manufactured. The monolithic Ti64 powder was also used to fabricate Ti64 parts for comparison purposes. The density measurement results revealed that for both Ti64 and TMC samples, the relative density of the parts first increased and then followed a decreasing trend by enhancing the energy density. At almost any given energy density, the TMC parts possessed higher relative density than their corresponding Ti64 counterparts. Microstructural characterization of the as-built TMC samples revealed the formation of nano-scale/sub-micron TiB needles which were homogeneously dispersed in a fully martensitic matrix. Owing the noticeably high cooling rates associated with the L-PBF process, both the equilibrium and Scheil-Gulliver non-equilibrium solidification models failed to predict the microstructure evolution of the fabricated TMCs. In the as-built condition, the TMC part showed 25% higher nanohardness, 8% higher yield strength, and 12% lower wear rate than the monolithic Ti64

counterpart. The calculations revealed that ~87% of the improvement in the yield strength of the TMC over the Ti64 sample was originating from the direct and indirect strengthening effects caused by TiB needles, while the rest (~13%) was arising from the solid solution strengthening of the matrix by carbon.

In order to tailor the mechanical properties and obtain TMC parts with the desired combination of mechanical properties, the TMC parts as well as the monolithic Ti64 counterparts were subjected to the subtransus and supertransus heat treatment cycles. Results revealed that the optimum heat treatment cycle was not the same for the Ti64 and TMC samples. This was attributed to the role that TiB needles in TMC parts played in restricting the growth of the prior β grains (PBGs) and nucleation/growth of α grains from the β phase. Although the employed subtransus heat treatment temperatures of 850 and 950 °C led to the full transformation of α' into the ($\alpha+\beta$) phases with a lamellar morphology in both Ti64 and TMC samples, they failed to eliminate the footprints of the laser scan tracks and the microstructural anisotropy caused by the elongated PBGs. The supertransus heat treatment cycle, on the other hand, removed the footprints and led to a fully isotropic microstructure with equiaxed PBGs. As opposed to the lamellar morphology of α in the supertransus treated Ti64 sample, this phase featured an equiaxed morphology in the supertransus treated TMC counterpart owing to the growth restricting effects of TiB needles. Moreover, TiB needles hindered the formation of the detrimental grain boundary α (GB-α) phase in the supertransus treated TMC sample. The presence of this detrimental phase in the supertransus treated Ti64 sample had a significant adverse effect not only on the strength, but also on the ductility by acting as preferential crack nucleation and propagation site.

From the strength-ductility combination perspective, subtransus heat treatment temperature of 950 °C and supertransus heat treatment temperature of 1050 °C were found to yield the optimum Ti64 and TMC samples, respectively. Since providing a fully isotropic microstructure with a good balance of strength and ductility, Ti64 and TMC samples subjected to the supertransus heat treatment cycle were considered for the short-term creep performance testing. For the sake of comparison, the as-built samples were also assessed. The best short-term creep performance (the longest rupture time and the lowest steady-state creep rate ($\dot{\varepsilon}_{ss}$)) among all samples was obtained for the heat treated TMC specimen. The superior creep performance of this sample was found to originated from several factors including: (i) the higher elastic modulus and threshold stress, (ii) the finer microstructure and higher density of interfaces (α-α, α-β, and α-TiB), acting as obstacles toward the movement of dislocations, and (iii) the load transfer from the matrix to the stiff TiB needles. The worst creep performance, on the other hand, was perceptible for the heat treated Ti64 sample in which the GB-α network acted as preferential crack nucleation and propagation sites during loading and consequently caused an intergranular fracture mode.

8.2 Strength, limitations, and future work

This research was aimed at fabricating high-performance titanium matrix composites (TMCs) using the laser powder bed fusion (L-PBF) additive manufacturing (AM) process. The L-PBF process is one of the most promising AM techniques which enables fabricating parts with complex geometries and intricate features in a single shot. Accordingly, it has recently gained a significant interest in low-volume production of custom-designed and near-net-shape components made of metallic materials and metal matrix composites (MMCs). However, one of the main challenges to the implementation of this technology in fabricating MMCs is the lack of commercially available composite powders serving as

the starting material in the L-PBF process. Researchers have proposed various techniques in recent years to produce composite powders for L-PBF processing. These techniques can be classified into two main categories of mechanical and non-mechanical methods. Since the incorporation of a second constituent into the powder system affects the powder properties, the characteristics and behaviors of the produced composite powders needs to be revisited to make sure that they meet the requirements of the L-PBF process. Although the behaviors (e.g., flowability, and packing density) of powders can be evaluated by various techniques, the technique(s) selected for assessing the behaviors of the produced composite powders should highly resemble the condition in the L-PBF process. To clarify, the results obtained by an inappropriate technique may provide misleading results regarding the applicability of the produced composite powder in the L-PBF process.

As the microstructural characterization in this research revealed, the equilibrium and non-equilibrium solidification models failed to accurately predict the solidification sequence during the L-PBF processing of the B_4C/Ti64 system with varying B_4C content. This was attributed to the extremely high cooling rates associated with the L-PBF process. The deviation of the microstructure from the equilibrium condition is a phenomenon which needs to be taken into consideration when designing a powder system for fabricating MMCs using the L-PBF process. It is worth noting that the extremely high cooling rates of the L-PBF process makes it possible to develop composites benefitting from reinforcements which are significantly finer than those observed in the same composites fabricated by conventional manufacturing processes. Combination of this refinement and the non-equilibrium microstructure of the matrix are the main factors leading to the improved mechanical properties of the L-PBF fabricated MMCs.

Although the L-PBF fabricated Ti64 and TMC parts in this research possessed noticeably high hardness, as well as yield and ultimate compressive strengths, they rendered ductilities lower than those of conventionally manufactured counterparts due to the fully martensitic microstructure of the matrix in both Ti64 and TMC. Based on our findings, the mechanical properties of the L-PBF fabricated Ti64 and TMC components can be successfully tailored by applying appropriate post-processing heat treatment strategies. The heat-treated components not only benefit from isotropic microstructure/mechanical properties, but also provide a good balance of strength and ductility. This makes the L-PBF fabricated TMCs of a high interest in various industries, especially the aerospace industry. It should be noted that although the TMCs reinforced with minor TiB featured a significant improvement in the compressive yield and ultimate strength in the heat-treated condition compared to their monolithic Ti64 counterparts, they did not show the same improvement in the tensile strength due to the presence of hard and brittle TiB needles in their microstructure. The characterization of the tensile properties and fracture toughness of the fabricated TMCs is a topic that is worth investigating in the future.

As the creep test results revealed, the short-term creep performance of the highly commercial Ti64 alloy can be improved by incorporating a minor amount of TiB reinforcement into the Ti64 matrix and employing appropriate post-processing heat treatment cycles. For future work, the author would suggest adding different amounts of TiB, TiC, or (TiB+TiC) reinforcements to the Ti64 alloy to develop various TMCs. These composites then need to be subjected to different post-processing heat treatments to investigate the role of reinforcement type and volume fraction on the creep performance of L-PBF fabricated TMCs. The creep test also needs to be performed at different temperatures and stresses to understand the creep mechanisms. The outcome of this

research is believed to introduce a new class of L-PBF fabricated TMCs with improved creep performance which can serve as fracture-critical members at elevated temperatures. For the future work, I would also suggest studying the fatigue performance of the fabricated TMCs and comparing them with the non-reinforced Ti64 counterparts fabricated by the L-PBF process.